Dynamic Behavior of Vibrated Dry Sand

Sphere Penetration Experiments and Discrete Element Modeling of Vibro-fluidization

Thèse présentée en vue de l'obtention du titre de
Docteur en sciences de l'ingénieur

par

Nicolas DENIES

Novembre 2010

This thesis was supervised by:

Prof. Dr. Ir. Alain Holeyman, Université catholique de Louvain

Members of the jury:

Prof. Dr. Ir. Jean-François Remacle, President, Université catholique de Louvain
Dr. Ir. Jean Canou, co-advisor, Université Paris-Est
Dr. Ir. Jean-Noël Roux, co-advisor, Université Paris-Est
Prof. Dr. Stefan Luding, University of Twente
Prof. Dr. Ir. Jean-François Thimus, Université catholique de Louvain

Acknowledgements

Le présent document résulte d'un travail de recherche doctorale de quatre années. Celui-ci n'aurait pas été possible sans l'aide, les encouragements et le support d'un grand nombre de personnes que je tiens à remercier.

Tout d'abord, le Professeur Alain Holeyman (UCL), mon promoteur, pour les nombreux échanges scientifiques que nous avons pu avoir tout au long de ma thèse de doctorat. Ses idées, ses connaissances mais surtout son ouverture d'esprit m'ont permis de travailler librement et de m'épanouir dans un domaine de l'ingénierie que j'affectionne plus particulièrement : la géotechnique. Je lui suis réellement reconnaissant de m'avoir laissé libre de mes choix scientifiques dans la définition du sujet et de ses approches expérimentale et numérique.

Je suis également redevable au Fonds pour la formation à la Recherche dans l'Industrie et dans l'Agriculture (FRIA) pour sa confiance et le financement de mes quatre années de recherche.

Je remercie les membres de mon jury de thèse, les Docteurs Jean Canou et Jean-Noël Roux (Université Paris-Est) ainsi que les Professeurs Stefan Luding (University of Twente) et Jean-François Thimus (UCL) pour leur lecture attentive du présent texte et pour leur enthousiasme lors de la défense privée, constituant une discussion scientifique que j'ai beaucoup appréciée. Merci également au Professeur Jean-François Remacle (UCL), président du jury, pour l'efficacité avec laquelle il a animé cette discussion et pour l'intérêt porté à ma thèse.

Je suis particulièrement reconnaissant envers les membres de mon Comité d'accompagnement, Jean Canou et Jean-Noël Roux pour la continuité de nos échanges tout au long de ma thèse.

Mes différents séjours, à l'Ecole Nationale des Ponts et Chaussées (ENPC), sous la guidance des Docteurs Jean Canou et Jean-Claude Dupla, m'ont permis d'acquérir les compétences techniques nécessaires à la réalisation d'une campagne expérimentale de qualité. Je tiens aussi à remercier l'ensemble des membres du laboratoire du CERMES pour leur accueil, leurs compétences et leur disponibilité.

Jean-Noël Roux a contribué à la réalisation de ma thèse par ses nombreux conseils dans le domaine du calcul numérique et le temps précieux qu'il m'a consacré, notamment lors de la relecture attentive du présent manuscrit.

Je suis redevable à José Flémal pour son magnifique travail sur les illustrations du présent document, ainsi que pour sa bonne humeur et son efficacité.

Je remercie Rosario Bonsangue (BBRI) pour son dynamisme et son aide dans la réalisation du dispositif expérimental de la présente thèse et Mr De Becker (Raymi) pour l'usinage des différentes pièces.

Un merci tout particulier à Valérie Whenham (BBRI) pour les nombreuses discussions techniques et les débats tout au long de ma recherche doctorale ainsi que pour ses nombreux conseils.

Je remercie les membres de l'Unité de Génie civil et environnemental de l'UCL, qui ont contribué à la réalisation de ma thèse. Plus particulièrement Quentin Fraselle et Laurent Goutière pour leur support constant et inconditionnel. Leur présence aura été un véritable moteur pour moi. Marie-Rose Bodart-Decelle et Viviane Misson-Delmarcelle, secrétaires, pour leur accueil, leur bonne humeur

infaillible et leur dévouement qui ont facilité la réalisation de ce travail. Vincent Forzee pour son aide dans l'utilisation du dispositif servo-hydraulique MTS. Antoine Bietlot, informaticien, pour sa disponibilité et sa sympathie. Mes collègues de bureau, Maud Nolmans, qui a réellement animé le bureau pendant deux ans, et Malek Allani, pour son enthousiasme constant pour la recherche en mécanique des sols. Merci à tous les deux d'avoir supporté et respecté mes longues réflexions silencieuses.

Je suis particulièrement reconnaissant envers le Professeur Jacques De Jaeger d'avoir initié ma passion pour la mécanique des sols par sa pédagogie et son enthousiasme. Je le remercie pour ses nombreux conseils et pour les échanges que nous avons eus tout au long de ma thèse. Je suis conscient d'avoir eu la chance de rencontrer quelqu'un partageant le même intérêt que moi pour le comportement des sols granulaires.

Merci aux professeurs Thierry Arnould, Jacques Dormal, Louis Ingels et Eddy Massart pour avoir aiguisé mon envie d'apprendre et pour leur patience.

Merci à mes amis pour leur amour, leur compréhension et leur attention dans la vie de tous les jours. Rien n'eût été possible sans leur présence et leur soutien constant : Gaëlle, Nicole et Yvons Aerts, Nicolas et Pierre André, Quentin Demolder, Sylvain Docquier, Thibaut Dupuis, Olivier d'Arripe, Kelvin Foo, Quentin Fraselle, Michel Guyette, Robert Haulait, Fabian Kumps, Raphaël Lahy, François Laurent, Stéphane Moyson, Mathieu Rekinger, Lee Roland, Nicolas Ronsmans, et tous les autres que je ne saurais citer.

Finalement, merci à mes parents, mon frère Amaury et ma sœur Anne-Catherine, pour leur amour et leur aide dans les moments difficiles.

Abstract

The research focuses on dynamic properties of vibrated dry sand within the framework of vibrodriving and vibrocompaction processes applied to granular soils.

Original experiments able to characterize the behavior of dry sand subjected to vertical vibration are first presented. In particular, the volume change and the motion pattern displayed by vertically vibrated sand particles are discussed. When cohesionless soil placed in a cylindrical container is vertically vibrated under the gravitational field (g), the UCL experiments performed on dry Fontainebleau sand allow one to distinguish three different types of dynamic behavior, depending on the acceleration amplitude (a): the densification ($a/g < 1$), the instability surface ($a/g \approx 1$), and the vibro-fluid behaviors ($a/g > 1$). In the densification range, the sand simply settles. When the acceleration is increased beyond 1g, granular convection is observed and there is an instability in the sand mass leading to the emergence of an inclined free surface. If the acceleration is further increased, the free surface progressively flattens. There is an impressive dilatation of the whole sample and grains saltation is noticed. The sand becomes fully vibro-fluidized.

Results of sphere penetration experiments (SPE's) are also presented. The sinking logs of the SPE's conducted at UCL do not follow Stokes law, as initially suggested by the 1962 Barkan experiments. An exponentially decreasing penetration profile is observed on one hand in the densification range although no refusal depth was reached. In the vibro-fluid regime, on the other hand, the sphere quickly sinks into the vibrated medium and stabilizes at a certain equilibrium penetration. Hence, the concept of vibro-viscosity coefficient, proposed by Barkan (1962), is to be reappraised in our opinion.

In order to emphasize the evolution of the internal state of sand during vibration, one resorts to Discrete Element Modeling (DEM). Numerical simulations of vibrated granular sample are conducted under lateral periodic boundary conditions, considering only the interactions between the grains. In this way, one tries to track down the fundamental origin of the vibro-fluidization. A stratified analysis is used to describe the assembly behavior from the microscopic to the macroscopic scale.

When the sample is vibrated at low acceleration amplitude ($a/g = 0.5$), it swiftly reaches a steady vibratory regime. There are successive compacting and dilating phases corresponding respectively to upward and downward acceleration phases of each cycle. The contact network is still preserved during the whole cycle and the granular material seems to behave like an elastic solid with regards to the macro- scale of the assembly. Once the acceleration amplitude is set to 1.02g, the contact network is cyclically disintegrated and the force chains get unbound resulting in shear strength degradation. Cyclic vibro-fluidization is therefore noticed. At the same time, the emergence of "fluid" stresses is observed, underscoring the dual nature of vibrated dry cohesionless soil.

Hence, vibrations result in a particular state of granular matter, called the "vibro-fluid" state. It is characterized by a phase transition corresponding to the transformation of a solidlike material into a complex fluid identified by an abrupt change in its properties resulting in shear strength degradation.

Key Words: vibrodriving, vibrocompaction, vibro-fluidization, sphere penetration experiments (SPE's), Discrete Element Modeling (DEM), vibrated dry sand, rheology, mechanical engineering

Résumé

La présente recherche s'intéresse à la caractérisation des propriétés dynamiques du sable sec vibré. L'intérêt pour ce domaine de l'ingénierie provient de l'étude des procédés du vibrofonçage et du vibrocompactage appliqués aux sols pulvérulents.

Dans cette perspective, des expériences, capables de caractériser le comportement du sable sec soumis à des vibrations verticales, y sont présentées. La variation de l'indice des vides et les phénomènes de recirculation des particules de sable, ainsi que les résultats d'expériences de pénétration à la sphère (SPE's) y sont discutés.

Quand un sable sec pulvérulent, placé dans un container cylindrique, est mis en vibration verticale sous le champ gravitaire (g), les expériences conduites sur le sable de Fontainebleau, identifient trois types de comportements dynamiques distincts, dépendant de l'amplitude de l'accélération des vibrations (a) : la densification ($a/g<1$), l'instabilité de surface ($a/g\approx1$) et la vibro-fluidification ($a/g>1$). Le régime de densification se traduit par un tassement du sable vibré. Quand l'accélération atteint 1g, le phénomène de convection granulaire est observé : celui-ci résulte en une instabilité de la surface libre qui se met en pente sous l'effet des vibrations. Si l'accélération est encore augmentée, la surface libre est progressivement disloquée. Une forte dilatation de l'échantillon est constatée accompagnée de saltation. Le sable devient vibro-fluidifié. Dans le cadre des expériences de pénétration à la sphère, réalisées à l'UCL, les profils d'enfoncement des SPE's, ne suivent pas la loi de Stokes comme annoncé par Barkan (1962). Un profil exponentiel décroissant est en effet observé dans le régime de densification bien qu'aucune profondeur de refoulement ne soit atteinte. Dans le régime vibro-fluide, la sphère s'enfonce rapidement dans le milieu vibré jusqu'à une hauteur d'équilibre. Il convient donc de réévaluer le concept de coefficient de vibro-viscosité, proposé par Barkan (1962).

Dans le but de mettre en évidence l'évolution de l'état interne du matériau granulaire durant la vibration, des simulations par la méthode des éléments discrets (DEM) ont été réalisées. De manière à ne considérer que les interactions entre grains, le modèle est muni de frontières latérales périodiques, afin d'approcher les mécanismes fondamentaux liés à la vibro-fluidification. Une analyse par strate est utilisée pour décrire le comportement du matériau de l'échelle microscopique des grains à l'échelle macroscopique de l'assemblage.

A faible amplitude d'accélération ($a/g=0.5$), l'échantillon atteint rapidement un régime vibratoire permanent caractérisé par une succession de phases de dilatation et de compaction correspondant aux phases d'accélération négative et positive du container. Le réseau des contacts est cependant préservé durant le cycle complet et le matériau granulaire semble se comporter comme un solide élastique, du moins à l'échelle macroscopique de l'assemblage. A 1.02g, une vibro-fluidification cyclique de l'échantillon se produit. Le réseau des contacts se désintègre et les chaînes de force sont rompues entraînant ainsi la dégradation de la résistance au cisaillement. Pour ce régime de vibration en particulier, l'apparition de contraintes « fluides » est constatée : celles-ci témoignent de la dualité du matériau granulaire vibré.

L'état vibro-fluidifié peut dès lors être caractérisé par une transition de phase pour laquelle un changement dans la structure du matériau est observé : la transformation d'un matériau solide en un fluide complexe identifié par un changement brusque de ces propriétés et par la dégradation de sa résistance au cisaillement.

Mots-clés : vibrofonçage, vibrocompaction, vibro-fluidification, expériences de pénétration à la sphère (SPE's), modélisation par éléments discrets (DEM), sable sec vibré, rhéologie, génie mécanique

Contents

Acknowledgements i
Abstract iii
Résumé v
Contents vii
1 Introduction 1
1.1 Context of the research 1
1.2 Purpose of the research 2
2 Vibratory driving process and shear strength degradation of vibrated sand 5
2.1 Introduction 5
2.2 Vibratory driving process 5
2.2.1 Definition and principles 5
2.2.2 Historical development 6
2.2.3 Engineering issues 6
2.2.4 Governing parameters of vibrodriving 7
2.2.5 Vibrodriving prediction models 11
2.2.6 Multiscale soil behavior 12
2.3 Vibratory driving in sand: experimental observations 13
2.4 Sand shear strength degradation 16
2.4.1 Cyclic behavior of saturated sand 16
a. Flow liquefaction phenomenon 16
b. Cyclic mobility phenomenon 17
c. Saturated sand degradation within the framework of vibrodriving 18
d. Intrinsic Coulomb failure criterion for saturated sand 21
2.4.2 Cyclic behavior of dry sand 21
a. Effects of vibrations on volume change 22
b. Effects of vibrations on internal friction of the sand 30
c. Vibro-fluidization phenomenon 37
d. Revisited intrinsic Coulomb failure criterion for vibrated dry sand 37
e. Barkan's conceptual SPE model (1962) 39
2.5 Conclusions and research perspectives 41
2.5.1 Influence of vibrations on the volume change of dry sand 41
2.5.2 Influence of vibrations on the shear strength of dry sand 43
2.5.3 Vibro-fluidization of dry sand 46
2.5.4 Sphere penetration experiments (SPE's) 49
3 Experimental research on dynamic behavior of vibrated dry sand 51
3.1 Introduction 51
3.2 New UCL-SPE apparatus 52
3.3 Fontainebleau sand 57
3.3.1 Fontainebleau sand characteristics 57
3.3.2 Fontainebleau sand sample preparation 60
3.4 Vertically vibrated dry sand behavior 60
3.4.1 Governing parameters 60
3.4.2 Volume change with time 61
3.4.3 Volume change with number of cycles 67
3.4.4 Dry sand vibratory behavior 67
a. Densification behavior 69

b. Instability surface behavior 69
c. Vibro-fluid behavior 74
3.4.5 Dry density after vibrations 75
3.5 Sphere penetration experiments (SPE's) 76
3.5.1 Field of application and procedure of the SPE's 76
3.5.2 Results of the UCL-SPE's and discussion of the results 78
a. SPE's in the densification range (Γ<1) 78
b. SPE's in the instability surface range (Γ ≈ 1) 82
c. SPE's in the vibro-fluid range (Γ > 1) 82
d. Synthesis of the SPE's 89
3.6 Discussion 91
3.6.1 Laboratory investigation of dynamic behavior of dry sand: Solid – fluid transition 91
a. Behavior classification according to the acceleration amplitude 91
b. Granular convection and vibro-fluid state of matter 91
c. Instability surface behavior 93
d. Micromechanical analysis of granular convection and vibro-fluidization 94
3.6.2 Comparison with reduced scale tests of vibratory driving 95
a. Behavior classification according to the cyclic force amplitude 95
b. Cyclic stability diagram 96
c. Connection between acceleration and cyclic force classifications 97
d. Influence of the boundaries of the reduced scale models 97
3.6.3 Analogy with vibrodriving experiments in sand 98
4 Discrete Element Modeling of vibrated dry sand 99
4.1 Introduction of the DEM simulations 99
4.1.1 Granular matter 99
4.1.2 Numerical modeling of granular matter 99
4.1.3 Discrete Element Method (DEM) 102
a. The PFC2D Particle-Flow model 102
b. Contact laws 102
c. Slip model of contact 105
d. Spin motion and rolling resistance at the contact 105
e. Viscous damping at the contact 106
4.1.4 Description of the numerical model 107
a. Generation of the DEM sample 107
b. Dimensional and physical properties of the numerical sample 109
c. Stratified characterization of the numerical sample at rest 111
4.2 Dynamic behavior of the numerical model 119
4.2.1 Elastic behavior of vibrated granular matter 120
a. Evolution of the internal state during vibration 121
b. Coupled influence of the displacement and the frequency 128
c. Discussion of the results 128
4.2.2 Vibro-fluidization of vibrated granular matter 136
a. Evolution of the internal state during vibration 136
b. Coupled influence of the displacement and the frequency 159
c. Discussion of the results 159
4.3 Conclusion 162
5 Vibro-fluidization of vibrated dry sand within the framework of vibrodriving 167

5.1 Vibro-driving resistance of dry sand 167
5.2 “Fast” and “slow” vibro-driving motions 168
5.3 Micromechanical modeling of vibro-driving motion 169
5.4 Liquefaction vs. vibro-fluidization 170
6 Conclusion and perspectives 175
6.1 Outline of the research 175
6.1.1 Review of the literature (Chapter 2) 175
a. Optimum vibrocompaction 175
b. Decrease of the shear strength 176
c. Vibro-fluidization 176
6.1.2 Laboratory investigation (Chapter 3) 176
a. Volume change 176
b. Dry sand vibratory behavior 176
c. Dry density after vibration 178
d. Sphere penetration experiments (SPE’s) 178
6.1.3 Discrete Element Modeling (Chapter 4) 178
a. Elastic behavior 178
b. Vibro-fluid behavior 179
6.1.4 “Vibro-fluid” resistance (Chapter 5) 179
6.2 Summary of the scientific contributions 179
6.3 Perspectives and future developments 180
6.3.1 Laboratory investigations 180
6.3.2 Discrete Element Modeling 180
6.3.3 Void ratio as the key of the degradation process 181
7 Appendix 183
7.1 Contact mechanics of spherical bodies 183
7.1.1 Introduction 183
7.1.2 Normal elastic contact of solids 183
a. Normal elastic indentation of spheres 183
b. Relative motions of surface in contact 189
7.1.3 Tangential loading and sliding contact 189
a. “Gross-slip” motion 189
b. “Stick-slip” motion 191
c. Torsional loading 195
d. Rolling contact 196
e. Energy loss during tangential cyclic loading 197
7.1.4 Elastic normal impact 198
7.1.5 Inelastic normal impact 200
a. Normal inelastic indentation of spheres 200
b. Normal coefficient of restitution 202
7.1.6 Elastic oblique impact 205
a. The Mindlin and Deresiewicz (MD) approach (1953) 206
b. Maw, Barber and Fawcett (MBF) approach (1976, 1981) 210
7.1.7 Inelastic oblique impact 214
7.1.8 Conclusions 217
7.2 Roughness analysis of the container and the sphere 220
7.3 Sphere penetration logs in the densification range 222
7.4 Influence of the contact laws on the behavior of a granular assemblage in DEM 225

7.5 Calculation of the damping forces in the Discrete Element Model 226
7.6 Calculation of the contact stresses in the Discrete Element Model 227
7.7 Influence of the displacement and the frequency in the elastic range (Γ = 0.5) for DEM simulations 230
7.8 Influence of the displacement and the frequency in the vibro-fluid range (Γ = 1.02) for DEM simulations 233
8 Bibliography 235
9 List of Symbols 249
9.1 Soil mechanics notations 249
9.1.1 Roman symbols 249
9.1.2 Greek symbols 250
9.1.3 Abbreviations 251
9.2 DEM and contact mechanics notations 251
9.2.1 Roman symbols 251
9.2.2 Greek symbols 253
9.2.3 Abbreviations 254
10 List of figures 255

1 Introduction

1.1 Context of the research

The need for the design of protective measures against the risk of major earthquakes has been stimulating research in the field of seismic engineering for decades. With a view to protect structures and human lives, researchers sought a better understanding of the soil response to cyclic straining resulting from earthquakes, and in particular the degradation of its shear strength characteristics due to vibrations. But civil engineers have also come up with ideas to use the degraded shear strength of vibrated soils at their advantage.

Vibratory driving – also called vibrodriving – is a technique using vibrations to insert a profile in the soil. This process, represented in Fig. 1-1, is faster, cheaper and consumes less energy than impact driving and jacking; in particular in soils such as dry or saturated sands.

Figure 1-1: Steel pile driven with vibrator in Belleville (F) (http://www.leductp.com/).

During vibrations, the soil surrounding the profile undergoes changes in its physical properties. These changes condition the efficiency of the process. However, it is very difficult to estimate the vibro-driveability of a profile considering only the soil data from the site survey. The assessment of the driving velocity and the refusal depth of the pile remains a challenge for the engineers. The current design methods

are often associated with impact-driven piles and do not provide guidelines for the design of vibratory -driven piles. However, both processes differ in the way the soil behaves and reacts during the installation.

For those reasons, a hesitation from the contractors is noticed in the use of this process for installing piles to their final design depth. Moreover, when it is used, a propensity for over-designed vibratory units is often observed due to the lack of reliable theory of power transference to the soil.

For the purpose of improving the mastery of vibrodriving, full-scale tests have been performed in several countries providing experimental databases appreciated by the profession. Such tests have been recently conducted in Belgium (BBRI, 1994, Whenham et al., 2006 and Whenham et al., 2009) and in France (Borel et al., 2002, Sieffert, 2004 and Réseau Génie Civil et Urbain, 2006).

Monitoring can provide information over the behavior of the vibrated profile and the soil reaction – with measurement of the acceleration, strain, pore pressure, penetration velocity, driving frequency and displacement amplitude, vibratory and static forces applied to the pile – or indications over the energy consumed by the power pack during the installation. Particle velocity measurements allow to mitigate the effects of the vibrations on the environment. The consideration of case histories of vibrodriving of fully instrumented profiles contribute to a better understanding and an improved control of the process.

Nevertheless, within the framework of these full-scale experiments, the soil conditions are only characterized but not controlled. In order to remedy this limitation, reduced-scale tests and conceptual model tests come into the picture. These kinds of experimental modeling ensure well-known soil conditions with a precise preparation of the sample and/or a continuous mastery of the confining pressure. Moreover, they are generally cheaper than full-scale tests.

Reduced-scale tests allow the achievement of parametric studies for the purpose of highlighting the governing parameters influencing the efficiency of the process. Laboratory experiments may also provide valuable information to prepare full-scale experiments.

The key of the problem lies in the harnessing of soil dynamic properties. The use of conceptual model tests allows removing the incertitudes related to the structural behavior of the profile and to the vibratory driving unit. It consists in a real opportunity to step down the inconsistencies between predictions and experimental observations by mastering little by little the behavior of soil once it is subjected to vibrations.

If shear strength degradation of saturated sand has been previously tackled by numerous researchers (Vanden Berghe, 2001), questions over dry sand behavior still remain unresolved. It can be explained by the abundance of groundwaters in the regions where the technique has been developed (Russia, Europe, USA,…). But the soar of the construction in desert regions coupled with the efficiency of the process particularly in dry loose sands justifies the interest for the dynamic properties of vibrated dry sand.

1.2 Purpose of the research

The purpose of the study is to highlight the influence of the acceleration amplitude of vibration on the behavior of dry sand. This latter will be therefore investigated with the help of a coupled approach combining the use of conceptual

model testing and discrete element modeling. Hence, the present work can be considered in line with fundamental research focusing only on the behavior of the soil. The study is organized in four steps.

In the first part of the text (corresponding to Chapter 2), the reader is introduced to the vibrodriving process. The behavior of the soil around the profile is explained in light of the literature. The core of the State-of-the-Art review is devoted to the influence of the acceleration amplitude of vibration on the volume change and on the shear strength of dry sand. The existence of a "vibro-fluidization" phenomenon is postulated to characterize the shear strength degradation which could be taken into account by a revisited intrinsic Coulomb failure criterion for vibrated dry sand.

The second part of the work (presented in Chapter 3) focuses on laboratory investigation of vertically vibrated dry Fontainebleau sand. The conceptual model test developed at UCL is described in detail. The volume change and the motion patterns displayed by sand grains during the vibration are investigated for different amplitudes of acceleration. Based on the conceptual work of Barkan (1962), sphere penetration experiments (SPE's) have been performed. The purpose of Chapter 3 is to highlight the effect of the acceleration amplitude of the vibration on the behavior of dry sand. Different regimes depending on the acceleration are identified and the influence of the lateral boundaries of the model on the vibro-fluidization phenomenon is discussed.

In the third part of the research (Chapter 4), the granular material is modelled with the help of the Discrete Element Method (DEM). The use of DEM underlines the evolution of the internal state of the granular sample during vibration. It gives a full desription of the sand behavior from micro- to macroscopic scale, for different acceleration amplitudes of vibration. The purpose of Chapter 4 is to tackle the fundamental origin of the vibro-fluidization considering only the interactions between the grains. The existence of vibro-fluidization is verified when the influence of rigid lateral boundaries is neglected.

In the last part of the work (Chapter 5), the results of the present research are integrated within the framework of vibratory pile driving. Vibro-driving resistance of dry sand is analyzed considering the vibro-fluidization phenomenon. Based on the work of Rodger (1976), micromechanical description of fast and slow vibro-driving motions is proposed in such a way to explore the influence of the initial sand density on the success of the vibrodriving process. Finally, a dimensionless characterization of liquefaction and vibro-fluidization is performed at macroscopic and microscopic scales with the help of the Discrete Element Method.

When an assemblage of grains is subjected to vibrations, its behavior depends on the arrangement of the grains and on the way they interact with one another. Section 7.1 (in the Appendix) focuses on the theoretical description of contact mechanics between spherical bodies.

Contact mechanics supports the assumptions of the Discrete Element Modeling and allows to investigate the behavior of vibrated dry granular materials in the view of a multi-scales approach considering the scales of the contacts, the grains and the assemblage.

2 Vibratory driving process and shear strength degradation of vibrated sand

2.1 Introduction

The purpose of this chapter is to position the present research concerning dynamic properties of vibrated dry sand relatively to the existing researches relating to the vibratory driving process.

The vibratory driving technique is briefly presented and references to previous or current contributions related to this process are given. Engineering issues related to this technique are reviewed considering the four major actors of the process: the pile, the vibrator, the power generator and the surrounding soil. The action of the vibrator and the governing parameters of the method are presented. Vibrodriving prediction models are referenced.

The associated soil behavior around the pile is then discussed only considering the shear strength degradation of granular soils. Vibrodriving experiments in sand are presented in such a view to identify the governing parameters of the "fluidization" phenomena which occur in the soil during vibratory driving. For the purpose of understanding these phenomena, vibrated sand behavior is critiqued under saturated or dry conditions.

Cyclic behavior of saturated sand is first analyzed. In this case, both phenomena hidden behind the term "fluidization" are identified: the "flow liquefaction" and the "cyclic mobility". They are shown to play an important role in the shear strength degradation of saturated sand arising during vibrodriving.

Cyclic behavior of dry sand is then investigated considering the influence of vibration on its volume change and on its shear strength. The existence of a "vibro-fluidization" phenomenon is postulated to characterize the shear strength degradation of a vibrated dry granular material which could be taken into account by a revisited intrinsic Coulomb failure criterion.

Finally, sphere penetration experiments of Barkan (1962) are presented in order to study the vibroviscous character of the soil resistance when it is subjected to vibrations. According to Barkan (1962), the internal friction resistance of dry sand tends to vanish and starts behaving like a viscous fluid when subjected to intense vibrations. Hence, sphere penetration experiments were designed to investigate this behavior and confirm the coefficient of vibro-viscosity, if warranted.

The following review does not pretend to be exhaustive. The aim is to introduce the reader to the vibratory driving technique and to the sand behavior around the vibrated profile. Then, it concentrates on the cyclic behavior of dry sand which constitutes the heart of the present research.

2.2 Vibratory driving process

2.2.1 Definition and principles

Vibrodriving is a technique for driving profiles as piles, tubes or sheet-piles swiftly into the soil by transmitting to the driving unit a longitudinal vibrating motion of predetermined frequency and displacement amplitude. The vibrations

result in a reduction of the ground resistance, allowing penetration under the action of a relatively small surcharge force (Rodger and Littlejohn, 1980).

2.2.2 Historical development

Historically, it seems that the vibratory driving technique appeared simultaneously in the 30's in Germany and in the former URSS. Pavyluk, who studied the effect of vibrations maintained on soil, introduced in 1931 the concept of driving profiles using vibrations. This work was later reported by Barkan (1962), who studied the effects of vibrations on the mechanical properties of soil, showing that the vertical vibration of a pile remarkably decreases the skin friction of surrounding soil.

In the 50's, vibrodriving was used for the first time for the installation of about 4000 steel sheet-piles 9-12 meter long during the construction of the Gorki Hydroelectric Station (now called Nizhny Novgorod Hydroelectric Station, located in Russia). Using vibratory driver BT-5 (working between 38 and 45 Hz), the production rates reached were 11m in two or three min. Encouraged by the previous successes obtained by the Russian constructors, major manufacturers of vibrators were developed in Germany, USA, France, The Netherlands and Japan. Unfortunately, although great progress has been made in the technological development of various vibratory hammers (Holeyman, 2000) adapted with engineering ability to different types of soil and specific piles (Rodger and Littlejohn, 1980), due to a lack of fundamental understanding of the complex power pack-vibrator-profile-soil interactions, the vibro-driveability of a given profile into a given soil remains difficult to estimate.

2.2.3 Engineering issues

Figure 1-1 illustrates the vibrodriving of a pile on a typical site. Four major actors play a role in the mechanics of the vibratory driving process: the pile to be driven, the selected vibrator, the power generator, and the imposed soil conditions. Indeed, if it is obvious that soil properties influence the process efficiency, it also depends on the geometrical and mechanical properties of the profile (Rao, 1993 and Wang, 1994), on the vibratory hammer capacity in terms of the weight of the nonvibrating part of the vibrator and of its eccentric moment (Holeyman et al., 1996) and on the effective power supply provided by the hydraulic group (Holeyman and Whenham, 2008).

In the vibrodriving process, constructors are interested by mastering the following engineering issues, illustrated in Fig. 2-1. In spite of the numerous field studies conducted to determine the long-term bearing capacity of the vibratory driven pile, its evaluation remains a challenge at the present time (Russian Standard SNIP II-B.5-67, Polish Standard PN-83/B-02482, RGCU Vibratory pile-driving technical guide 2006). Research is needed to establish a vibratory testing procedure allowing the determination of the long-term bearing capacity from the monitoring of the vibratory driving.

The prediction of vibro-driveability remains an issue, depending on the soil resistance to vibratory driving. If this latter can be calculated considering constant degradation parameters depending on the types of soil and based on soil investigations results (Holeyman, 1996 and 2000), there is a lack of experimental data to confirm this approach.

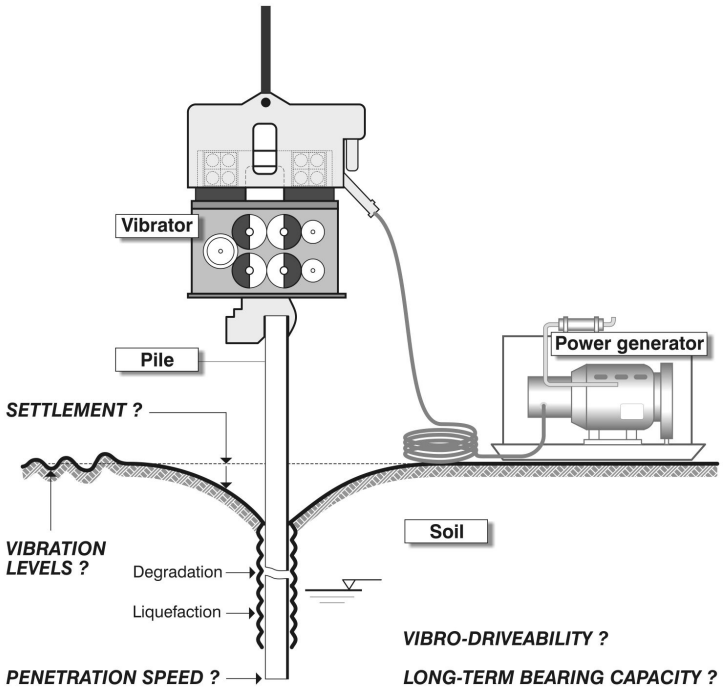

Figure 2-1: Vibrodriving : engineering issues, after Holeyman (2000).

The coupled influence of the displacement amplitude and frequency on the driving velocity of the profile into the soil remains relatively misunderstood. Indeed, if vibrodriving is used more and more to insert piles or sheet-piles into the soil, the required acceleration and frequency to enforce penetration still remain difficult to estimate. It is not always necessary to operate the hydraulic group at the maximum energy consumption to obtain the maximum penetration velocity.

Other engineering issues concern the soil vibro-compaction and the change in strength parameters in the near field around the vibratory driven pile. Finally, mastering the propagation of vibrations to the surrounding soil to avoid vibratory nuisance (noise pollution or structural damages) to the environment remains a challenge.

2.2.4 Governing parameters of vibrodriving

In vibrodriving, the vibrations are applied to the pile with the help of a vibrator, illustrated in Fig. 2-2. Figure 2-3a details the different components of this latter. As explained in Holeyman (2000) and Vanden Berghe (2001), the vibrator has a double vibratory and a stationary effect on the vibrated profile.

The vibratory action is produced by the counter-rotating eccentric masses actuated inside an “exciter block”. Each pair of masses is turning around its axis at the same frequency in opposite direction. This rotating motion induces a centrifugal force, as illustrated in Fig. 2-4, where F_v is the generated vertical dynamic force component, F_c is the centrifugal force and F_h is the horizontal dynamic force

component. As observed in Fig. 2-4, the horizontal force components are eliminated and the inertial effects of the symetrically moving masses lead to the following sinusoidal vertical force:

Figure 2-2: Vibrodriver PTC 50HD2 (http://www.ptc.fayat.com/)

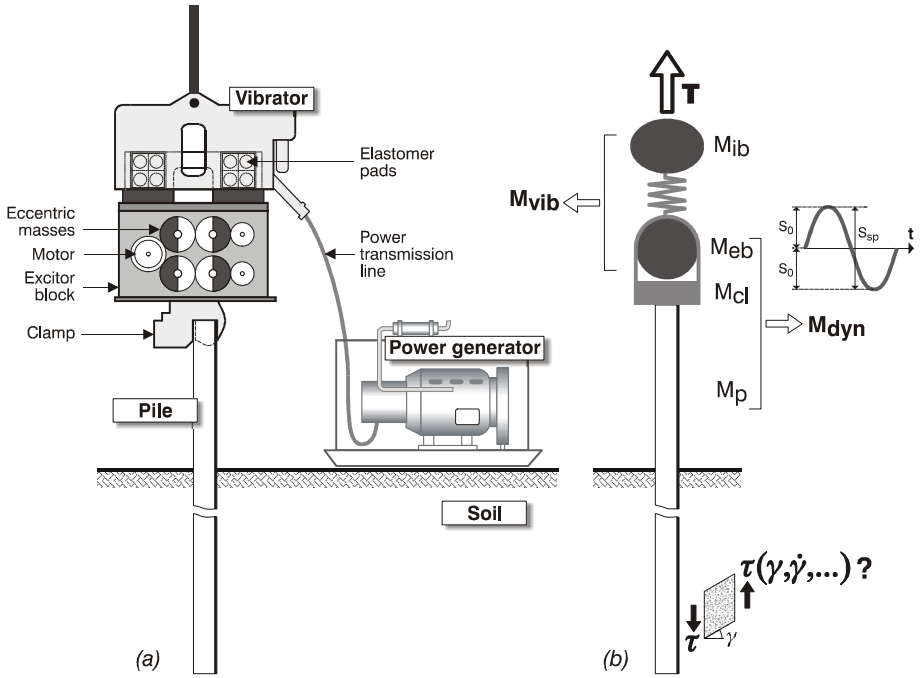

Figure 2-3: Components of the hydraulic vibrator, Holeyman 2000.

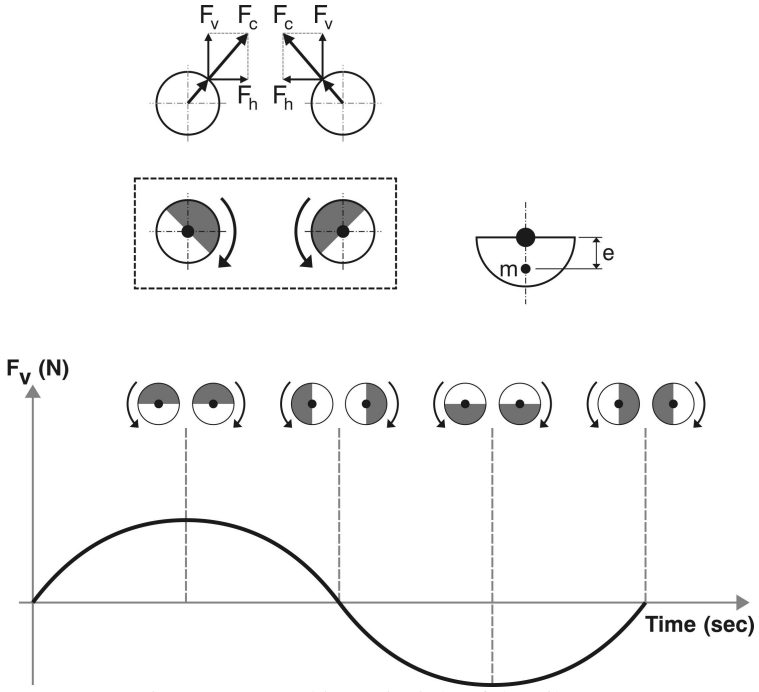

Figure 2-4: Working principle of the vibrator.

$$F_v = me.\omega^2 \sin(\omega.t) = F_c \sin(\omega.t) = F_c \sin(2\pi fr.t) \quad \text{(Eq. 2-1)}$$

where *me* is the total eccentric moment of the vibrator (kg.m), ω the angular frequency of the vibrator (rad/s), fr the frequency of the vibrator (Hz) and t the time (s).

The vibratory action is balanced by the soil reaction and the reactive inertial effects of the masses subjected to the vertical dynamic force. The exciter block is assumed to apply a longitudinal vibrating motion to the profile as long as the center of gravity of the whole rotating masses system is aligned with the neutral axis of the profile.

The connection between the vibrator and the vibrated pile is provided by a clamping device which transmits the vibration to the profile without damaging it.

The vibrator is generally suspended to a carrier. As illustrated in Fig. 2-3b, it can be viewed as a two degrees of freedom system moving in the longitudinal direction: an exciter block of mass M_{eb} and an isolator block of mass M_{ib}, sometimes called bias mass. Therefore, the mass of the vibrator is $M_{vib} = M_{eb}+M_{ib}$.

A vibration isolator mechanism is installed in order to avoid energy transfer to the carrier. This system is constituted of a quasi-stationary heavy mass directly suspended to the suspension hook and an intervening spring, generally consisting of elastometer pads.

The mechanical action of the vibrator includes a cyclic term, F_v, given by equation (2-1) and a static term taking into account the sum of the weight of the bias mass, the exciter block, the clamping device and the pile. It is also possible to

consider the retaining force, T_c, applied by the carrier. The total load applied on the soil during vibratory pile driving is given by:

$$F(t) = (M_{ib} + M_{eb} + M_c + M_p)g + me.\omega^2 \sin(\omega t) - T_c \quad \text{(Eq. 2-2)}$$

where F is the total vertical load applied to the soil (N), M_{ib} the bias mass (kg), M_{eb} the mass of the exciter block (kg), M_c the mass of the clamping device (kg), M_p the mass of the pile (kg), g the gravitational acceleration (m/s²) and T_c the suspension force (N).

The movement of the vibrated boby is refered to the "maximum amplitude", listed in the product specifications. The "maximum amplitude", S_{sp}, corresponds to the double amplitude of the movement for a free hanging vibrator assuming a dynamic mass consisting of the exciter bloc and the clamping device:

$$S_{sp} = 2s_0 = \frac{2me}{M_{eb} + M_c} \quad \text{(Eq. 2-3)}$$

where s_0 is the single amplitude of the vibrator (mm). Assuming rigid body dynamics, the amplitude of the free hanging pile can be derived from equation (2-3):

$$2A = \frac{2me}{M_{eb} + M_c} \frac{M_{eb} + M_c}{M_{eb} + M_c + M_p} = \frac{2me}{M_{eb} + M_c + M_p} = \frac{2me}{M_{dyn}} \quad \text{(Eq. 2-4)}$$

where A is the single amplitude of the dynamic mass, M_{dyn}, consisting of the sum of the masses of the exciter block, the clamp and the pile.

Two types of vibrator are commercially available: the electrical and the hydraulic vibrators. Hydraulic vibrators are the most commonly used. They present light weight and ease of adjustement of the operating parameters. Moreover, they can be utilized for on shore jobs, as well as for offshore jobs and in underwater conditions. The motor is located in the exciter block and it is powered by a diesel-hydraulic power generator, as illustrated in Fig. 2-1. Several types of hydraulic vibrators are commercially available and described in RGCU Vibratory pile-driving technical guide 2006. Five types of vibrators can be distinguished, identified in Table 2-1.

The governing parameters used to define the movement of the vibrated profile are then the displacement amplitude and the frequency of the vibrator. It is to note that the "maximum amplitude", S_{sp}, and the amplitude of the free hanging pile, A, do not depend on the frequency of the vibrator.

The two governing parameters of the process induces the application of a dimensionless acceleration, Γ, to the vibrated pile:

$$\Gamma = \frac{a}{g} \quad \text{(Eq. 2-5)}$$

where a is the acceleration amplitude (m/s²) given by:

$$a = A(2\pi fr)^2 \quad \text{(Eq. 2-6)}$$

Type	Frequency range (rpm)	Eccentric moment (kg.m)	Maximum centrifugal force (kN)	Free hanging double amplitude (mm)
"Standard frequency"	1300-1800	up to 230	up to 4600	up to 30
High frequency	2000-2500	6 to 45	400 to 2700	13 to 22
Variable eccentricity	2300	10 to 54	600 to 3300	14 to 17
Excavator accessory	1800 to 3000	1 to 13	70 to 500	6 to 20
Resonant driver	6000	50	20000 (in theory)	Self destructing

Table 2-1: Vibrator types, after Holeyman (2000).

2.2.5 Vibrodriving prediction models

Models that have been proposed to predict power pack-vibrator-pile-soil interactions differ in the way they account for mechanical engineering principles. According to Viking (1997), they can be classified in four groups:

- Models based on force equilibrium,
- Models based on momentum conservation,
- Models based on energy conservation,
- Models based on integration of the equation of laws of motion.

The purpose of these models is to be able to predict the ability of a vibrator to drive a pile in specific soil conditions, to determine the refusal depth, to evaluate the environmental disturbance and to estimate the penetration velocity. A review of these models is available in Viking (1997 and 2002), Holeyman (2000) and Vanden Berghe (2001).

More recently, Whenham and Holeyman (2010) have performed a confrontation between several vibrodriving prediction models and experimental observations. The results of fully instrumented real scale vibrodriving tests come from various experimental databases. They were collected in Belgium (BBRI, 1994, Whenham et al, 2006 and Whenham et al., 2009), in France (Sieffert, 2004 and RGCU Vibratory pile-driving technical guide 2006) and in The Netherlands (via the online database GeoBrain as reported in Hemmen and Bles, 2005). The conclusions of Whenham and Holeyman (2010) are the following.

Assumptions usually adopted in vibrodriving prediction models contrast with experimental evidence and can lead to significant consequences for the prediction of the "vibrodriveability" of the profile. Discrepancy mainly concerns the vibratory action (load and energy) actually transmitted to the pile (as explained in Holeyman and Whenham, 2008).

Some methods consider two criteria: one based on a force equilibrium between acting and resisting forces, the other based on minimum displacement amplitudes. A combination of these two criteria leads to a better estimation of refusal depth.

The friction ratio deduced from CPT results has to be taken into account in soil degradation calculation and displacement amplitude criterion definition. Whenham and Holeyman (2010) investigated this question considering a method assessing the vibrodriveability of profiles and published in the dutch CUR166 manual. The CUR166 method is only based on cone penetration resistance results regardless of the friction ratio values. When the authors compared the results of this method with the results of GeoBrain and BBRI databases, soil resistances estimated for cohesive soils were systematically lower than soil resistances evaluated for granular soils because friction ratio was not taken into account by the CUR166 method.

Differentiation between soil degradation laws for shaft and base resistances should prevent a systematic overestimation of shaft resistance as compared to base resistance. Indeed, the processes governing the degradation along the shaft and beneath the pile toe differ and vary with the type of soil.

The application of a particular model for driveability predictions depends on conditions of validation of the model. An accurate procedure for the estimation of the model parameters is also essential.

2.2.6 Multiscale soil behavior

If the pile can be described by its mechanical and geometrical properties (Holeyman 2000) including the consideration of its transversal and flexural properties and if the vibrator and the power pack can be chosen in function of a particular operational range, the interaction between these actors and the surrounding soil is more complex. The description of the behavior of the soil under large cyclic strains is really complicated. Once the soil along the profile is vibrated with sufficient energy, the soil structure degrades and continuum modeling becomes less suited. It requires a multiscale computational framework.

In the far field, the elastic properties of soil govern its behavior. The soil structure is not much modified. The energy transmitted by the vibrated pile is radially propagated and geometric damping is observed. Geometrical damping does not correspond to a dissipation phenomenon but the energy of the wave is simply redistributed on a growing surface when it moves away from the source. Equations of waves propagation in an elastic half-space can be regarded (Kramer, 1996).

In the near field, the soil is subjected to large distortions and its mechanical properties are progressively reduced until the zone located along the vibrated pile is strongly degraded.

Figure 2-5 illustrates these phenomena. R is the radius of the vibrated pile and G is the tangent shear modulus of the soil. In the linear elastic zone or the far field, the shear modulus of the soil remains unchanged in spite of the transmission of the vibrations : $G_{FF} = G_{init}$. In the non linear elastic zone or near field, the shear modulus is progressively reduced until a residual value. Along the profile, a strongly remolded zone is postulated where important convective movements of the remolded soil take place. In this plastic zone, it becomes difficult to define a tangent shear modulus (Gazetas and Dobry, 1984, El Naggar and Novak, 1994 and Michaelides et al., 1998). Moreover, slippage can occur along the pile shaft.

The way the soil degrades depends on its nature. Indeed, different physical processes govern cyclic soil structure degradation in function of its geological origin.

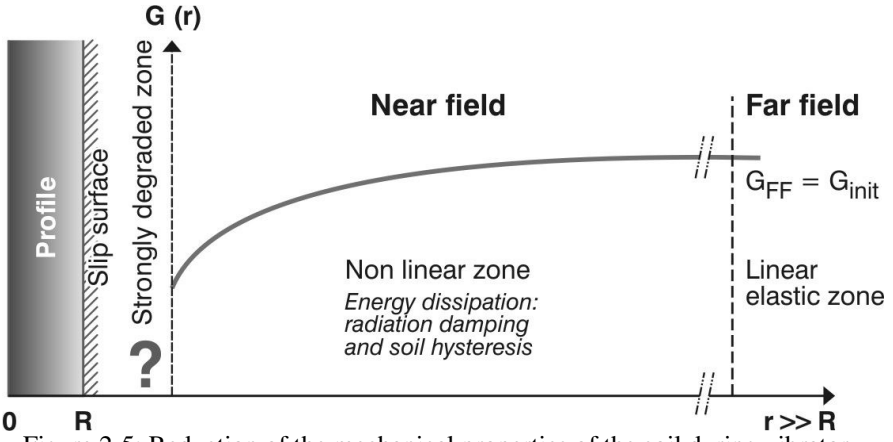

Figure 2-5: Reduction of the mechanical properties of the soil during vibratory driving.

Cohesive soils subjected to cyclic shearing degrade because of the fatigue of the soil skeleton (Vucetic, 1994). Geometrical, hysteretical and viscous damping can occur depending on the magnitude of the shear strain or shear strain rate. The shear modulus is degraded in a way depending on the cyclic shear strain amplitude and on the plasticity index (Vucetic and Dobry, 1991). Viscosity effects depend on the strain rate and plastic index of the soil (Dobry and Vucetic, 1987). The readers can refer to Holeyman (2000) for more considerations about the cyclic behavior of cohesive material exposed to vibratory driving.

The present work will focus on the dynamic behavior of cohesionless soil under large cyclic strains, in the strongly remolded zone.

2.3 Vibratory driving in sand: experimental observations

Because of its granular nature, cohesionless soil behavior is difficult to categorize. It is a geometrically complex assemblage of grains of various sizes and shapes resulting in a particular granulometry and the presence of voids defines its porous character. This pore space can be filled with some liquid according to its degree of saturation.

Many research efforts have been dedicated to strength degradation of cohesionless soils under large cyclic strains. Concerning the vibratory driving practice, the soil shear strength resisting the pulling out of a vibrating steel sheet-pile has been investigated by Russian researchers. They considered the study of the interface friction of saturated sand on vibrated sheet-piles which had been previously installed. Figure 2-6 presents the influence of the acceleration amplitude of the vibrations on the sandy soil friction resistance, measured on the lateral surfaces of straight web or U-shaped sheet-piles during vibro-extracting process (performed by Preobrajenskaïa and reported by Barkan, 1963).

At low amplitude of acceleration, an effective decrease of the sand friction resistance is observed. If the increase of the acceleration excitation allows a reduction of the effective friction applying to the lateral surfaces of the sheet-piles, beyond a threshold value, the lateral frictional resistance reaches an asymptotic value depending on the soil and sheet-piles properties. Then, there is no more

influence of the acceleration amplitude on the vibro-extracting process. The sand is assumed to reach its "vibro-fluid" limit. The results show that the side resistance varied exponentially with the amplitude of acceleration, Γ, with the maximum reduction in resistance occuring around 1-2g.

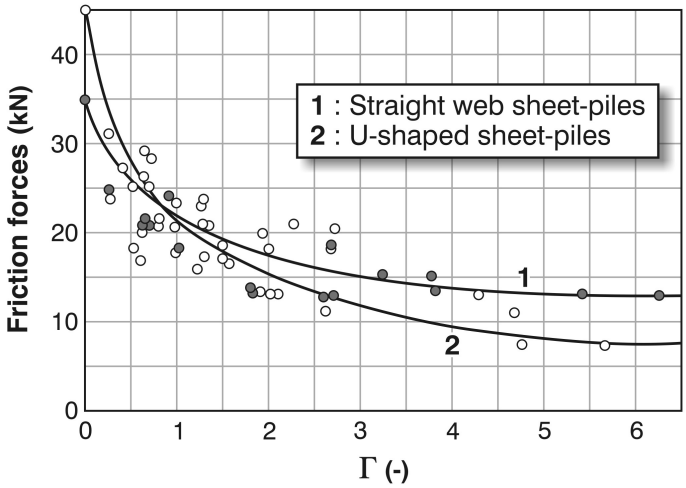

Figure 2-6: Influence of acceleration amplitude of the oscillations imposed by the vibratory hammer on the friction forces of the sand on lateral surface of two types of sheet-piles (after Barkan, 1963).

The following relationship was fitted to the results:

$$R_S = R_M + (R_{St} - R_M)\exp(-\alpha_1 \Gamma) \qquad \text{(Eq. 2-7)}$$

where α_1 is a constant (for a given experiment), R_S the dynamic side resistance, R_M the minimum dynamic side resistance and R_{St} the static side resistance.

Rodger and Littlejohn (1980) highlighted that the shear strength degradation of the granular soils depends on the choice of the governing parameters used to define the movement of the vibrated profile: the displacement amplitude and the frequency of the vibrator.

According to the experiments and field verifications of Rodger and Littlejohn (1980), the choice of the frequency of vibrations is related to the type of soil:

- For coarse grained soils: 4 to10 Hz;
- For fine-medium sands: 10 to 40 Hz.

The choice of the displacement amplitude (and therefore of the eccentric moment) is related to the tip-resistance encountered in the soil:

- For large point resistance: high displacement amplitude,10 to 20 mm;
- For low point resistance: small displacement amplitude, 1 to 10 mm.

The recommendations of the authors are reproduced in Table 2-2 for cohesionless soils.

During pile driving by vibrations in loose cohesionless soils, the shear strength reduction is assimilated to a "fluidization" phenomenon.

Dense cohesionless soils		Loose cohesionless soils	
Low point resistance	High point Resistance	Heavy piles	Light piles
Requires high acceleration Predominant side resistance Class A	Requires low frequency and large displacement amplitude for maximum impact to permit elasto-plastic penetration Predominant end resistance Class B		Requires high acceleration for fluidization Predominant side resistance Class A
Recommended parameters			
fr: 10 to 40 Hz Γ: 5 to 15 A: 1 to 10 mm	fr: 4 to 16 Hz Γ: 3 to 14 A: 9 to 20 mm		fr: 10 to 40 Hz Γ: 5 to 15 A: 1 to 10 mm

Table 2-2: Vibrators classification, after Rodger and Littlejohn (1980).

The degree of "fluidization" depends on the frequency and on the displacement amplitude of the vibrations. The fluidized zone is located along the sides of the vibrated pile and is assumed to extend beneath the pile. When the granular soil around the pile is fully fluidized, the penetration motion is then controlled by the applied bias load. The geometrical and inertial properties of the vibrated pile become the governing parameters of the sinking.

The granular soil is expected to behave in a similar way with piles of low point resistance driven in denser cohesionless soils (medium dense soils), where the major component of resistance experienced during vibrodriving comes from the pile sides. But the decrease of the shear strength resistance beneath the vibrated pile is not clearly demonstrated.

Considering piles of larger point resistance, the "fluidization" phenomenon will be located only along the pile sides and will be limited. Indeed, experiments highlight the fact that there is no "fluidization" beneath the pile end. Instead, the occurrence of an impact situation is assumed. Indeed, the large point resistance leads to the fact that the sinking of the pile requires an elasto-plastic penetration which is assisted only if an impact situation develops with a separation of the pile from the soil (Rodger and Litllejohn, 1980).

These considerations lead to the following vibrator driver classification system, summarized in Table 2-3.

Considering these experimental observations, it seems obvious that there is a coupled influence of the displacement amplitude and frequency on the way the shear strength of granular soil degrades. If a reduced frequency and a high displacement amplitude are necessary to induce elasto-plastic penetration in case of larger point resistance, the governing parameter of the "fluidization" seems to be the acceleration amplitude.

Class	Acceleration range (g)	Power demand (kW)	Remarks
A	12 to 40	2 to 60	Upper mechanical limits for vibratory driver without including resonance. Application of class A machine defined by the acceleration amplitude
B	1 to 12	20 to 200	Application of class B machine defined by the displacement amplitude

Table 2-3: Classification by acceleration of vibration.

2.4 Sand shear strength degradation

In the continuation of this chapter, the behavior of vibrated sand is explored. The phenomena hidden under the term “fluidization” and its governing parameters are highlighted. For the purpose of investigating this question, the presence or the absence of water is considered in the interstices between sand particles.

2.4.1 Cyclic behavior of saturated sand

Under the water table, saturation of the soil is a key parameter in sand cyclic degradation. Vibrodriving technique is then based on the “liquefaction” of the soil around the vibrated profile.

Under drained conditions, if a loose saturated cohesionless soil is subjected to large cyclic shearing, there is an immediate volume reduction. Under undrained conditions, there is no change in volume and liquefaction phenomenon can occur.

Sladen et al. (1985) proposed to define the term “liquefaction” as: “a phenomenon wherein a mass of soil loses a large percentage of its shear resistance, when subjected to monotonic, cyclic, or shock loading, and flows in a manner resembling a liquid until the shear stresses acting on the mass are as low as the reduced shear resistance”.

In saturated conditions, flow liquefaction and cyclic mobility phenomena have been explored to explain the shear strength degradation of the sand, sujected to large cyclic strains (Seed and Lee, 1966 and 1967, Lee and Seed, 1967, Casagrande, 1971 and Castro, 1969 and 1975).

a. Flow liquefaction phenomenon

Casagrande (1938), Geuze (1948) and Koppejan et al. (1948) postulated that flow liquefaction could only occur above a certain critical void ratio, as illustrated in Fig. 2-7.

They developed the critical void ratio concept into a formalized design procedure which is termed the “steady state” method. The steady state approach is a method of limit equilibrium analysis developed for potentially liquefiable soils.

Poulos (1981) defined the “steady state of deformation” as the “state, for any mass of particles, in which the mass is continuously deforming at constant volume, constant normal effective stress, constant shear stress, and constant velocity. The steady state of deformation is achieved only after all particle orientation has reached a statistically steady state condition and after all particle breakage, if any, is complete, so that the shear stress needed to continue deformation and the velocity of deformation remain constant”.

Flow liquefaction will be the result of undrained failure, due to the increase of the pore pressure, of a fully saturated highly contractive loose sand, ending on the critical state line in continuous flow condition with large shear distortion. Upon reaching the critical state, the soil can flow at constant void ratio, constant effective mean stress and constant deviatoric stress,as explained by Poulos (1981). Cyclic or static loads causing shear stresses larger than the steady state strength can cause flow liquefaction. (Castro and Poulos, 1977).

Flow liquefaction plays a mostly important role in several landslide and earthquake disasters (Lade and Yamamuro, 1999).

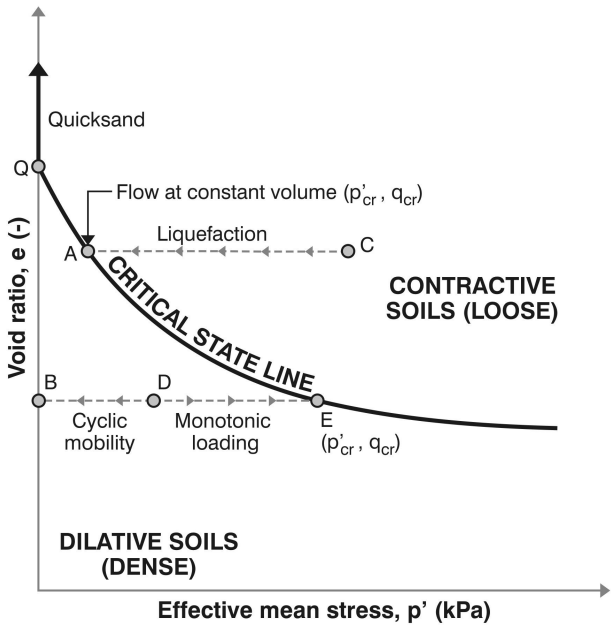

Figure 2-7: Undrained tests on fully saturated sands, after Castro and Poulos (1977).

b. Cyclic mobility phenomenon

As illustrated in Fig. 2-7, cyclic mobility arises when a fully saturated dilative dense sand is subjected to cyclic loading in undrained conditions. It occurs if the cyclic stresses are large enough to involve a progressive structural degradation. The grain skeleton is reorganized. It tends to compact and decrease in volume during the contractive phases of the cyclic loading. Since the drainage conditions are undrained, the pore pressure increases, leading to the reduction of the effective normal stresses and the shear resistance. Contrarily to the flow liquefaction

phenomenon, the strength degradation is stopped when cyclic loading is interrupted (Vanden Berghe, 2001).

c. Saturated sand degradation within the framework of vibrodriving

Concerning the recent vibratory driving study, Vanden Berghe (2001) focused on the characterization and the modeling of saturated sand behavior under cyclic loading conditions. According to that work, the undrained cyclic triaxial test and the constant volume cyclic direct simple shear test are the most representative laboratory tests to model soil conditions around a vibrated profile. Since vibratory driving is preferably used in sandy soil, laboratory tests were conducted on Brusselian sand (d_{50} = 0.18 mm and the Uniformity coefficient of Hazen (d_{60}/d_{10}) is C_u = 2.2, ρ_s = 2.65 gr/cm³, e_{min} = 0.63 and e_{max} = 1.18) and investigated the influence of large strain amplitudes on the soil degradation.

Figure 2-8 illustrates the cyclic mobility phenomenon occuring during a cyclic strain controlled undrained triaxial test on a very dense specimen of Bruxelian sand (Vanden Berghe, 2001).

Considering the Cambridge's school definition, p' is the effective mean stress (kPa), defined by:

$$p' = \frac{\sigma'_1 + 2\sigma'_3}{3} \qquad \text{(Eq. 2-8)}$$

and q is the deviator (kPa):

$$q = \sigma'_1 - \sigma'_3 \qquad \text{(Eq. 2-9)}$$

where σ_1' is the effective axial normal stress (kPa) and σ_3' the effective radial normal stress (kPa). These are defined considering the pore pressure, u, in the specimen:

$$\sigma'_1 = \sigma_1 - u \qquad \text{(Eq. 2-10)}$$

and

$$\sigma'_3 = \sigma_3 - u \qquad \text{(Eq. 2-11)}$$

where σ_1 is the axial total normal stress (kPa) and σ_3 the radial total normal stress (kPa).

The specimen was saturated under an initial pore pressure, u_{init} = 200 kPa. Then, it was isotropically consolidated (K_0 = 1) by a total consolidation stress, p = 400 kPa resulting in an effective consolidation stress, p_0' = 200 kPa. During the cyclic triaxial test, the total axial stress, σ_1, was measured and the total radial stress, σ_3, imposed in order to maintain the total mean stress, p, close to 400 kPa.

The test was conducted on a very dense specimen (D_r = 86%). The relative density of sand can be defined by the index, D_r:

$$D_r = \frac{e_{max} - e}{e_{max} - e_{min}} \times 100(\%) \qquad \text{(Eq. 2-12)}$$

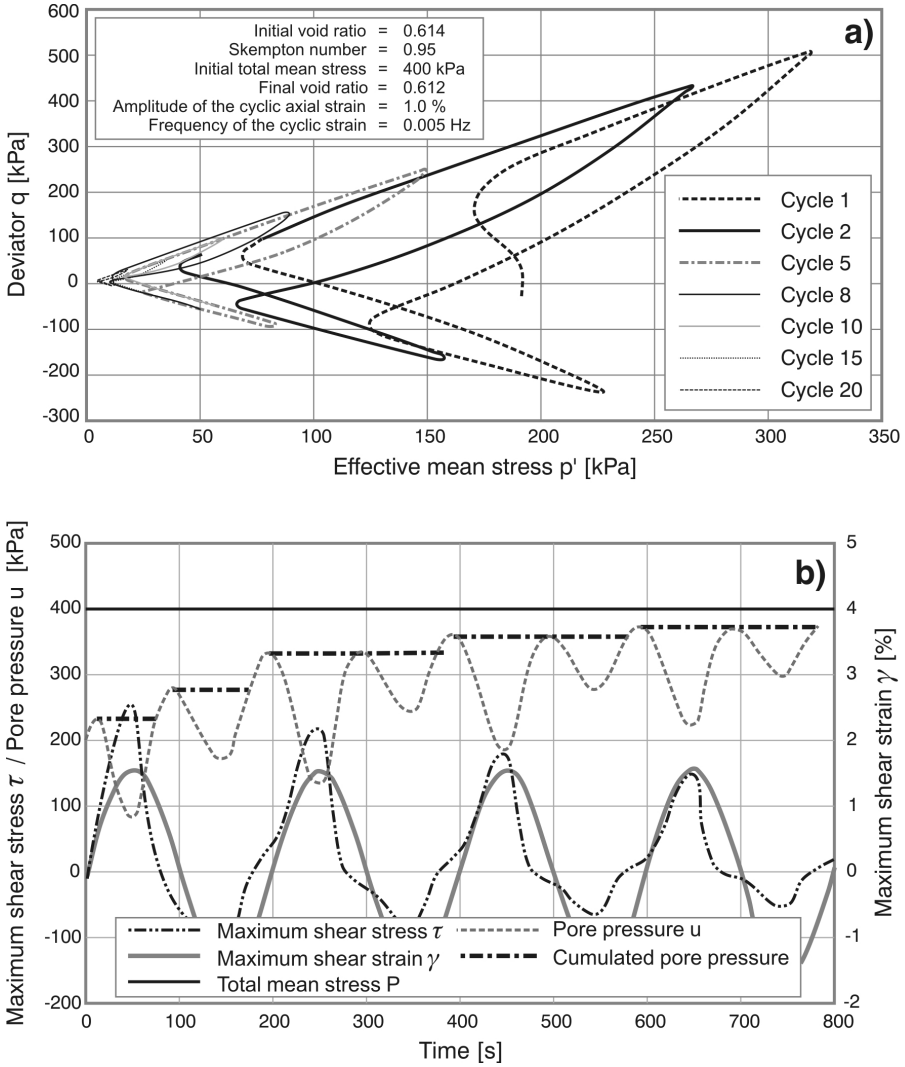

Figure 2-8: Cyclic mobility phenomenon occuring during a cyclic undrained triaxial test a) Stress path followed during a cyclic triaxial test. b) Comparison between the evolution of maximum shear stress τ and pore pressure u during a cyclic triaxial test, Vanden Berghe (2001).

The cyclic triaxial test was conducted under undrained conditions. If no volume change is expected, tendency to dilation or contraction can be observed during the test.

In Fig. 2-8a, the stress path presents the "butterfly" shape of the loops. During one cycle of shearing, two dilative phases and two contractive phases are observed. During each dilative phase, the specimen follow a straight line: the stress path becomes tangent to the critical state line. The shape of the stress path followed during each loop seems to be an homothetic transformation of each other. The effective mean stress can be ultimately reduced to zero because the pore pressure rises due to the no volume change condition. Then, the soil behaves like a "fluid".

According to Vanden Berghe (2001), the results of all the tests performed with large strain amplitudes showed that even if large dilation phases are observed, the specimen will always reach cyclic mobility state after a few cycles. There is no equilibrium where the dilation phases could compensate the contraction phases. An increase of the pore pressure at the end of each cycle is always observed. In spite of the decrease of the pore pressure during the dilating phase, there is always an increase of the cumulated pore pressure, even for very dense sands, as illustrated in Fig. 2-8b.

In Fig. 2-8b, the increase of the pore pressure, u, and the reduction of the maximum shear stress, τ, are observed during the shearing of the specimen. The maximum shear stress is derived from the difference between the two total stresses:

$$\tau = \frac{\sigma_1 - \sigma_3}{2} \qquad \text{(Eq. 2-13)}$$

The pore pressure presents a frequency twice that of the shear strain. The cumulated pore pressure grows progressively from an initial value of 200 kPa to the value of the total mean stress, 400 kPa. When the cumulated pore pressure reaches this threshold value, the effective mean stress vanishes. The specimen behaves momentally like a "fluid", deformations can develop, the sand is softened and no more shear resistance is observed, as illustrated in Fig. 2-8b where the maximum shear stress progressively vanishes with the number of applied cycles.

One major conclusion of the experimental work of Vanden Berghe (2001) is that the initial void ratio has an important influence on the soil degradation. The higher the void ratio, the faster the soil degradation. There is a limit void ratio corresponding to the critical void ratio where no cycles are required to liquefy the soil, and where flow liquefaction can occur, as illustrated in Fig. 2-7.

Hence, the vibration of a profile into saturated sand can cause a degradation of the surrounding soil, by flow liquefaction or cyclic mobility, depending on the in situ void ratio.

At the microscopic scale of the grains, amplitude and orientation of contact forces between the grains are modified by the increase of the pore pressure resulting from the quasi-incompressibility of the interstitial fluid which cannot escape from the assemblage. Then, the force chains get unbound resulting in a particular liquefied state wherein particles become freer to move. Figure 2-9 presents the change in granular structure during undrained cyclic loading.

The volume reduction (in drained conditions) or the increase of pore pressure (in undrained conditions) can be considered as the expression of the same phenomenon, the irreversible tendency for a particular granular skeleton to reorganize itself into a denser arrangement when subjected to large amplitude cyclic loading.

According to Vanden Berghe (2001), during the dilative phase, the grains are rolling on each other to follow the imposed deformation, and are trying to increase the volume of the sample. Because of the undrained condition, this tendency creates a decrease of the pore pressure and an increase of the effective intergranular stress. When the direction of the deformation changes, the stress distribution between particles is modified and the grains move backward in the gap they were in before dilation. During this reorganization, the intergranular stresses decrease, the contacts between grains can even be broken leading to the destruction of the force chains. The grains become freer and tend towards a more stable state by

trying to reduce the volume of the specimen. This tendency results in an increase of the pore pressure. For a certain deformation, a new granular structure is formed and the sample cannot be deformed anymore by reducing the volume any further. To follow the imposed further deformation, the grains have to roll on each other and a new phase of dilation is observed.

The successive reorganizations of the granular skeleton progressively lead the specimen to a structure where the grains can move freely without being in contact. No intergranular stresses are observed and no more resistance is measured. The specimen is liquefied by cyclic mobility.

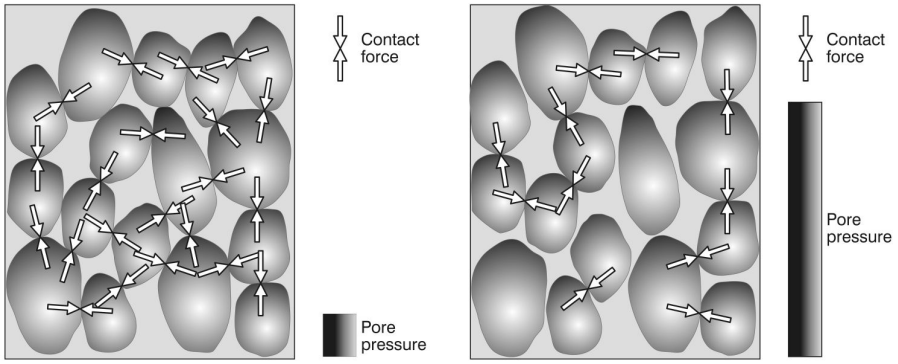

Figure 2-9: Grain structure degradation during undrained cyclic loading: a) initial saturated state and b) liquefied state, after www.ce.washington.edu.

d. Intrinsic Coulomb failure criterion for saturated sand

The macroscopic expression of this behavior can be considered with the help of the intrinsic Coulomb failure criterion for the shear strength of saturated sand:

$$\tau_{SS} = (\sigma - u)\tan\phi_{mob} \qquad \text{(Eq. 2-14)}$$

where τ_{ss} is the ultimate shear strength of the sand (kPa), σ the normal stress (kPa), u the pore pressure (kPa) and ϕ_{mob} the mobilized angle of friction (°). The index *ss* identifies saturated sand. (σ-u) is the effective normal stress or intergranular stress. There is no cohesive term because of the cohesionless nature of the sand. If u increases and becomes equal to or greater than σ, τ_{ss} vanishes.

2.4.2 Cyclic behavior of dry sand

If under saturated conditions, the "fluidization" of the sand can be explained by flow liquefaction or cyclic mobility, what kind of phenomenon can explain the shear strength degradation of dry sand when it is subjected to vibrations? What can explain the success of vibratory driving in dry granular soil or above the water level?

There is a lack of consistent experimental data to illustrate the behavior of vibrated dry sand. The purpose of the present thesis is then to concentrate on the behavior of vibrated dry sand during vibrodriving.

The continuation of the present chapter will focus on the effects of vibrations on volume change and strength degradation of dry granular soils, and on the application of vibratory driving to this particular case.

a. Effects of vibrations on volume change

The considerations about vibrated sand behavior can be related to the engineering issues concerning the vibrocompaction of granular soils. This industrial process was introduced in Germany in the 30's. Applied to granular media, it is more efficient than static compaction. The purpose of this dynamic compaction is generally improving deformation properties and shear strength of the soil. The result of the compaction is commonly related to soil density. Although research has been conducted on compaction, the physical mechanisms at work during vibrocompaction of sand are poorly understood and the description of the grains behavior remains incomplete.

Mogami and Kubo (1953), Barkan (1962), Selig (1963), Prakash and Gupta (1967), D'Appolonia D. J. and D'Appolonia E. (1967), Ermolaev and Senin (1968a) and Kolmayer (1970) have conducted some experiments to study the effects of vibrations on the volume change of dry granular soils considering the following variables:

- the direction of the vibrations,
- the harmonic vibration parameters (acceleration amplitude, Γ, frequency, fr, and displacement amplitude, A of motion),
- the duration of the vibrations,
- the size of the container,
- the grain size of sand,
- the surface overload.

Mogami and Kubo (1953)

Mogami and Kubo (1953) have conducted some experiments on the behavior of sand when subjected to vertical harmonic vibration. The authors noticed that, when vibrated, dry sand acts in the same way as a liquid and can settle. Figure 2-10 presents the result of the vibration of a transparent box fixed on a electrical vibrating table which was able to move vertically and sinusoidally. Disturbance of the patterns is observed in the sand when it is vibrated. The sand particles demonstrate a very irregular motion during vibrations. Unfortunately, there is no description of the experimental set-up used to observe this behavior and no indication concerning the imposed motion.

Barkan (1962)

Experiments of Barkan (1962) show that the governing parameter of the dynamic compaction is the acceleration amplitude of the imposed vibrations, or rather the inertial force, which acts on the soil particles during the vibration. Indeed, the granular assemblage is subjected to an inertial force proportional to the density of the sand particles. Barkan has studied the evolution of the porosity in function of the acceleration amplitude of horizontal vibrations. No surcharge was applied to the free surface of the specimens. Figure 2-11 presents such results for dry sand. Unfortunately, there is no description of the experimental set-up used to build this vibratory compressibility curve.

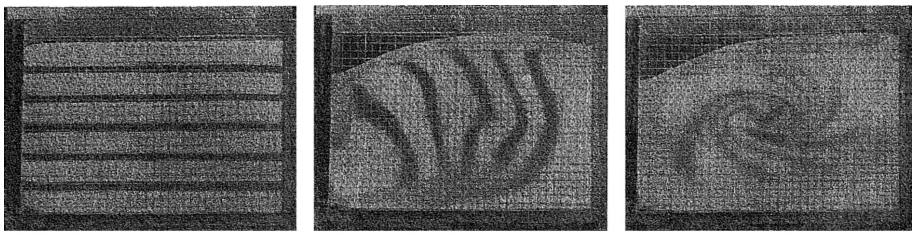

a b c

Figure 2-10: a) Patterns in the sand at rest, b) and c) disturbance of patterns in the sand when it is vibrated, after Mogami and Kubo (1953).

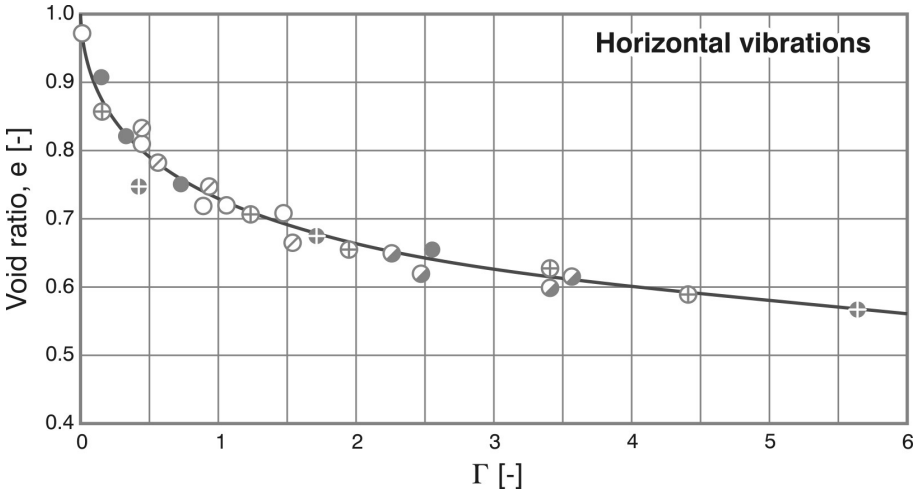

Figure 2-11: Vibratory compressibility curve of sand fill, after Barkan (1962).

All sands, tested by Barkan (1962) at different frequencies, present the same results. In the initial state, the sand is deposited with a void ratio close to its maximum value, e_{max}. Once the horizontal vibrations are imposed, the sand undergoes an effective compaction. As the void ratio is decreased, it becomes more difficult to change with vibration acceleration. For large values of Γ, the void ratio reaches a value close to the minimum void ratio, e_{min}. No particular phenomenon is observed once the acceleration amplitude becomes larger than 1g.

Barkan (1962) has suggested a relationship between void ratio and duration of the vibrations for horizontal vibrations:

$$e(t) = e_{\Gamma} + (e_{init} - e_{\Gamma}) \exp(-\beta_t t) \qquad \text{(Eq. 2-15)}$$

where e (-) is the void ratio, e_{init} (-) the initial void ratio resulting from dry pouring, t the time (min), e_{Γ} (-) the minimum void ratio which can be reached with the imposed acceleration amplitude, Γ (-), and β_t (min^{-1}) a coefficient depending on the nature of the soil and on the acceleration amplitude. It characterizes the rate of compaction.

Barkan (1962) has suggested the following equation for e_{Γ}:

$$e_{\Gamma} = e_{\min} + (e_{init} - e_{\min}) \exp(-\alpha_t \Gamma) \qquad \text{(Eq. 2-16)}$$

where α_t (-) is the index of vibratory compaction depending on the nature of the soil. α_t expresses the fact that the granular assemblage requires a given acceleration amplitude to reach a predetermined void ratio. If α_t is high, the necessary acceleration amplitude will be lower.

As observed in Fig. 2-11, no decompaction is noticed for any values of the dimensionless acceleration, Γ, considering horizontal vibrations.

Prakash and Gupta (1967)

Prakash and Gupta (1967) studied the variation of relative density of horizontally or vertically vibrated dry Solani river sand. The test set-up consisted in a tank, full of sand, mounted on steady state horizontally or vertically vibrating tables. The size of the tank was 30 cm by 30cm and the height of the sand deposit was 15 cm. Sand was deposited in uniform layers by pouring in dry condition. The d_{50} of the Solani river sand is 0.13 mm, $C_u = 2.06$, and e_{min} and e_{max} are 0.50 and 0.93 respectively.

The motion of the vibrating tables was assumed sinusoidal by the authors. No surcharge was applied to the free surface of the specimens.

Figure 2-12 presents the evolution of the relative density and the void ratio change of the sand as a function of the time of vibration for different acceleration amplitudes.

The volume change varies in a similar way for horizontal or vertical vibration while the acceleration amplitude stays inferior to 1g. Hence, the equations (2-15) and (2-16) governing the volume change of the granular material for horizontal vibrations, are considered valid for vertical vibrations with acceleration amplitude inferior to 1g. Indeed, for vertical vibrations, there is an optimum acceleration amplitude, close to 1g, approaching the minimum void ratio ($D_r = 80\%$). Once the acceleration reaches this threshold value, an increase in acceleration can cause a decrease in compacted density, as illustrated in Fig. 2-13.

Prakash and Gupta (1967) observed that for vertical vibrations, as the optimum acceleration amplitude was approached dry sand started boiling forming vertical pipes in the sand mass, and the sand settled in densest state when vibrations were stopped. On further increasing the acceleration amplitude a heap was formed and when vibrations were stopped it settled into relatively looser state. On the contrary, for horizontal vibrations, no mound was formed.

These observations indicate the simultaneous existence of a state of dynamic density and a state of density after vibration corresponding to the same acceleration amplitde, Γ. Moreover, the emergence of particular geometrical shapes seems to be observed at the free surface of the sample.

Horizontal vibrations seem to allow a better compaction than vertical vibrations (Prakash and Gupta, 1967). Table 2-4 presents experimental values of β_t computed with the help of equation (2-15) considering the curves of Fig. 2-12. For horizontal vibrations, β_t seems to increase with the acceleration amplitude, Γ, but there is a lack of additional experiments to draw a real tendancy. For vertical vibrations, β_t seems to be independant of the acceleration amplitude.

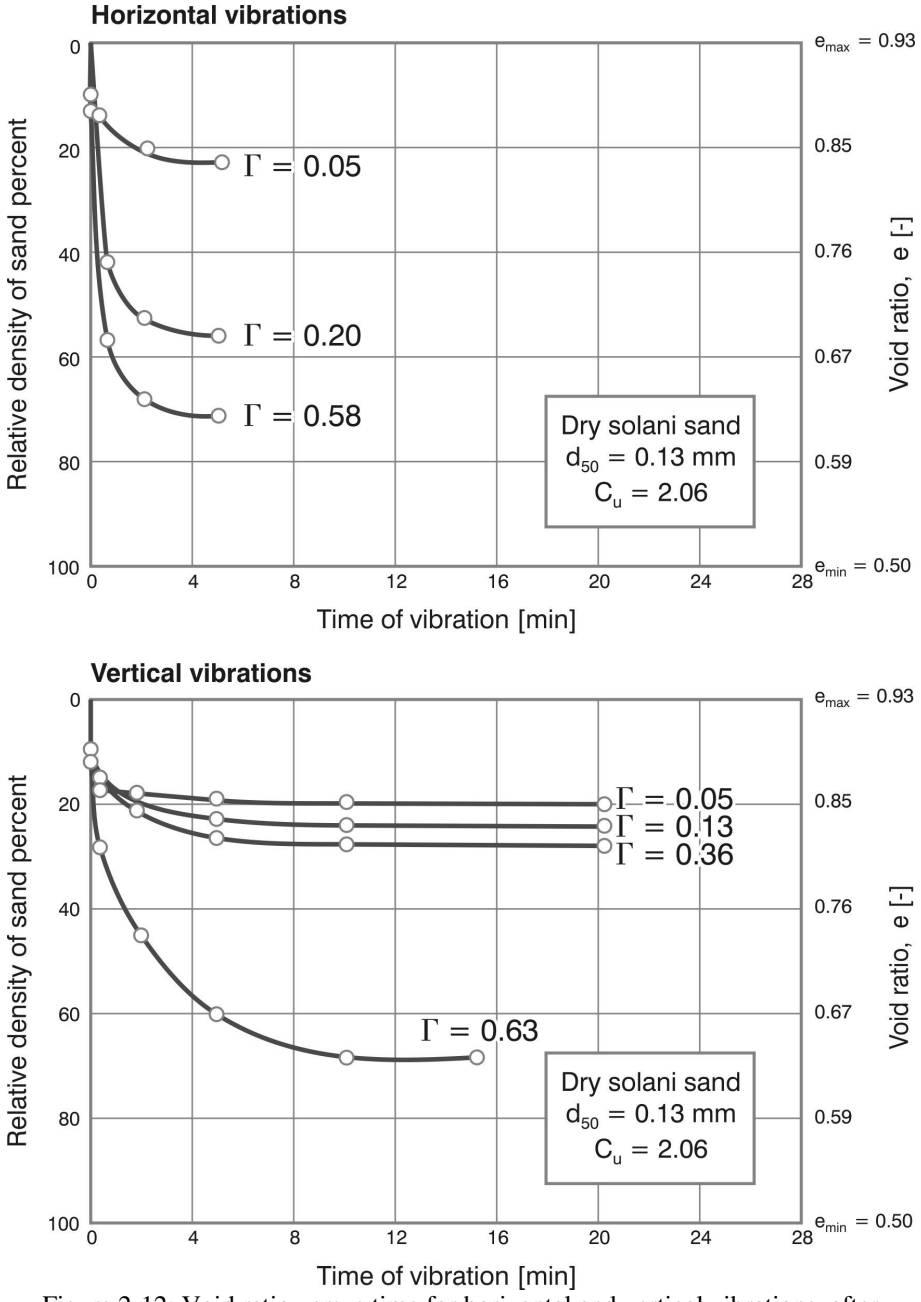

Figure 2-12: Void ratio versus time for horizontal and vertical vibrations, after Prakash and Gupta (1967).

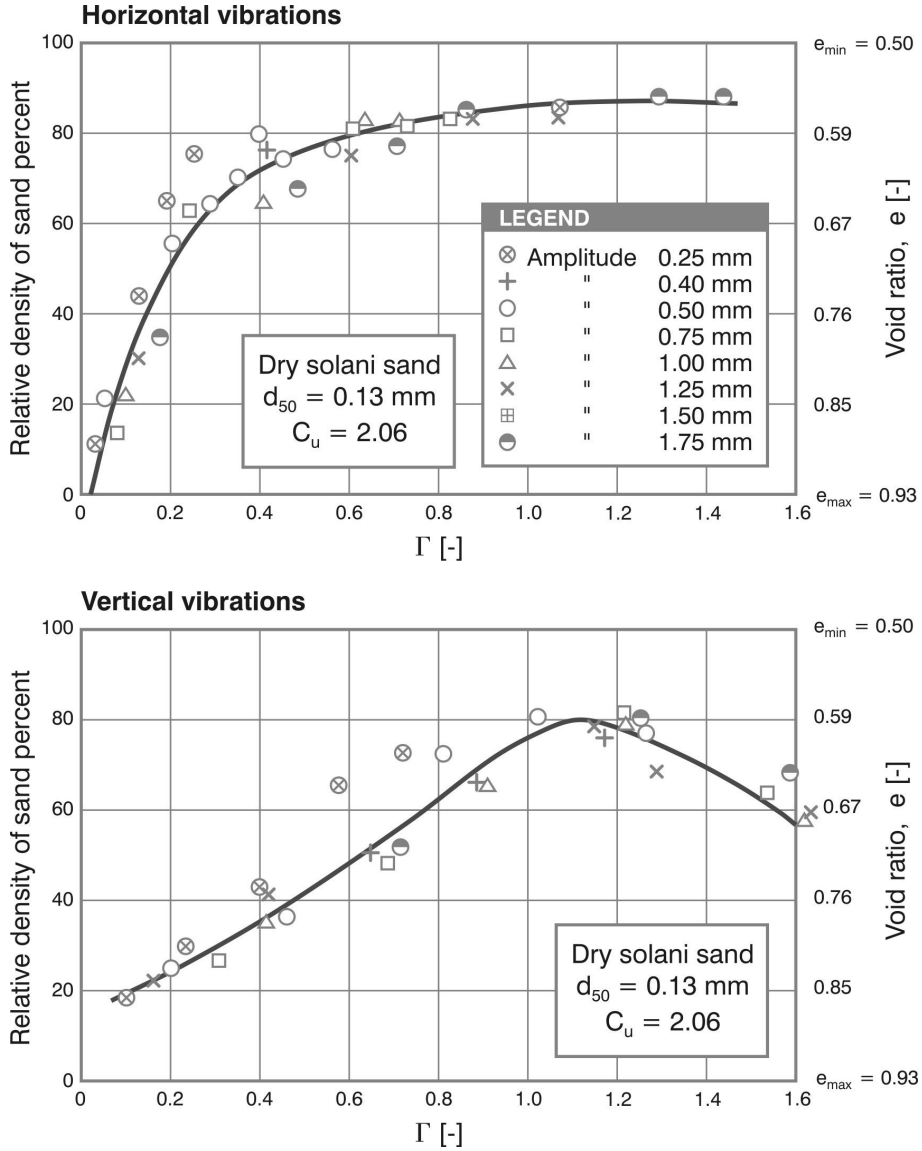

Figure 2-13: Void ratio change vs acceleration amplitude for horizontal and vertical vibrations, after Prakash and Gupta (1967).

Horizontal vibrations		Vertical vibrations	
Acceleration, Γ (-)	β_t (min^{-1})	Acceleration, Γ (-)	β_t (min^{-1})
0.05	0.79	0.13	0.55
0.20	1.46	0.20	0.45
0.58	1.70	0.35	0.40
		0.62	0.44

Table 2-4: Experimental values of β_t, after Prakash and Gupta (1967).

D'Appolonia D. J. and D'Appolonia E. (1967)

D'Appolonia D. J. and D'Appolonia E. (1967) have conducted laboratory tests where an open container of air-dry dune sand is placed upon a shaking table and subjected to vertical vibration. The sample is contained in a cylindrical mold 10 cm in diameter and 9 cm high. The d_{50} of the dune sand is 0.6 mm and C_u = 1.5. No surcharge was applied to the free surface of the specimen. Figure 2-14 illustrates the relationship between sand density after vibrations and acceleration for these experiments. If the peak acceleration is less than 1g, a progressive densification of the sample is surmised.

According to D'Appolonia D. J. and D'Appolonia E. (1967), when the acceleration is greater than 1g, the sand cannot fully follow the downward motion of the container and goes into free-fall. When the sand reaches the bottom of the container, there is an impact and a propagation of stresses within the granular medium in the form of force chains which lead to the densification of the sample. But during the cycle of vibration, there is an uncoupling of the walls of the container and the particles in suspension. That leads to the dilatation

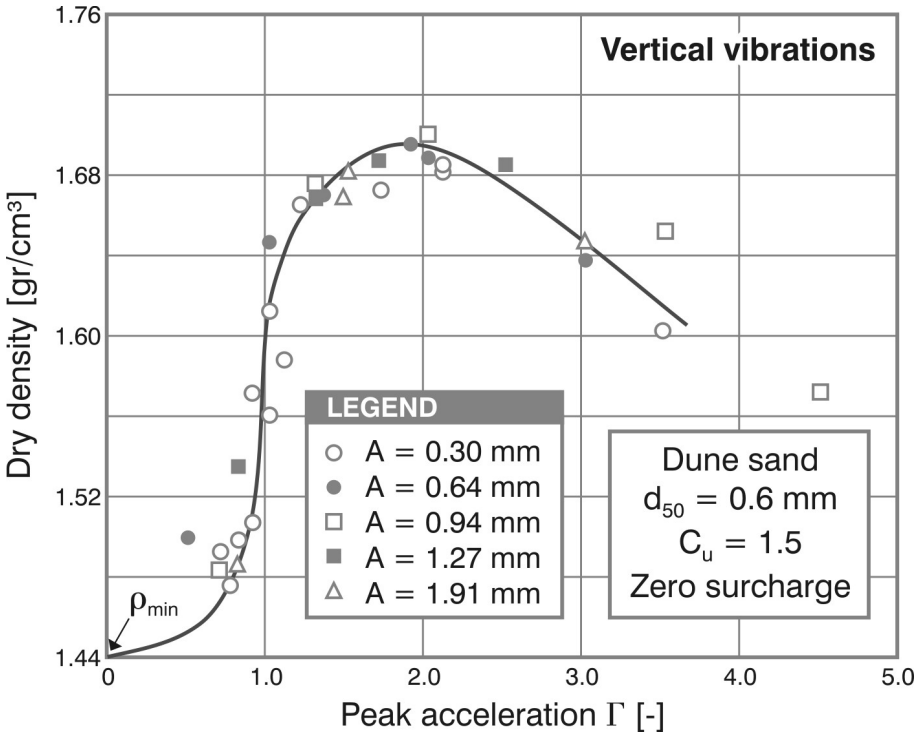

Figure 2-14: Dry density of dune sand vs. acceleration amplitude (D'Appolonia D. J. and D'Appolonia E., 1967).

of the sample. The free-fall-impact phase inducing compaction is then followed by a dedensification phase which is repeated each cycle.

In this study, the optimum acceleration amplitude allowing the minimum void ratio seems to be superior to 1g. The authors explained this observation by the

free-fall impact condition which could lead to efficient compaction between 1g and 2.5g.

The frequency, fr, or the displacement amplitude, A, of the vertical vibrations seem to have no influence on the dry density results, as illustrated in Fig. 2-14.

D'Appolonia D. J. and D'Appolonia E. (1967) have also conducted tests to study the influence of the granulometry of dune sands on its dry density after vibration, as illustarted in Fig. 2-15. The optimal acceleration appears to vary with grain-size distribution and the "vibrocompactability" of a sand increases with its Uniformity coefficient, C_u. Coarse and well graded sands can be compacted with much less effort as compared to uniform fine sands. The size of cohesionless soil particles possessing the same specific gravity influences the change in void ratio.

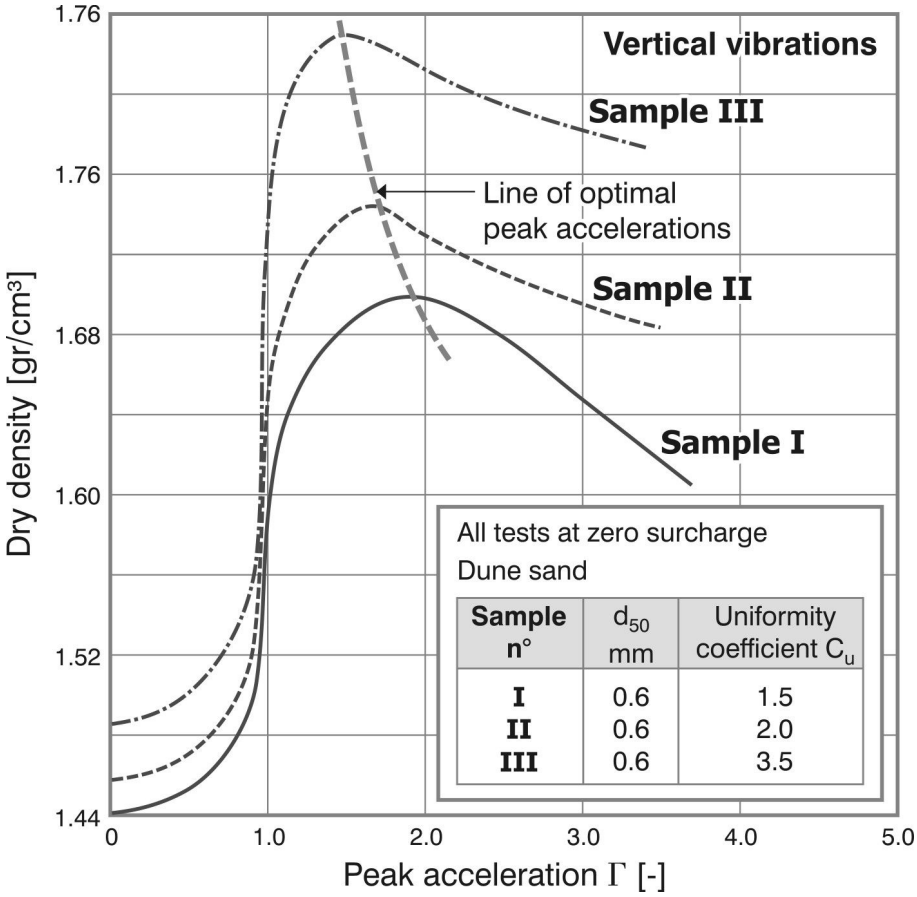

Figure 2-15: Variation of dry density after vibration with peak acceleration for dune sands of various granulometry, after (D'Appolonia D. J. and D'Appolonia E., 1967).

The influence of a surface overload was studied by D'Appolonia D. J. and D'Appolonia E. (1967), as illustrated in Fig. 2-16. The application of a static surcharge at the free surface of the sample leads to the decrease of the coefficients β_t and α_t, introduced by equations (2-15) and (2-16), as illustrated in Table 2-5.

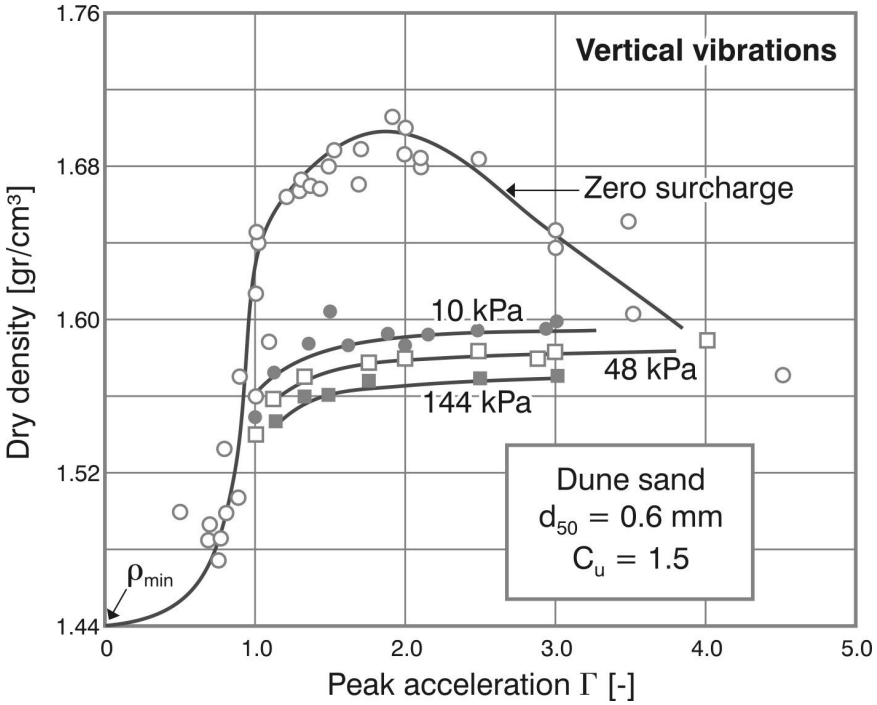

Figure 2-16: Variation of dry density after vibration with peak acceleration and surcharge, after D'Appolonia D. J. and D'Appolonia E. (1967).

Static overload, σ (kPa)	β_t (min^{-1})	α_t (-)
0	0.70	6 to 8
10	0.20	5 to 7
48	0.18	5 to 6
144	-	4 to 5

Table 2-5: Influence of the static surcharge on coefficient β_t, after D'Appolonia D. J. and D'Appolonia E. (1967).

Surcharge and increased depth of sand could have the same effect on the volume change in the sample: limiting density. A certain amount of additional vibration energy should be required to overcome the resistance to density change as a result of the reinforcement of the force chains in the sample increasing internal friction. This friction is increased by surcharge and added weight of sand. It is to note that "overvibration" loosens the particles and decreases the density. Nevertheless, figure 2-16 seems to show that surcharge will resist this effect.

According to the previous work of Selig (1963), the results of D'Appolonia D. J. and D'Appolonia E. (1967) suggest that the highest densities achieved by vibrating the sand through the container are obtained with no surface overload and a minimum of sand overburden. Moreover, the sand must not be vibrated too intensely.

Kolmayer (1970)

Kolmayer (1970) has proposed an empirical relationship to descrive the influence of the static overload on the coefficient β_t:

$$\beta_t = f\left(\frac{\Gamma^{\xi}}{\sigma}\right) \qquad \text{(Eq. 2-17)}$$

where $\xi = 3/2$ in the cases of Bourgoin sand ($d_{50} = 0.18$ mm and $C_u = 2.2$) and laboratory sand ($d_{50} = 0.85$ mm and $C_u = 1.8$). The test set-up consisted in a circular box containing dry sand sample 7 cm in diameter and 4 cm high. The box was fixed on a vertical vibrating table producing vertical harmonic motion. Figure 2-17 illustrates the concordance of the relationship (2-17) with the experimental results for the Bourgoin and the laboratory sands. The experiments were conducted for static overload varying in the range $50 < \sigma < 200$ kPa and for vertical acceleration ranges respectively equal to $1.1 < \Gamma < 3.3$ for Bourgoin sand and $1.1 < \Gamma < 5.5$ for laboratory sand.

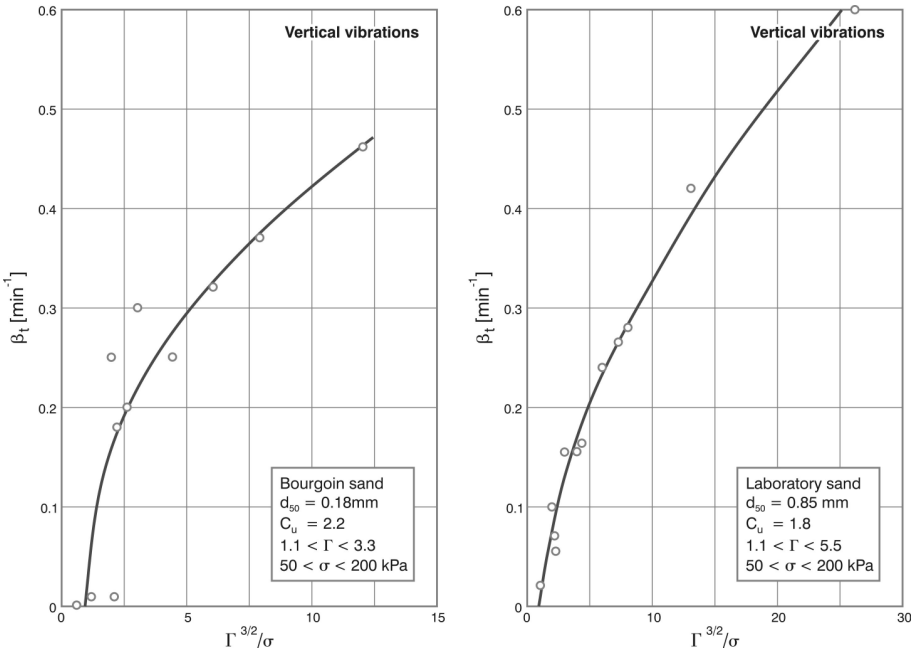

Figure 2-17: Variation of the coefficient β_t with the acceleration amplitude and the static surcharge, after Kolmayer (1970).

b. Effects of vibrations on internal friction of the sand

Considering the internal friction in the sand, the intrinsic curve of the dry cohesionless soil can be expressed as:

$$\tau_{ds} = \sigma \tan \phi_{mob} \qquad \text{(Eq. 2-18)}$$

where τ_{ds} is the ultimate dry shear strength (kPa) and the pore pressure term is absent because of the dry condition. The index *ds* identifies dry sand.

Several studies have been performed to characterize the influence of vibrations on the coefficient of internal friction ($f = \tan \phi_{mob} = \tau_{ds}/\sigma$), as reported in Mogami and Kubo (1953), Barkan (1962), Youd (1967), Ermolaev and Senin (1968b) and Kolmayer (1970).

Mogami and Kubo (1953)

Mogami and Kubo (1953) have conducted some experiments to characterize the shearing resistance of dry Soma sand when subjected to vertical harmonic vibrations. The sand was filled into a metal box fixed on an electrical vibrating table. The motion of the vibrating table was assumed sinusoidal by the authors. The scheme of the test set-up is illustrated in Fig. 2-18. The shearing strength of the sand decreases as a function of the acceleration of the vibration, as illustrated in Fig. 2-19. According to Mogami and Kubo (1953), it decreases almost to zero, which could justify the expression "liquefaction". Nevertheless, considering the dry conditions of these tests, the term "vibro-fluidization" is chosen to avoid confusion with flow liquefaction phenomenon arising only in saturated sand (Section 2.4.1a). Hence, the term "vibro-fluidization" will characterize the shear strength degradation of a dry granular material subjected to vibrations.

Savchenko

Under horizontal vibrations, Savchenko has characterized the decrease of the friction coefficient with the amplitude of acceleration, using modified shear box tests (as reported in Barkan, 1962). The experimental set-up of Savchenko is illustrated in Fig. 2-20. It consists of a shear box which can be subjected to vibrations, a vibrator (1) and a recording instrument (2).

The shearing device consists of three principal parts: the box (3) wherein the soil is sheared, a spring jack (4) to apply vertical pressure on the sample, and the set-up (5) which produces the shearing. This latter consists of a cable spanned over a pulley and a loading platform. For the purpose of preserving the static character of the shear load, the shearing system (5) was mounted on dampers. The shear box (3) is rigidly fixed to the vibratory platform (6). The box consists of a lower cylinder closed at its bottom and two rings inserted into a socket. The support (7) of the jack is rigidly attached to the vibrating platform (6) of the device. This latter can slide on rollers fixed to a support rigidly connected to the foundation of the installation. The horizontal vibrations are imposed by means of a vibrator (1) which is connected to the vibrating platform (6) with the help of a turnbuckle (8). The vibrator can slide on rollers (9) mounted on the guide frame (10) rigidly attached to the foundation of the installation.

The influence of horizontal vibrations on the coefficient of internal friction was analyzed comparing its value in static conditions with values obtained for different amplitudes of acceleration. Figure 2-21a illustrates the relationship between $\tan\phi_{mob}$ and Γ. This relationship can be defined by the following formula:

$$\tan \phi_{mob} = \tan \phi_{res} + (\tan \phi_{st} - \tan \phi_{res}) \exp(-\varepsilon\Gamma) \qquad \text{(Eq. 2-19)}$$

where $\tan\phi_{st}$ is the value of the static internal friction coefficient without vibration, $\tan \phi_{res}$ the asymptotical value of the friction coefficient and ε (-) an empirical factor determining the effect of vibrations. The previous equation (2-19) could be already introduced in equation (2-18) to describe vibrated intrinsic curve of the sand.

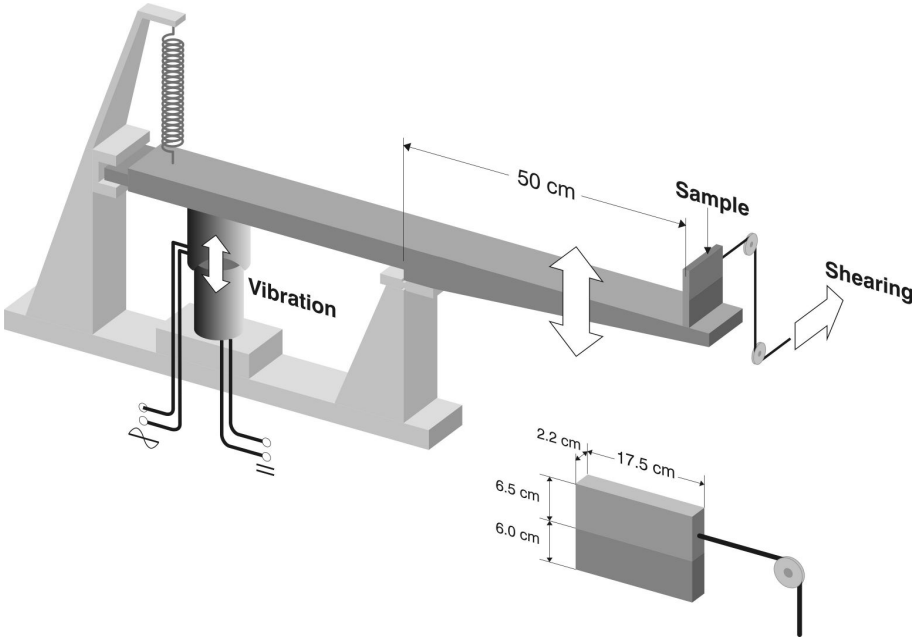

Figure 2-18: Experimental scheme of Mogami and Kubo shear box tests.

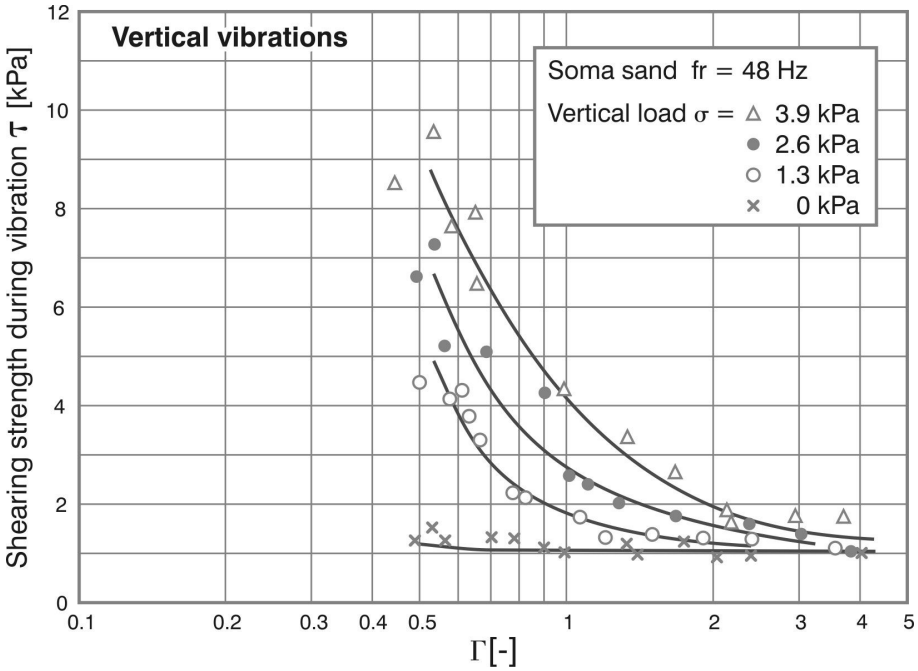

Figure 2-19: Relationship between the shearing strength of dry Soma sand and the acceleration of the vibration for constant frequency (48 Hz) and various static surcharges, after Mogami and Kubo (1953).

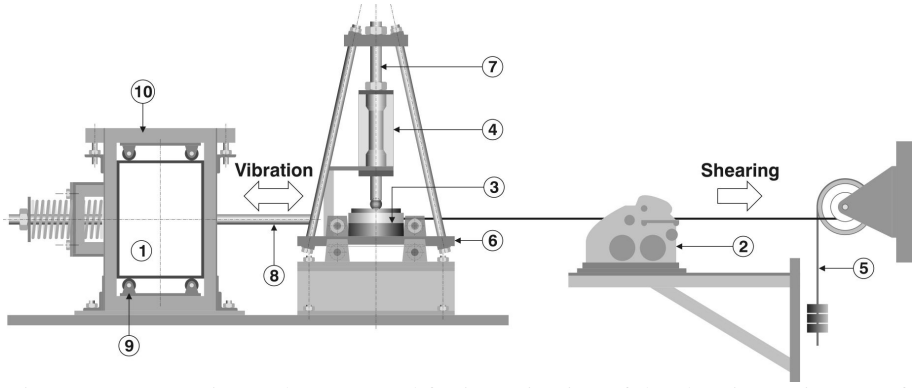

Figure 2-20: Experimental set-up used for investigation of the shearing resistance of soil, after Barkan (1962).

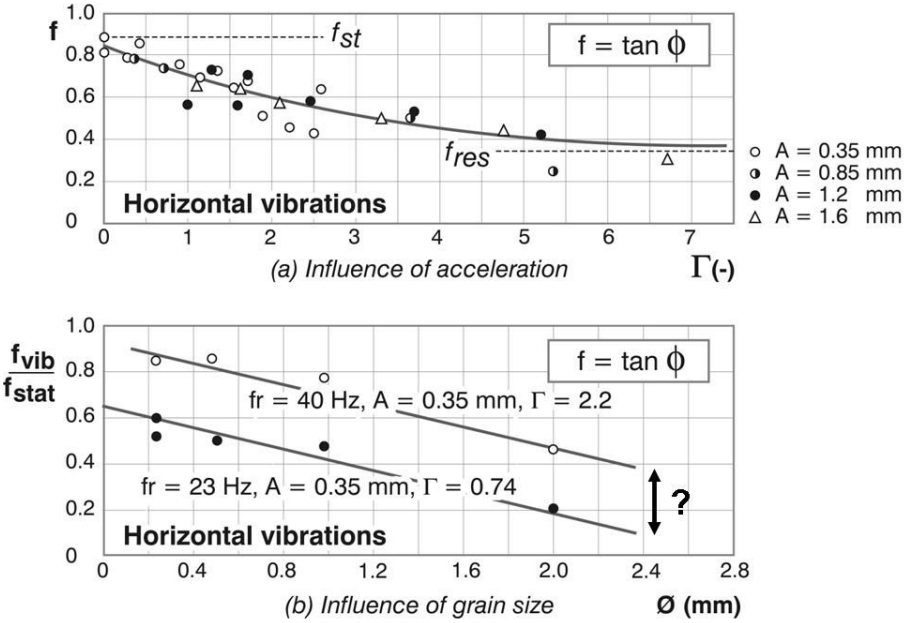

Figure 2-21: a) Relationship between the coefficient of internal friction of sand a) and the acceleration of vibrations for various displacement amplitudes and frequencies, b) Relationship between the effect of vibrations and the diameter of sand grains (A = 0.35 mm for both curves), after Barkan (1962).

Figure 2-21b shows that the effect of vibrations increases in proportion to sand-grain diameter. It is likely that the caption of the curves has been inverted by the author.

Youd (1967)

Nevertheless, none of the previously mentioned investigators has reported any studies concerning the effect of vibration on the void ratio during the shearing.

Youd (1967) studied the reduction of critical void ratio (CVR) during vibration. A direct shear apparatus was mounted on a shaker table which was a

horizontal one-direction table motion. The shear box was oriented on the table in such a manner that the shear displacement was horizontal and perpendicular to the direction of table motion. The normal load was applied vertically. Figure 2-22 illustrates the experimental scheme of Youd shear box tests. The shear box was 6.4 cm in diameter and the height of the sand specimen was between 1.5 and 1.8 cm. Oven-dried Ottawa sand was used in the investigations.

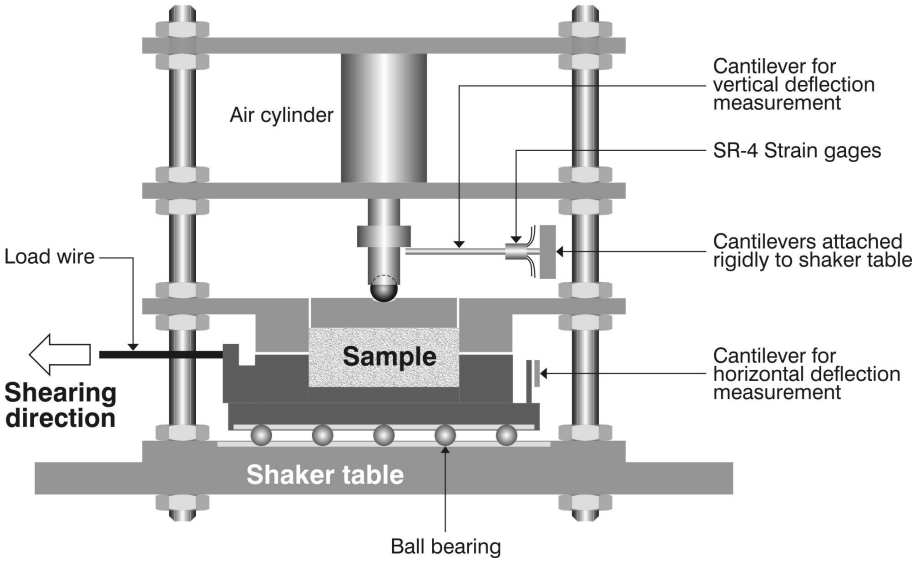

Figure 2-22: Experimental scheme of Youd shear box tests.

In certain tests, the sand was horizontally vibrated until it reaches its vibratory equilibrium void ratio (EVR) corresponding to the minimum void ratio which can be reached with the imposed acceleration amplitude, e_Γ (-), as described by Barkan (1962). Secondly, a shear test was conducted at the same frequency and displacement amplitude.

In other tests, no particular frequency or displacement amplitude were used to compact the sample. The test frequency and displacement amplitude, different from those used in compaction, were then set and the sample was sheared while subjected to the vibration.

Figure 2-23 is a constant frequency plot of the internal friction coefficient of the dry Ottawa sand versus void ratio for 70 kPa normal pressure. According to De Jaeger (1991), the d_{50} of the Ottawa sand is 0.71 mm, $C_u = 1.18$, $e_{min} = 0.52$ and $e_{max} = 0.74$. In this case, tan ϕ is the ratio of the maximum shear force, T_{max}, to the normal force, N. The initial void ratio is considered before shearing. The internal friction coefficient decreased with increasing void ratio, and decreased with increasing displacement or acceleration amplitude of vibration. Constant amplitude lines were linear down to a void ratio of 0.57. Below this value, the coefficient of internal friction sharply increased for the static and lower amplitude tests. According to Youd (1967), this sharp increase in tanϕ with decreasing void ratio was thought to be due to increased interlocking of the sand grains. The reduction of the amount of this sharp increase with increasing acceleration amplitude further illustrates the

effect of vibration in reducing the shear resistance due to interlocking. An EVR line is illustrated in Fig. 2-23.

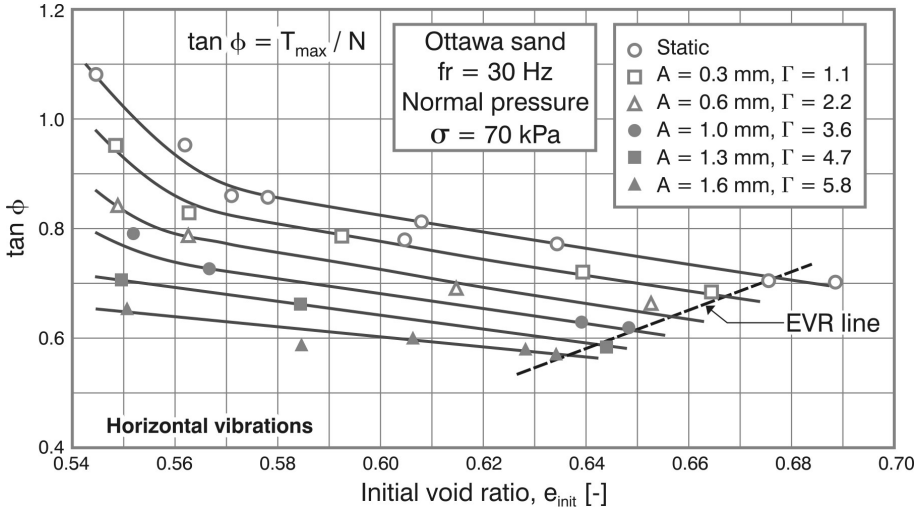

Figure 2-23: tan ϕ versus initial void ratio (before shearing), after Youd (1967).

For the purpose of determining the critical void ratio from the shear tests, tests in which initial void ratio and the void ratio observed at constant volume state were near the same value, were used in estimating the CVR, assuming the void ratio was nearly homogeneous throughout the sample. The tests where these values were closest to being equal were those conducted at the EVR condition. Hence, the authors presumed that the CVR was also the EVR. If the sample was dilating to a void ratio above the EVR, the vibratory energy would be sufficient to densify the granular material to its EVR value.

Figure 2-24 presents the EVR line, for Ottawa sand at 30 Hz and 70 kPa normal pressure, on a void ratio versus acceleration amplitude plot. It is to note that the relative densities are computed with regards to the values of e_{min} and e_{max} from De Jaeger (1991). Experimental values of EVR and CVR are represented along the EVR line and seem to confirm the assumption of Youd (1967): within the limits of experimental accuracy, EVR and CVR are the same value and EVR line also corresponds to CVR line. CVR is then reduced by vibration. Therefore, if a dry granular soil is densified by a particular acceleration amplitude, Γ, until its vibratory equilibrium void ratio (EVR), e_Γ, and then sheared at the same vibration, the initial void ratio, e_{init} (corresponding to e_Γ), is also the critical void ratio, e_c.

Ermolaev and Senin (1968b)

Ermolaev and Senin (1968b) subjected some specimen of sandy loam, with a water content close to 16.5%, to shearing in a shear box under the effect of vertical harmonic vibrations. There is no description of the experimental set-up. The analysis of their experimental data highlighted three stages of change in τ, depending on the acceleration amplitude. At low acceleration ($\Gamma < \Gamma_0$), the shear strength is close to its static value.

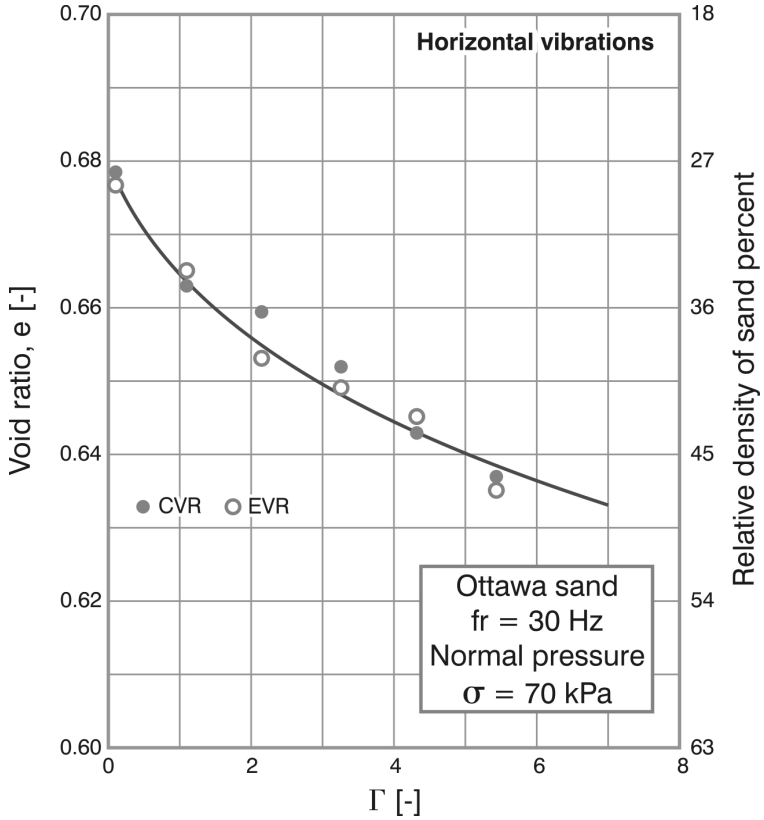

Figure 2-24: EVR and CVR values as a function of the acceleration of the vibration, after Youd (1967).

Then, there is a trans-threshold region where the shear strength is swiftly decreased until a residual value. They proposed the following expression to describe this behavior:

$$\tau = \tau_{res} + (\tau_{st} - \tau_{res}) \exp(-\lambda(\Gamma - \Gamma_0)) \qquad \text{(Eq. 2-20)}$$

where τ_{res} is the asymptotical value of the shear strength (kPa), τ_{st} the value of the static shear strength (kPa), λ an empirical factor (-), called vibro-shear exponent and Γ_0 the relative threshold dimensionless acceleration close to 1 (-). The loss of shear strength is limited to τ_{res} and the decreasing rate is defined by λ and Γ_0, both parameters depending on the normal pressure, σ. If the material cannot be considered as tested in dry conditions, their observations are similar to the experimental data of Mogami and Kubo (1953) and the empirical relationship (2-20), describing the decrease of the shear strength with acceleration, can be related to the empirical relationship (2-19) proposed by Savchenko for horizontal vibrations. Moreover, the presence of the threshold acceleration, Γ_0, could be understood as the acceleration necessary for bringing sufficient energy in order to break the apparent cohesive forces due to the water content.

c. Vibro-fluidization phenomenon

When vibrations are applied to a dry granular soil, a degradation of the granular skeleton is also observed, but there is no more interstitial fluid to explain the shear strength decrease of the material observed during cyclic loading. As in saturated conditions, it is possible to approach the physics of the phenomenon considering the microscopic point of view, illustrated in Fig. 2-9. When a dry granular material is vibrated, the contact forces between the grains can be progressively reduced, depending on the amplitude of vibrations. The force chains are interrupted and they can no longer transmit the shear stresses through the assemblage. The decrease of the contact lifetime leads to a particular state wherein the sand behaves like a fluid. The soil is then "vibro-fluidized" in absence of an interstitial fluid. This phenomenon, called "vibro-fluidization", characterizes the shear strength degradation of a dry granular material subjected to vibrations.

d. Revisited intrinsic Coulomb failure criterion for vibrated dry sand

L'Hermite and Tournon proposed a theory to express this behavior in a macroscopic point of view (as reported in Kolmayer, 1970). During cyclic loading, the vibrations would lead to the emergence of a "shaking pressure", σ_S, which tends to decrease the normal pressure in a way similar to the pore pressure in presence of interstitial fluid. When the normal pressure is smaller than the shaking pressure, the shear strength of the sand gets close to zero. When the normal pressure becomes greater than the shaking pressure, the shear strength can increase. The shaking pressure could be seen as an expanding pressure countering the normal pressure. Hence, in dry condition, the shaking pressure can be substituted for the pore pressure in Fig. 2-9. The intrinsic curve of the vibrated sand becomes:

$$\tau_{ds} = (\sigma - \sigma_S)\tan\phi_{mob} \qquad \text{(Eq. 2-21)}$$

where τ_{ds} is the ultimate dry shear strength (kPa) and σ_S the shaking pressure (kPa). The index *ds* identifies dry sand.

Kolmayer (1970) has investigated the influence of vibrations on the intrinsic curve of dry laboratory sand ($d_{50} = 0.85$ mm and $C_u = 1.8$). The experimental set-up of Kolmayer is illustrated in Fig. 2-25. The test set-up consisted in a circular box containing dry sand sample 7 cm in diameter and 4 cm high. The box was fixed on a vibrating table producing vertical harmonic motion. Before shearing, the sand was previously vibrated until it reaches a void ratio close to its vibratory equilibrium void ratio, $e_{\Gamma,}$ in order to avoid volume change due to vibrations during shearing.

Figure 2-26 presents the influence of the acceleration amplitude on the intrinsic curve of vibrated dry sand.

The vibrations decrease the shear strength of the material. The intrinsic curves are straight lines but they do not go through the origin of the graph. They intersect the axis of normal pressure at a value corresponding to the shaking pressure, σ_S. The shaking pressure increases with increasing acceleration of vibrations. The friction angle slightly decreases with increasing acceleration.

Figure 2-27 presents the influence of vertical acceleration on the friction coefficient, tan ϕ, and on the shaking pressure, σ_S, for the shear test results presented in Fig. 2-26.

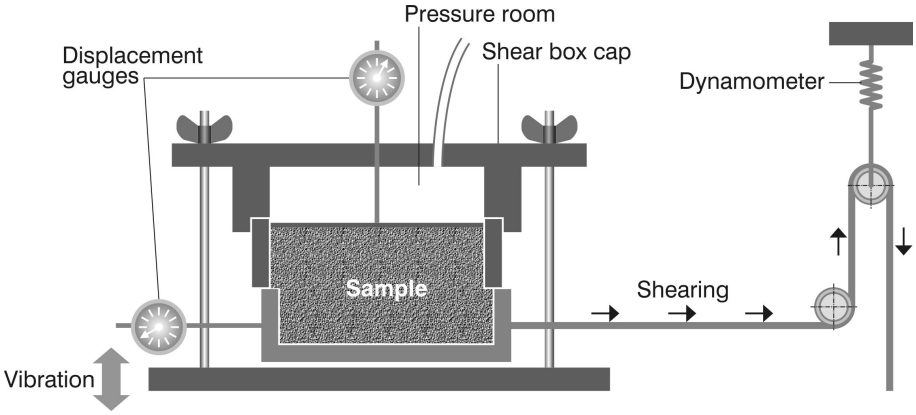

Figure 2-25: Experimental scheme of Kolmayer shear box tests.

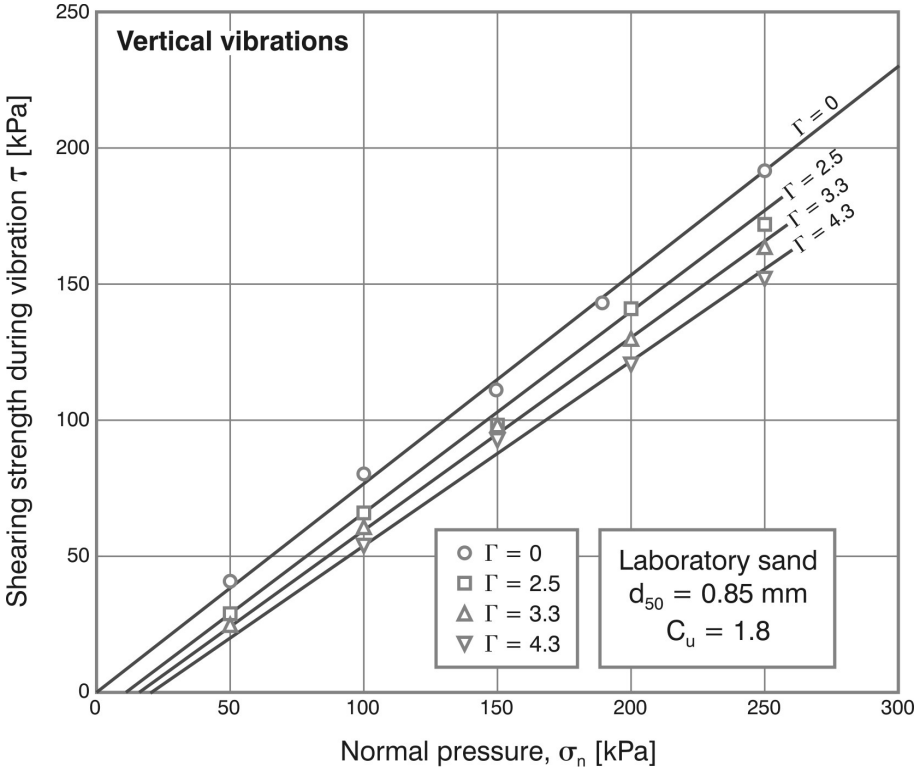

Figure 2-26: Influence of acceleration amplitude on the intrinsic curve of sand, after Kolmayer (1970).

Considering the aforementioned studies, the governing parameter of volume change and shear strength reduction of dry sand in presence of vibrations seems to be the acceleration amplitude, Γ.

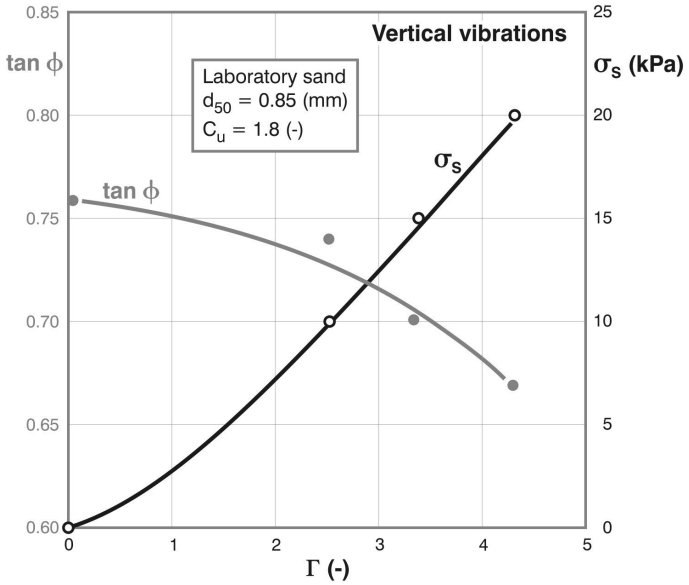

Figure 2-27: Influence of the acceleration amplitude on the internal friction coefficient and on the shaking pressure of dry sand, after Kolmayer (1970).

e. Barkan's conceptual SPE model (1962)

If the influence of vibrations on dry sand resistance is now highlighted, the previous discussions do not encompass the progressive penetration of the profile into the soil during the vibrodriving process.

A major part of a pile or profile driving resistance usually comes from soil skin friction, which can be considered as the sum of "dry" friction and "viscous" friction depending on velocity. Barkan (1962) showed that internal friction resistance tends to vanish and that a granular soil starts behaving like a viscous fluid when subjected to intense vibrations. Following his own observations, this soil property could be expressed in terms of the coefficient of "vibro-viscosity". Barkan (1962) attempted to determine this latter with the help of the penetrating sphere method considering the well-known Stokes law.

Barkan designed the sphere penetration experiment (SPE) to investigate this behavior and establish the coefficient of vibro-viscosity (Fig. 2-28a). He recorded the sinking velocity of a metallic sphere into a vertically vibrated container filled with sand to the height of 30 to 35 cm. The container, 30 by 30 cm in cross section, 40 cm height, was placed on a vibratory platform enforcing the vertical vibrations. Various "bias" loads could be applied to the sphere by means of a loading system. The penetration of the sphere was recorded with the help of a recorder and counterweights. The sand used was white quartz sand with a grain size ranging between 0.2 and 0.5 mm. The moisture content of this latter was close to zero. Before performing a sphere penetration experiment, the sand was vibrated until its minimum void ratio, approximately 0.5 (-), was reached, leading to a volumetric mass of soil about 1.77 gr/cm³.

The use of the Stokes method assumes the presence of a penetration phase wherein the sinking velocity of the sphere is constant. If the steady driving force

acting on the sphere only comes from gravity, Stokes law can be applied to the sphere penetrating at a constant rate into vibrated sand, considered like a viscous medium:

$$\mu V = \frac{2}{9} r^2 (\gamma_1 - \gamma_2) \qquad \text{(Eq. 2-22)}$$

where μ (Pa.sec) is the "liquid" medium viscosity, V ($m.sec^{-1}$) the steady sinking velocity, r the sphere radius (m), γ_1 ($N.m^{-3}$) the equivalent sphere unit weight and γ_2 ($N.m^{-3}$) the "liquid" unit weight.

From the SPE results (Fig. 2-28b), the sinking velocity of the sphere seemed to obey Stokes law allowing the determination of the vibro-viscosity coefficient, μ. These curves are plotted for constant acceleration of vibrations (Γ = 1.68) and variable loads (curve 1, load = 1.9 kg; curve 2, load = 1.5 kg; curve 3, load = 1.2 kg; curve 4, load = 1.0 kg; curve 5, load = 0.6 kg; curve 6, load = 0.3 kg).

The inverse of μ was shown to vary linearly with the relative level of acceleration:

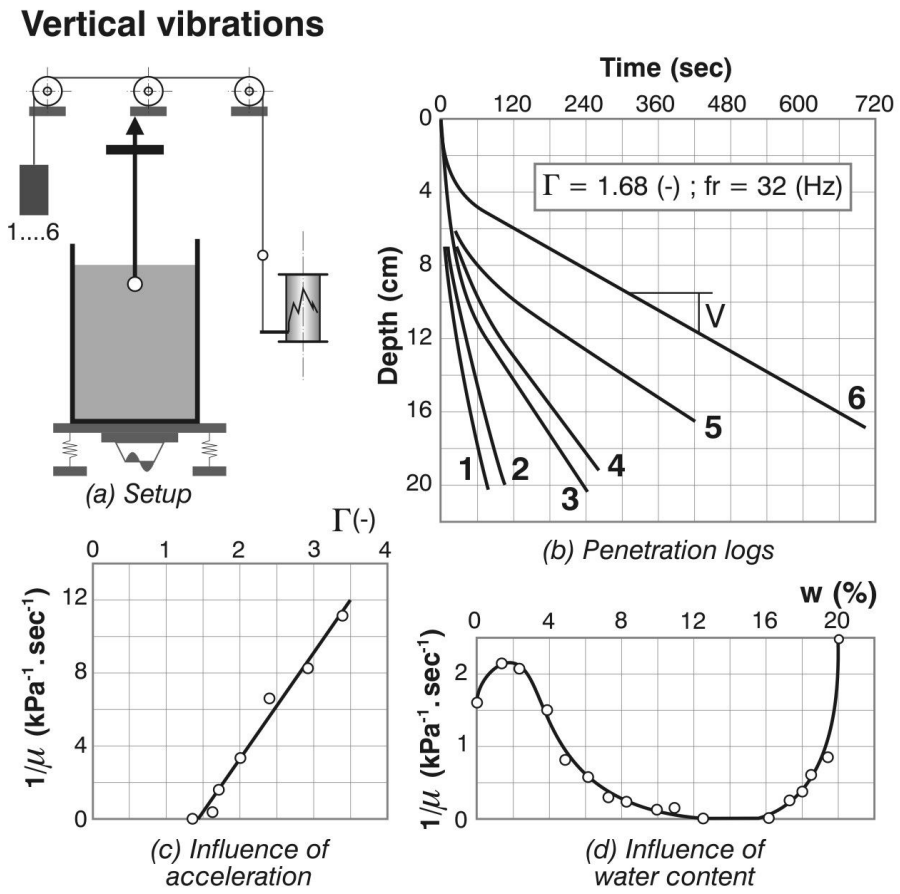

Figure 2-28: Sphere penetration experiments (after Barkan, 1962).

$$\frac{1}{\mu} = b(\Gamma - \Gamma_0) \qquad \text{(Eq. 2-23)}$$

where b ($Pa^{-1}.sec^{-1}$) is an empirical parameter and Γ_0 (-) a threshold value approximately equal to 1.5. Upon exceeding this threshold value, there is a significant increase of 1/μ and Barkan considered that soil enters in a vibro-fluidized state and behaves like a viscous liquid.

2.5 Conclusions and research perspectives

The present chapter has introduced the reader to the vibratory driving process and the equipments used on working site. Engineering issues related to this technique are reviewed considering the four major actors of the process: the pile, the vibrator, the power generator and the surrounding soil. The action of the vibrator and the governing parameters used to define the movement of the vibrated profile are presented: the displacement amplitude and the frequency of the vibrator. The two governing parameters of the process induces the application of a dimensionless acceleration, $\Gamma = a/g$, to the profile. Existing vibrodriving prediction models are refered.

The associated soil behavior around the pile is then discussed only considering degradation of the shear strength of granular soils. Vibrodriving experiments in sand are presented and highlight "fluidization" phenomena occuring in soil during vibratory driving. According to Preobrajenskaïa (as reported in Barkan, 1963) and Rodger and Littlejohn (1980), the side resistance of a vibrated sheet-pile varies exponentially with the acceleration amplitude, Γ, with the maximum reduction in resistance occuring around 1-2g.

For the purpose of understanding "fluidization" of sand, vibrated sand behavior is critiqued under saturated or dry conditions. Cyclic behavior of saturated sand is first analyzed. In this case, the experimental work of Vanden Berghe (2001) is explored. This latter notably modelled the behavior of sand during vibrodriving with the help of cyclic triaxial tests on saturated sand. He explored the major role of the void ratio on the shear strength degradation. Indeed, both phenomena are hidden behind the term "fluidization": the "flow liquefaction" and the "cyclic mobility" arising in function of the density of the soil around the vibrated profile.

The core of the State-of-the-Art review is devoted to dynamic behavior of dry sand with regards to the influence of vibrations on its volume change and on its shear strength.

2.5.1 Influence of vibrations on the volume change of dry sand

A review of previous studies on vibrocompaction of dry granular material was presented considering the following variables: the direction of the vibrations, the vibration parameters (fr, A and Γ), the duration of the vibrations, the size of the container, the nature of the sand and the surface overload. Table 2-6 summarizes the experimental conditions and results of the different studies.

According to the authors, acceleration amplitude, Γ, is the governing motion parameter of the vibrocompaction of dry granular soils for horizontal and vertical vibrations.

Barkan (1962) proposed relationships to express the volume change as a function of the duration of the horizontal vibrations and defined the equilibrium void

ratio (EVR), e_Γ, as the stable void ratio for a sample densified at a particular acceleration, Γ.

Authors	Type of sand	Direction of the vibrations	Motion amplitude	Static overload	Experimental set-up	Observations and main contributions
Mogami and Kubo (1953)	No indication	Vertical, sinusoidal	No indication	Zero surcharge	Transparent box fixed on an electrical vibrating table	When subjected to vibrations, dry sand acts in the same way as a liquid and can settle; disturbance of patterns are observed in the sand
Barkan (1962 and 1963)	No indication	Horizontal	$0.04<\Gamma<6$ $0.04<A$ (mm)<2.8 $17<fr$ (Hz)<50	Zero surcharge	No indication	- Equations (2-15) and (2-16) : $e(t) = e_\Gamma + (e_{init} - e_\Gamma)\exp(-\beta_t t)$ and $e_\Gamma = e_{\min} + (e_{init} - e_{\min})\exp(-\alpha_t \Gamma)$ - No decompaction was observed for horizontal vibrations in the studied range of acceleration
Prakash and Gupta (1967)	Solani river sand d_{50}=0.13mm C_u=2.06 e_{min}=0.50 e_{max}=0.93	Horizontal and vertical, sinusoidal	Horizontal: $0.05<\Gamma<1.25$ $0.25<A$ (mm)<1.75 $5<fr$ (Hz)<16.47 Vertical: $0.123<\Gamma<1.63$ $0.25<A$ (mm)<1.75 $7<fr$ (Hz)<25	Zero surcharge	Tank 30 cm by 30 cm in cross section filled with sand to the height of 15cm	For horizontal vibration: similar observations to Barkan (1962) and $0.79<\beta_t<1.7$; $\beta_t=f(\Gamma)$ For vertical vibration: - Eq. (2-15) and (2-16) valid for vertical vibration as long as $\Gamma<1$ - $\Gamma\approx1$leads to the minimum void ratio (D_r=80%) - $\Gamma>1$ causes decompaction and heaping - $0.4<\beta_t<0.55$ and $\beta_t\neq f(\Gamma)$
D'Appolonia,D.J. and D'Appolonia,E. (1967)	Dune sand d_{50}=0.6mm $1.5\leq C_u\leq3.5$ ρ_{min}=1.44 gr/cm³ ρ_{max} : no indication	Vertical	$0.5<\Gamma<4.5$ $0.3<A$ (mm)<1.91 $10<fr$ (Hz) <60	$0<\sigma<144$ kPa	Cylindrical mold 10 cm in diameter and 9 cm high	- $1<\Gamma<2.5$ leads to minimum void ratio - $0.18<\beta_t<0.7$ and $\beta_t=f(\sigma)$ - $4<\alpha_t<8$ and $\alpha_t=f(\sigma)$ - minimum void ratio reached with no surface overload and a minimum of sand overburden - increasing of the "vibrocompactibility" with C_u
Kolmayer (1970)	Bourgoin sand d_{50}=0.18mm C_u=2.2 ρ_s=2.68 gr/cm³	Vertical	$1.1<\Gamma<3.3$ A=0.6mm $20<fr$ (Hz) <50	$50<\sigma<200$ kPa	Cylindrical mold 7 cm in diameter and 4 cm high	$\beta_t = f(\frac{\Gamma^\xi}{\sigma})$ where ξ=3/2 $0<\beta_t<0.5$ for Bourgoin sand $0<\beta_t<0.6$ for Laboratory sand
	Laboratory sand d_{50}=0.85mm C_u=1.8 ρ_s=2.68 gr/cm³		$1.1<\Gamma<5.5$ A=0.6mm $20<fr$ (Hz) <50	$50<\sigma<200$ kPa		

Table 2-6: Experimental researches investigating the influence of vibrations on the volume change of dry sand.

Prakash and Gupta (1967) observed that the volume change varies in a similar way for vertical vibration while the acceleration amplitude stays inferior to 1g. Indeed, for vertical vibrations, once the acceleration reaches this particular threshold value, an increase in acceleration can cause a decrease in compacted density. This phenomenon is the result of the sand particles separating during vibration and settling in a looser state when vibration is halted. Hence, in vibrocompaction, horizontal vibrations are more effective than vertical vibrations.

The research of D'Appolonia D. J. and D'Appolonia E. (1967) highlights the influence of the surface overload on the final dry density for vertical vibrations. Maximum dry density was reached with zero surcharge applied at the free surface to the sample. Varying the value of the Uniformity coefficient, C_u, the authors showed that the granulometry of the sand also plays a role in the mechanism of vibrocompaction. Coarse and well graded sands can be compacted with much less effort as compared to uniform fine sands. It is to note that similar results were observed by Greenfield and Misiaszek (1968) for horizontal vibrations.

Kolmayer (1970) concentrated on the coupled influence of the dimensionless acceleration amplitude, Γ, and the surface overload, σ, on the rate of compaction characterized by the coefficient β_t. Tests were performed for vertical vibrations.

Figure 2-29 illustrates the domains of the vibration, imposed in the different researches, in a bi-logarithmic diagram (Velocity vs. Period).

The inclined axis of this diagram correspond to the displacement or acceleration amplitudes. The advantage of this presentation is to give simultaneously all the information concerning the motion. Displacement, velocity and acceleration amplitudes, frequency and period are represented in the same graph. With regards to the different domains of vibration exploited by the authors, it would be very interesting to compare the influence of the acceleration amplitude, Γ, on the dry relative density, D_r, obtained after horizontal and vertical vibrations. Unfortunately, the authors did not provide sufficient data to perform such comparison. Minimum and maximum void ratios are not systematically provided.

2.5.2 Influence of vibrations on the shear strength of dry sand

Previous researches investigating the shear strength of dry sand were presented. The studies characterize the influence of vibrations on the coefficient of internal friction ($f = \tan \phi_{mob} = \tau_{ds}/\sigma$). Table 2-7 summarizes the experimental conditions and results of the different studies. In Fig. 2-30, the domains of investigation of the influence of vibrations on the shear strength are added to the domains of vibration used to characterize the volume change of dry sand.

According to the authors, acceleration amplitude, Γ, is the governing motion parameter of the shear strength degradation. Figure 2-31 summarizes their results. When Γ is increased, there is an exponential decrease of the internal friction coefficient, f.

The most remarkable contribution of these studies is given by Youd (1967) which highlighted the influence of the volume change occuring during the shearing on the internal friction coefficient, f. Figure 2-32 illustrates the coupled influence of the acceleration amplitude, Γ, and the initial void ratio, e_0, on $\tan \phi_{mob}$. The black points are the experimental results obtained for $e_0 = e_\Gamma$.

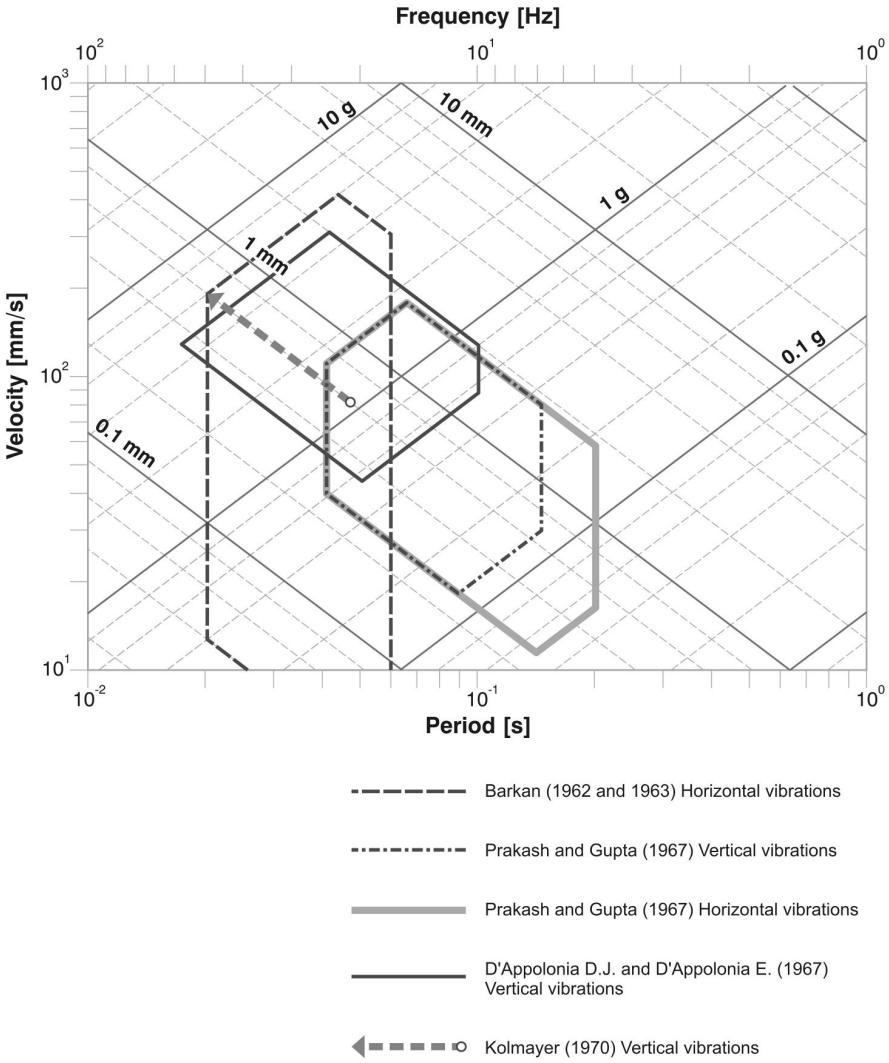

Figure 2-29: Domains of investigation of the studies characterizing the influence of vibrations on the volume change of dry sand.

Youd (1967) demonstrated that the equilibrium void ratio (EVR), e_Γ, ultimately attained by a loose uniform granular system subjected to vibration, is also the critical void ratio (CVR), e_c, for the system if sheared while subjected to the same vibration. Moreover, e_Γ, e_c and f are reduced considerably by vibration and exponentially decreased with Γ.

This result presents a particular interest with regards to critical state soil mechanics (CSSM). Following the CSSM, the complete state boundary surface formed in the (q: p': e) space forms a boundary beyond which any test paths, applied to a soil specimen, do not go. Figure 2-33 illustrates this surface which is assumed unique for each type of soil (Atkinson and Bransby, 1978). Nevertheless, considering the work of Youd (1967), the application of the vibrations to the sample

leads to the deformation of this surface because of the influence of the acceleration on the CVR.

Authors	Type of sand	Direction of the vibrations	Motion amplitude	Static overload	Experimental set-up	Observations
Mogami and Kubo (1953)	Soma sand	Vertical, sinusoidal	0.45<Γ<4 0.05<A (mm)<0.43 fr=48 Hz	0<σ<3.9 kPa	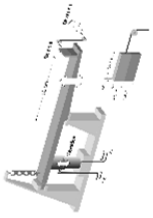 Rectangular shear box on an electromical vibrating table	1.92>f>0.16 for 0.45<Γ<4
Savchenko in Barkan (1962 and 1963)	No indication	Horizontal	0<Γ<6.75 0<A (mm)<1.7 0<fr (Hz)<50	39<σ<147 kPa	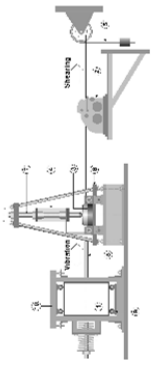 Rectangular shear box on a vibrating table	0.85>f>0.37 for 0<Γ<6.75
Youd (1967) According to De Jaeger (1991) : d_{50}=0.71mm C_u=1.18 e_{min}=0.52 e_{max}=0.74	Ottawa sand	Horizontal	0<Γ<5.8 0<A (mm)<1.6 fr=30 Hz	σ=70kPa	 Rectangular shear box on a vibrating table	0.95>f>0.56 for 0<Γ<5.8
Kolmayer (1970)	Laboratory sand d_{50}=0.85mm C_u=1.8 ρ_s=2.68 gr/cm³	Vertical	0<Γ<4.3 A=0.6mm 0<fr (Hz) <42	0<σ<250 kPa	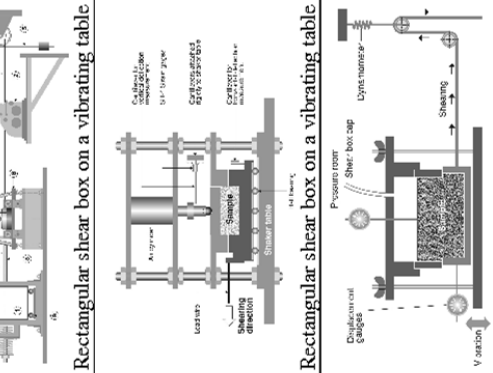 Cylindrical shear box on a vibrating table	0.76>f>0.66 for 0<Γ<4.3

Table 2-7: Experimental researches investigating the influence of vibrations on the shear strength of dry sand.

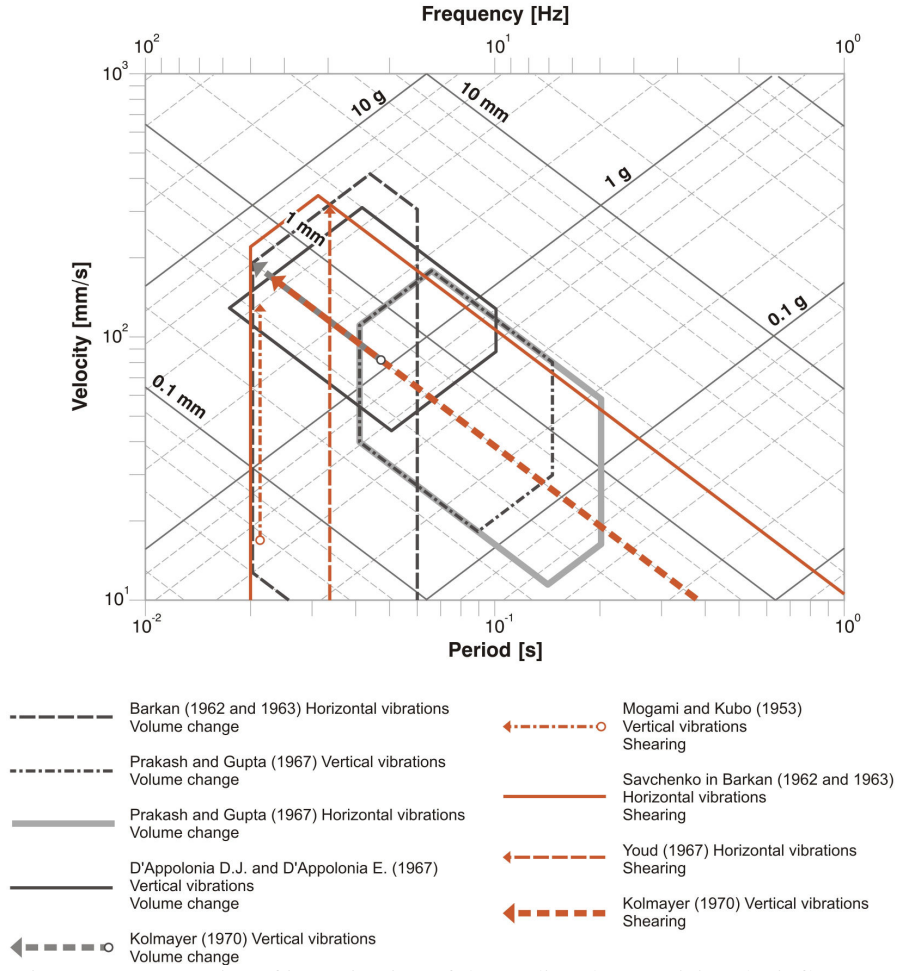

Figure 2-30: Domains of investigation of the studies characterizing the influence of vibrations on the shear strength of dry sand.

If the granular material is compacted to a void ratio less than the static CVR, it may shear at that void ratio without dilating above it, or may even densify further and shears at a smaller void ratio.
This means that for different acceleration amplitudes, new dynamic complete state boundary surfaces formed in (q: p': e) space could be build conducting additional experiments in deviatoric conditions with various effective stresses applied on the sample. New critical state lines should be discovered for each acceleration. Hence, the application of vibrations to the soil sample could lead to the emergence of an ensemble of complete state boundary surfaces in (q: p': e) space depending only on the acceleration amplitude, Γ.

2.5.3 Vibro-fluidization of dry sand

The "vibro-fluidization" characterizes the shear strength degradation of a dry granular material subjected to vibrations. When a dry sand is vibrated, the force

chains in the sample are assumed to be progressively degraded depending on the acceleration amplitude of the vibrations, Γ. The sand behaves like a fluid and is said "vibro-fluidized". A revisited intrinsic Coulomb failure criterion is proposed to take into account the presence of a "shaking pressure" playing a similar role to the pore pressure in saturated conditions.

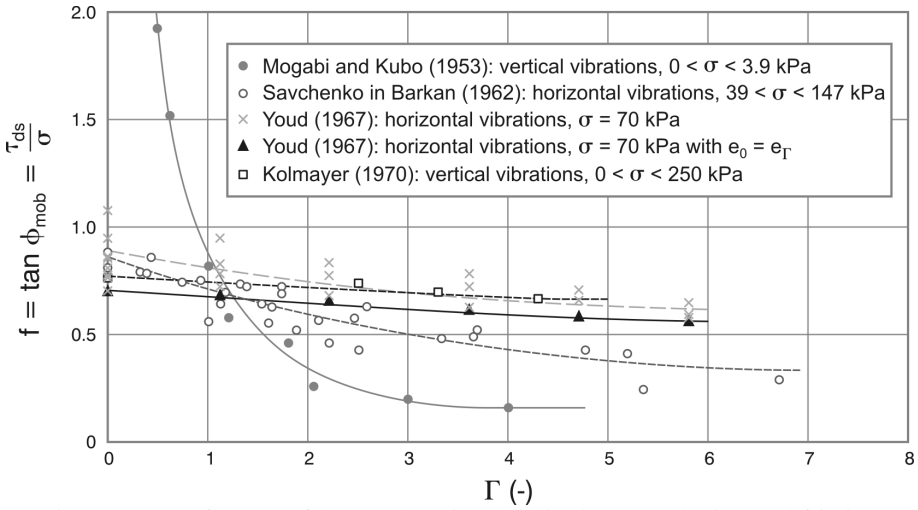

Figure 2-31: Influence of the acceleration amplitude, Γ, on the internal friction coefficient, f, of dry sand.

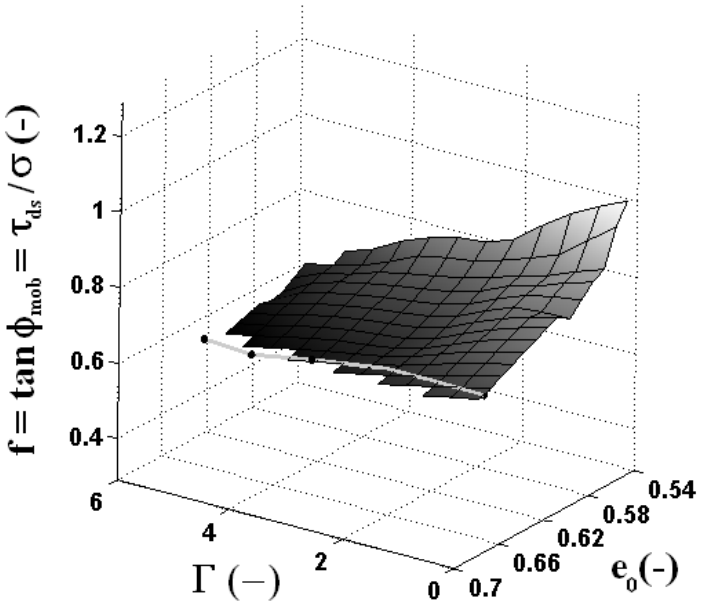

Figure 2-32: Coupled influence of the acceleration amplitude, Γ, and the initial void ratio, e_0, on the internal friction coefficient, f, after Youd (1967).

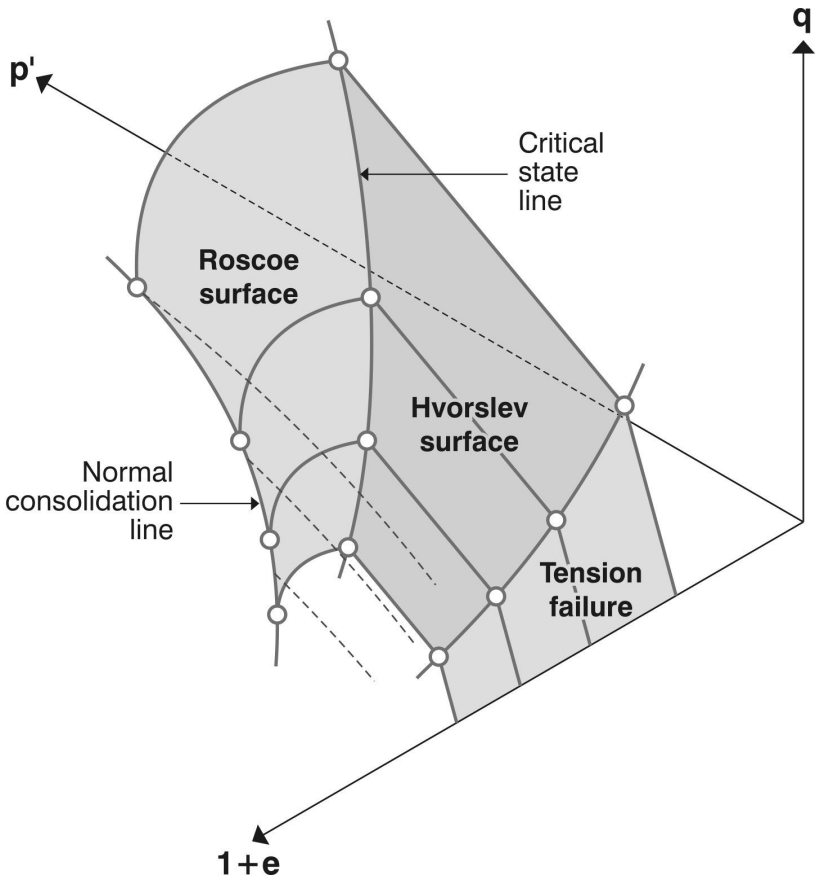

Figure 2-33: The complete state boundary surface in q: p': e space, after Atkinson and Bransby (1978).

Liquefaction or cyclic mobility in saturated sands and vibro-fluidization phenomenon in dry sands seem to present points in common not only at the microscopic scale but also considering the expression of the intrinsic Coulomb failure criterion. Moreover, all these phenomena contribute to the success of the vibrodriving process and are included in the "fluidization" process described by Rodger and Littlejohn (1980).

The urge to build an analogy between both types of processes is large. But in saturated conditions, the degradation of the granular skeleton is due to the increase of the pore pressure (because of the no change volume condition), while in dry conditions, the granular skeleton degradation is due to the application of the vibrations which could lead to volume change. Hence, there is a fundamental difference between both processes. A strong connection could be made between both kinds of phenomena if it is demonstrated that "vibro-fluidization" can occur without volume change.

2.5.4 Sphere penetration experiments (SPE's)

Finally, sphere penetration experiments of Barkan (1962) were regarded in order to study the vibroviscous character of the soil resistance when it is subjected to vibrations. According to Barkan (1962), the internal friction resistance of dry sand tends to vanish and starts behaving like a viscous fluid when subjected to intense vibrations. From the SPE results, the sinking velocity of the sphere seemed to obey Stokes law allowing the determination of the vibro-viscosity coefficient. The inverse of this latter was shown to vary linearly with the acceleration amplitude, Γ.

In spite of the variety of all these studies, the important role of the acceleration amplitude, Γ, on the behavior of the vibrated dry sand is highlighted. The equilibrium void ratio (e_Γ), the critical void ratio (e_c), the shear strength of vibrated dry sand and the side resistance of a vibrated sheet-pile, all vary exponentially with Γ. But all these results must be regarded with caution due to the uncertainties concerning the experimental setups and because of the different procedures followed by the aforesaid authors.

When a granular sample is exposed to vibration a wealth of phenomena may be observed such as segregation, convection, arching, heaping, fluidization,… Particle recirculation patterns will be discussed in Chapter 3.

3 Experimental research on dynamic behavior of vibrated dry sand

3.1 Introduction

The sphere penetration experiments (SPE) performed by Barkan (1962) deserve interest. They allow us to make a connection between the study of the dynamic properties of dry sand and the vibratory driving process. Indeed, the penetration of a profile can be observed in a vibrated dry granular soil.

As explained in the previous chapter, the shear modulus of the soil is progressively degraded when the zone around the vibrated profile is approached. In this strongly remolded zone, the concept of shear modulus must be reappraised. The behavior of the soil could be therefore characterized by the vibro-viscosity coefficient. Barkan (1963) has attempted to build a model of soil based on this concept. He notably determined the sinking velocity of a profile in presence of soil lateral resistance and compared the results of its analytical model with vibrodriving experiments with relative success. Therefore, the consideration of the vibro-viscosity coefficient could represent a quantum leap towards the understanding of the vibrodriving process in dry sands. Nevertheless, a number of critical observations can be formulated regarding the early results of Barkan (1962).

According to our own researches (Denies and Holeyman, 2007 and 2008), the shape of the penetrating logs (Stokes law for all Barkan's results) could depend on the one hand, on the vibration level applied to the sand (coupled influence of the displacement amplitude and frequency) and on the other hand, on the initial void ratio of the granular medium in the container before beginning the sphere penetration experiment.

Below the threshold value, Γ_0, there is no information about potential sphere refusal conditions, as Stokes' law does not entail such limitation.

Considering the previous study of Ermolaev and Senin (1968b) on shear strength degradation under vertical vibrations, the absence of progressive states depending on acceleration amplitude, Γ, is surprising.

Moreover, the inverse of the vibro-viscosity coefficient seems to vary linearly with the acceleration amplitude. However, with regards to Fig. 2-6 illustrating vibro-extracting process results, when soil is vibro-fluidized, the increase of the acceleration amplitude probably does not allow to increase the penetration velocity of the profile.

There is a lack of indication about the vibrated sand behavior. Barkan (1962) did not describe the movement of the soil particles. Is the sand submitted to general convective motion or is there just a downward segregation movement of the sphere, A, in the vibrated sand, B, in settlement?

Finally, some uncertainties remain about the 1962 Barkan SPE results. Indeed, considering the English translation (Barkan, 1962) of the original Russian book: "DYNAMIKA OSNOVANIY I FUNDAMENTOV" (Barkan, 1948) and the French translation (Barkan, 1963) of the original Russian book: "VIBROMETOD V STROÏTELJSTVE" (Barkan, 1960), several differences in the SPE results and a lot of errors in the definition of the units are observed.

For the purposes of investigating these questions and exploring the dynamic behavior of dry sand, a new SPE apparatus was designed.

3.2 New UCL-SPE apparatus

Figure 3-1 presents the SPE apparatus designed and constructed at UCL. Figure 3-2 illustrates the experimental scheme of the UCL-SPE apparatus.

Figure 3-1: UCL Sphere Penetration Experiment (SPE) apparatus, after Denies et al. (2009).

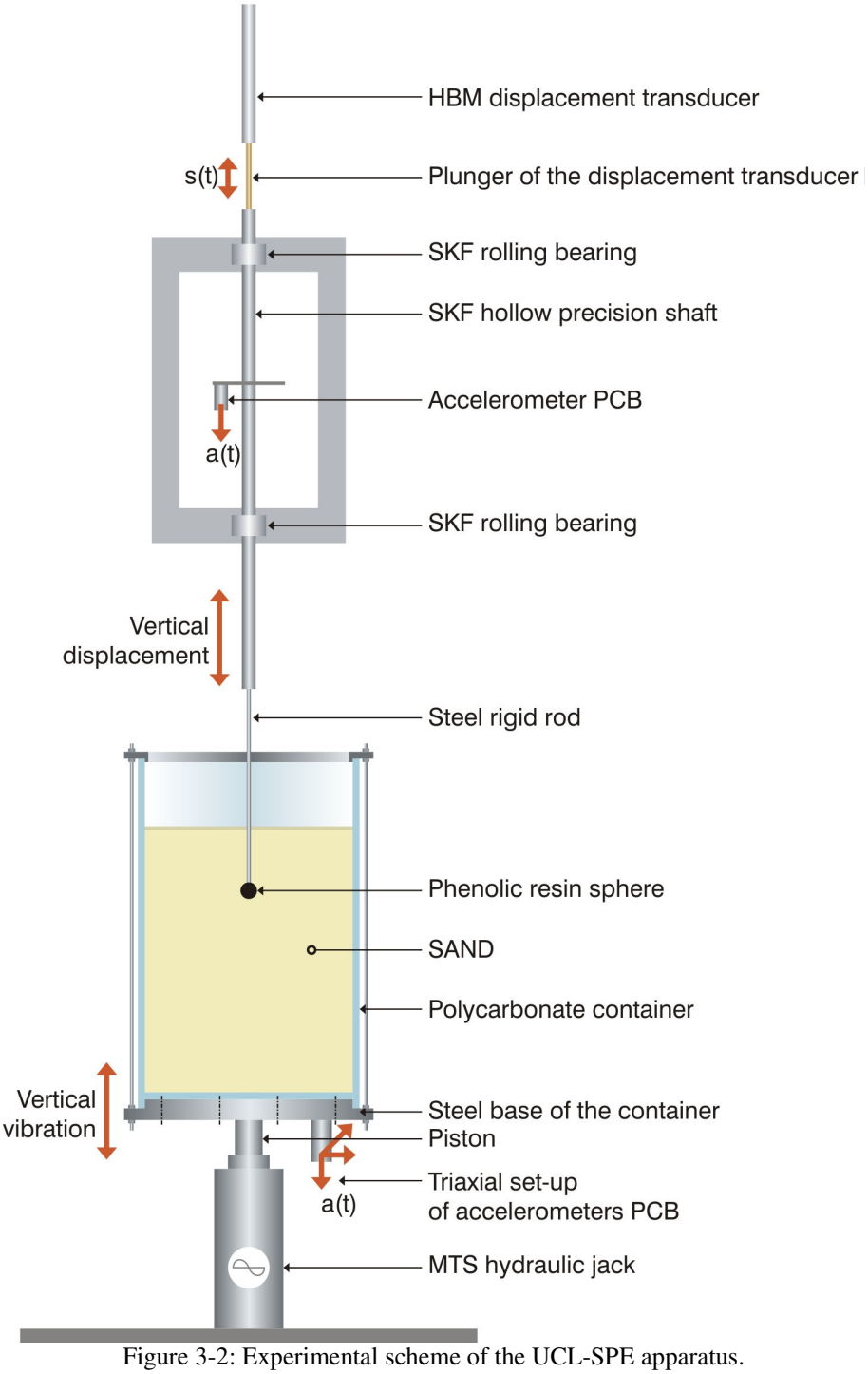

Figure 3-2: Experimental scheme of the UCL-SPE apparatus.

In the lower part, a cylindrical transparent polycarbonate container (52 cm height and 40 cm diameter) is vertically actuated by a servo-controlled MTS hydraulic jack, illustrated in Fig. 3-3.

Figure 3-3: MTS hydraulic jack.

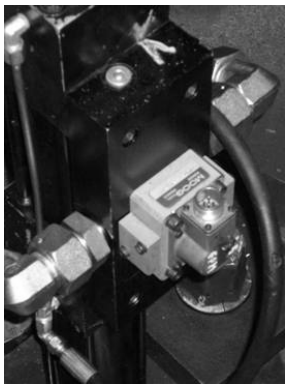

Figure 3-4: Servovalve Moog.

The movement programmed to the container is assumed sinusoidal. Displacement amplitude and frequency are imposed with the help of a servovalve Moog, illustrated in Fig. 3-4. Servovalves are electrohydraulic, continuously acting valves that transform a changing analog or digital input signal into a stepless hydraulic output (flow or pressure). The flow of oil is regulated and actuates the piston in the hydraulic jack. A rigid rod is fixed to the piston to transmit the displacement and the frequency to the bottom of the cylindrical container.

The system is equiped with a servomechanism device that uses error-sensing feedback (a regulation loop) to correct the performance of the oil flow regulation which provides an accurate control of the mechanical position of the piston. Nevertheless, the working of the servomechanism and the regulation of the servovalve can lead to the occurence of shocks in the piston for several frequencies at the end of the stroke. While the displacement is well-controlled, the resulting signal of acceleration can be corrupted.

Figure 3-5 illustrates the working scheme of the servo-hydraulic system of the Laboratory of Civil Engineering of the UCL. The imposed displacement amplitude and frequency are imposed to the system with the help of a computer workstation (1) connected to the control unit Zwick/Roell 9690 (2). The control unit constitutes the heart of the servo-hydraulic system. It controls the regulation loop with a measurement sample rate of 10kHz with a resolution of 19 bits which confers to the system exceptional characteristics in terms of frequency response and accuracy of the measurements. The control unit manages the working of the Bosch pump (3) which is supplied by an electrical board (4). The pump unit consists in two 37 kW motors, each controlling a gear pump with a flow capacity of 90 l/min. The pump unit is also equiped with a pressure regulator allowing to maintain a pressure of 220 bars in the hydraulic circuit. The pump is connected to an hydraulic control station (5) which distributes the oil flow to the servovalve of the hydraulic jack (6). It also plays the role of safety valve with an automatic shut-off in the event of hose failure. It is equiped with a filter to mitigate the abrasive action of the particles. The hydraulic control station is designed to provide a stable pressure to the servovalve of

the hydraulic jack. The frequency and the displacement of the piston rod are regulated with the help of a conditioner and piloting device (7).

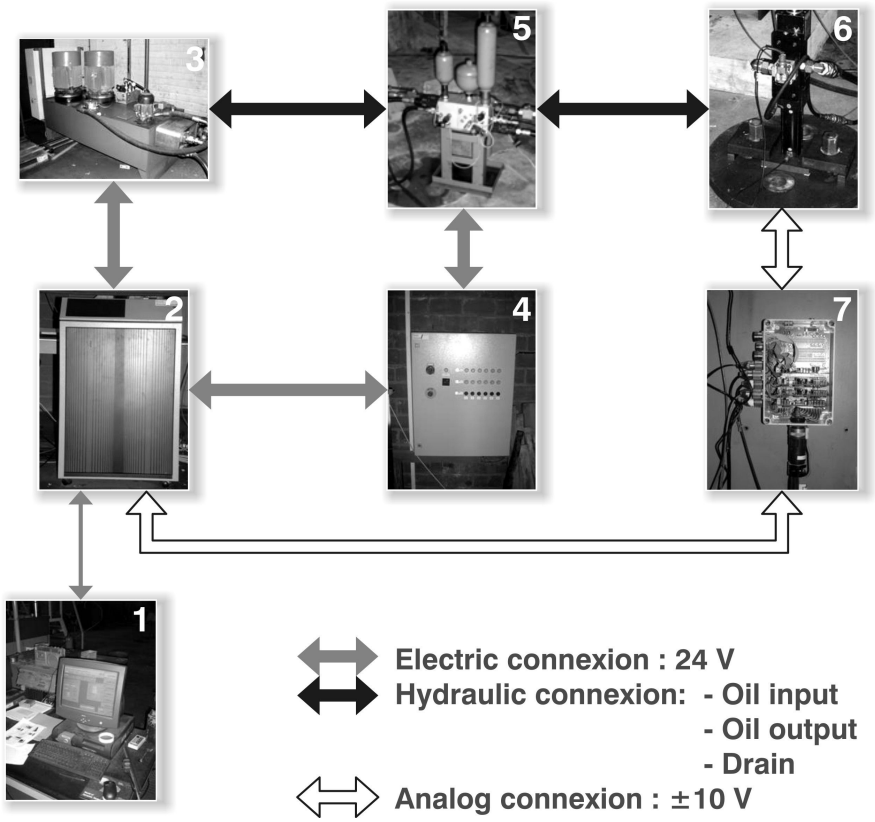

Figure 3-5: Working scheme of the servo-hydraulic system.

As illustrated in Fig. 3-6, the effective motion of the bottom of the sand container is measured, regardless of the MTS system, with a triaxial set-up of accelerometers PCB (5g amplitude range in the radial and tangential directions and 5g or 50g amplitude range in the vertical direction with respective precision of 0.08g and 0.1g).

The measurements are taken using a data acquisition equipment, represented in Fig. 3-7. A laptop (computer) is used to record and process the data. It is connected to a data acquisition card DAQPad-6070E (1.25 MS/s, 12-Bit) from National Instruments. The DAQPad-6070E is a high-performance multifunction analog, digital, and timing device for computers. It uses the Real-Time System Integration (RTSI) bus to easily synchronize multiple measurement functions to a common timing event. The DAQ-Pad-6070E is connected to a signal conditioner SCXI from National Instruments which supplies power to the accelerometers and the different sensors.

In the upper part of the UCL-SPE apparatus, the sphere penetrometer is free to move only vertically. The sphere penetrometer consists in a SKF hollow precision shaft 16 mm in diameter. A steel rigid rod 6 mm in diameter and 45 cm length is

fixed at the end of the precision shaft. Only this rigid rod is sinking in the sand during SPE's. A sphere is connected to the toe of the rigid rod. The sphere is manufactured with phenolic resin. Its diameter is 28.58 mm. The total mass of the sphere penetrometer is 1.57 kg leading to an apparent density of the sphere close to $1.28\ 10^6$ kg/m³.

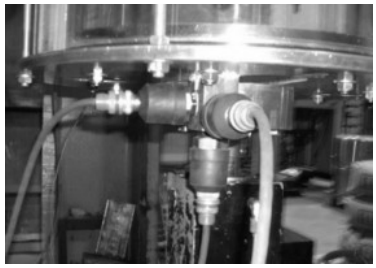

Figure 3-6: Triaxial set-up of accelerometers PCB.

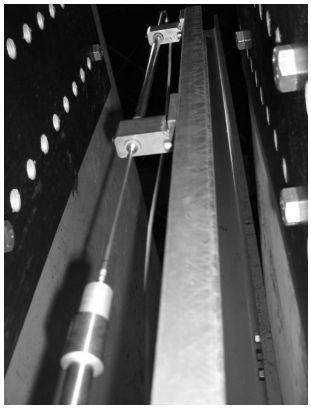

Figure 3-8: Inductive HBM standard displacement transducer.

Figure 3-7: Data acquisition equipment for SPE measurements.

Two SKF rolling bearings allow the vertical motion of the precision shaft. These linear ball bearings are bushings with recirculating ball tracks which provide low friction movement and the possibility of unlimited stroke.

The penetration of the sphere was recorded with the help of a 500 mm range inductive HBM standard displacement transducer connected to the upper extremity of the precision shaft, as illustrated in Fig. 3-8. The HBM tranducer is characterized by a precision of 0.5 mm and a carrier frequency of 4.8±1% kHz.

The acceleration of the sphere was measured with an accelerometer PCB (5 or 50g amplitude range).

A surface roughness analysis of the polycarbonate container boundaries and the phenolic resin sphere is provided in Appendix 7.2. The RMS roughnesses, at a

length scale of 10 µm, are 7.8 nm and 63.2 nm respectively for the polycarbonate boundaries and the phenolic resin sphere.

3.3 Fontainebleau sand

3.3.1 Fontainebleau sand characteristics

The Fontainebleau sand outcrops in the area of the Fontainebleau Forest lying sixty kilometres southeast of Paris, France. The Fontainebleau sand, used during our investigation, is extracted in Nemours and commercialised by the firm Sifraco under the reference: Ne34.

The Fontainebleau sand is a fine quartz sand with uniform grain size (d_{50} = 0.19 mm and C_u = 1.6). The grain-size distribution obtained following the NBN EN 933-1 norm ranges from 0.1 to 0.4 mm, as illustrated in Fig. 3-9. The grain shape was analyzed using scanning electron microscope. Figure 3-10 characterizes the grain-size distribution and the grain shape of Fontainebleau sand grains. Fontainebleau sand can be characterized as subangular or subrounded. Indeed, the grains have preserved their intial shape. They present a subangular character because they are free from sharp edges and corners but several angles have preserved their acuity. Nevertheless, the angularity has been smoothed by the wearing effect of time and several grains are subrounded. The surface roughness of the grains is characterized by some marks of attrition (Russel R. D. and Taylor R. E., 1937). Grain shape and surface roughness of both Fontainebleau sand particles are shown in Fig. 3-11, with resolution bars of 200 µm, 50 µm and 10 µm respectively. The volumetric mass of the sand grains is 2.642 gr/cm³.

The chemical composition is given by the Sifraco technical form and reproduced in Table 3-1.

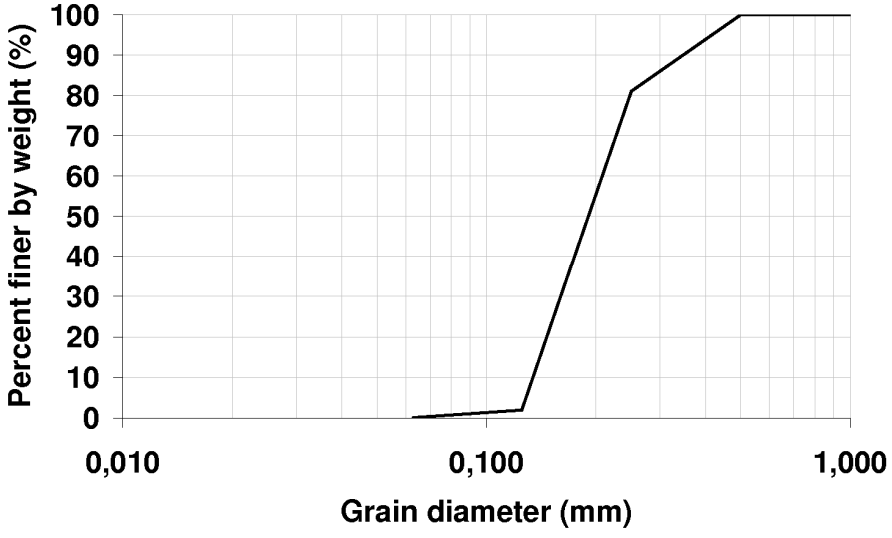

Figure 3-9: Grain size curve of Fontainebleau sand.

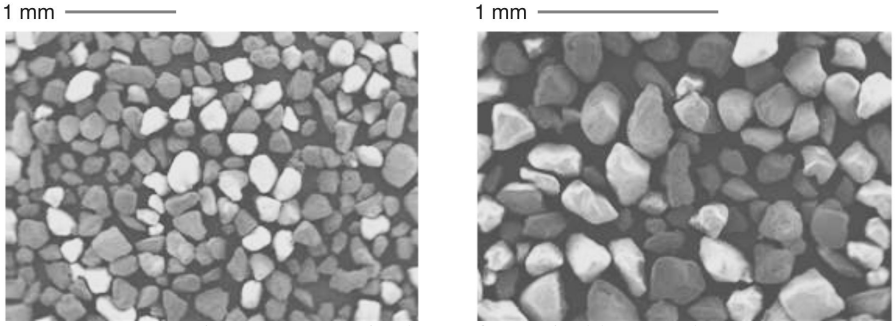

Figure 3-10: Grain shape of Fontainebleau sand.

SiO_2	superior to 99.7 %
Fe_2O_3	inferior to 0.030 %
Al_2O_3	inferior to 0.150 %
TiO_2	inferior to 0.033 %
CaO	inferior to 0.040 %
K_20	inferior to 0.035 %

Table 3-1: Chemical composition of Fontainebleau sand, after Sifraco technical form.

The minimum volumetric mass of dry sand, reached with loose bulk density (LBD) test (De Jaeger, 1991), is $\rho_{min} = 1.405$ gr/cm³, $e_{max} = 0.88$ (-) and the maximum volumetric mass of dry sand, reached with Kolbuszewski method (Kolbuszewski, 1948), is $\rho_{max} = 1.705$ gr/cm³, $e_{min} = 0.55$ (-).

Figure 3-12 illustrates results of drained triaxial compression tests for low level of consolidation stress, after Dupla and Canou (1994). The tests were performed with the help of a Bishop and Wesley triaxial cell coupled with a GDS pressure-volume controller. The sand was initially poured with an initial relative density, $D_r = 60\%$, in specimens 70 mm in diameter and 140 mm high. The triaxial test specimens were built with 7 successive layers 2 cm of thickness. The rate of shear was 0.5% axial strain per minute and the maximal axial strain was limited to 15%. The triaxial compression tests were performed for four levels of consolidation stress, σ_c: 25, 50, 75 and 100 kPa. In Fig. 3-12a, the specimens exhibit limited peaks of shear strength in their q'/p': ε_a curves followed by a softening phase, where ε_a represents the axial strain (%). When consolidation stress is larger, the shear strength of the specimen is increased. The peak shear strength is proportional to the consolidation stress with homothetic shearing curves, as illustrated by the superposition of q'/p' curves. In Fig. 3-12b, the volumetric strains of the triaxial test specimens present a marked dilatancy phase after an initial contracting behavior. At the end of the test, the samples have not achieved an ultimate state, there are always changes in stresses or in volumetric strains: the critical state has been not reached. Nevertheless, according to the work of Bolton (1986), it is possible to estimate the value of the critical state angle of friction, Φ_c, which is expected to be close to 30° for Fontainebleau sand.

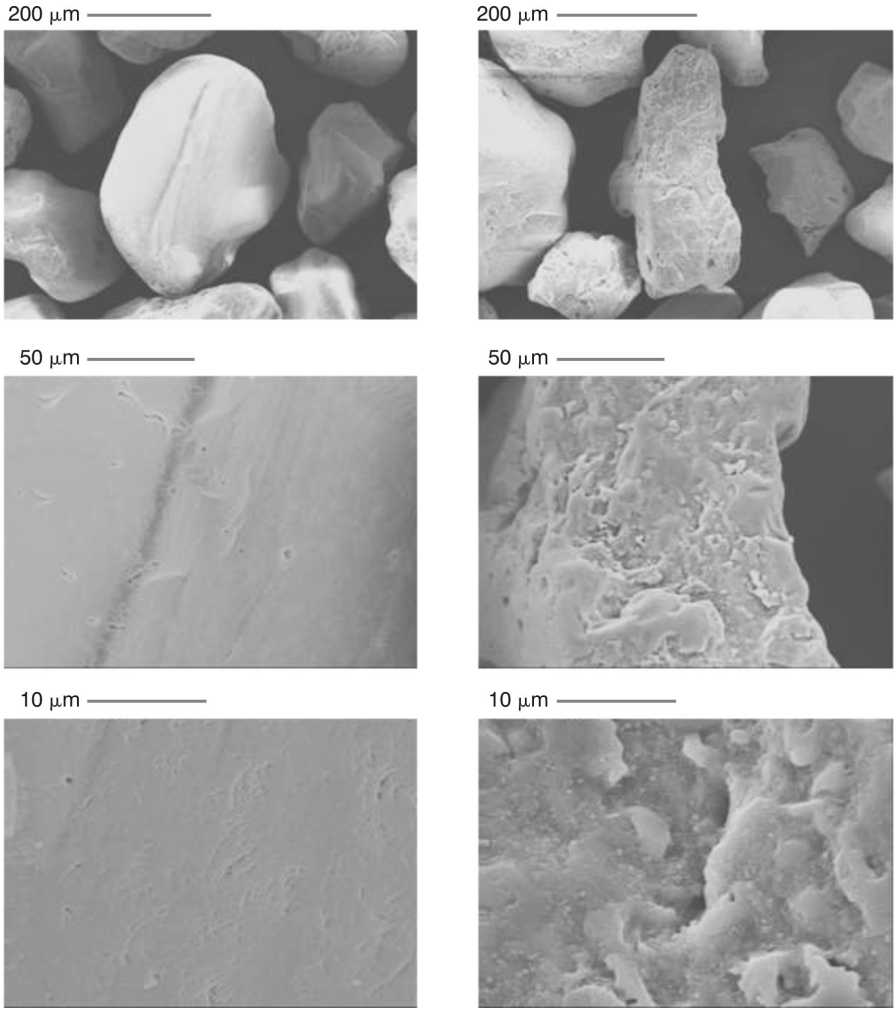

Figure 3-11: Grain shape and surface roughness of both Fontainebleau sand particles.

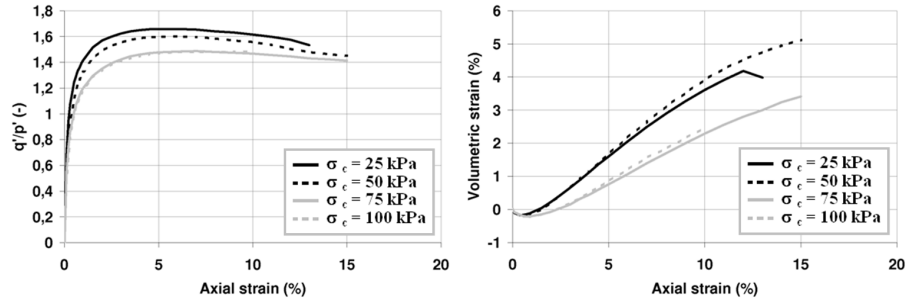

Figure 3-12: Data for drained triaxial compression tests on Fontainebleau sand (after Dupla and Canou, 1994).

The choice of Fontainebleau sand for our experiments is justified by its subrounded character which could promote the vibro-fluidization of the sand subject to vibrations. According to Alanyak (1961), fluidization could be achieved at lower accelerations with uniform round sands than in uniform angular sands because of the grain interlocking phenomenon.

3.3.2 Fontainebleau sand sample preparation

In our experiments, samples of 65 kg of Fontainebleau sand are prepared dry by pouring into the container with a diameter of 400 mm and a height of approximately 35 cm, resulting in a dry density close to 1.47 gr/cm³ or initial void ratio, e_{inti} = 0.80 (-) (D_r = 24%), assumed homogeneous in the sample.

According to Dupla and Canou (2005), there are mainly two methods to reconstitute sand samples in the laboratory namely, by successive layers or by pluviation. Since no pluviation device was available for our experiments, the first method was used. This latter is based on the precise control of the density of each layer, but can also result in heterogeneity between layers. It is also necessary to consider the human factor which has a strong impact on the state of sample. These factors influence the repeatability of the technique. Each deposit was therefore manufactured by the same operator resulting in a weak variability in terms of the relative density. D_r was shown to vary from 24 to 27%.

Each specimen was reconstituted by successive layers using a 1 inch open laboratory funnel, illustrated in Fig. 3-13, with a pluviation height of 10 cm.

Figure 3-13: Laboratory funnel used for sample preparation.

3.4 Vertically vibrated dry sand behavior

3.4.1 Governing parameters

As explained in Section 2.4.2a, when subjected to vibrations, dry sand exhibits a behavior depending on the following variables: the direction of the harmonic vibrations, the vibration parameters (fr, A and Γ), the duration of the vibrations, the size and the roughness of the container, the grain size of sand and the surface overload.

In the present research, Fontainebleau sand is vertically vibrated without applying a surface overload. Figure 3-14 illustrates the domain of the vibrations imposed to the container in a bi-logarithmic diagram (Velocity vs. Period). The black points represent the experimental points of the domain explored during the present research. The domain of the vibrations is bounded by the physical limits of the servohydraulic MTS system. The accuracy of the imposed displacement is on the order of the micrometer in this domain. Beyond the limits, the system retains the frequency but the imposed displacement amplitude is damped and decreased. Table 3-2 identifies the experimental points.

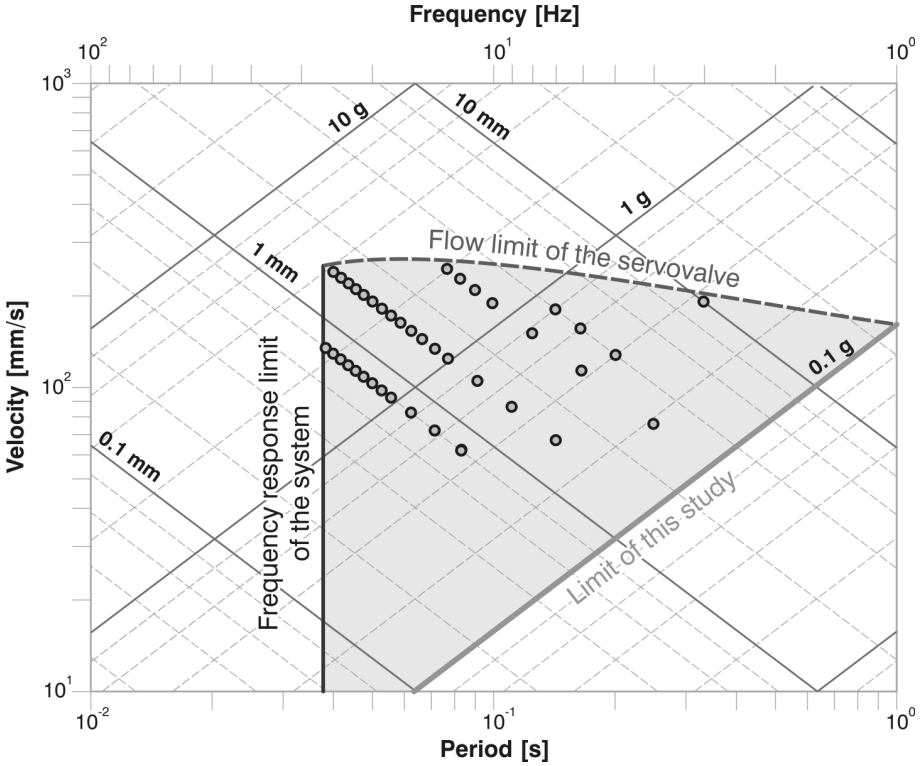

Figure 3-14: Bi-logaritmic diagram of the domain of vibrations.

3.4.2 Volume change with time

Before performing sphere penetration experiments (SPE), dry sand behavior is initially explored without inserting profile into the vertically vibrated container. The following paragraphs concern the void ratio change with time and the void ratio change with the number of cycles applied to the container, for acceleration amplitudes $\Gamma < 1$. Figure 3-15 presents the void ratio vs. time curves for these experiments. The displacement amplitudes were set to A=0.8, 1.5, 3, 4 and 10 mm. For all displacement amplitudes, the results present common characteristics. Initially, the void ratio quickly decreases. Then the volume change is slowing down and the void ratio leads towards an asymptotic value, e_Γ (-), depending on the acceleration amplitude of the vibrations.

A (mm)	fr (Hz)	T (s)	V (mm/s)	Γ (-)
0.8	12	0.083	60.3	0.46
0.8	14	0.071	70.4	0.63
0.8	16	0.063	80.4	0.82
0.8	18	0.056	90.5	1.04
0.8	19	0.053	95.5	1.16
0.8	20	0.050	100.5	1.29
0.8	21	0.048	105.6	1.42
0.8	22	0.045	110.6	1.56
0.8	23	0.043	115.6	1.70
0.8	24	0.042	120.6	1.85
0.8	25	0.040	125.7	2.01
0.8	26	0.038	130.7	2.18
1.5	7	0.143	66.0	0.30
1.5	9	0.111	84.8	0.49
1.5	11	0.091	103.7	0.73
1.5	13	0.077	122.5	1.02
1.5	14	0.071	131.9	1.18
1.5	15	0.067	141.4	1.36
1.5	16	0.063	150.8	1.55
1.5	17	0.059	160.2	1.74
1.5	18	0.056	169.6	1.96
1.5	19	0.053	179.1	2.18
1.5	20	0.050	188.5	2.41
1.5	21	0.048	197.9	2.66
1.5	22	0.045	207.3	2.92
1.5	23	0.043	216.8	3.19
1.5	24	0.042	226.2	3.48
1.5	25	0.040	235.6	3.77
3	4	0.250	75.4	0.19
3	6	0.167	113.1	0.43
3	8	0.125	150.8	0.77
3	10	0.100	188.5	1.21
3	11	0.091	207.3	1.46
3	12	0.083	226.2	1.74
3	13	0.077	245	2.04
4	5	0.200	125.7	0.40
4	6	0.167	150.8	0.58
4	7	0.143	175.9	0.79
10	3	0.333	188.5	0.36

Table 3-2: Summary of the tests performed with the UCL-SPE apparatus to study the behavior of dry sand during vertical shaking.

The black lines are the estimated void ratios, computed using equations (2-15) and (2-16) with β_t (-) and α_t (-) depending on the acceleration amplitude, Γ. The expression (2-15) of the void ratio change with time and the expression (2-16) of the asymptotic void ratio, e_Γ, seem to be convenient for the description of our experiments, except for the test performed at A = 10 mm. When the imposed

displacement increases and comes near the boundary of the attainable domain of vibrations, the acceleration signal becomes corrupted due to the emergence of a shock at the end of the piston stroke. The result of the 10 mm test must be therefore considered with caution.

The volume change covers an important part of the accessible range of void ratios. Table 3-3 summarizes the tests performed to study the volume change during vertical shaking and indicates the values of the empirical coefficients α_t and β_t.

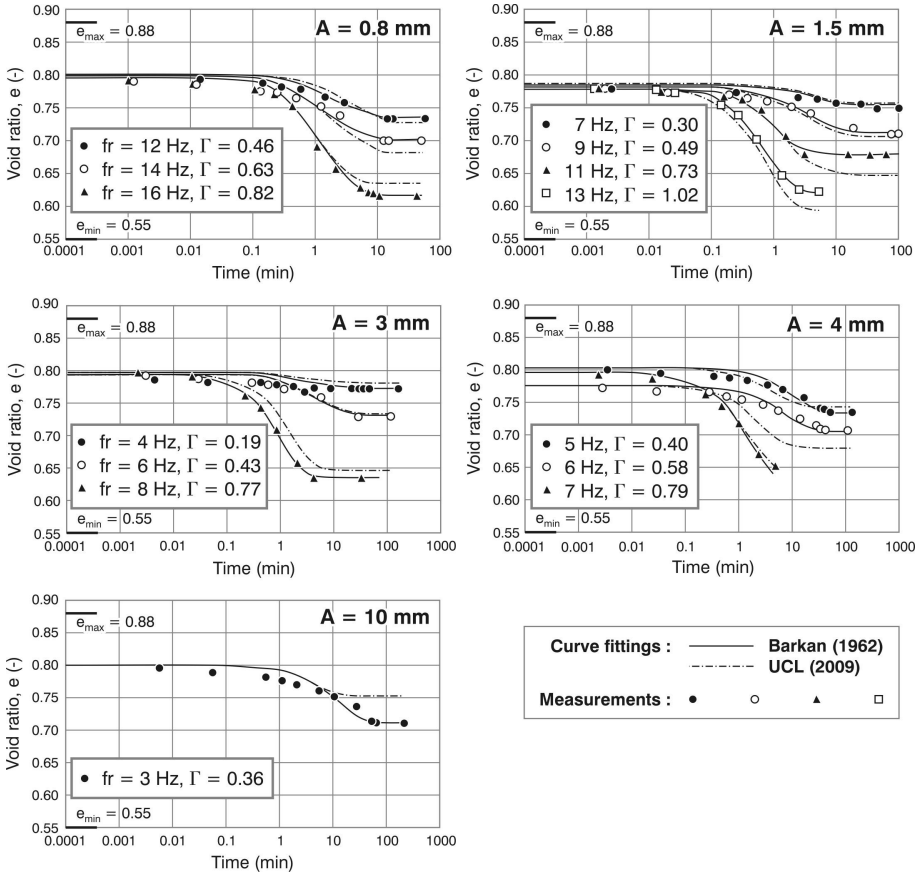

Figure 3-15: Void ratio-time curves for UCL experiments for $\Gamma < 1$, with displacement amplitudes of vibration: A = 0.8, 1.5, 3, 4 and 10 mm.

Figure 3-16 illustrates the good repeatability of volume change results for two acceleration amplitudes.

Figure 3-17 illustrates the governing role of the acceleration amplitude, Γ. As illustrated in Fig. 3-17, for different displacement amplitudes and various frequencies, the volume change seems to behave similarly for identical acceleration amplitude, Γ. The light differences could be due to the limits of accuracy in acceleration of the MTS system. Figure 3-18 illustrates the relationship between the imposed acceleration amplitude, Γ, and the vibratory equilibrium void ratio, e_Γ. The curve represents the vibratory compressibility curve of Fontainebleau sand.

A (mm)	fr (Hz)	Γ (-)	β_t (min^{-1})	α_t (-)
0.8	12	0.46	0.5	0.66
0.8	14	0.63	0.6	0.78
0.8	16	0.82	0.7	1.62
1.5	7	0.30	0.2	0.5
1.5	9	0.49	0.3	0.73
1.5	11	0.73	0.9	0.82
1.5	13	1.02	1.3	1.2
3	4	0.19	0.2	0.43
3	6	0.43	0.22	0.73
3	8	0.77	1	1.41
4	5	0.40	0.1	0.79
4	6	0.58	0.14	0.63
4	7	0.79	0.65	1.45
10	3	0.36	0.08	1.21

Table 3-3: Summary of the experiments characterizing the volume change of dry Fontainebleau sand subjected to vertical vibration in the range $\Gamma < 1$.

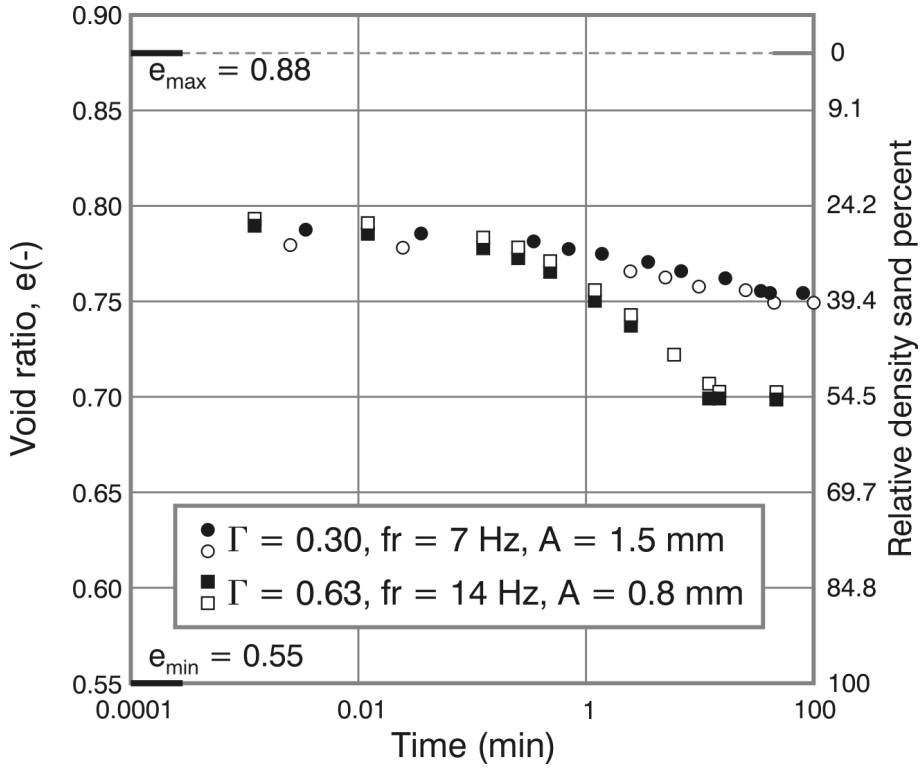

Figure 3-16: Repeatability of the process of volume change of the sample during vibration for two acceleration amplitudes.

Figure 3-19 presents experimental values of β_t computed with the help of equation (2-15) considering the curves of Fig. 3-15, for vertical vibration. β_t seems

to increase with the acceleration amplitude, Γ. Although, it seems difficult to draw a real tendancy, this relationship is fitted with an exponential curve.

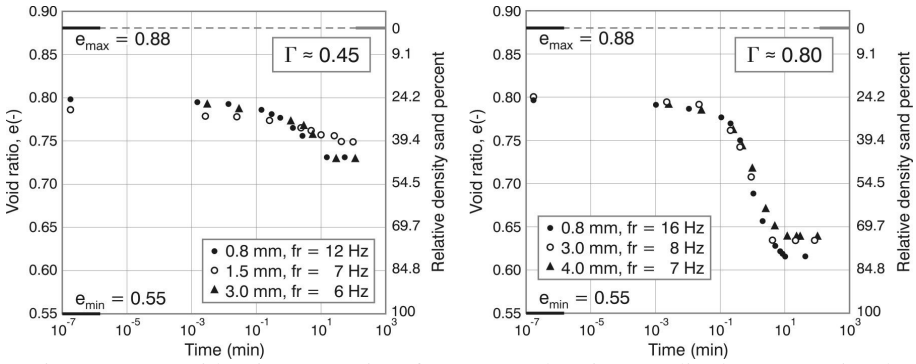

Figure 3-17: Void ratio versus time for two acceleration amplitudes Γ ≈ 0.45 and Γ ≈ 0.8 for different amplitudes of displacement and various frequencies.

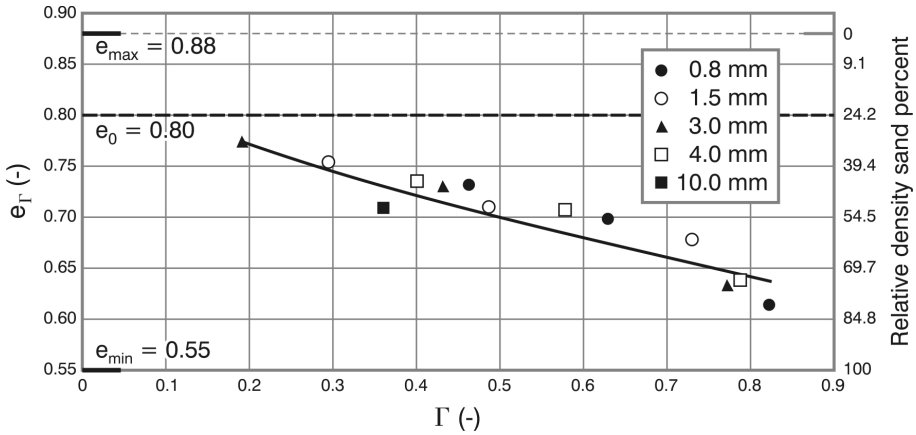

Figure 3-18: Vibratory compressibility curve of Fontainebleau sand.

Figure 3-20 presents the experimental values for α_t computed with the help of equation (2-16) for vibratory equilibrium void ratio, considering the vibratory compressibility curve of Fig. 3-18.

As for β_t, the index of vibratory compaction, α_t, increases with the acceleration amplitude, Γ. The relationship can be also approximated by an exponential curve eliminating the 10 mm displacement amplitude test result.

Considering the UCL observations and assuming β_t and α_t directly dependent on the acceleration amplitude, Γ, it is possible to describe the void ratio vs. time curves with the following empirical expressions depending on Γ and on constant empirical coefficients:

$$e(t) = e_\Gamma + (e_{init} - e_\Gamma)\exp[-0.0741\exp(2.8643\Gamma)t] \qquad \text{(Eq. 3-1)}$$

to describe the evolution of the void ratio as a function of the time for vertical vibrations with acceleration amplitude inferior to 1g, and:

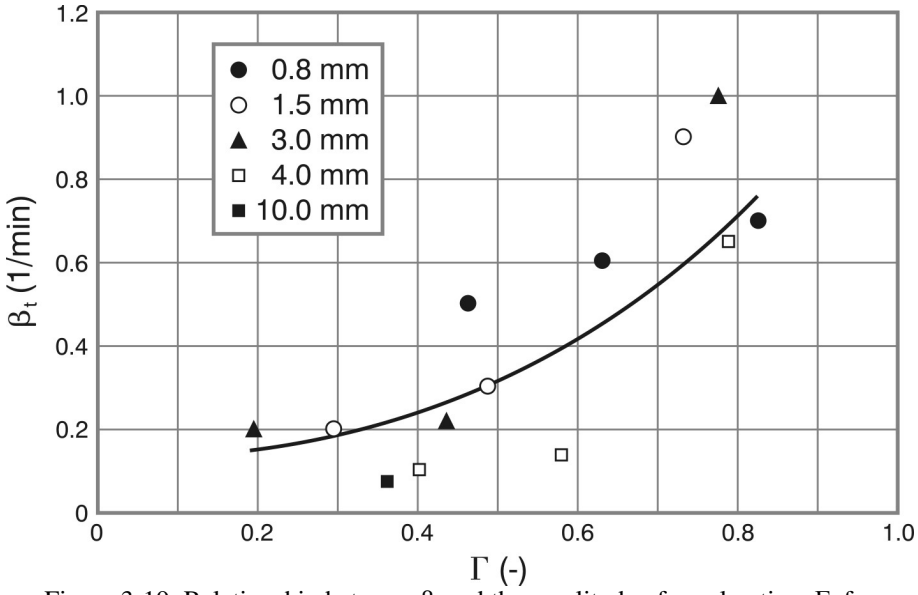

Figure 3-19: Relationship between β_t and the amplitude of acceleration, Γ, for Fontainebleau sand.

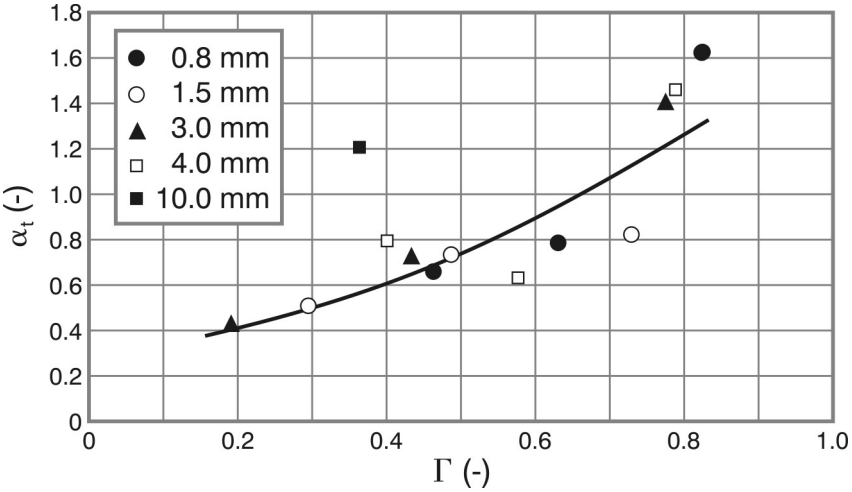

Figure 3-20: Relationship between α_t and the acceleration amplitude, Γ, for Fontainebleau sand.

$$e_\Gamma = e_{\min} + (e_{init} - e_{\min})\exp(-1.6232\Gamma^2) \quad \text{(Eq. 3-2)}$$

to express the vibratory equilibrium void ratio as a function of the acceleration amplitude, Γ. Considering the UCL results (Fig. 3-15), such approximation (represented by dashed grey lines in Fig. 3-15) will lead to a questionable precision, on the order of 5% with respect to the accessible range of void ratio, [0.55-0.88].

Finally, the influence of sand depth in the container is studied. Figure 3-21 presents the volume change for two samples of 65 and 32.5 kg with similar initial void ratio, $e_0 = 0.79$.

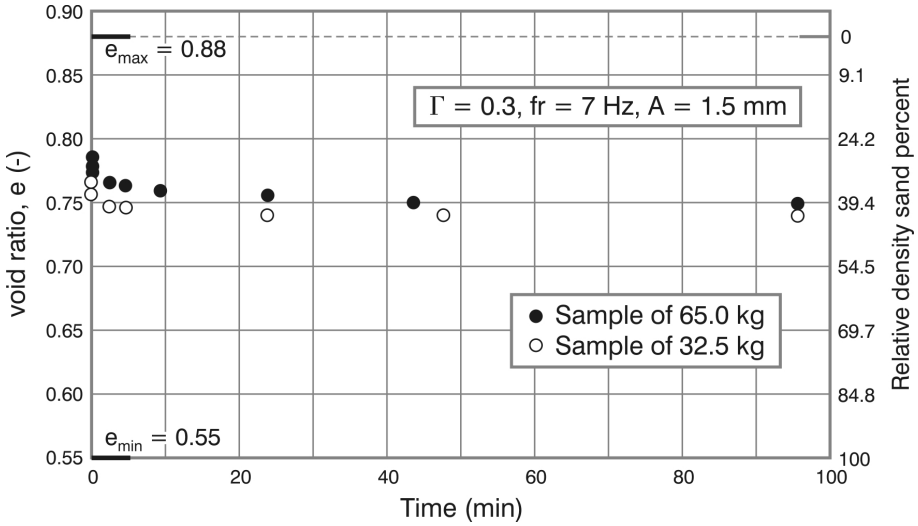

Figure 3-21: Variation of void ratio for specimens of various heights.

Decreasing the height of specimen tends to improve the rate of compaction. Indeed, the coefficient β_t is increased when the weight of the vibrated sand is decreased. Sand overburden is then opposed to the densification of the sample. The coefficient α_t seems to be independent from the sand depth in the container. According to Selig (1963), the vibratory equilibrium void ratio reached in both cases are close to the same value.

3.4.3 Volume change with number of cycles

Figure 3-22 represents the void ratio vs. number of cycles curves during vertical shaking for the experiments illustrated in Fig. 3-15.

The following relationship is proposed to describe the volume change:

$$e(N) = e_\Gamma + (e_{init} - e_\Gamma)\exp(-\beta_n N) \qquad \text{(Eq. 3-3)}$$

where N is the number of cycles applied to the container, β_n caracterizes the cyclic rate of compaction and e_Γ is given by equation (2-15). These relationships are represented by black lines in Fig. 3-22. In Fig. 3-23, no discernable influence of the acceleration amplitude, Γ, could be observed on β_n.

3.4.4 Dry sand vibratory behavior

The following paragraphs focus on the description of the behavior of sand particles during shaking in order to highlight particular movements of the granular assemblage such as settlement, segregation, recirculation, convection,…

When sand is vertically vibrated under gravitational field, three types of behavior are identified, depending on the acceleration amplitude : the densification behavior, the instability surface behavior, and the vibro-fluid behavior. The different patterns of particle recirculation will be described and the boundaries between the different regimes defined.

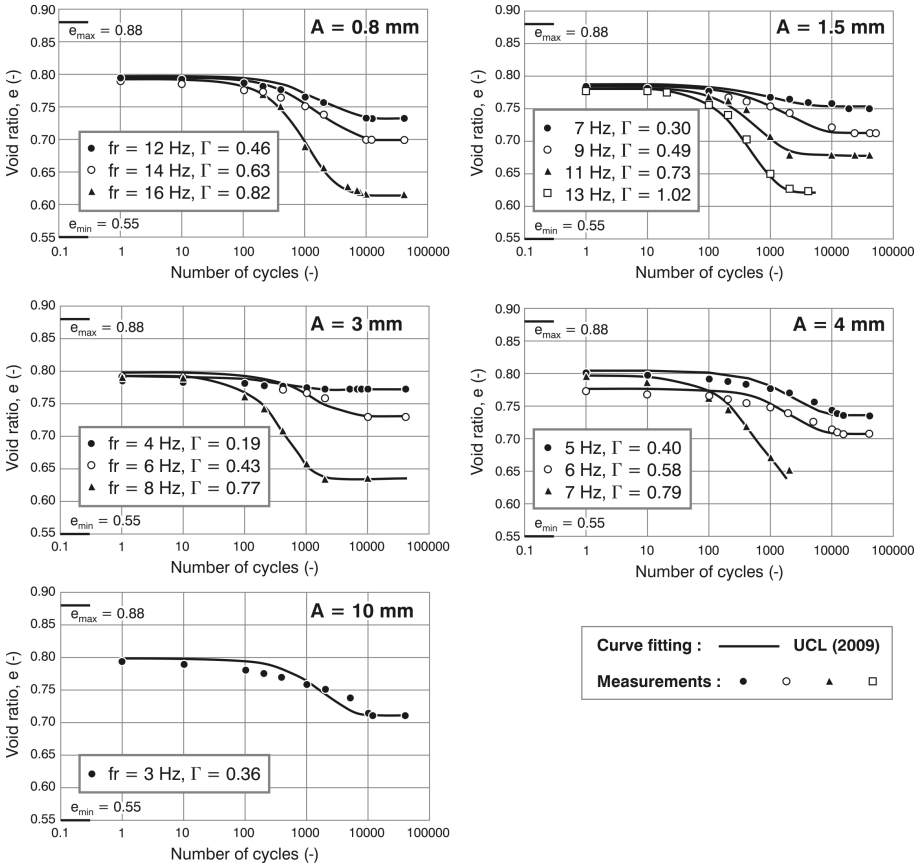

Figure 3-22: Void ratio-number of cycles curves for UCL experiments for $\Gamma < 1$, with displacement amplitudes of vibration: A = 0.8, 1.5, 3, 4 and 10 mm.

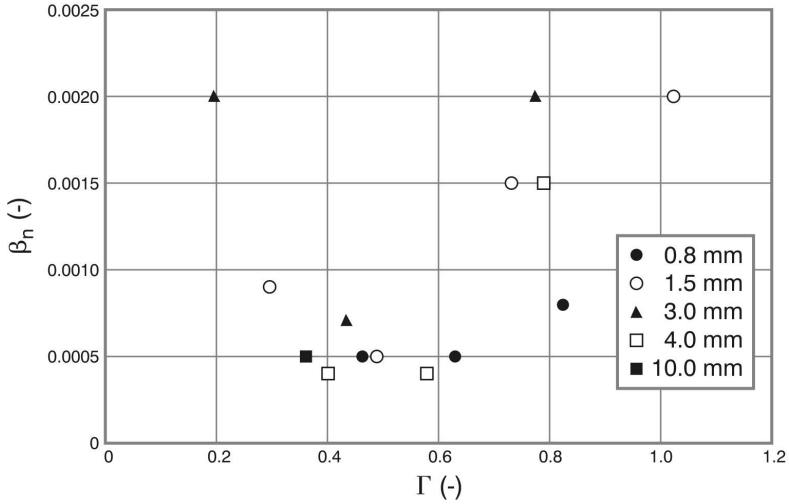

Figure 3-23: Influence of the acceleration amplitude, Γ, on the empirical coefficient β_n.

a. Densification behavior

When non cohesive soil is vertically vibrated under gravitational field, Mogami and Kubo (1953) and Barkan (1962) assert that the volume change depends mainly on the acceleration of the vibrations. The influence of acceleration amplitude was explored with the UCL-SPE apparatus and vertically vibrated sand behavior was observed during shaking. These experiments lead to the following observations. If the peak acceleration is less than 1g, there is a densification of the sample resulting in a global settlement of the sand particles in the sample. No recirculation or segregation of particles was observed in the transparent container. Figure 3-24 illustrates this behavior.

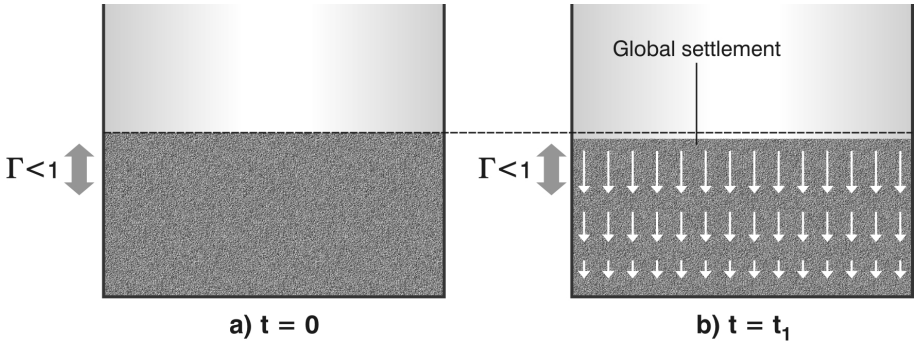

Figure 3-24: Densification behavior.

The efficiency of the densification depends on the initial void ratio of the sample and on the acceleration amplitude. The equations (2-15) and (2-16) or equations (3-1) to (3-3) appear to be valid only within this densification range.

b. Instability surface behavior

When acceleration amplitude reaches 1g, several phenomena come into competition. The first phenomenon is the free-fall-impact condition, described by D'Appolonia D. J. and D'Appolonia E. (1967). When the acceleration is greater than 1g, the sand cannot fully follow the downward motion of the container and goes into free-fall. When the sand catches up with the bottom of the container, there is an impact, and large dynamic stresses and accelerations occur within the sand. This pattern should result in efficient densification.

Nevertheless, as observed in the UCL experiments, when the acceleration is increased beyond 1g, there is an instability in the sand mass leading to the emergence of an inclined free surface, as illustrated in Fig. 3-25. It is characterized firstly by a continuous flow of particles rolling down the inclined surface and secondly by a convective transport inside the vibrated sample which recirculates sand grains at the top of the heap, as observed previously by Evesque and Rajchenbach (1989). The cause of this particular phenomenon seems to be the convective motion accompanied by an upward wave pulse.

During convection, the granular medium convects in response to vertical vibrations (Knight et al., 1993). There is an upward granular flow in the center of the container and a downward granular flow within a thin veneer along the sides. This

phenomenon is due to the inelastic frictional interactions between the grains and the walls of the container (Grossman, 1997).

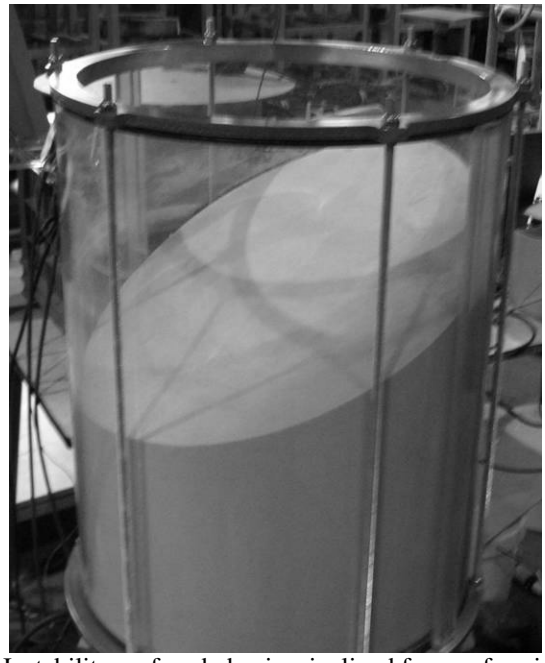

Figure 3-25: Instability surface behavior: inclined free surface in the vibrated sample.

When the container is raised up, the gravitational acceleration is opposed to the displacement of the grains and there are few relative movements between the sand particles. When the container begins to go down, there is a relative acceleration between the grains and the container (Γ-1)g. Then, the grains are momentarily separated from the container. There are more relative movements between particles. Lee (1994) and Grossman (1997) analyzed the density change and the motion of the grains throughout a cycle to explain the convection. Lee (1994) emphasised the effect of the variation in density over the course of a cycle on the shear forces exerted by the sides of the container on the grains. During vertical vibration, the particles are closely packed on the way up, but expand to a lower density on the way down. As observed by Lee (1994), at higher densities, the side of the container can exert a larger drag force on the particles. This means that the grains, as a whole, experience a larger pull downward in the first part of the cycle than upward in the second. This leads to a net downward shear force exerted by the walls on the particles over the course of a cycle and this effect can explain the motion downward along the sides of the container in granular convection. Figure 3-26 illustrates this behavior. During the relative upward motion of the grains relative to the side, the grains are closely packed and display high density, as observed in Fig. 3-26a, while during the relative downward motion, illustrated in Fig. 3-26b, they expand to a lower density. The grey arrows represent the absolute displacements of the grains during each part of the cycle. Figure 3-26c presents the evolution of the absolute

vertical displacement of the black grain. The cumulated displacement per cycle is oriented towards the bottom of the container.

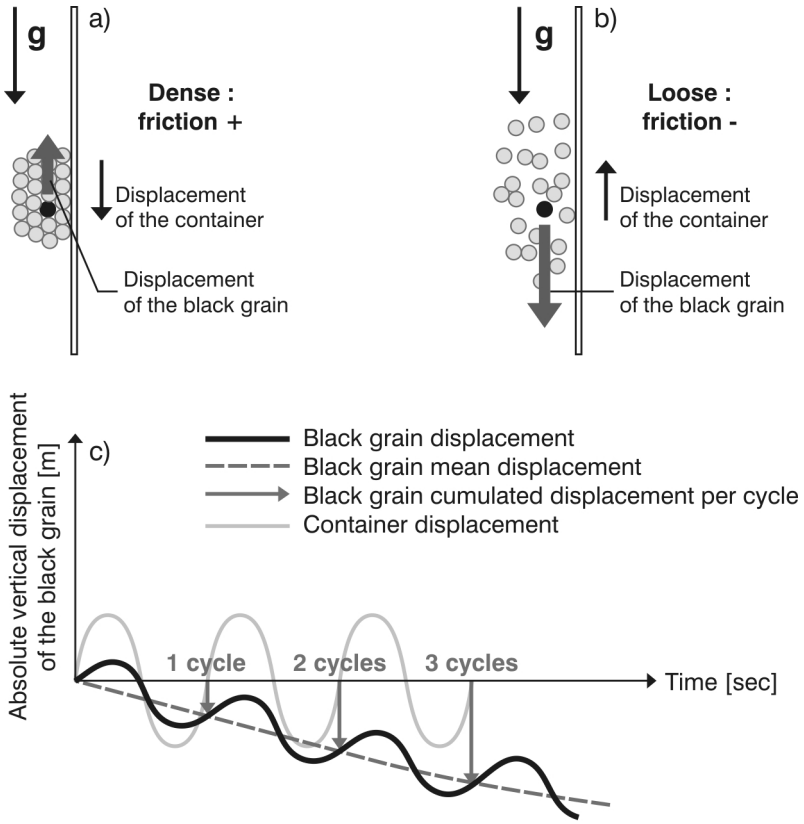

Figure 3-26: Convective behavior of the grains along the sides during vertical vibrations. a) during relative upward motion of the grains relative to the side, b) during relative downward motion of the grains relative to the side, c) Relationship between absolute cumulated displacement of the grains and time during convection.

At the same time, there is a progressive inclination of the free surface. According to Pak and Behringer (1993), the inclination could be due to an upward wave.

When the granular matter is vertically vibrated, there is a dissipation of the introduced kinetic energy by multiple inelastic interactions between grains. This energy loss depends on the particle assemblage. The energy dissipation per unit length in the vertical direction varies as a function of the angular position and depends on the number of grains in contact at different locations. This inevitable asymmetry, in the structure of the sample and in the way the kinetic energy is dissipated, would be at the origin of the emergence of an upward wave in the container. Hence, the choice of the direction of the slope corresponds to a spontaneous breaking of symmetry in the granular assemblage.

The propagation of the upward wave could be explained in this way. There is a supply of sand at the top of the bump by the avalanches. In contrast, at the lower

edge of the bump, the slope becomes steeper and the avalanche rate is higher in comparison with the uphill edge of the bump leading to the spreading of the pulse. This complex process leads to the forming of an inclined plane free surface in the vertically vibrated container.

The angle of the free surface is limited by the nature of the sand particles. During the upward phase, the sand is compacted and behaves like a solid. The slope of this latter cannot exceed a maximum dynamic angle which mainly depends on the nature of the grains. When this maximum angle is reached, the excess of matter flows in continuous avalanches. In this study, the term avalanche references superficial landslide.

In spite of the complexity related to its physical description, the upward wave was clearly observed during our experiments.

Figure 3-27 illustrates the slope emergence in a container vertically vibrated with Γ close to 1, in the course of the vibration. Initially, the convection phenomenon is initiated along the walls (Fig. 3-27a). Then, due to the asymmetry of the assemblage, upward waves are generated and they lead to the emergence of an inclined free surface in the container. The convective rolls recirculate sand grains at the top of the emergent heap. Intermittent avalanches appear at the free surface (Fig. 3-27b). Then, due to the upward waves, there are successive bumps under the inclined free surface covered with continuous avalanches. The slope progressively develops (Fig. 3-27c). Finally, the instability surface regime is developed. Keeping the balance between the upward waves and the maximum dynamic angle, avalanches determine the slope of the inclined free surface (Fig. 3-27d).

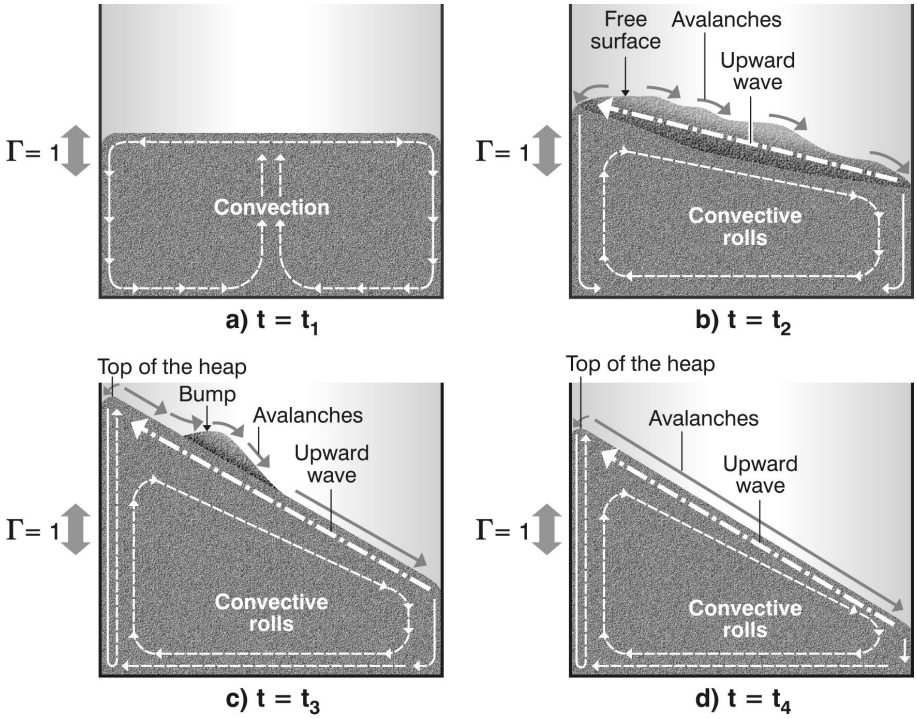

Figure 3-27: Instability surface behavior.

If the acceleration amplitude is still increased, the inclined free surface is progressively dislocated, as illustrated in Fig. 3-28. There is the apparition of a bulge in the sample accompanied by the onset of grain saltation. The emergence of chaotic convective rolls is assumed. They lead to the progressive destruction of the inclined free surface. Table 3-4 summarizes the tests performed with the UCL-SPE apparatus to study the degradation of the inclined free surface during vertical shaking. θ is the dynamic angle of the inclined free surface which is measured during vibration. Figure 3-29 presents the progressive destruction of θ as a function of the acceleration amplitude.

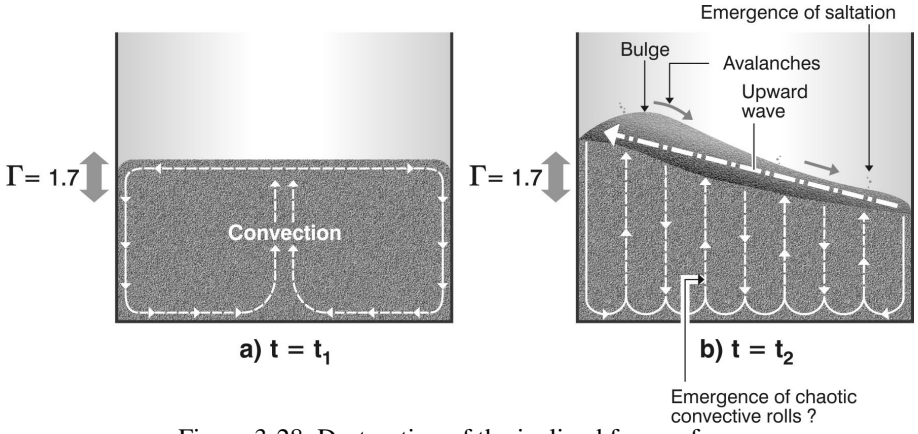

Figure 3-28: Destruction of the inclined free surface.

A (mm)	fr (Hz)	Γ (-)	θ (°)
0.8	18	1.04	32.00
0.8	19	1.16	27.6
0.8	20	1.29	26.6
0.8	21	1.42	23.00
0.8	22	1.56	4.6
0.8	23	1.70	3.9
0.8	24	1.85	0
1.5	13	1.02	35
1.5	14	1.18	31.7
1.5	15	1.36	26.1
1.5	16	1.55	20.5
1.5	17	1.74	9.4
1.5	18	1.96	6.5
1.5	20	2.41	0
3	10	1.21	29.7
3	11	1.46	24.7
3	12	1.74	16.3
3	13	2.04	9.8

Table 3-4: Summary of the experiments characterizing the destruction of the inclined free surface during vertical shaking in the range $1 < \Gamma < 2.5$.

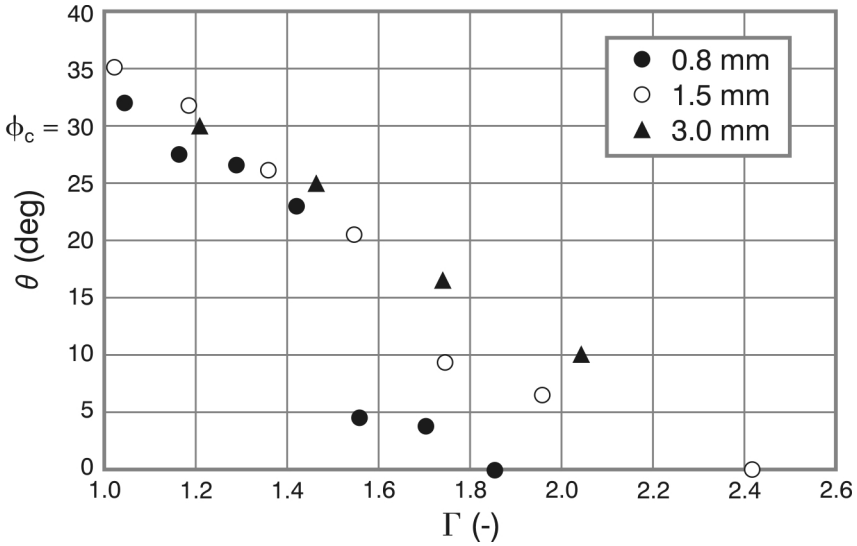

Figure 3-29: Relationship between the dynamic angle of the inclined free surface, θ, and the acceleration amplitude, Γ.

c. Vibro-fluid behavior

At $\Gamma \approx 2.4$, the development of an impressive bulge is observed in the center of the container. It tends to expand the whole sample. The sand becomes fully vibro-fluidized. The convection still remains but it presents a more chaotic character. Additionally, a new state of the horizontal free surface can develop with the emergence of particular geometrical shapes intermittently accompanied by chaotic grain saltation, as illustrated in Fig. 3-30.

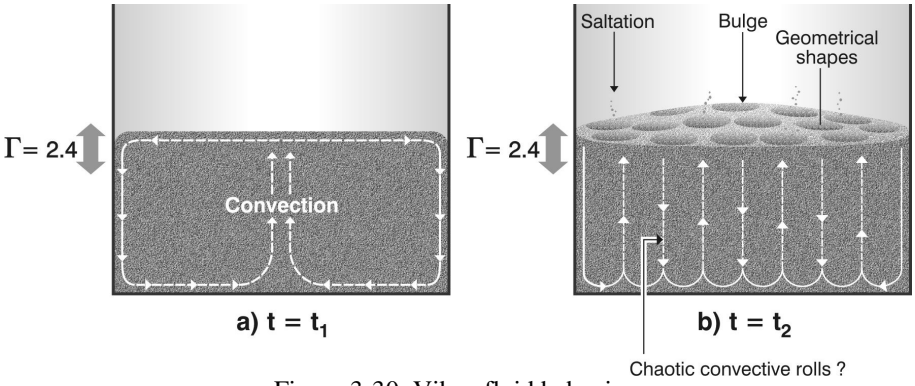

Figure 3-30: Vibro-fluid behavior.

The dynamic density of the sand during vibration probably goes out the range of accessible void ratio characterized by $e_{max} = 0.88$. The dilatation of the sand is such that the granular material actually behaves like a complex fluid. This behavior seems to correspond to the "vibro-fluidization" phenomenon, described in Section 2.4.2c. The grains recirculate in the container under the effects of short life-time contacts leading to a particular state presenting no more shear strength. It is

possible to push one's hand into the vibro-fluid material without encountering any penetration resistance.

The boundary between vibro-fluid and instability surface behaviors is not obviously defined. The performance of sphere penetration experiments (SPE's) will characterize this boundary in terms of penetration logs. Vibro-fluidization seems to occur at the free surface of the sample and propagate inside the granular material when the acceleration is increased.

Melo et al. (1995) conducted experiments on vertically oscillated granular layers. They report the shaping of spatial patterns, at the free surface of the sample, composed of standing waves that oscillate at either one-half or one-quarter of the drive frequency, fr. According to the authors, the stability region for each pattern is a function of the frequency and the acceleration amplitude, Γ.

3.4.5 Dry density after vibrations

Figure 3-31 illustrates the relationship between relative density of dry sand after vibrations and vertical acceleration for the UCL experiments. The displacement amplitude is set to 1.5mm for all experiments.

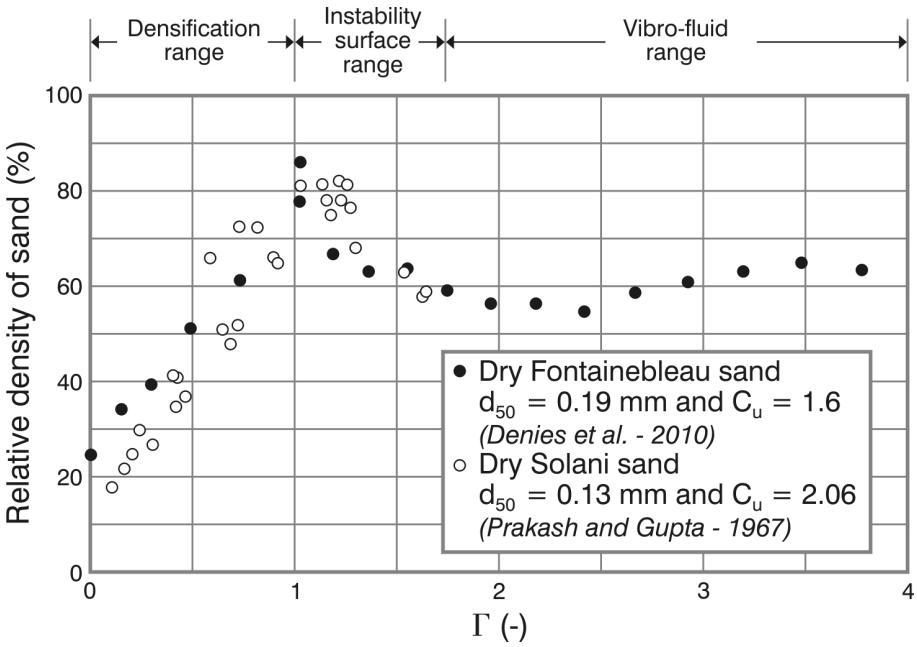

Figure 3-31: Relative density of dry sand after vibration vs. acceleration amplitude, Γ. In Denies et al. (2010), the displacement amplitude of vibration is set to 1.5 mm for all experiments.

In the densification range, a progressive increase in the final density is observed until the acceleration amplitude reaches 1g. Beyond this value, the convective process accompanied by the inclined free surface tends to dilate the vibrated granular matter and the dry density after vibrations decreases progressively to reach a value oscillating around $D_{r,\Gamma} = 60\%$ when the sand is vibrated in the vibrofluid range.

The triaxial compression tests, presented in Section 3.3.1, are conducted on Fontainebleau sand at a relative density close to $D_r = 60\%$. Hence, it becomes possible to define a frictional angle corresponding to that relative density. As illustrated in Fig. 3-12, the ratio q/p' tends to 1.66 at failure. Considering the following relationship valid for a cohesionless soil at failure (Atkinson and Bransby, 1978):

$$\frac{q}{p'} = \frac{6\sin\phi}{3-\sin\phi} \qquad \text{(Eq. 3-4)}$$

The ratio q/p' is equivalent to a frictional angle, ϕ, equal to 40.5°.

In Fig. 3-31, relative densities measured with the UCL-SPE apparatus are compared with the Prakash and Gupta observations (1967). They studied the variation of relative density of vertically vibrated dry Solani river sand following a procedure described in Section 2.4.2a. Our experimental observations corroborate their results. For vertical vibrations, there is an optimum acceleration amplitude, close to 1g, allowing the minimum void ratio. Once the acceleration reaches this threshold value, an increase in acceleration can cause a decrease in compacted density. Therefore, vertical accelerations, in excess of 1g, are counter-productive to the effective dynamic compaction of sand.

In the range beyond 1g, the dry density after vibration could be related to the way the vibration is stopped. Each experimental setup presents its own characteristics of control. In the present research, the servomechanism device actuates the motion of the hydraulic jack. The shutdown of the vibration varies in function of the frequency imposed to the system, as illustrated in Fig. 3-32 where the acceleration measured on the container is taken into account. When the frequency is increased, a delay is necessary to reach the full stop of the motion. The time needed to stop the jack is larger than the period of the imposed oscillation. That could lead to the dedensification of the sample by the application of an additional transient phase of vibration.

3.5 Sphere penetration experiments (SPE's)

The performance of sphere penetration experiments (SPE's) should allow us to characterize the influence of vibrations on the sinking logs of a sphere in the different regimes (the densification range, the instability surface range, and the vibro-fluid range) and to investigate the loss of shear strength when "vibro-fluidization" is observed in the container.

3.5.1 Field of application and procedure of the SPE's

Figure 3-14 outlines the domain of the vibrations imposed to the container in a bi-logarithmic diagram. The black points represent the different sphere penetration experiments (SPE's) performed, in the three identified dynamic regimes, with respect to the following procedure.

In Barkan's experiments, the sand seemed to be prepared for all sphere penetration experiments following the same procedure. It was always vibrated at an acceleration level allowing minimum void ratio, $e_{min} = 0.5$ (-). The UCL procedure is different in that regard, depending on the vibration range.

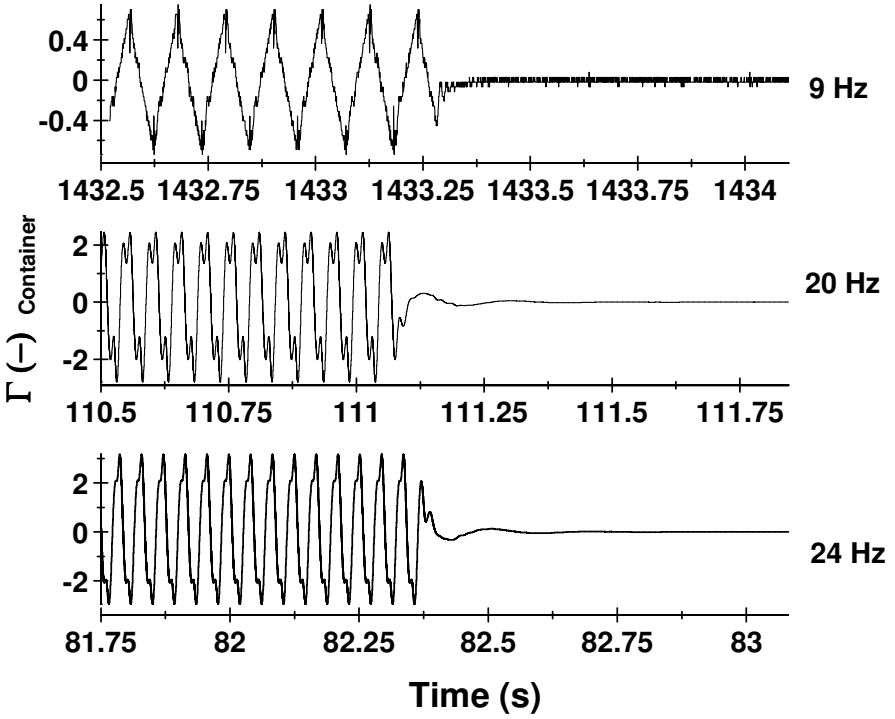

Figure 3-32: Shutdown of the vibration for A = 1.5 mm and fr = 9, 20 and 24 Hz respectively.

For the UCL-SPE's conducted within the densification range, the sand is initially vibrated until its equilibrium vibratory void ratio, e_Γ, corresponding to the chosen acceleration amplitude, Γ, is reached. Then, vibrations are stopped and the sphere is lowered onto the sample, in the center of the container, resulting in a quasi-static penetration. Once static equilibrium is reached, vibration of the container is resumed and sphere vibratory sinking is recorded.

For the UCL-SPE's conducted within the instability surface range, the sand is vibrated until the slope is formed in the container. Once dynamic angle becomes stationary, the sphere is lowered onto the inclined free surface of the sample, in the center of the container, and the sphere vibratory sinking is recorded.

For the UCL-SPE's performed within the vibro-fluid range, the sample is vibrated until the vibro-fluidization is complete. Then the sphere is lowered onto the vibrated surface of the sample, in the center of the container, and its vibratory sinking recorded.

Figure 3-33 illustrates the conventions related to the sphere penetration in the sand sample. In the present analysis, the quasi-static penetration of the sphere is defined as the vertical distance between the lower part of the sphere and the free surface of the sand sample, as illustrated in Fig. 3-33a. It displays negative values. Sphere vibratory sinking corresponds to the penetration of the sphere occuring during vibration. It also displays negative values. Finally, sphere position is defined as the vertical distance between the lower part of the sphere and the bottom of the container. It is characterized by positive values.

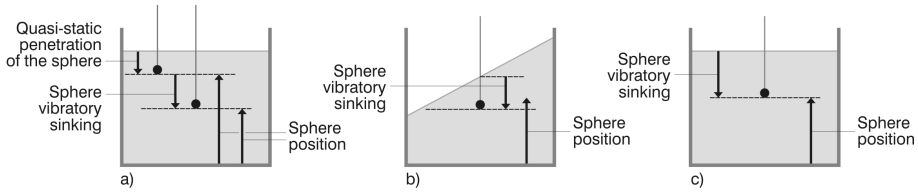

Figure 3-33: Conventions related to the penetration of the sphere in the sand sample.

3.5.2 Results of the UCL-SPE's and discussion of the results

a. SPE's in the densification range (Γ<1)

Following the previously described procedure, SPE's are performed within the densification regime, for $\Gamma < 1$. The sand is vibrated until its vibratory equilibrium void ratio, e_Γ, is reached, in such a way to avoid volume change during the dynamic penetration of the sphere. Then, vibrations are stopped and the sphere is lowered onto the sample.

Figure 3-34 presents the quasi-static sphere penetration as a function of the relative density, $D_{r,\Gamma}$, corresponding to the vibratory equilibrium void ratio, e_Γ. The quasi-static penetration is normalized with regards to the sphere diameter for the purpose of highlighting its relative penetration into the sample.

When $D_{r,\Gamma}$ increases, the quasi-static sphere penetration decreases. It emphasises the level of compaction at the surface of the sample resulting from vibration. The result strongly depends on the operator's care when laying down the sphere onto the sample.

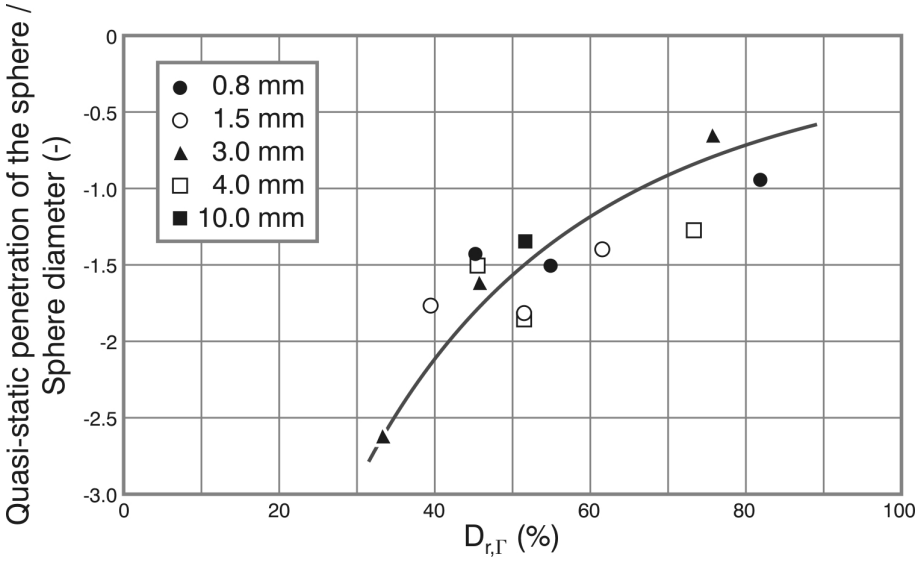

Figure 3-34: Dimensionless quasi-static penetration of the sphere as a function of the relative density, $D_{r,\Gamma}$.

Each deposit was therefore conducted by the same operator to increase the repeatability. Once static equilibrium is reached, vibration of the container is resumed and vibratory sinking is recorded.

Influence of the acceleration amplitude

Figure 3-35 presents sinking logs for several amplitudes of vibration. The displacement amplitude is 0.8 mm for the three curves shown while the frequency varies. The resulting acceleration amplitudes and the equilibrium void ratio (EVR or e_Γ) reached before quasi-static sinking are noted in Fig. 3-35.

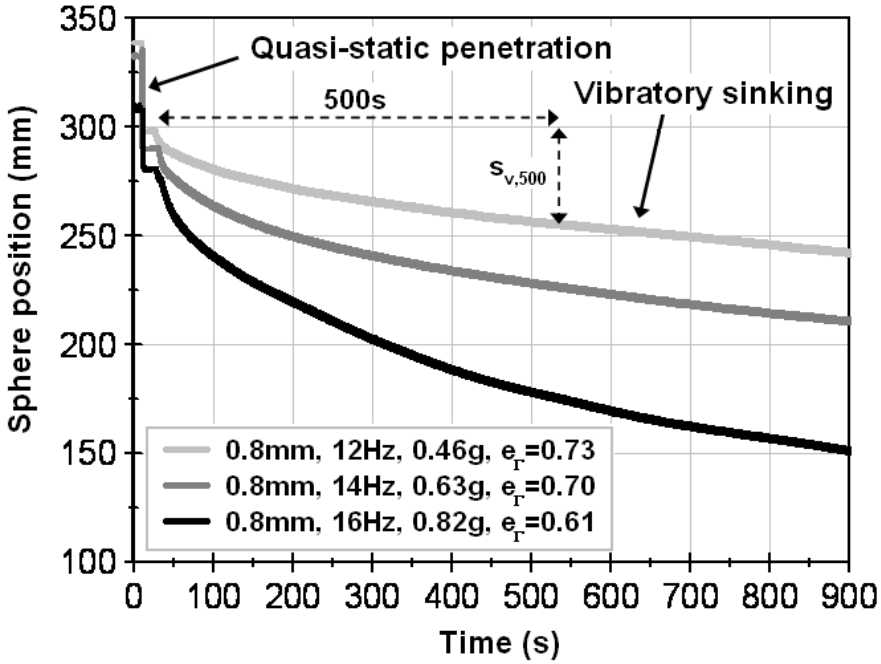

Figure 3-35: Sphere penetration logs for A = 0.8 mm and various frequencies in the densification range.

Similar sphere penetration curves are obtained for different displacement amplitudes in the densification range as illustrated in Fig. 7-25, 7-26, 7-27 and 7-28 in Appendix 7-3. Figure 3-36 summarizes the sphere penetration logs obtained in the densification range for different displacement amplitudes.

At low acceleration amplitude ($\Gamma < 1$), the sinking logs seem to follow an exponentially decreasing profile although no refusal depth was reached. No stabilization is assumed even if the duration of the vibrations is increased. The rate of penetration depends on the vibration parameters and on the initial void ratio of the sample. As illustrated in Fig. 3-37, the sphere motion is approximately sinusoidal. It still presents a triangle-shaped character due to the working of the MTS system. The frequency and the displacement amplitude of the sphere motion are close to the imposed motion of the container with a residual sinking component.

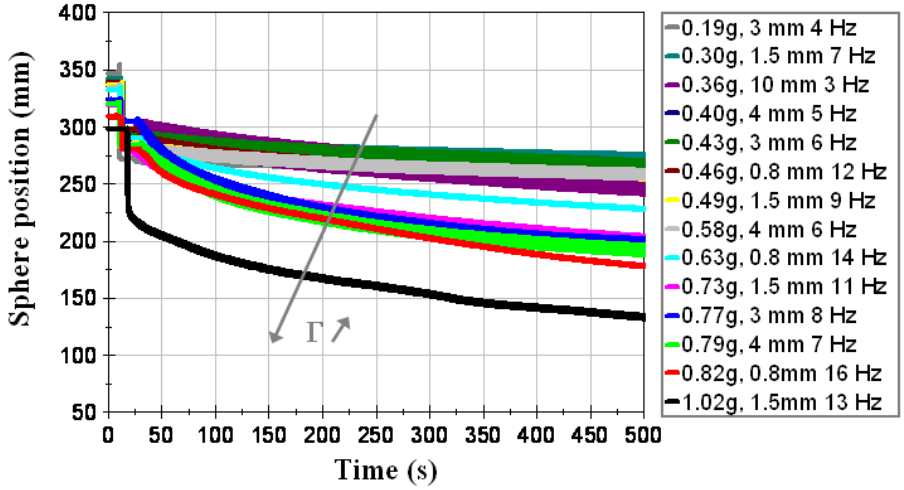

Figure 3-36: Sphere penetration logs in the densification range for different amplitudes of vibration.

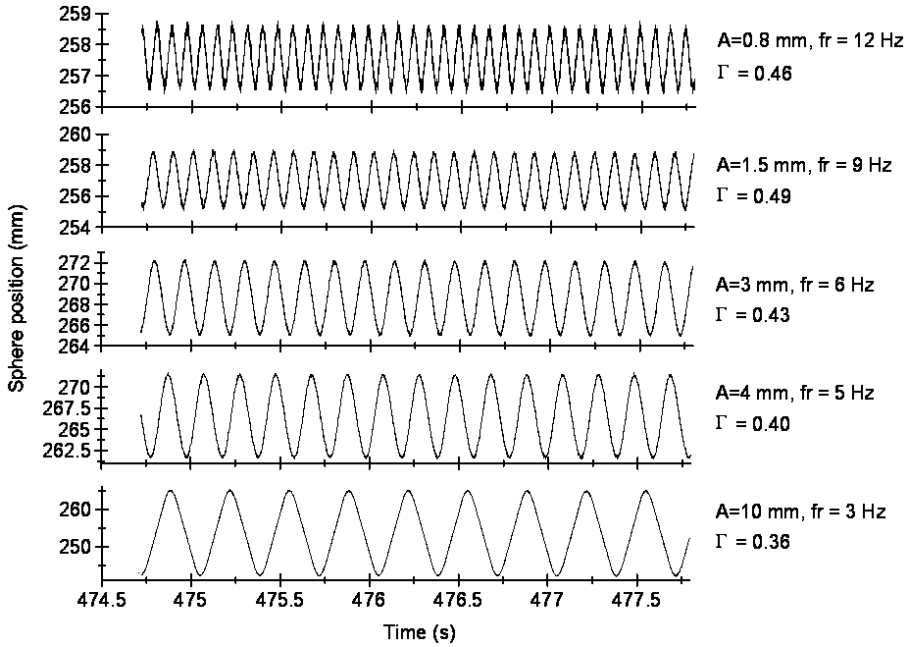

Figure 3-37: Sphere motion during vibratory sinking in the densification range, for several displacement amplitudes and various frequencies.

Sphere penetration logs are represented in Fig. 7-29 in Appendix 7-3 in terms of the number of cycles applied to the container. Figure 3-38 presents the value of the sphere vibratory sinking after 500s as a function of the acceleration of vibration for different displacement amplitudes. The sphere vibratory sinking, $s_{v,500}$, is computed as indicated in Fig. 3-35. The sphere sinking is considered relatively to the sphere diameter. Considering Fig. 3-36 and 3-38, the govering parameter of the

sphere penetration in the vibrated granular sample seems to be the acceleration amplitude of the vibration.

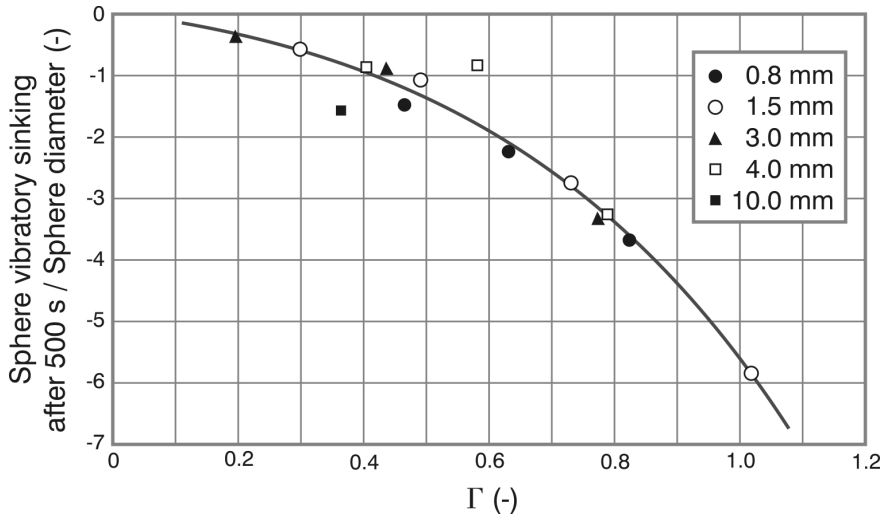

Figure 3-38: Normalized vibratory sphere sinking after 500s as a function of the acceleration for different displacement amplitudes.

Figure 3-39 presents the dimensionless sphere sinking after 2500 cycles of vibration as a function of the acceleration of vibration for different displacement amplitudes. The sphere sinking is considered with regards to the sphere diameter. Considering several results obtained with high displacement amplitudes (3, 4 and 10 mm), it seems that there is a coupled influence of the displacement amplitude and acceleration on the sphere penetration.

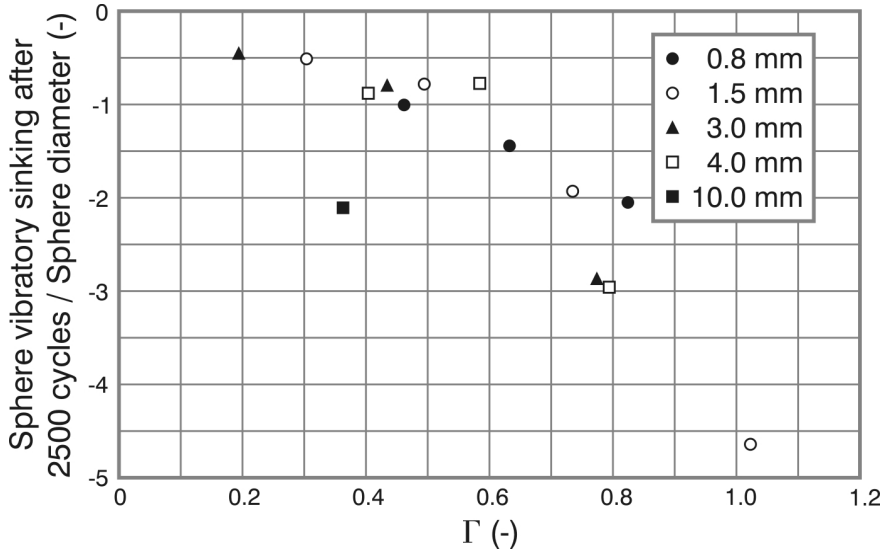

Figure 3-39: Normalized vibratory sphere sinking after 2500 cycles as a function of the acceleration for different displacement amplitudes.

Repeatability of the process

Figure 3-40 illustrates the good repeatability of the SPE results in the densification range.

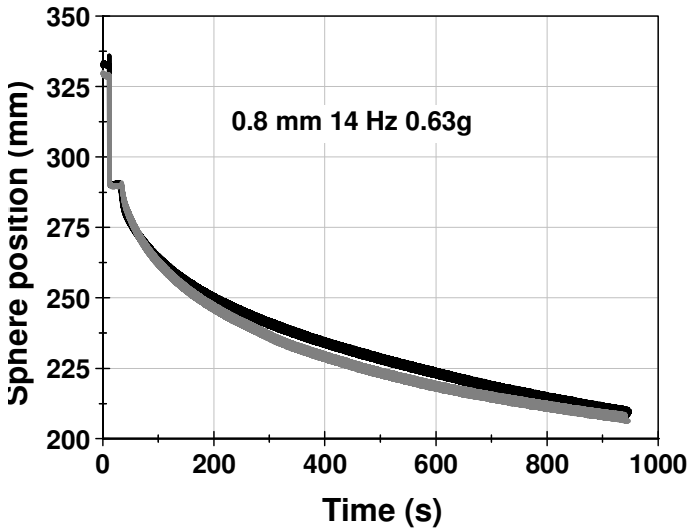

Figure 3-40: Repeatability of the SPE in the densification range.

Influence of the sand mass

Finally, the influence of the sand depth in the container is studied. Figure 3-41 presents the results of two sphere penetration experiments performed in samples of 65 and 32.5 kg. There is an influence of the sand mass on the penetration rate of the sphere in the specimen. Decreasing the thickness of the sand bed tends to increase the sphere sinking velocity.

b. SPE's in the instability surface range ($\Gamma \approx 1$)

For the UCL-SPE's conducted within the instability surface range, the sinking logs are strongly disrupted by the convective rolls present in this range, as illustrated in Fig. 3-42. The sinking logs present a transient character between the nature of the profiles developed in the densification and the vibro-fluid ranges. In Fig. 3-42, the elasto-plastic penetration is perturbed by the internal convective rolls which even cause the rising of the sphere at 16 Hz.

In the present research, sphere penetration experiments are mainly conducted in vibrated sand sample presenting a horizontal surface, hence, within the densification and vibro-fluid ranges wherein a good repeatability of the SPE's is observed.

c. SPE's in the vibro-fluid range ($\Gamma > 1$)

For the UCL-SPE's conducted within the vibro-fluid range, the sample is vibrated until the vibro-fluidization is complete. Then the sphere is lowered onto the vibrated surface of the sample and its dynamic penetration recorded.

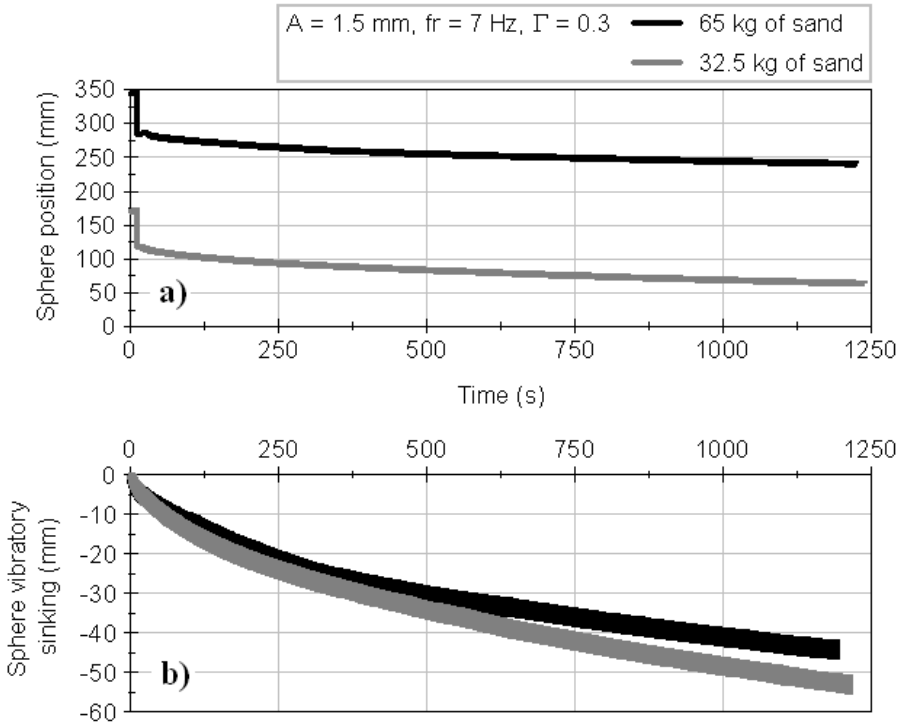

Figure 3-41: SPE's for specimens of various depth: a) Sphere position with time, b) Sphere sinking with time.

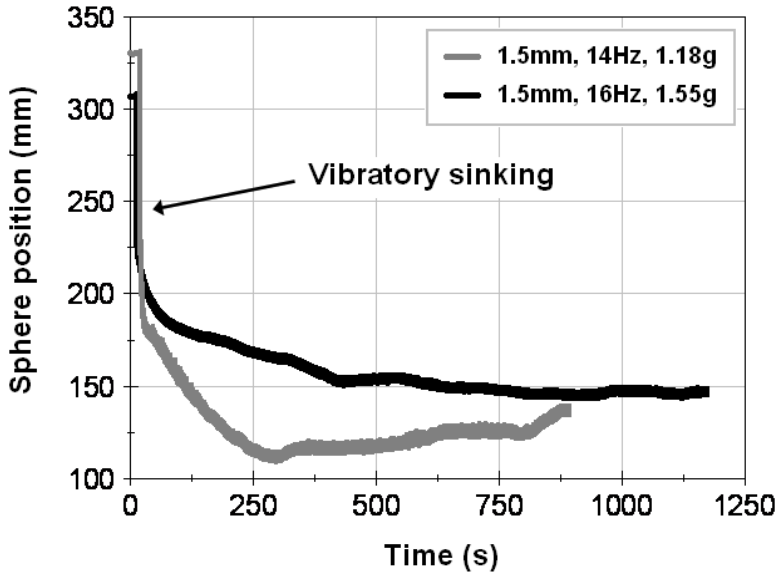

Figure 3-42: Sphere penetration logs for A = 1.5 mm at two frequencies within the instability surface range.

Influence of the acceleration amplitude

Figure 3-43 presents sinking logs for several amplitudes of vibration. The displacement amplitude is 1.5 mm for the SPE's shown while the frequency varies. The resulting acceleration amplitudes are noted in Fig. 3-43.

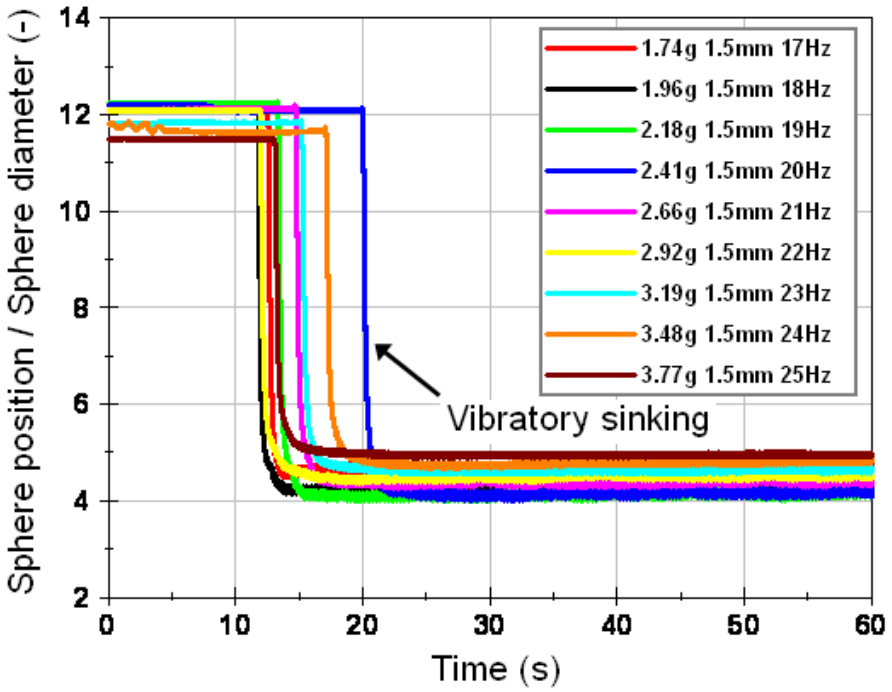

Figure 3-43: Sphere penetration logs for A = 1.5 mm and various frequencies in the vibro-fluid range.

At high acceleration amplitude, after a short transient sinking phase resulting from its initial position (lowered onto the highly tumultuous horizontal free surface), the sphere reaches an equilibrium penetration. The fluctuations, around this equilibrium position, are due to the variation of the collisions and dry frictions with the upward convective flow of surrounding particles. Hence, at the equilibrium height, the sphere penetrometer weight seems to be balanced by a "buoyant" force augmented by the flow of surrounding sand grains. The sand behaves like a complex fluid actuated by the convection. It is to note that the penetration equilibrium does not depend on the vibratory equilibrium void ratio, e_Γ.

Repeatability of the process

Figure 3-44 illustrates the good repeatability of the SPE results in the vibro-fluid range.

Influence of the displacement amplitude

Figure 3-45 presents sinking logs for several amplitudes of vibration. The displacement amplitudes are 0.8, 1.5 and 3 mm while the frequency varies. The resulting acceleration amplitudes are noted in Fig. 3-45.

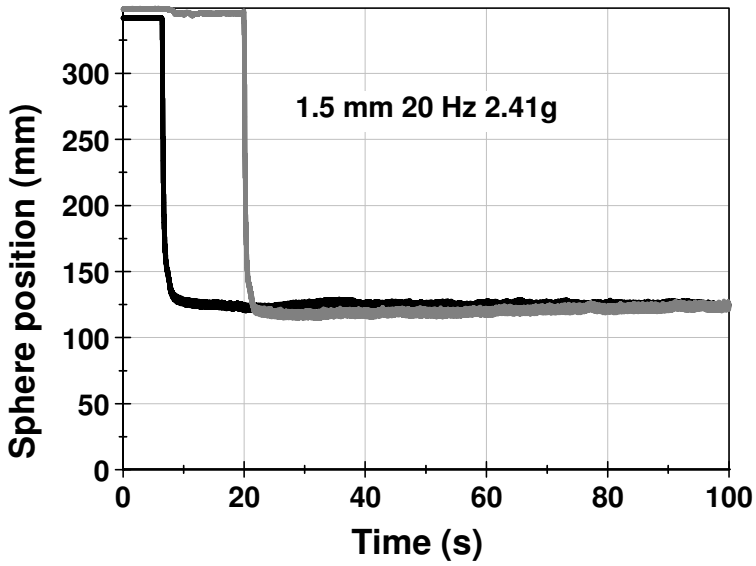

Figure 3-44: Repeatability of the SPE in the vibro-fluid range.

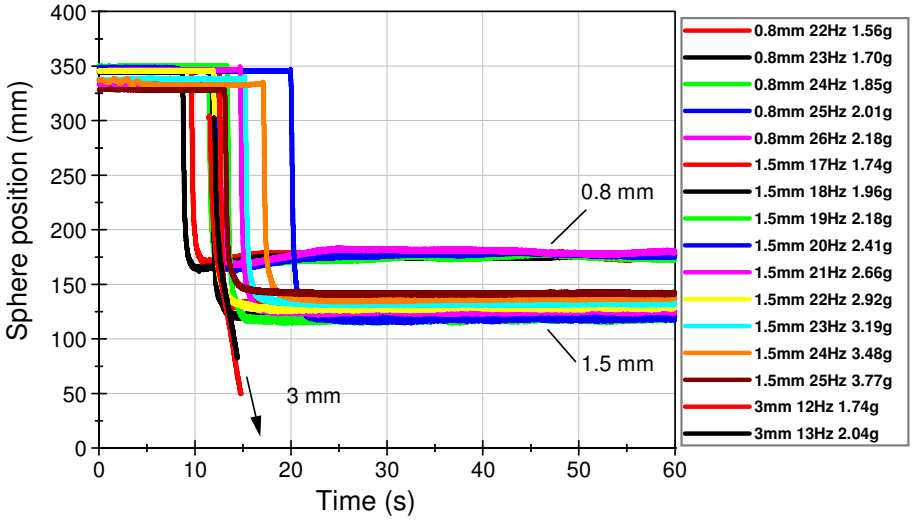

Figure 3-45: Sphere penetration logs for A = 0.8, 1.5 and 3 mm for various frequencies in the vibro-fluid range.

It is to note that the sinking profiles for A = 3 mm do not reach an equilibrium height and collide with the bottom of the container. The sinking logs are similar to the previously described curves of Fig. 3-43 but highlight the role of the displacement amplitude in the determination of the equilibrium height in the vibrated granular medium. That can be explained by the influence of the displacement amplitude on the way the convective flow of particles recircultates in the container. It will be discussed in Section 3.6.1b.

Transient sinking phases

Figure 3-46 illustrates the transient sinking phase of the SPE's performed with A = 0.8 mm. The sinking logs do not follow Stokes law, they are very similar and the equilibrium position seems to become independent of the acceleration amplitude in contradiction with the early results of Barkan (1962).

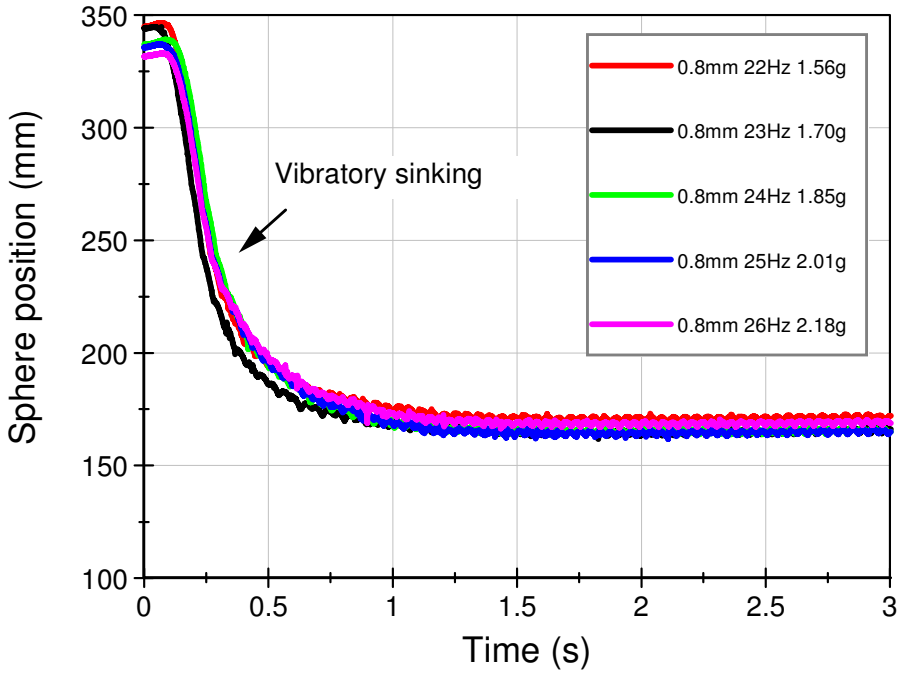

Figure 3-46: Transient sinking phase of the sphere penetrometer in the vibro-fluid range.

Vibratory sinking velocities

Figure 3-47 presents the sphere sinking velocities corresponding to curves of Fig. 3-46. No curves show penetration phase wherein the sinking velocity is constant. The Stokes method may not be used to determine any coefficient of vibro-viscosity. The concept of the vibro-viscosity coefficient of vibrated granular soil, proposed by Barkan (1962), needs to be reappraised.

Influence of the geometrical and inertial properties

In the vibro-fluid range, the governing parameters of the sphere equilibrium height become its apparent mass and its diameter, as illustated in Fig. 3-48. Each point represents the equilibrium height reached by the sphere for different sphere penetrometer masses and two sphere diameters. Linear influence of the sphere penetrometer mass is observed on the equilibrium height.

Nevertheless, the sphere penetrometer cannot be considered to play the role of a densimeter because of the presence of the upward convective flux inside the granular material increasing the sphere penetration resistance. Similar linear mass

dependance was observed for SPE's performed in air flow-fluidized sand deposit by Lohse et al. (2004).

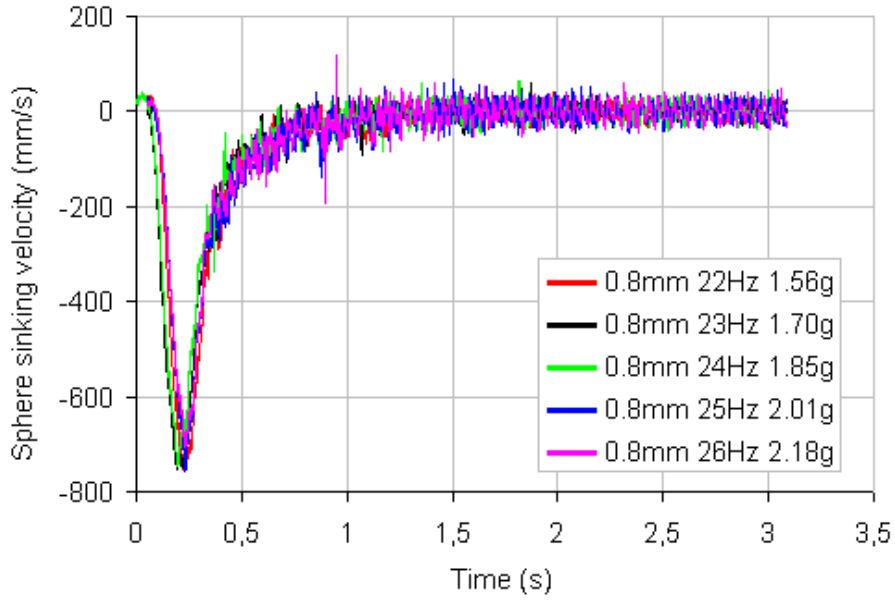

Figure 3-47: Sphere sinking velocities in the vibro-fluid range.

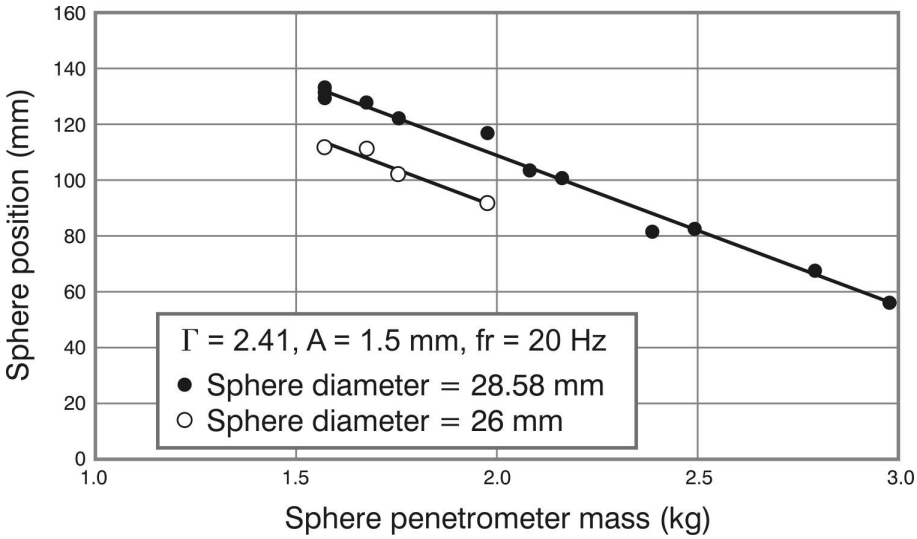

Figure 3-48: Influence of the sphere mass and diameter on its equilibrium height in the vibro-fluid regime.

Figure 3-49 concentrates on the influence of the apparent sphere density on the equilibrium height. Considering this point of view, it seems that all the points can be lined regardless of the sphere size. Other experiments were conducted in the vibro-fluid range with sphere diameters 20 and 12.7 mm respectively. They resulted

in sinking to the bottom of the tank. In Fig 3-50, maximum values of sphere sinking velocity are compared for different sphere diameters. Sphere size displays a linear influence.

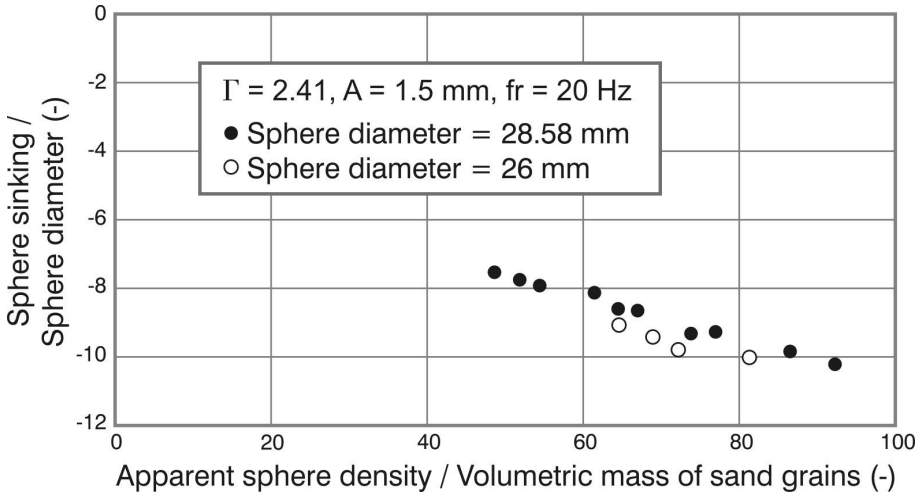

Figure 3-49: Influence of the apparent sphere density on its equilibrium height in the vibro-fluid regime.

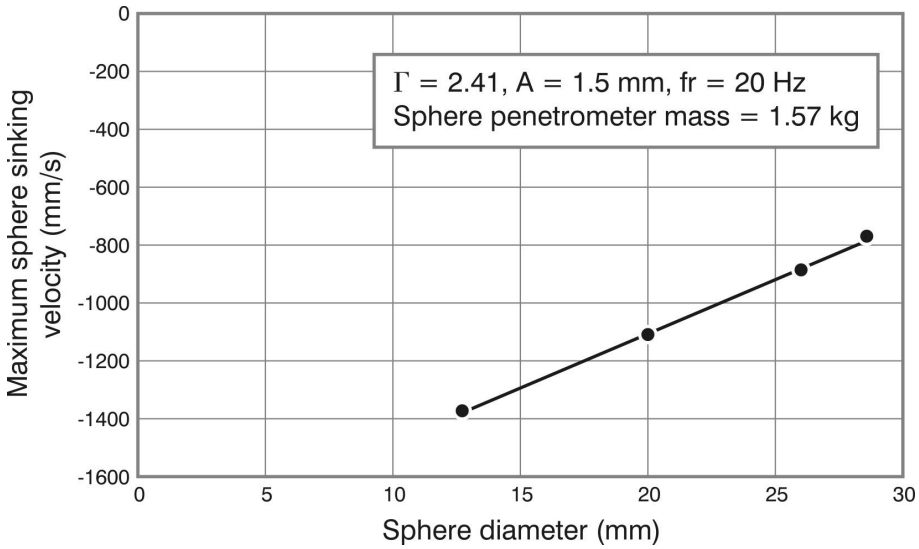

Figure 3-50: Influence of the sphere size on the maximum value of sphere sinking velocity in the vibro-fluid regime.

In Fig. 3-51, the influence of apparent sphere density on the maximum value of the sphere sinking velcocity is presented.

Influence of the sand mass

It is to note that additional experiments were performed in the vibro-fluid range to characterize the influence of the sand depth in the container. Sample of

32.5 kg of Fontainebleau sand was used but regardless of the sphere diameter (28.58, 26, 20 and 12.7 mm), sinking to the bottom of the container was always observed.

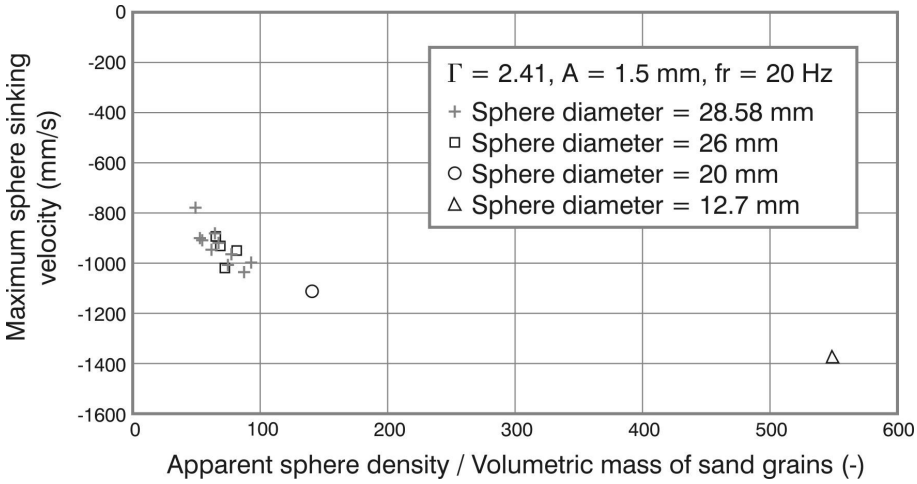

Figure 3-51: Influence of the the apparent sphere density on the maximum value of sphere sinking velocity in the vibro-fluid regime.

d. Synthesis of the SPE's

Figure 3-52 summarizes all the sphere penetration curves obtained in the three dynamics regimes. The sinking profiles present different characteristics and are developed on different time scales.

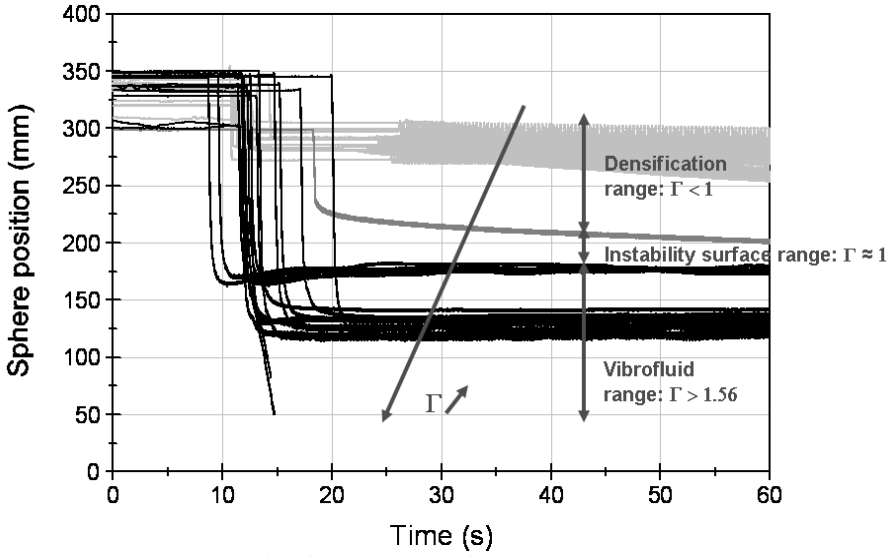

Figure 3-52: Synthesis of the SPE's performed in the three dynamic ranges.

In the densification regime ($\Gamma < 1$), the sinking logs seem to follow an exponentially decreasing profile although no refusal depth was reached after a long time of vibration.

In the instability surface range ($\Gamma \approx 1$), the sinking logs are perturbed by the internal convective rolls which result in long released times following by new sphere motion. Finally, SPE profiles, characterizing the shear strength degradation, were met at a threshold value, Γ_{VF}, around 1.55. A rapid sinking of the sphere is observed until an equilibrium height was reached.

Figure 3-53 zooms in the displacement curves followed by the sphere once the sand was subjected to different amplitudes of vibration. The sphere displacement varies in function of the dynamic range of the experiment. In the densification regime, for low acceleration amplitude (fr = 9 Hz and $\Gamma = 0.49$), the sphere motion is sinusoidal and presents a frequency and a displacement amplitude close to the imposed motion of the container with a residual sinking component. In the vibro-fluid range, at high acceleration amplitude (fr = 20 or 24 Hz and $\Gamma = 2.41$ or 3.48), the sphere is subject to turbulent ascendant flux in the center of the container due to the granular convection. The motion is no more sinusoidal. The sphere seems to be periodically lifted up maybe when the granular flow momentally increases, and then it falls again and it is back to its equilibrium height. That observation highlights the fact that the upward convective flow is probably discontinuous or periodic.

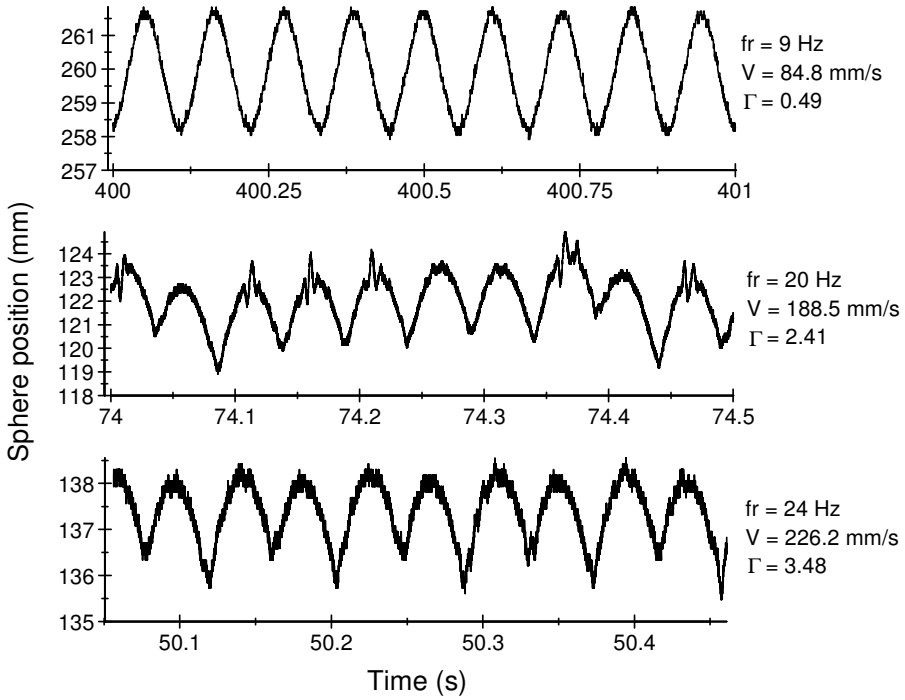

Figure 3-53: Sphere displacement during vibratory sinking for vibrations with A = 1.5 mm and various frequencies.

3.6 Discussion

3.6.1 Laboratory investigation of dynamic behavior of dry sand: Solid – fluid transition

a. Behavior classification according to the acceleration amplitude

When dry sand is vertically vibrated under gravitational field, the UCL experiments conducted on dry Fontainebleau sand distinguish three different sand dynamic behaviors depending on the acceleration amplitude: the densification behavior ($\Gamma < 1$), the instability surface behavior ($\Gamma \approx 1$), and the vibro-fluid behavior ($\Gamma > 1$).

If the acceleration of the vibration is less than 1g, there is a densification of the sample resulting in a global settlement of the sand particles in the sample. The volume change can be described by equations (2-15) and (2-16) or equations (3-1) to (3-3). The SPE's performed in this range highlight the "solid" character of the vibrated sand in the densification regime. The sinking logs correspond to an elasto-plastic penetration enforced by increasing acceleration amplitude of vibration. The sphere sinking is slow and no refusal depth was reached after 15 minutes of vibrating time, as illustrated in Fig. 3-35.

When the acceleration is increased beyond 1g, there is an instability in the sand mass which results in the emergence of an inclined free surface. If the acceleration amplitude is further increased, the free surface is progressively dislocated. A bulge develops and tends to expand the whole sample leading to the vibro-fluidization of the granular material.

Vibro-fluidization is related to the development of granular convection resulting from the particles-wall interactions.

b. Granular convection and vibro-fluid state of matter

Knight et al. (1996) experimentally studied granular convection in three-dimensional cyclinders using tracer particles technique and magnetic resonance imaging. They characterized the depth dependance of the vertical flow velocity as following:

$$v(z, r = 0) = \frac{\xi}{\tau} \exp(-\frac{z}{\xi}) \qquad \text{(Eq. 3-5)}$$

where v is the "average" particle velocity, in the sense that it describes the net motion of a particle resulting from one cycle of vibration. z is the depth and r is the radial distance with r = 0 along the cylinder axis. ξ and τ are a length and a time scale. Knight et al. (1996) showed that the parameter ξ depends on the displacement amplitude of the vibration. That could explain the influence of the displacement amplitude on the equilibrium height reached by the sphere penetrometer during SPE's conducted in vibro-fluid range, as illustrated in Fig. 3-45.

Hence, the upward flow velocity along the cylinder axis exponentially decays from the top free surface (z = 0) into the bulk of the material. This flow decreases and changes direction as the bottom of the container is approached, displaying a radial dependance closely approximated by either a hyperbolic cosine or a modified Bessel function of order zero:

$$v(r) = v_c + B\left[1 - \cosh\left(\frac{r}{r_c}\right)\right] \quad \text{(Eq. 3-6)}$$

and

$$v(r) = v_c + B\left[1 - I_0\left(\frac{r}{r_c}\right)\right] \quad \text{(Eq. 3-7)}$$

where v_c, B and r_c are adjustable parameters. I_0 is a modified Bessel function of order zero satisfying the following equation:

$$\frac{d^2 v(\rho)}{d\rho^2} + \frac{1}{\rho}\frac{dv(\rho)}{d\rho} + v(\rho) = 0 \quad \text{(Eq. 3-8)}$$

with $\rho = r/r_c$.

Knight et al. (1996) proposed a simple model of granular convection consistent with the previously described depth and radial dependances.

Concerning the depth dependance of the axial velocity, it is possible to build a simple model in which convective flow is dominated by scattering grains from the walls. Flow in the container depends on three components: an upward flux $j_u(z)$ in the central region (where the sphere penetrometer is plunged in the UCL-experiments), a downward flux $j_d(z)$ along the lateral walls, and an inward transverse flux $j_i(z)$ from the downward flow into the ascendant flow.

The transverse flow could arise from the spreading of the grains in the downward flow, by collisions with other particles or with the walls. The rate of change with depth of the downward flux is then proportional to the transverse flux:

$$\frac{dj_d(z)}{dz} \propto -j_i(z) \quad \text{(Eq. 3-9)}$$

The authors assumed that $j_i(z)$ can be directly proportional to the number of particles available to be scattered $j_i(z) = pj_d(z)$. Hence:

$$\frac{dj_d(z)}{dz} \propto -pj_d(z) \quad \text{(Eq. 3-10)}$$

where p is the probability of inward scattering. The probability p could be depending on the wall roughness and could remain independent from the depth, z. Then,

$$j_u(z) \propto j_d(z) \propto \exp(-pz) \quad \text{(Eq. 3-11)}$$

The authors consider that both flux $j_d(z)$ and $j_u(z)$ are proportional because in steady state the total number of grains at any depth is conserved in the system. According to this assumption, the flux of particles is proportional to the velocity, equation (3-11) is equivalent to the empirical relationship (3-5), where the scattering probability can be identified with the inverse length scale: ξ^{-1}.

The authors confirmed the scattering of the grains from the downward flow into the upward flow by implanting dyed tracer particles, otherwise indistinguishable from those in the bulk, into the downward flow. They observed that, in the context of their model, introducing a linear depth dependance to the scattering propability p, $p = p_0 + \varepsilon z$, results in the type of deviation experimentally measured. It seems to be physically coherent, since near the bottom of the container,

the particles undergo very slow convection: the collective behavior of the grains can be imagined to be increasingly solidlike. That can explain why in the SPE's, conducted in vibro-fluid regime, the sphere penetrometer sinks into the "liquefied" bulk, before it slows down and it reaches an equilibrium penetration when the surrounding particles behave again like a solid, as illustrated in Fig. 3-43 and 3-47. Additionally, SPE's underline the periodic character of the convective flow considering the sphere motion, for $\Gamma = 2.41$ and 3.48 (see Fig. 3-53).

Considering the expression of the radial dependance of the flow velocity, the modified Bessel function which solves equation (3-8) is particularly interesting. The two first terms of equation (3-8) describe the viscous drag on a Newtonian fluid moving through a pipe (the radial components of the Laplacian of $v(\rho)$). The urge to build an analogy with the work of Barkan (1962), which determined the soil vibro-viscosity coefficient, is high but the final term in equation (3-8) does not arise from simple fluid mechanics. It could be an effective pressure term proportional to $v(r)$ or one of its derivatives in z, as proposed by Knight et al. (1996). Moreover, the sinking logs of the UCL-SPE's do not follow Stokes law. Therefore, it becomes difficult to estimate a vibro-viscosity coefficient in such a view to characterize the vibrated granular soil. It seems that vibro-fluid behavior of vibrated dry sand may not be assimilated to a simple fluid viscous model as proposed by Barkan (1962). Nevertheless, granular convection results in a particular state of granular matter which can exhibit some characteristics of a Newtonian fluid: the vibro-fluid state which is characterized by a phase transition. There is a change in the structure of the granular material: the transformation from a solid material into a complex fluid identified by an abrupt change in properties (volume change and shear strength degradation in the UCL-experiments). The vibro-fluid state must be regarded conserving its solid and complex fluid characteristics underscoring its dual nature.

The passage throughout these different states of granular matter have also an influence on the final density state observed after the cessation of the vibration (see Fig. 3-31). Indeed, the optimum acceleration amplitude, close to 1g, corresponds to the end of the densification regime wherein the sand again behaves like a solid.

c. Instability surface behavior

Active and passive phases

The instability surface behavior can be understood as a stage of the transition from the solid state to the complex fluid state. de Gennes (as reported in Evesque and Rajchenbach, 1989) proposed a theoretical approach to this instability based on successive passive and active phases.

In the passive regime, the container is raised up and the grains are compacted under the effect of an increased apparent weight. No intergranular rearrangement can arise. The granular assemblage is considered in a solid state.

In the active regime, the container goes down with an imposed acceleration, $\Gamma \geq 1$. Sand grains are freer to move. The granular medium becomes momentally fluidized.

The instability surface behavior is then characterized by a succession of active and passive phases. The active phases allow relative interparticles motion and slope formation due to the convection and the assemblage asymmetry while the passive phases limit the angle of the inclined free surface. According to de Gennes, during the passive regime, the granular material behaves like a solid. Hence, the

slope cannot pass the maximum value for the angle of repose of the sand heap at equilibrium. The excess of sand grains which has been raised up on bumps during the active phase flows in avalanches downward during the passive phase.

Influence of the nature of the granular material

The granulometry, the grain shape and the surface roughness of the grain have an influence on the way the instability surface develops. To illustrate this topic, Evesque and Rajchenbach (1989) conducted experiments on glass spheres of different diameters (0.2, 0.4, 1 and 2 mm) and observed that instability surface transition appears in all experiments except for the 2 mm diameter. According to the authors, it would be related to the existence of arch effects which could inhibit internal convective rolls.

d. Micromechanical analysis of granular convection and vibro-fluidization

Intergranular friction

Clément et al. (1992) have studied the mechanical conditions leading to the emergence of the instability surface behavior. They confirmed that spontaneous heaping and slope generation are due to granular convection. They were interested in the microscopic origin of the granular convection and identified the main actors of this phenomenon. They conducted experiments dealing with monodisperse assemblage of metallic beads under vertical vibrations.

According to the authors, the friction between the grains and the walls is the first cause of the convection, as confirmed by Grossman (1997). Nevertheless, it seems that this process requires high intergranular friction to allow the emergence of convective rolls. The microscopic parameter governing the granular convection is therefore the coefficient of intergranular friction.

Coefficient of restitution

Clément et al. (1992) highlighted the role of the restitution coefficient of particles in the emergence of vibro-fluidization. When the granular material is vibrated with an acceleration around 1g, convective rolls appear in response to the intergranular friction and relative friction with the walls of the container. At the same time, an other actor comes into the picture: the coefficient of restitution. Indeed, when particles collide, they dissipate a part of their kinetic energy under the effect of inelastic contact or impact conditions (Section 7.1.5). The restitution coefficient quantifies the kinetic energy restituted to the particle after impact. The authors observed that high restitution coefficients lead to the onset of the vibro-fluidization of the free surface. This latter would be the first victim of the vibro-fluidization because of the transmission mechanism of vibrating energy throughout the sample.

Actually, there is an energy transmission from the bottom to the surface of the sample when the restitution coefficient is close to 1 and an energy dissipation in the bulk of the granular assemblage for weaker restitution coefficients. If the amount of particles and the intergranular friction coefficient are high enough to dissipate the introduced energy, there is no vibro-fluidization of the free surface. Otherwise, the free surface cannot dissipate the excess of energy and becomes “vibro-fluidized”. That could explain why, in the instability surface range, the sphere penetrometer

initially sinks through the free surface without encountering any penetration resistance, as illustrated in Fig. 3-42.

Nevertheless, all conditions remaining unchanged, when the acceleration is further increased and reaches a threshold value, there is no more enough dissipations in the bulk and "vibro-fluidization" becomes inevitable.

In this way, the SPE's show that decreasing the sand mass in the container leads to the increase of the penetration rate – in the densification range (see Fig. 3-41) – and supports the vibro-fluidization at high acceleration amplitude ($\Gamma = 2.41$): sinking to the bottom of the container was observed when the sand height was decreased.

3.6.2 Comparison with reduced scale tests of vibratory driving

Reduced scale tests of vibrodriving process were reviewed in Holeyman (2000). Testing model profiles in soil tanks were initially attempted by Schmid and Hill (1966) and Bernhard (1968) continued by Rodger and Littlejohn (1980), Billet and Siffert (1985) and O'Neill et al (1990), and more rencently by Viking (1998). The tests were generally conducted using a lightweight vibrator acting on a heavily instrumented profile. The soil used was excusivelly sand (dry, moist, or saturated), placed at a controlled density, and in some cases, confined at a controlled radial stress.

a. Behavior classification according to the cyclic force amplitude

In the present work, the dynamic behavior of dry sand is classified according to the motion parameters imposed to the vibrated container but most authors establish their classification according to the cyclic force amplitude, F_{cyc}, applied to the profile during the vibrodriving process.

Recently, Le Thiet (2005) presented a physical model of vibrodriving process in the calibration chamber of the CERMES laboratory (Université Paris-Est). The aim of the research was to perform a parametric study highlighting the governing stakeholders of the vibrodriving process. Fontainebleau sand was lowered into the calibration chamber at a controlled relative density using pluviation process (Dupla and Canou, 2005) before applying a predetermined consolidation. The test procedure first consisted in the installation of the penetrometer in the reconsituted sample by jacking. Once the penetrometer reached 40 cm depth, the jacking was stopped and a static load F_0 was applied at the head of the penetrometer to take into account the action of a static bias load. A cyclic sinusoidal load, F_{cyc}, oscillating around F_0, was then applied to model the action of the cyclic force.

The influence of the cyclic force amplitude is illustrated in Fig. 3-54. where the sinking of the penetrometer was plotted as a function of the number of applied cycles. Two cyclic forces amplitudes were used: $F_{cyc} = 2.1$ kN and $F_{cyc} = 2.5$ kN. They correspond to distinct dynamic regimes. In the first one (for $F_{cyc} = 2.1$ kN), after an initial transient phase, a progressive penetration is observed. The author assumes that this kind of curve corresponds to the "elasto-plastic" behavior of the sand. The second regime (for $F_{cyc} = 2.5$ kN) is characterized by a sinking where no distinct phase can be noticed. The sinking velocity gradually decreases with the time but remains considerable at the end of the test. It is called the "vibratory" regime. Moreover, an other regime was explored by the Le Thiet experiments: the

"vibrodriving" regime wherein high penetration rate, close to real in situ data, was observed.

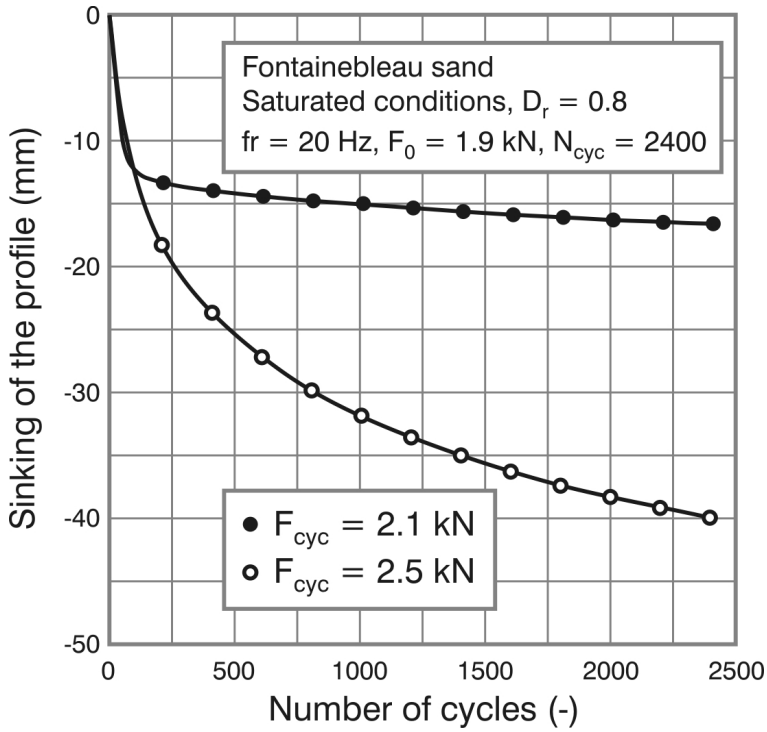

Figure 3-54: Elasto-plastic and vibratory sinking regimes, Le Thiet (2005).

b. Cyclic stability diagram

In the aim of defining some dimensional criteria for the design of cyclically loaded piles, Poulos (1988) has introduced a cyclic stability diagram, illustrated in Fig. 3-55, allowing the characterization of pile response when subjected to cyclic loads. It is defined for a number of applied cycles and consists in three distinct zones wherein the pile behavior differs : the stable zone (that could correspond to the elasto-plastic regime), the metastable zone (vibratory regime) and the instable zone (vibrodriving regime).

The experimental results of Le Thiet (2005) are represented in the (F_0/Q_c, F_{cyc}/Q_c) diagram where Q_c is the static load capacity. According to Le Thiet (2005), the limit of the vibrodriving regime is defined by the following expression:

$$\frac{F_0}{Q_c} + \frac{F_{cyc}}{Q_c} = 0.6 \qquad \text{(Eq. 3-12)}$$

No marked difference was observed between saturated and dry sand experiments. On the contrary the level of consolidation was shown to have a considerable influence on the penetration rate. All parameters remaining unchanged, the sinking velocity increases with decreasing the consolidation stress.

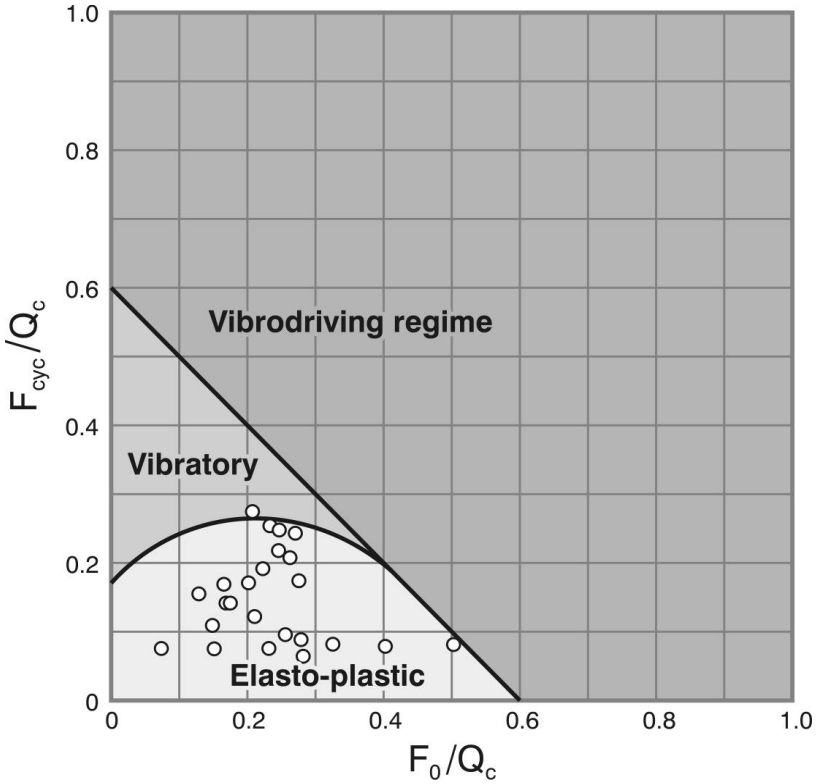

Figure 3-55: Cyclic stability diagram for Le Thiet experiments (2005).

c. Connection between acceleration and cyclic force classifications

The influence of the frequency was studied during the experimental research of Le Thiet et al. (2006). It seems that the frequency plays a similar role to the cyclic force amplitude. Le Thiet et al. (2006) proposed to explain this result considering that, in the "elasto-plastic" regime (for low frequency or low cyclic force amplitude), the sinking is controlled by the elasto-plastic properties of the sand whereas in the "vibratory" regime (for high frequency or high cyclic force amplitude), the penetration is dominated by the vibratory motion parameters, which lead to the decreasing of the skin friction and result in the sinking of the penetrometer by means of local "vibro-fluidization" (and not liquefaction) of the granular material.

d. Influence of the boundaries of the reduced scale models

As underlined by Holeyman (2002), although reduced scale models are of use, they suffer from improper boundary conditions (at the tank limits). Indeed, the introduction of the vibrated profile into the tank results in the emergence of waves propagation throughout the sample. The presence of the boundaries significantly prevent the vibration energy from propagating away from its source. In reduced scale tests, the scientists focus on the full-characterization of the vibro-penetration of the profile into the sample but the reflection of waves from boundaries modifies the soil behavior in the tank and can lead to distort the measurements related to the

penetration. In our experiments, this matter is circled using the boundaries to introduce the energy into the sample. The vibrated dry sand behavior directly results from the vibration of the container. The sphere penetrometer sinking is then a direct consequence of the boundary action; vibro-fluidization being actually the result of granular convection.

3.6.3 Analogy with vibrodriving experiments in sand

Considering the vibro-extracting experiments performed by Preobrajenskaïa, figure 2-6 demonstrates that increasing the acceleration of a sheet-pile allows a reduction of its effective lateral friction resistance. Beyond an acceleration threshold value, the lateral frictional resistance reaches an asymptotic value. That observation is interpreted in this way: once the sand has reached its vibro-fluid limit, there is finally no more influence of the acceleration amplitude on the profile sinking velocity and on the shear strength reduction of the material, as respectively observed in the SPE's (see Fig. 3-47) and in the direct shear tests (see Fig. 2-31). An asymptotic value is finally reached corresponding to the complex fluid state of the granular material. When the granular soil around the pile is vibro-fluidized, the penetration velocity is controlled by the geometrical and inertial properties of the vibrated pile, as observed in the SPE's performed in the vibro-fluid range, for different sphere diameters and various apparent densities (see Fig. 3-50 and 3-51).

4 Discrete Element Modeling of vibrated dry sand

4.1 Introduction of the DEM simulations

In the experiments of this study, the vibro-fluidization is caused by the frictional interactions between the walls and the grains. In the numerical simulations, vibro-fluidization will be regarded considering only the interactions between the grains in order to track down the fundamental origin of the phenomenon and to verify its occurence in absence of granular convection.

The computational approach has to concentrate on the evolution of the internal state of the granular structure during the application of the vibrations. Measurements of porosity, contact density and contact orientation should be conducted and the presence of passive grains taken into account. The problem has to be considered at the grain scale (called “microscopic” - scale). The influence of the acceleration amplitude on the assemblage behavior and on the stress field has to be analyzed.

It is therefore necessary to determine a numerical method with respect to this outline. This latter has to be able to simulate a dynamic problem, where sand grain assemblage is subjected to vibrations, neglecting the wall-effects of the sample and offering the possibility to take a look inside the material.

The following paragraph is interested in the general issue of granular matter in several engineering domains and on the way to model it.

4.1.1 Granular matter

Granular matter is an aggregate of a large number of discrete solid particles. It exists in numerous industrial fields such as fine chemicals, pharmacology, powders, composite materials, polymers, food and agriculture, and so on. They take place in several storage, flow or transport processes.

Granular matter also concerns the natural environment dealing notably with sand behavior in soil mechanics. The behavior of the granular material depends, a. o., on the relative density of the particle arrangement and on the way the grains are in contact with each other.

There are several physical mechanisms in granular medium difficult to understand using continuum mechanics such as segregation, granular convection, heaping, arching effect, dilatancy and vibro-fluidization. For the purposes of investigating these questions, a discrete approach where each grain can be considered as an actor of the problem has to be envisaged. The macroscopic properties of an ensemble are then studied via the microscopic properties of all the particles.

4.1.2 Numerical modeling of granular matter

There is no fundamental theory describing the behavior of granular medium. In “diluted” system where the particles mainly interact in binary collisions, the kinetic theory for molecular gases (Jenkins and Savage, 1983; Haff, 1983 and Campbell, 1990) and the statistical Monte-Carlo (MC) approach (Binder and

Hermann, 2002) were adopted considering the inelasticity of the impacts. Application of these theoretical approaches to the analysis of granular assemblage is still questionable and they are not suitable for dense granular medium where the contacts between the particles endure.

With the simple Event-driven approach (ED), the calculation flow is determined by the treatment of several events. In the field of granular matter, the events are referred to collisions between the particles. These are often considered as inelastic spherical rigid bodies. After impact, the resultant velocity of the particle is calculated with the help of a restitution coefficient. Friction can be considered with the help of a friction coefficient. Nevertheless, in simple ED approach, the contact duration and the details of the interaction between particles are ignored. Instantaneous binary collisions are assumed. The ED approach is therefore valid in dilute granular systems where binary collisions dominate over multiparticle contacts. On the contrary, the Contact Dynamics (CD) method (Jean, 1999) is well adapted to the study of dense granular systems subjected to dynamic loading but it does not consider contact deformations. Contact dynamics deals with the motion of multibody assemblage subjected to unilateral contacts – without overlap of bodies – and friction.

In the 70's, Cundall, inspired by Molecular Dynamics (MD), developed the distinct element method more commonly called discrete element method or DEM (Cundall and Strack, 1979). In DEM, the trajectory of each particle is computed considering all the forces acting on it and integrating Newton's second law of motion (Newton, 1687) and kinematics equations to estimate the position and orientation of the particle.

Considering the bi-dimensional coordinate systems defined in Fig. 4-1, the translational equations of motion of particle [A] are given by:

$$m_{[A]}\ddot{u}_1 = \sum_{contacts} P.z_1 + Q.x_1 - D_z.z_1 - D_x.x_1 \qquad \text{(Eq. 4-1)}$$

in the horizontal direction, $\vec{1}$, and:

$$m_{[A]}\ddot{u}_2 = m_{[A]}g + \sum_{contacts} P.z_2 + Q.x_2 - D_z.z_2 - D_x.x_2 \qquad \text{(Eq. 4-2)}$$

in the vertical direction, $\vec{2}$. $m_{[A]}$ is the mass of particle [A], $\ddot{u}$ its acceleration and g the gravitational acceleration ($g = 9.81\ m/s^2$). The particle motion depends on the resultant contact normal and tangential forces, P and Q, arising during the contact, and on the gravitational acceleration acting upon it. D_z and D_x are the normal and tangential damping forces of contact.

The rotational motion equation of the particle [A] is given by:

$$M = \dot{H} \qquad \text{(Eq. 4-3)}$$

where M is the resultant moment acting on the particle and $\dot{H}$ is the angular momentum of the particle. If the local coordinate system referring to the particle is oriented in such a way that it lies along the principal axes of inertia of the particle, what is valid for all spherical particles, equation (4-3) can be expressed by Euler's equation of motion:

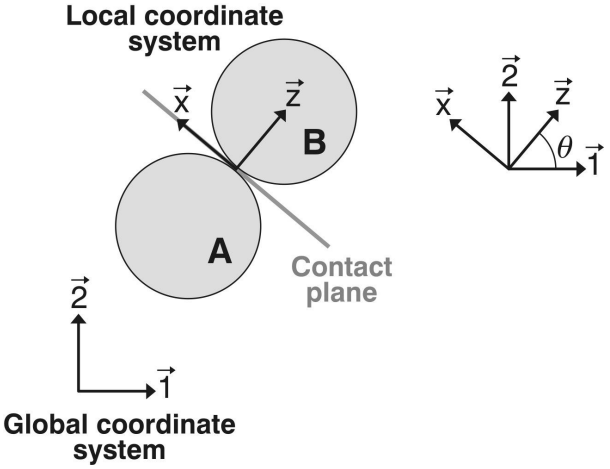

Figure 4-1: Global and local coordinate systems.

$$I_A \dot{\omega}_3 = \sum_{contacts} e_{3jk} \left(u_j^{[C]} - u_j^{[A]}\right)\left(P z_k + Q x_k - D_z z_k - D_x x_k\right) \quad \text{(Eq. 4-4)}$$

where I_A is the principal moment of inertia of particle [A], $\dot{\omega}_3$ the angular acceleration about the out-of-plane axis, e_{3jk}, the permutation symbol, $u_j^{[C]}$ the location of the contact point and $u_j^{[A]}$ the location of the center of particle [A]. It can be noted that $I = 2mR^2/5$ for sphere and $I = mR^2/2$ for two dimensional cylinders where R is the particle radius.

The force system may be in static equilibrium – there is no motion – otherwise it may cause the particles to flow. There is no hypothesis concerning the rheological behavior of the medium, only the nature of the contact is defined with the help of contact and damping laws. Contrarily to other methods, the details of the interaction between the bodies are developed.

The evolution of the granular assemblage as a function of the time can be computed integrating the motion (accelerations and velocities) and the contact laws in a centered finite difference scheme with a predetermined timestep. A basic assumption of the DEM is that the timestep, Δt, must be small enough so that, during only one timestep, a stress wave cannot travel from any particle further than its neighbors. $\Delta t < (m/k)^{-1/2}$ where m is the particle mass and k the contact stiffness (Itasca, 2004).

The DEM is sometimes considered as an Event-driven dynamic approach where the deformations, occuring during contact, are taken into account. In 1994, Luding et al. presented a series of simulations on systems of particles enclosed in two-dimensional boxes and subjected to vibrations. They compared the results of molecular dynamics (MD) and event-driven (ED) algorithms. In the diluted regime – called fluidized by the authors – the results of MD and ED simulations agree with each other. Luding et al. (1994) proposed to consider the ratio of the average time between collision events, t_{ev}, and the contact time, t_c, in such a way to validate this agreement. It is to note that $t_{ev}/t_c >> 1$, in the fluidized regime. In comparison, when the ratio t_{ev}/t_c was smaller than 1, the results of MD and ED simulations were shown to differ strongly. For $t_{ev}/t_c << 1$, the contact time becomes a major part of the simualtion time and the particles can interact with several others. The ED

simulations are still based on the assumption of binary collisions. A restitution coefficient describes energy dissipations but this latter is defined for two-particle collisions and not for enduring multiple contacts. When it is necessary to study the behavior of dense assembly, the use of DEM is therefore suitable.

Discrete element method allows to study more fundamentally diluted, loose or dense assemblies, subjected to shearing (Campbell, 2002 and GDRMiDi, 2004) or vibrations (Kudrolli, 2004).

In the present work, we will focus on circular particles to model sand grains although currently, the general discrete element method, in contrast to molecular dynamics can model deformable polygonal-shaped particles – originally Cundall (1971), Cundall (1988) and Hart et al. (1988) or recently, Jean (1999) with LMGC90, Komodromos and Williams (2004) with MIMES and Kozicki and Donzé (2008) with YADE –.

4.1.3 Discrete Element Method (DEM)

a. The PFC2D Particle-Flow model

The PFC2D Particle-Flow model is developed by the Itasca Consulting Group, Inc. It can be considered as a simplified implementation of the DEM because of the restriction to rigid circular particles (Itasca, 2004).

The particles are considered like distinct cylindrical rigid bodies that displace independently from one another and interact at contacts between particles or walls.

The particles are assumed rigid – there is no crushing or unrecoverable deformation – but the behavior of the interactions is described using a soft contact approach. There is a finite normal stiffness which is considered to characterize the interpenetration arising during the contact.

The details of the contact are supported by the following assumptions. The contacts occur over a vanishingly small area – i.e., at a point – . The soft-contact approach induces the presence of an overlap between particles. The particles overlap one another at contact points and the magnitude is function of the contact force via a force-displacement relationship. Overlaps are small in comparison with the particle sizes. Friction and energy dissipation at the contact are also considered. It should be noted that grains and walls interact with one another considering the forces that arise during contacts.

Figure 4-2 describes the caclulation cycle in the PFC2D model. At the beginning of the timestep, the contact list is updated considering the position of the particles and the walls. Force-displacement law is applied to each contact with respect to the contact law and relative motion between particles to deduce new contact forces. Then, equations of motion are computed, considering the force and the moment on each body resulting from the contact between the particles. The velocity and the position of each body are updated. This timestepping algorithm often leads to a significant calculation time.

b. Contact laws

If motion laws are well-established, interactions or collisions between the grains require a rigorous investigation. Indeed, in granular materials, thermal and electrostatic energies are often negligible as compared to gravitational energy. Thus,

forces acting on the particles are mainly gravitation and contact forces due to collisions.

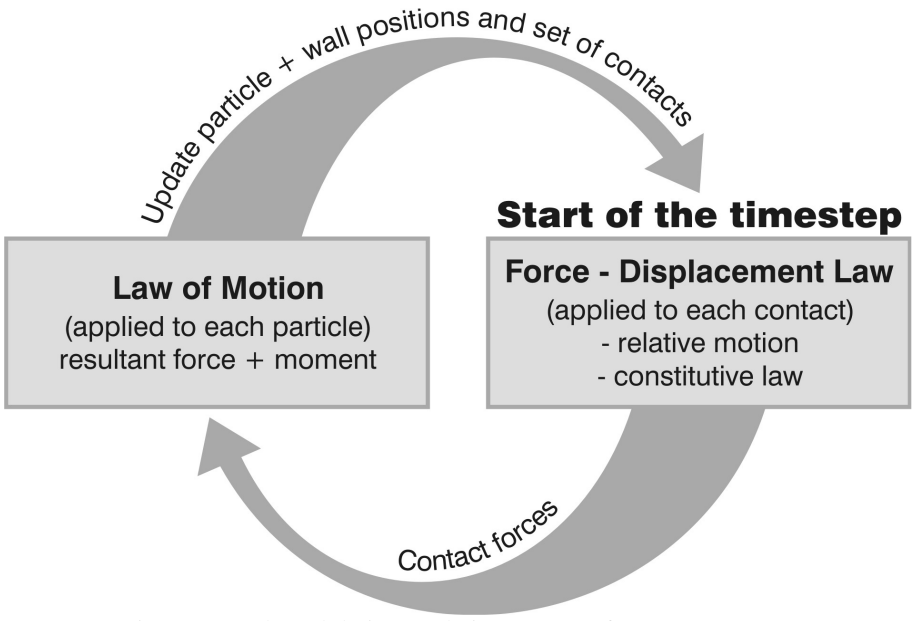

Figure 4-2: The calulation cycle in PFC2D, after Itasca (2004).

In Appendix 7.1, the details of contact mechanics between spherical bodies are explained for the purposes of providing contact and damping laws to the discrete element modeling. The reader can refer to the synopsis in Section 7.1.8.

In the discrete element method, the nature of the contact can be modelled with the help of a simplified rheological model as illustrated in Fig. 4-3.

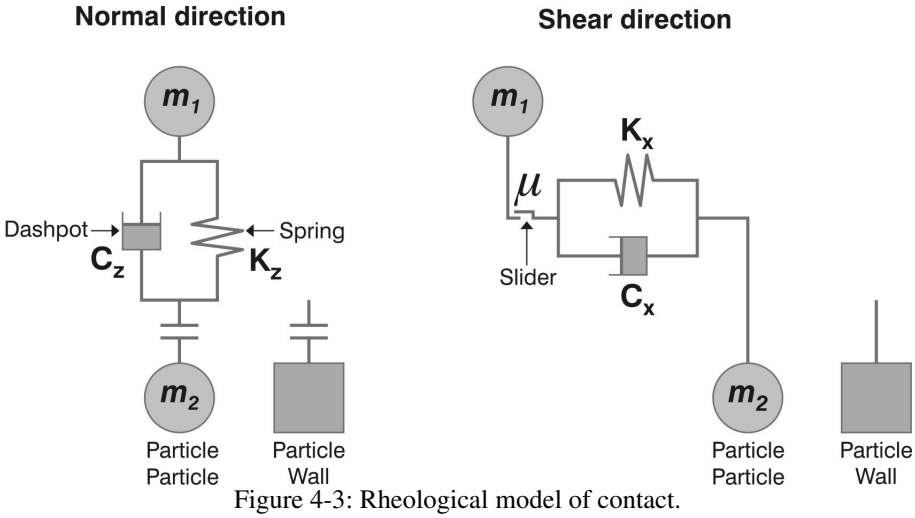

Figure 4-3: Rheological model of contact.

In the normal direction, the rheological model is composed of a spring coupled with a dashpot. The spring symbolises the normal stiffness of the contact during elastic normal contact or impact between the particles. The dashpot represents the normal damping characterizing the loss of energy during normal contact or impact.

The shear rheological model is similar to the normal model with an additional slider modeling the friction limit at the contact.

The contact force vector is the sum of the normal and tangential contact force components:

$$F_i = Pz_i + Qx_i \qquad \text{(Eq. 4-5)}$$

for the direction i, where i = ($\vec{1}$, $\vec{2}$).

The magnitude of normal contact force, P, is calculated by the force-displacement relationship:

$$P = K_z \delta_z \qquad \text{(Eq. 4-6)}$$

where K_z is the normal stiffness of the contact. It is a secant modulus which relates total normal displacement, δ_z, and normal force, P.

The shear contact force, Q, is computed in an incremental way, by the force-displacement relationship:

$$\Delta Q = -k_x \Delta \delta_x \qquad \text{(Eq. 4-7)}$$

where k_x is the tangential stiffness of the contact. It is a tangent modulus which relates the incremental tangential displacement, $\Delta\delta_x$, and the incremental tangential force, ΔQ.

When the contact is initialized, the total shear force Q is set to zero. Then, the increment of tangential displacement at the contact, $\Delta\delta_x$, is estimated considering the shear contact velocity:

$$\Delta \delta_x = V_x \Delta t \qquad \text{(Eq. 4-8)}$$

where Δt is the timestep and V_x is the tangential velocity at the contact.

When ΔQ is calculated, the new tangential force of contact, Q, is estimated summing the previous tangential force, at the start of the timestep, with the increment ΔQ:

$$Q = Q + \Delta Q \qquad \text{(Eq. 4-9)}$$

To model dry cohesionless sand, only repulsive normal forces are considered because non cohesive interactions are only treated. Hence, tensile forces cannot develop between particles.

The normal and tangential stiffnesses of the contact are estimated with the help of a simplified linear elastic contact model. This choice is justified in Appendix 7.4. K_z and k_x are computed assuming that the stiffnesses of the two contacting particles [A] and [B] acting in series:

$$K_z = \frac{k_z^{[A]} k_z^{[B]}}{k_z^{[A]} + k_z^{[B]}} \qquad \text{(Eq. 4-10)}$$

and

$$k_x = \frac{k_x^{[A]} k_x^{[B]}}{k_x^{[A]} + k_x^{[B]}} \qquad \text{(Eq. 4-11)}$$

It should be noted that for the linear model, k_x is equivalent to K_x, the secant modulus.

c. Slip model of contact

Different relative motions can occur at the contact between two contacting particles: sliding, rolling and spin motion (Section 7.1.3).

Sliding is defined as the development of a relative translational velocity along an axis included in the contact plane, as illustrated in Fig. 4-4. Sliding leads to the emergence of a tangential load, Q, on the contact area.

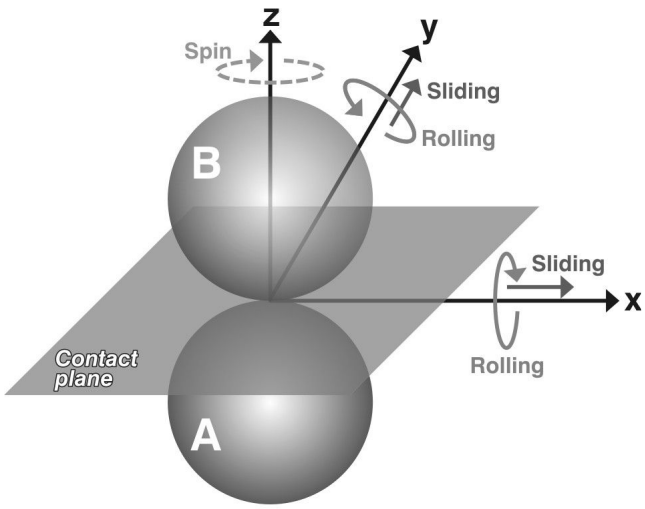

Figure 4-4: Scheme of reference for relative motions arising at the contact area.

The present sliding model is based on the well-known slip Coulomb condition:

$$|Q| = \mu P \qquad \text{(Eq. 4-12)}$$

where μ is the friction coefficient.

During the calculation of the contact force Q, the condition (4-12) is checked at the end of each timestep. If it is encountered, slip is allowed to occur during the next timestep of calculation setting the magnitude of the tangential force of contact to μP (Itasca, 2004):

$$Q = Q\left(\frac{\mu P}{|Q|}\right) \qquad \text{(Eq. 4-13)}$$

d. Spin motion and rolling resistance at the contact

Spin motion (Section 7.1.3c) is defined by the emergence of a relative angular velocity around the axis perpendicular to the contact surface resulting in a

torsional loading of the contact area, as illustrated in Fig. 4-4. In the present study, the bidimensional character of the simulations implies that no spin motion are considered.

Rolling (Section 7.1.3d) is caused by a relative angular velocity around an axis included in the contact surface, as illustrated in Fig. 4-4. Recent DEM developments introduce a rolling resistance in order to take into account the roughness of grains (Belheine et al., 2009). In the present model, the rolling resistance is not taken into account.

e. Viscous damping at the contact

Considering the inelasticity of the normal contacts or impacts between spherical bodies, several developments are presented in Section 7.1.5a or in Johnson (1985) and Stronge (2000) who provide a complete synopsis of force-displacement laws relating P and δ_z in the elastic, elasto-plastic and fully plastic ranges.

Another way to consider the energy dissipation during normal contact or impact is to define a coefficient of normal restitution, ε. This latter quantifies the energy loss in terms of the resultant velocity, V', of the impacting spheres at impact velocity, V:

$$\varepsilon = \frac{V_z^{'}}{V_z} \qquad \text{(Eq. 4-14)}$$

Similarly, the coefficient of tangential restitution is given by:

$$\beta = \frac{V_x^{'}}{V_x} \qquad \text{(Eq. 4-15)}$$

This latter is used for collisions which restore, to the tangential velocity, a part of the energy stored in the tangential deformations of the contact surface.

In DEM, the energy dissipation can be directly handled in the acceleration-terms of the motion equations using restitution coefficients and considering the resultant velocities after impact or indirectly in the force-terms by the way of an additional damping force.

In the present model, a viscous damping model of contact is assumed (see Fig. 4-3). The energy dissipation is introduced by the way of additional damping normal and tangential forces, D_z and D_x, introduced in the equations of motion.

The visous damping forces are added before checking the slip Coulomb condition (4-12). This latter becomes:

$$|Q - D_x| = \mu(P - D_z) \qquad \text{(Eq. 4-16)}$$

The viscous forces are opposed to the relative motion between the particles in contact but they are not inevitably in a direction opposed to the elastic component force. For the purpose of avoiding attraction forces between particles, the following no tensile force condition is imposed:

$$D_z \geq -P \qquad \text{(Eq. 4-17)}$$

The detail of the calculation of the damping forces is illustrated in Appendix 7-5.

4.1.4 Description of the numerical model

a. Generation of the DEM sample

Periodic boundary conditions

In the present numerical study, the influence of the walls must be removed to avoid granular convection. The deposit is thus performed in a rectangular container of lateral size L, under periodic boundary conditions in horizontal direction, eliminating wall effects on the sides.

In DEM simulations, periodic boundary conditions (PBC) are used to simulate a large system by modeling a small part hereof, which is located far away from its edges. Using lateral periodic boundary conditions (LPBC), the rectangular container can be imagined as replicated by a rigid translation in the lateral direction. A particle, located at a position, u, in the container is assumed to be reproduced at the following locations: $u \pm n.L$ where n is an integer number. All the virtual particles will move together but only one of them will be taken into account in the computation. Hence, the PBC also reduces the computation time by decreasing the number of particles, when the phenomenon of solving problem is expected to be cyclic in space.

Pouring method

They are many ways to generate a granular sample under gravitational field but they can lead to an inhomogeneous porosity in the assemblage (Combe and Roux, 2010).

In the present study, the granular sample is assembled with four successive drops of a particles block to decrease the computational time of the deposit. This method is less reliable than the air pluviation procedure (Emam et al., 2005) in terms of homogeneity but it reduces the calculation-time (Combe and Roux, 2010). Each particle block is created above the free surface of the sample and it is dropped under the gravitational field in the container. The drop height is about 90 times the diameter, d_{50}, of the particles. The calculation cycle, illustrated in Fig. 4-2, is then initiated and continues cycling until the model reaches a specified stopping condition: the deposit is considered at rest when the ratio of unbalanced force to contact force falls below a specified limit (Itasca, 2004 or Combe and Roux, 2010). The ratio of mean unbalanced force to mean contact force and the ratio of maximum unbalanced force to maximum contact force are taken into account.

The mean ratio is defined as the ratio of the average, over all particles, of the absolute values of all out-of-balance force components to the average, over all contacts, of the absolute value of the normal contact force. The maximum ratio is then defined as the ratio of the maximum magnitude of any component of the out-of-balance force vector of all particles to the maximum, over all contacts, of the absolute value of the normal contact force.

The ratio limits are set to 1‰ (-). It is a global equilibrium criterion. At the end of each of the four block deposits, the specified condition is checked.

In another way, the local equilibrium in the sample can be considered with the help of the following ratios, estimated for each particle:

$$\frac{\left\| \sum_{Contacts} \vec{F} \right\|}{mg} \leq \Xi \qquad \text{(Eq. 4-18)}$$

and

$$\frac{\left\| \sum_{Contacts} \vec{r} \otimes \vec{F} \right\|}{mgd} \leq \Xi \qquad \text{(Eq. 4-19)}$$

where the magnitude of $\vec{r}$ is the distance between the particle center and the contact location – approximately the value of the particle radius, R – and d is the particle diameter. $\vec{F}$ is the contact force vector given by equation (4-5). $\Xi \leq 10^{-3}$ seems to be a sufficient condition to assume the sample at rest (Combe and Roux, 2010).

Figure 4-5 illustrates the granular asssemblage at rest. Lateral periodic boundaries are represented with black lines. At the boundaries of the assembly, black-colored particles are included in the periodic boundary logic.

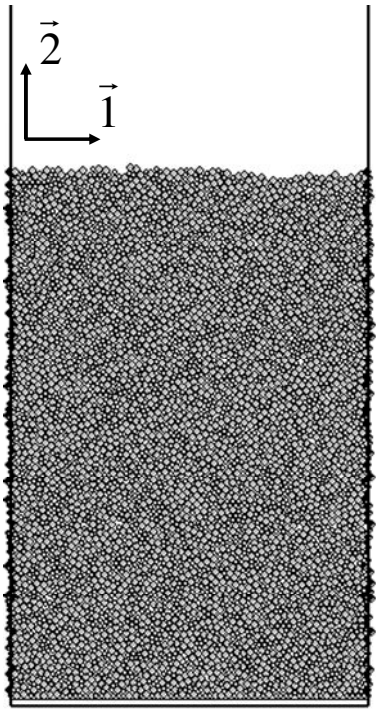

Figure 4-5: Numerical sample of sand grains.

Figure 4-6 illustrates the grain deposit, in the bottom of the sample at rest. The black lines indicate the contact force intensities and illustrate the development of the force chains through the granular assemblage.

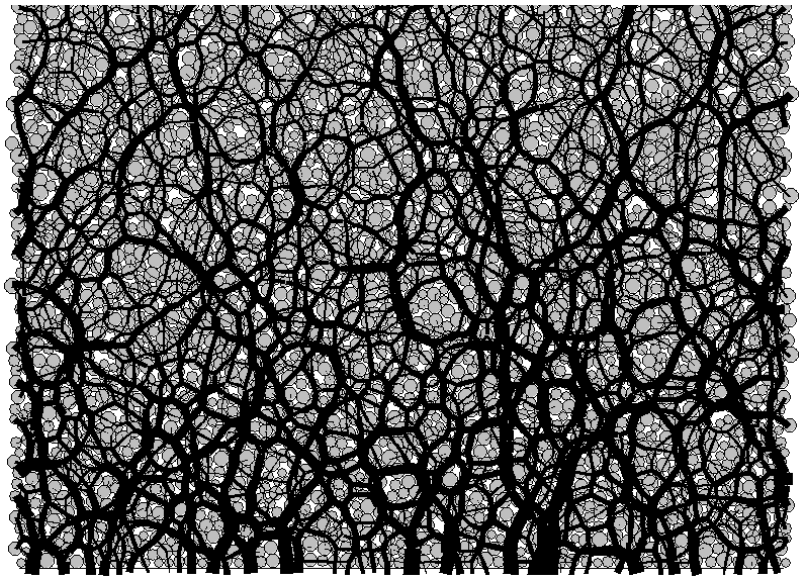

Figure 4-6: Bottom of the granular assembly: development of the force chains.

b. Dimensional and physical properties of the numerical sample

In comparison with the Fontainebleau sand grain size distribution (Section 3.3), the granulometry of the numerical granular medium is reduced to decrease the calculation-time. The minimum and maximum diameter, d_{min} and d_{max}, are respectively equal to 0.7 mm and 1.2 mm. Figure 4-7 represents the uniform grain size of the numerical sample (d_{50} = 1.018 mm and C_u = 1.35).

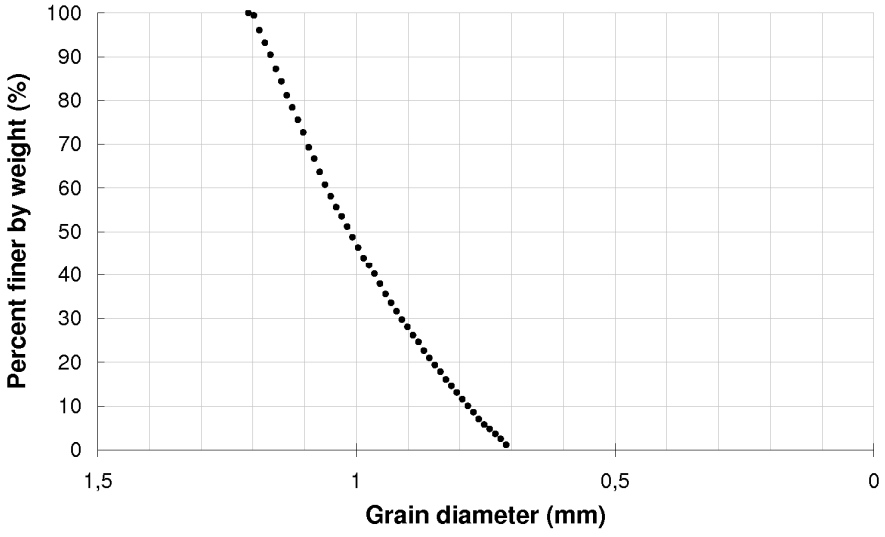

Figure 4-7: Numerical particle size distribution curve.

The deposit is performed in a rectangular container of lateral size L = 0.06 m. H_{eff} is the effective height of the granular assembly. It is computed considering the height corresponding to a porosity value of 0.5 (-). H_{eff} is around 0.09 m. The number of the particles in the sample is set to 6100.

The sample is described with the following non-dimensional ratios: $H_{eff}/d_{max} \approx 90$, $L/d_{max} \approx 60$ and $d_{max}/d_{min} = 1.7$.

The volumetric mass of the particle is $\rho_s = 2642$ gr/cm³, such as for the Fontainebleau sand.

Considering the mechanical properties of the particles, the contact model parameters must be defined.

The friction coefficient between the particles, μ_p, is set to 0.5 (-) in order to simulate frictional interactions between sand quartz grains (after Bromwell, 1966 and Dickey, 1966). The friction coefficient between particle and wall, μ_w, is also set to 0.5 (-).

The magnitude of the normal stiffness, k_z, is settled considering Hertz's law with $\nu = 0.15$ (-) and E = 97 Gpa for Quartz (Bardet, 1998). The derivative $dP/d\delta_z$ at which value of P or in $\delta_z^{max}/2$ can be considered to estimate the normal stiffness. k_z is set to $3.2\ 10^6$ N/m.

In the case of normal impact, it is possible to estimate the magnitude of the normal stiffnesses considering the secant slope P^{max}/δ_z^{max}. Indeed, if the maximum normal impact velocity, V_z, is known, δ_z^{max} is computed with the help of equation (7-47) and P^{max} with Hertz's law.

Moreover, the normal stiffness constant can be compared with the pressure magnitude in the sample. A dimensionless stiffness parameter is introduced:

$$\kappa^* = \frac{k_z}{p_{eff}.1} \qquad \text{(Eq. 4-20)}$$

where p_{eff} is the vertical effective pressure at the bottom of the sample which can be defined by:

$$p_{eff} \approx \Phi \rho g H_{eff} \qquad \text{(Eq. 4-21)}$$

where Φ is the solid concentration: $\Phi = 1-n$ and n the porosity of the sample. The porosity of the sample at rest, illustrated in Fig. 4-5, is expected to be close to 0.2 (-), then p_{eff} is around 2 kPa. In such a way to consider the bidimensional character of the simulations, the vertical effective pressure is multiplied by 1 m, the unit thickness of the variable-radius cylinders. κ^* is then equal to $1{,}7.10^3$ (-).

It is also noted that:

$$\frac{1}{\kappa^*} \div \frac{\delta_z}{d_{50}} \qquad \text{(Eq. 4-22)}$$

$1/\kappa^*$ is close to $5{,}9.10^{-4}$ (-) which is a reasonable value according to the assumptions of Hertz's law (Agnolin and Roux, 2007).

The tangential contact stiffness, k_x, can be computed considering the stiffness contact ratio, κ:

$$\kappa = \frac{k_x}{k_z} \qquad \text{(Eq. 4-23)}$$

For elastic similar materials, the stiffness contact ratio reduces to $\kappa = (2-\nu)/(2-2\nu)$ where ν is the poisson ratio of the particles in contact. This coefficient is often close to unity and k_x can be thus considered approximately equal to k_z (Bathurst and Rothenburg, 1988).

In such a way to simulate the dissipative behavior of the vibrated dry sand, the normal and tangential restitution coefficient, ε and β, are set to 0.2 (-).

Table 4-1 provides a summary of the numerical model properties.

NUMERICAL MODEL (2D)	
Granulometry	
Uniform grain size d_{max} = 1.2 mm d_{min} = 0.7 mm d_{50} = 1.018 mm	$d_{max}/d_{min} \approx 1.7$ $C_u = 1.35$
Sample dimensions	
H_{eff} = 0.09 m L = 0.06 m 6100 particles	$H_{eff}/d_{50} \approx 90$ $L/d_{50} \approx 60$
Particles properties	
ρ_s = 2.642 gr/cm³ $k_z = k_x$ = 3.2 10^6 N/m p_{eff} = 2 kPa	n = 0.2 $\mu_p = \mu_w = 0.5$ $\kappa = 1$ $\kappa^* = 1{,}7.10^3$ $\varepsilon = \beta = 0.2$

Table 4-1: Numerical model description.

c. Stratified characterization of the numerical sample at rest

A stratified analysis is well adapted to emphasise the evolution of the internal states of the numerical sample. Indeed, without wall influence, the internal characteristics (porosity or coordination number) are generally uniform everywhere in the assemblage and the parameters related to the forces vary linearly with the depth except for the zones located near the free surface and near the bottom of the sample where the presence of the rigid boundary perturbs the state of the assembly (Emam et al., 2006).

The present section presents the stratified characterization of the numerical sample at rest, before vertical vibrations. A finite number of measurement layers is considered. The minimum thickness of the strata corresponds to $8d_{50}$ in such a way to obtain smooth representative macroscopic averaged values with the depth.

The analysis is performed taking into account the height in the granular assemblage, h, with respect to the total height of the container, H. This latter is set to $120d_{50}$ in order to allow the measurement of the sample dilatation.

Figure 4-8 emphasises the degree of uniformity of the assemblage.

Porosity

The porosity of the sample is represented as a function of h/H in Fig. 4-8a. Satisfaying uniformity is observed in the sample with a limited decrease of the porosity near the bottom of the container due to the particle stiffness and the application of the gravitational field.

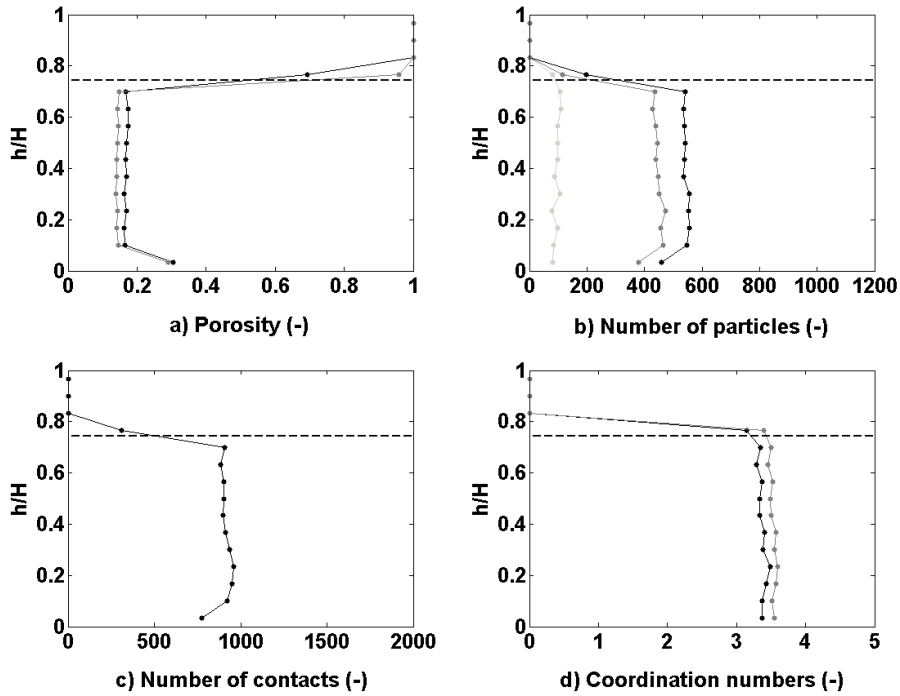

Figure 4-8: Degree of uniformity of the numerical assembly. a) Porosity at rest (black line) and minimum porosity (grey line), b) number of particles (black line), number of active particles (grey line) and number of passive particles (light grey line), c) number of contacts, d) coordination number C_n (black line) and coordination number C_n* (grey line). The dashed black lines represent the effective height of the sample.

The global porosity of the assemblage is close to 0.186 (-).

Maximum volumetric mass

The density of the numerical sample at rest is close to 2150 kg/m³ (n = 0.186). It is also possible to obtain an estimate of its maximum density relaxing the contacts between the grains. Initially, the particles present an interparticle friction coefficient, $\mu_p = 0.5$. Once, this coefficient is set to zero, the assemblage collapses and reaches a new equilibrium state under the effect of the gravity. Then, it is possible to compute a new density considered as an approximation of the maximum density: 2224 kg/m³ for n = 0.158. The minimum porosity profile is represented by the grey line in Fig. 4-8a.

Passive and active grains

Figure 4-8b illustrates the number of particles, N_p, as a function of h/H. The distribution of the particle number emphasises the degree of uniformity of the assemblage.

Several grains of the assembly do not actively participate to the construction of the granular skeleton. In the absence of gravitational field, they are

called “rattler grains” and they have no weight. In the present model, the sample is subjected to the gravitational acceleration, there are no rattler grains, but several grains are not included in the force chains (illustrated in Fig. 4-6). They settle inside the arches formed in the granular structure. If they transmit their own weight to the force chains which support them, they are not active with regards to the external forces of the system although their weight may help other grains take part in the force chains. They do not transmit the forces corresponding to the macroscopic local stress. It is proposed to call them “passive grains”.

Figure 4-9 illustrates the presence of a passive grain. The black lines represent the network of contacts. The grey-colored (dark-shaded) grain is settled on two contacts inside an arch and is only subjected to its own weight.

Passive grains have to be considered in the calculation of the stress field because their presence leads to an increase of the intensity of the force chains. They apply an additional load on the granular skeleton. Figure 4-8b illustrates the number of passive grains, N_{pp}, in comparison with the number of “active particles”, N_{ap}, for the sample at rest. The number of passive grains is not negligible in the numerical sample at rest.

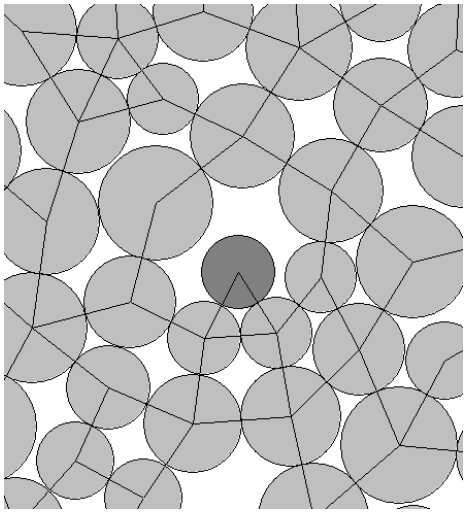

Figure 4-9: Illustration of a passive grain.

Contact density

Figure 4-8c illustrates the number of contacts, N_c, existing in the different layers. The contact number rises to 10000 in the whole sample.

Considering the contact number and the particle number in these strata, it is possible to define the coordination number:

$$C_n = \frac{2N_c}{N_p} = \frac{S}{N_p} \qquad \text{(Eq. 4-24)}$$

where $S=2N_c$.

C_n is the average number of contact per particle and its distribution in the sample is illustrated in Fig. 4-8d. C_n is close to 3.37 for the whole sample.

It is possible to define a second coordination number which takes into account the presence of the passive grains in the sample:

$$C_n^* = \frac{2N_c^*}{N_{ap}} = \frac{S}{N_{ap}} \qquad \text{(Eq. 4-25)}$$

where the contacts arising on active particles, N_c^*, are taken into account. C_n^* characterizes an equivalent numerical sample in absence of gravitational field but subjected to external forces wherein the passive grains would become rattler grains. The distribution of C_n^* is illustrated in Fig. 4-8d. $C_n^* = 3.53$ for the whole sample.

The assembly contact density can be defined as:

$$D_c = \frac{2N_c}{V} \qquad \text{(Eq. 4-26)}$$

where V is the volume of the considered part of the assembly (or its area in the bidimensional case). V can be computed taking into account the width and the thickness of the measurement layer: $V = 60d_{50}.8d_{50} = 48d_{50}^2$.

Contact orientations

The contact density or the contact number are limited descriptors of the state of packing as they provide no information on orientations of interparticle contacts. The contact forces are still strongly dependent on contact orientation. The understanding of the force chains in the granular material requires information on the distribution of contact orientations – called the "fabric" of the sample. Figure 4-10 emphasises the fabric of the assemblage.

For each measurement layer, the portion of contacts, $\Delta S(\theta)$, is normalized for a given angular interval, $\Delta\theta$, by the total contact number in the layer, S, for all orientations. The normalized contact orientation distribution is given by: $\Delta S/(S\Delta\theta)$. Then, the average, over all the measurement layers, of this distribution is computed in such a way to control the fabric characteristics of the whole assemblage.

According to Rothenburg and Bathurst (1989), the normalized contact orientation distribution for plane assemblies can be described with the help of an analytical function $E(\theta)$:

$$E(\theta) = \frac{1}{2\pi}\{1 + a\cos 2(\theta - \theta_a)\} \qquad \text{(Eq. 4-27)}$$

where a is the coefficient of contact normal anisotropy (-), θ is the considered orientation and θ_a is the direction of contact anisotropy. $a = 0$ leads to an isotropic distribution with $E(\theta) = 1/2\pi$.

In such a way to check the isotropic character of the depth-averaged normalized (D-A N) contact orientation distribution, this latter is compared with the function $E(\theta)$. Figure 4-10a illustrates this comparison for $a = 0.091$ and $\theta_a = 1°$, the values which minimize the gap between the numerical and the analytical values considering the least squares method. The angular interval, $\Delta\theta$, is set to 10°.

In a similar way, the angular distribution of the normal contact forces is defined for all the measurement layers. The normal contact force, $f_n(\theta)$, for a given angular interval, $\Delta\theta$, is normalized by the average normal force, over all the contacts and for all orientations, $\overline{f_0}$.

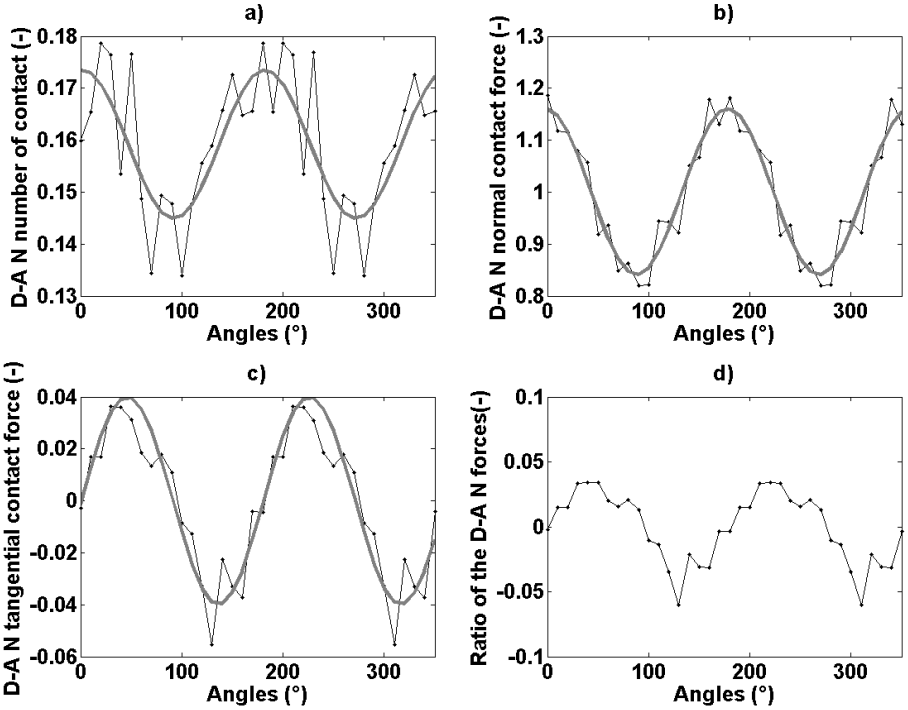

Figure 4-10: Characteristics of fabric of the numerical assembly: a) depth-averaged normalized orientations of contact (black line) and E(θ) (grey line), b) depth-averaged normalized normal contact force orientations (black line) and $\overline{f_n}(\theta)/\overline{f_0}$ (grey line), c) depth-averaged normalized tangential contact force orientations (black line) and $\overline{f_t}(\theta)/\overline{f_0}$ (grey line), d) ratio of the depth-averaged normalized tangential to normal contact force orientations.

It is necessary to normalize the normal contact force by an average value which represents the stress level developed in the measurement layer. Indeed, the intensities of the normal contact forces tend to increase with the depth due to the application of the gravitational field. The depth-averaged values of this normalized distribution is calculated to control the anisotropy of the normal contact forces in the whole sample.

According to Rothenburg and Bathurst (1989), the normalized angular distribution of the normal contact forces for plane assemblies can be approximated by the following analytical expression:

$$\overline{f_n}(\theta) = \overline{f_0}\left\{1 + a_n \cos 2\left(\theta - \theta_f\right)\right\} \qquad \text{(Eq. 4-28)}$$

where a_n is the coefficient of average normal force anisotropy (-) and θ_f is the direction of average normal contact force anisotropy.

In such a way to illustrate the anisotropy of the depth-averaged normalized angular distribution of the normal contact forces, this latter is compared with the

function $\overline{f_n}(\theta)$. Figure 4-10b illustrates the comparison with $a_n = 0.158$ and $\theta_f = 178°$, considering the least squares method.

The tangential contact force, $f_t(\theta)$, for a given angular interval, $\Delta\theta$, is also normalized by the average normal force, $\overline{f_0}$.

According to Rothenburg and Bathurst (1989), the normalized angular distribution of the tangential contact forces for plane assemblies can be approximated by:

$$\overline{f_t}(\theta) = \overline{f_0}\{a_t \sin 2(\theta - \theta_t)\} \qquad \text{(Eq. 4-29)}$$

where a_t is the coefficient of average tangential force anisotropy (-) and θ_t is the direction of average tangential contact force anisotropy. The tangential distribution is modelled with the help of a sinus due to the perpendicularity between the normal and tangential forces.

In such a way to illustrate the anisotropy of the depth-averaged normalized angular distribution of the tangential contact forces, this latter is compared with the function $\overline{f_t}(\theta)$. Figure 4-10c illustrates this comparison with $a_t = 0.037$ and $\theta_t = 2°$.

θ_a, θ_f and θ_t are close to zero due to the symmetry of the assembly and the application of the gravitational field in this direction.

If the particle [B], represented in Fig. 4-1, moves with a positive shearing velocity, V_x, with respect to the local coordinate system $\{\vec{z}, \vec{x}\}$, the resulting tangential force will be negative because of the equation (4-7).

Figure 4-10d compares the tangential and normal depth-averaged normalized distribution of contact forces.

Stress field

Stress is a continuum quantity but the discrete character of a granular assembly leads to the fact that stress does not exist at each point of a granular medium. Averaging procedure is therefore necessary to make the connection between the microscopic and the macroscopic scales. The micro-contact forces are considered to compute the macro-stress tensor in terms of a continuum model.

In the present model, the averaging procedure is based on the previous works of Rothenburg and Bathurst (1989) and Bagi (1999) and is implemented considering the PFC2D model of Itasca (2004). The calculation of the stress tensor is presented in Appendix 7.6. The stresses are positive in compression and negative for tensile stresses. The components of the average stress tensor in the measurement layers are noted σ_{22}, σ_{11}, σ_{12} and σ_{21}. Figure 4-11 illustrates the development of the stress field in the numerical assembly.

Figure 4-11a illustrates the development of the stresses in the measurement layers for the numerical sample at rest. The stresses are inhomogeneous: σ_{22} and σ_{11} linearly increase with the depth after a transient phase located near the free surface (Emam et al., 2006). In the bottom of the sample, the stresses are perturbed by the presence of the rigid boundary.

Considering these results, one can wonder how it is possible to observe an homogeneous porosity in in the whole sample and simultaneously an increase of the stresses σ_{22} and σ_{11} with the depth? Actually, Agnolin and Roux (2007) have observed that, for the range of stresses developed in the present model, weak

variations of the stresses lead to very limited variation of porosity, in the absence of plastic effects.

The earth pressure coefficient $K_0 = \Delta\sigma_{11}/\Delta\sigma_{22}$ is close to 0.70 (-) in the numerical sample, as illustrated in Fig. 4-11b, wherein the slope of the straight line is the coefficient K_0. The grey line is build using the points of intersection between horizontal and vertical stresses, respectively σ_{11} and σ_{22}.

Due to the absence of lateral wall effects, the stresses σ_{12} and σ_{21} are close to zero according to the symmetry of the problem.

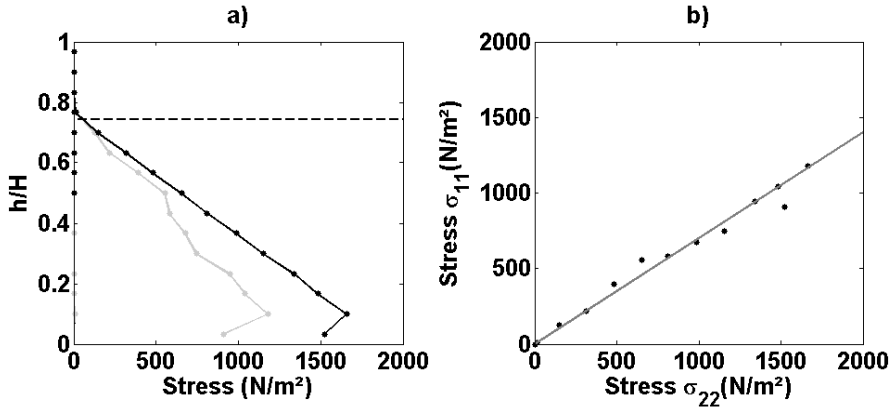

Figure 4-11: Stress field in the numerical assembly. a) Development of the stress components: σ_{22} (continuous black line), σ_{11} (continuous grey line), σ_{12} (dashed black line), σ_{21} (dashed grey line). b) Development of the earth pressure coefficient K_0: slope of the straight line.

Stress-force-fabric relationship for plane systems

According to Rothenburg et Bathurst (1989), it is possible to define a relationship between the anisotropy coefficients a, a_n and a_t and the normal and tangential components of the stresses (in the form of the Mohr circle parameters):

$$\frac{\sigma_t}{\sigma_n} = \frac{\frac{1}{2}\left(a + a_n + a_t\right)}{\left(1 + \frac{a_n a}{2}\right)} \qquad \text{(Eq. 4-30)}$$

assuming $\theta_a = \theta_f = \theta_t$ and considering θ_a as the major principal direction of stress (i.e. the direction of anisotropy in contact orientations as well as the assumed preferred direction for average forces). This ratio is independent of the contact number and is frequently associated with the mobilized friction angle for cohesionless material (i.e. $\sin\phi_{mob} = \sigma_t/\sigma_n$). Moreover, the product $aa_n/2$ in the denominator of equation (4-30) is small and can be neglected, resulting in the basic relationship:

$$\sin\phi_{mob} = \frac{1}{2}\left(a + a_n + a_t\right) \qquad \text{(Eq. 4-31)}$$

This latter can be referred as the stress-force-fabric relationship. This expression is based on the assumption that the shear strength of a cohesionless granular assembly, subjected to deviatoric loading, would be the result of its ability to develop some contact orientation anisotropy or it would be due to its capacity to develop a resistance to change of direction of the averaged contact forces. Indeed, during shearing, contacts oriented along the direction of maximum tensile strain disintegrate more swiftly than contacts of other directions. Consequently, the distribution of contact orientations becomes distinctly anisotropic. In our study, the numerical sample at rest displays a mobilized angle of friction close to 8°.

The calculation of the anisotropy coefficients during the vibration of the numerical sample could turn out to be interesting but the interpretation of that result must be considered with caution. The theoretical development of Rothenburg and Bathurst (1989) are based on the consideration of static equilibrium in granular assemblies where particles interact by means of contact forces. It will be necessary to preserve the major part of the contacts to compute representative values of the anisotropy coefficients and to deduce mobilized friction angle according to the assumption $\theta_a = \theta_f = \theta_t$. Thus, the meaning of the results will be dependent on the conservation of the contact network during the vibration.

Elastic moduli

In the present numerical model, the sample can only deform in the vertical direction, $\vec{2}$. According to this direction, it is possible to define two elastic moduli, C_{12} and C_{22}.

An increase of the gravitational acceleration, g, is applied in such a way to determine C_{22} which corresponds to the coefficient of compressibility of the numerical assembly. The sample at rest was initially subjected to a gravitational acceleration of 9.81 m/s². When g is set to 9.90 m/s², the sample settles until it reaches a new equilibrium state at which the assemblage is assumed at rest. The value of 9.90 m/s² is determined in such a way to ensure an elastic response of the granular assembly. The vertical deformation, ε_{22}, is computed considering the settlement of each particles of the sample:

$$\varepsilon_{22} = \frac{\Delta\sigma_{22}}{C_{22}} = \frac{ds_2}{dy} = \frac{(H_{eff} - u_2)\Delta g\rho_S}{C_{22}} \qquad \text{(Eq. 4-32)}$$

where u_2 represents the vertical location of the center of the particles and $s_2 = u_2^a - u_2^b$. u_2^a and u_2^b respectively define the vertical location of the particle after and before the application of the gravitational acceleration increment, Δg. H_{eff} is considered before the settlement. Then, s_2 can be expressed by:

$$s_2 = \int_0^{u_2^b} \frac{\left(H_{eff} - \ell\right)\Delta g\rho_s}{C_{22}} d\ell = \left(H_{eff} u_2^b - \frac{\left(u_2^b\right)^2}{2} \right) \frac{\Delta g\rho_s}{C_{22}} \qquad \text{(Eq. 4-33)}$$

The elastic modulus, C_{22}, is calculated fitting equation (4-33) with the numerical results, as illustrated in Fig. 4-12. The best approximation is obtained by the least squares method with $C_{22} = 1.0676$ Mpa which corresponds to the coefficient of compressibility E_0 obtained with the help of the oedometer test. From the stress measurement, the second elastic modulus, C_{12}, is deduced: $C_{12} = C_{22}(\Delta\sigma_{11}/\Delta\sigma_{22}) = 0.396$ Mpa.

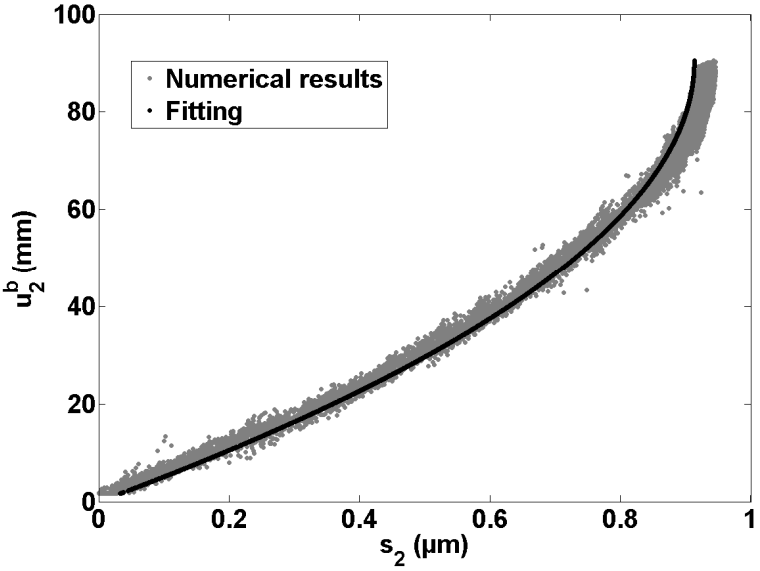

Figure 4-12: Computation of the elastic modulus C_{22}.

The velocity of propagation of a longitudinal wave in the medium is given by:

$$c_0 = \sqrt{\frac{C_{22}}{\rho_s}} \qquad \text{(Eq. 4-34)}$$

Hence, c_0 is equal to 20.1 m/s.

The corresponding propagation time of the elastic longitudinal wave in the numerical sample is $T_0 = H_{eff}/c_0$. H_{eff} is equal to 0.091 m, thus T_0 is close to 0.0045 s.

Figure 4-13 illustrates the propagation of a longitudinal wave in the numerical sample when a vibration is imposed to the bottom of the container. In this example, the imposed motion is a weak vertical sine curve, with a displacement amplitude, $A/d_{50} = 0.027$, a frequency, $fr = 9$ Hz and an acceleration amplitude, $\Gamma = 0.009$. The observed propagation time – around 0.0042 s – is close to the theoretical value, $T_0 = 0.0045$, calculated with the help of equation (4-34). The period of imposed vibrations is $T = 2\pi/\omega$, where ω is the angular frequency of the vibrations. The ratio T/T_0 is close to 25.

4.2 Dynamic behavior of the numerical model

The particle motion and the assembly behavior are analyzed during vibration. The analysis is performed as a function of the number of cycles. Each cycle of vibration is discretized in ten intermediate points. The granular sample is subjected to sinusoidal vibrations for different displacement amplitudes and various frequencies. The table 4-2 summarizes the numerical simulations. No simulation presents ratio T/T_0 close to the unity.

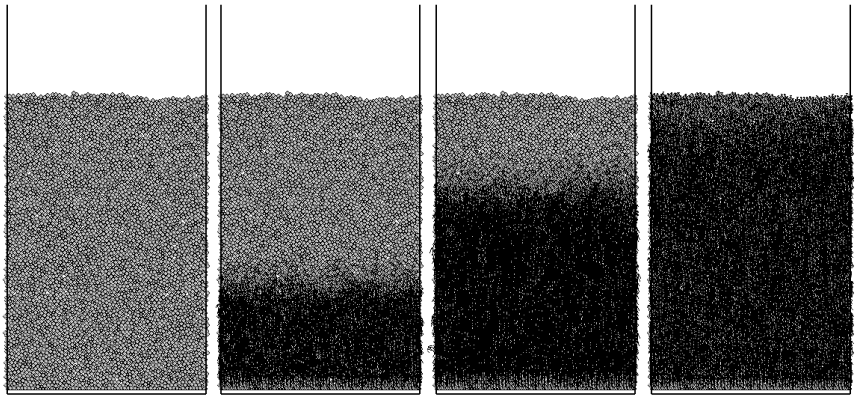

Figure 4-13: Propagation of an elastic longitudinal wave in the numerical sample: $t_1 = 0$ s, $t_2 = 1.40\ 10^{-3}$ s, $t_3 = 2.78\ 10^{-3}$ s and $t_4 = 4.17\ 10^{-3}$ s.

Figure 4-14 illustrates the domain of the vibrations imposed to the numerical container in a bi-logarithmic diagram (Velocity vs. Period). Numerical simulations are represented by black crosses and experimental points are indicated by black circles for comparison.

4.2.1 Elastic behavior of vibrated granular matter

The evolution of the vibrated granular matter properties is first regarded at low acceleration amplitude. The numerical sample is subjected to 10 cycles of sinusoidal vibrations with a displacement amplitude of 1.5 mm and a frequency of 9 Hz corresponding to $\Gamma = 0.5$ (-). The imposed vertical displacement is defined by:

$$A_2(t) = A\sin(\omega t) \qquad \text{(Eq. 4-35)}$$

The imposed vertical velocity is given by:

$$v_2(t) = V\cos(\omega t) \qquad \text{(Eq. 4-36)}$$

and the dimensionless imposed vertical acceleration by:

$$\eta_2(t) = -\Gamma\sin(\omega t) \qquad \text{(Eq. 4-37)}$$

where $V = A\omega$.

Displacement amplitude, A (mm)	Dimensionless displacement amplitude, A/d_{50} (-)	Frequency, fr (Hz)	Velocity amplitude, V (mm/s)	Dimensionless acceleration, Γ (-)	T/T_0 (-)
0.8	0.79	12.46	63	0.5	17.83
0.8	0.79	17.8	89	1.02	12.48
1.5	1.47	9	85	0.5	24.69
1.5	1.47	13	123	1.02	17.09
1.5	1.47	18.2	172	2	12.21
2	1.96	7.882	99	0.5	28.19

Table 4-2: Summary of the DEM simulations of the vibrated numerical sample.

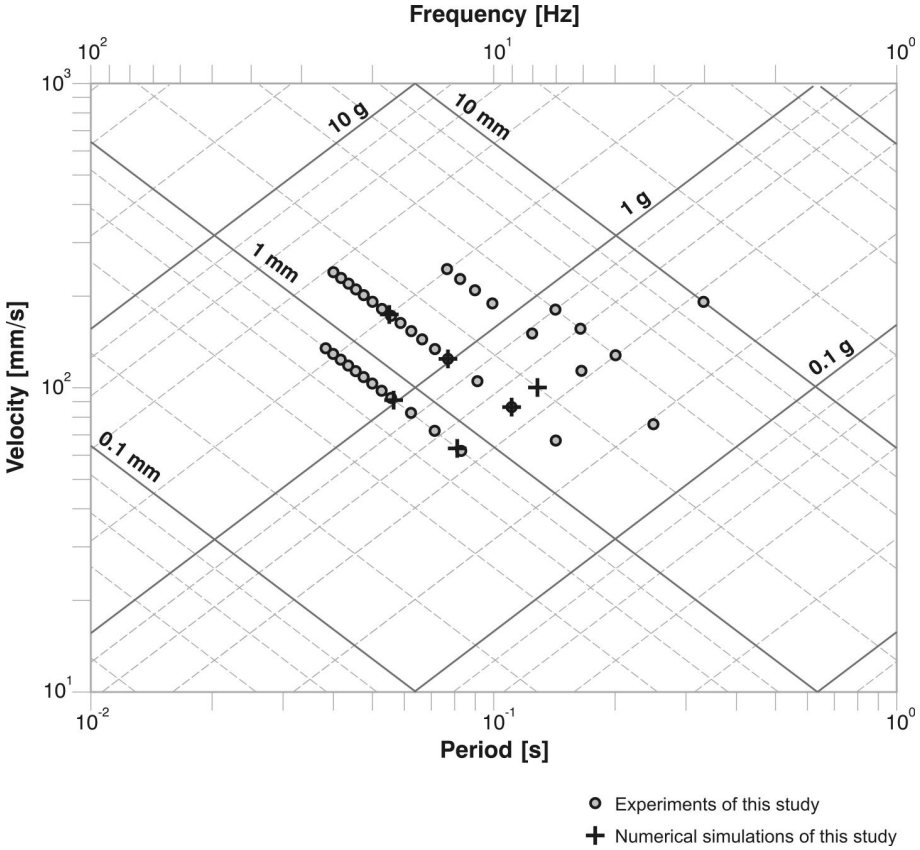

Figure 4-14: Domain of vibrations for numerical simulations and experiments.

a. Evolution of the internal state during vibration

At the macroscopic scale of the assembly

Before vibration, the assemblage is in static equilibrium notably because of the interparticulate friction. The vibration is applied to the container with the help of a dynamic ramp, as illustrated in Fig. 4-15.

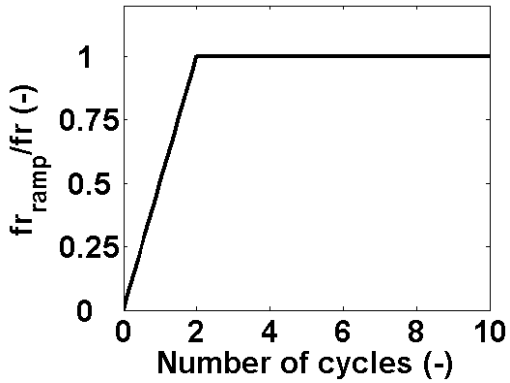

Figure 4-15: Dynamic ramp.

The frequency is progressively increased during two cycles preventing the sample from excessive acceleration. Once the dynamic regime is established, there is a cyclic evolution of the sample mechanical properties. The cycles are similar from one another marked by random fluctuations but there is no tendency of the assembly in any direction. Figure 4-16 illustrates the volume change in the granular assemblage during the ten cycles of vibration.

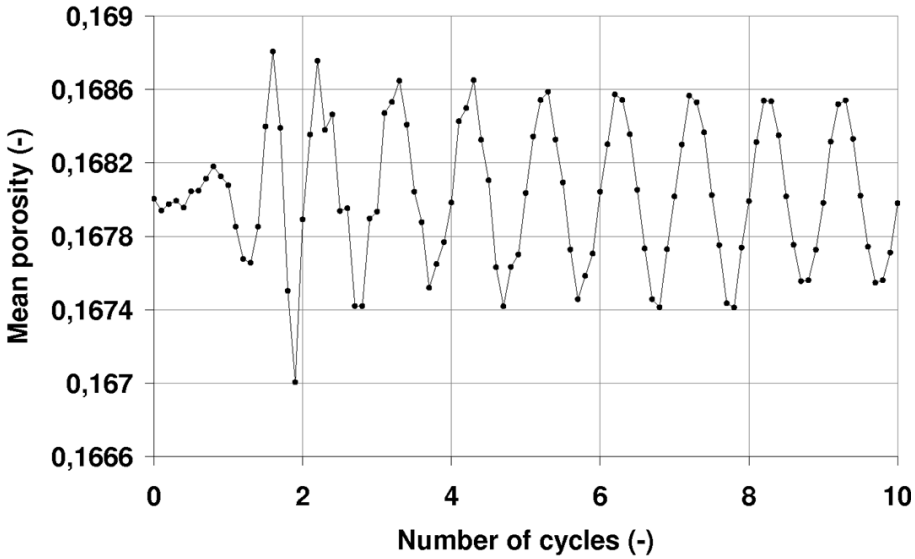

Figure 4-16: Mean porosity variation of the granular sample during the vibration (A = 1.5 mm and Γ = 0.5).

In the steady vibratory regime, the porosity variation is very small (on the order of 1‰). A sinusoidal evolution is observed. Porosity increases when the acceleration imposed to the container decreases and inversely. The granular medium is compacting when the container bottom is accelerating upward ($\eta_2 > 0$) and dilating when the container bottom is accelerating downward ($\eta_2 < 0$).

Dynamics of an elastic solid, subjected to similar motion, can be considered to approach the assemblage behavior (Roux, 2010).

Considering an homogeneous elastic layer vibrated under gravitational field, the one-dimensional longitudinal wave equation (Kramer, 1996) is given by:

$$\rho_s \frac{\partial^2 u}{\partial t^2} = C_{22} \frac{\partial^2 u}{\partial z^2} \qquad \text{(Eq. 4-38)}$$

where ρ_s is the layer density and u the displacement in the vertical direction, z. The solution of equation (4-38), in the steady-state, is given by:

$$u(z,t) = \frac{A\sin(\omega t)}{\cos kH}\cos(k(H-z)) \qquad \text{(Eq. 4-39)}$$

where A is the imposed displacement amplitude, H the layer height and k the wave number ($k = \omega/c_0$). The vibration leads to the vertical stress variation:

$$\Delta\sigma_{22} = -C_{22}\frac{\partial u}{\partial z} \qquad \text{(Eq. 4-40)}$$

which can be rewritten:

$$\Delta\sigma_{22} = -\frac{kAC_{22}}{\cos(kH)}\sin(k(H-z))\sin(\omega t) \qquad \text{(Eq. 4-41)}$$

Because of the low value of the ratio T_0/T, $kH \ll 1$ and the solution (4-39) will be close to the solution for a solid rigid layer:

$$u(z,t) = A\sin(\omega t) \qquad \text{(Eq. 4-42)}$$

The vertical stress variation will be given by:

$$\Delta\sigma_{22} = -A\rho_s\omega^2(H-z)\sin(\omega t) \qquad \text{(Eq. 4-43)}$$

Figure 4-17 describes the vertical stress variation due to the contacts between grains, at the bottom of the sample during vibration. The points represent the measured values. The grey dashed line represents the evolution of the vertical stress at the base of an equivalent solid rigid layer and the red line this evolution at the base of an equivalent elastic layer. As expected, the difference between the elastic and the solid rigid layers is insignificant. In first approximation, the granular assemblage displays an elastic behavior in the steady vibratory regime at least at the macroscopic scale of the stresses.

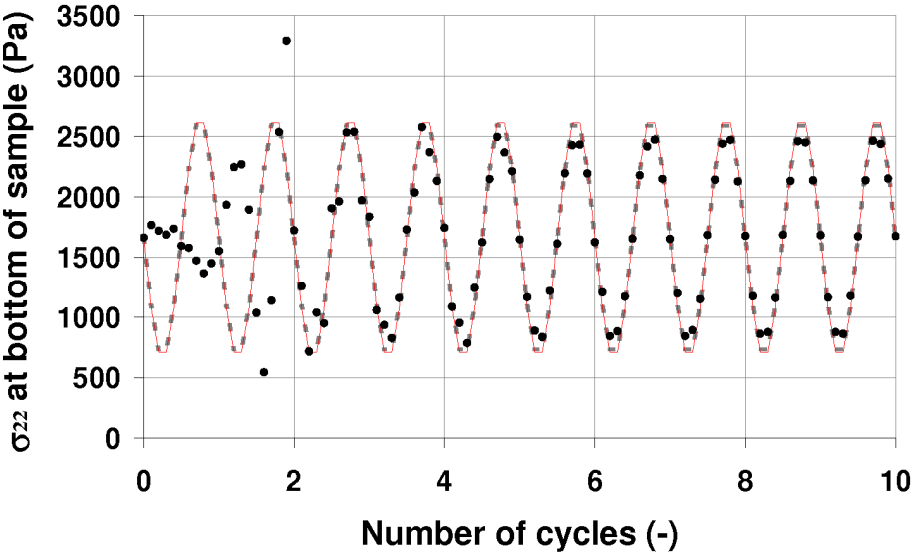

Figure 4-17: Relationship between the vertical stress, σ_{22}, in the granular medium at the bottom of the sample and the number of cycles (A = 1.5 mm and Γ = 0.5).

Figure 4-18 displays the evolution of the stress field in the granular material during the 10th cycle of vibration. The cycle is discretized in ten parts. Except for the zone close to the container bottom, the vertical stress σ_{22} linearly varies with the

depth indicating the good transmission of the contact stresses throughout the granular assembly by the means of force chains.

The horizontal stresses, σ_{11}, are weaker than the vertical stresses. They also linearly vary with the depth, as observed in Fig. 4-18b).

Due to the absence of lateral rigid boundaries, the stresses σ_{12} and σ_{21} remain close to zero during the vibration (see Fig. 4-18c) and 4-18d)).

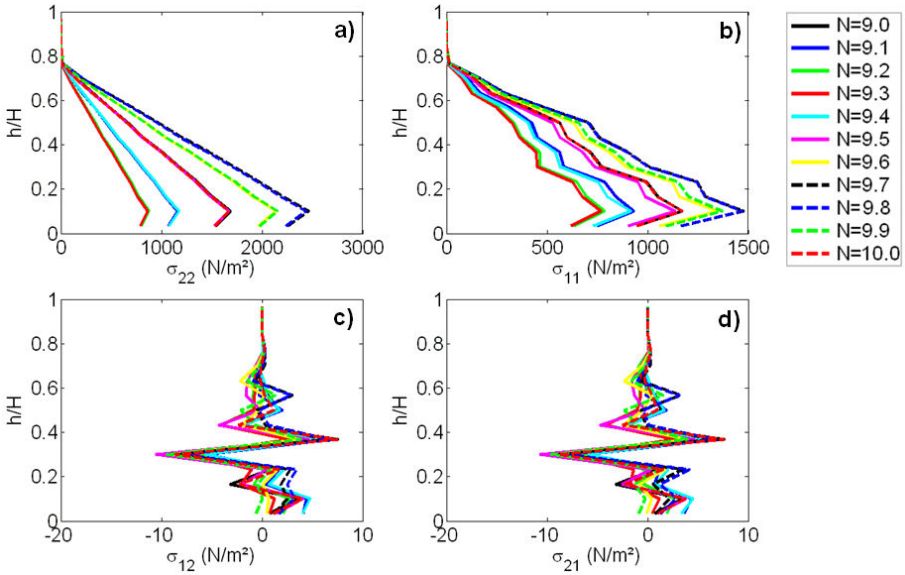

Figure 4-18: Evolution of the stress field in the numerical sample during the 10th cycle of vibration (A = 1.5 mm and Γ = 0.5).

Figure 4-19 illustrates the evolution of the ratio, σ_{11}/σ_{22}, during the vibration. The black points are the measured values and the red line represents the elastic solution. The range of the measured values spreads on [0.57 - 0.90]. The difference between the curves highlights the inelastic phenomena which mainly occur during the dilating phase of the vibration with the emergence of a great number of passive grains.In Fig. 4-17, this difference does not appear because the weight of the passive particles is still transmitted throughout the sample and directly influences the vertical stress. Horizontal stresses are more sensitive to the presence of passive particles.

During the vibration, each particle of the granular material develops kinetic energy:

$$W_{kin} = \frac{mv^2}{2} + \frac{I\omega^2}{2} \qquad \text{(Eq. 4-44)}$$

where m is the particle mass, v the velocity magnitude, I its principal moment of inertia and ω its rotational velocity. The kinetic energy, developed on a measurement layer, is computed summing all the kinetic energy components due to the particles of the given layer.

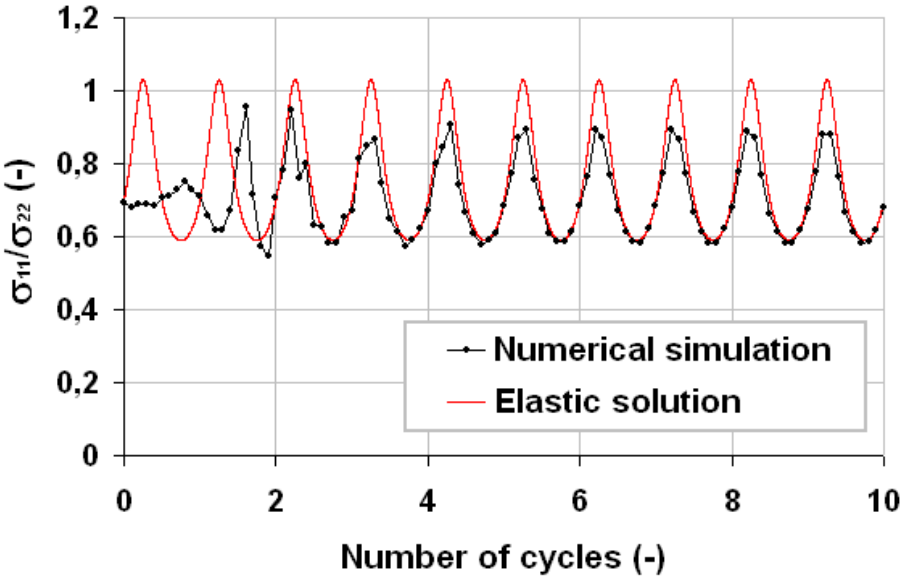

Figure 4-19: Evolution of the ratio of the horizontal to vertical stresses during the vibration (A = 1.5 mm and Γ = 0.5).

Nevertheless, because of the gravitational field, it is necessary to take into account the level of vertical stress developed in the layer to compare them. Thus, dimensionless kinetic energy of the measurement layer i is given by:

$$W_{kin,i} = \frac{\frac{1}{2}\sum_{j=1}^{N_{p,i}}\left(m_j v_j^2 + I_j \omega_j^2\right)}{\sigma_{22,i} d_{50}^2 1} \qquad \text{(Eq. 4-45)}$$

where j indicates the particle j.

The layer kinetic energy is adimensionalized by the vertical stress in the measurement layer, $\sigma_{22,i}$. Vertical stress is multiplied by 1 m, the unit thickness of the problem and by the square of d_{50} to obtain energy unit at the denominator. The particle velocity components are computed according to the global coordinate system $\{\vec{1}, \vec{2}\}$ in an eulerian view.

The total dimensionless kinetic energy in the sample is computed summing its components in all the measurement layers. Its evolution during the vibration is represented in Fig. 4-20. It periodically varies in the steady vibratory regime but does not follow a sinusoidal variation because it takes simultaneously into account the evolution of the imposed velocity and the variation of the vertical stresses which vary sinusoidaly with a phase lag of π/2.

The 10th cycle of vibration is investigated in Fig. 4-21. The discretization and the caption are similar to Fig. 4-18. As the sample approximately behaves like an elastic solid, the particle velocities are close to the velocity imposed to the container bottom. The shape of the curves is due to the linear variation of the vertical stress with the depth.

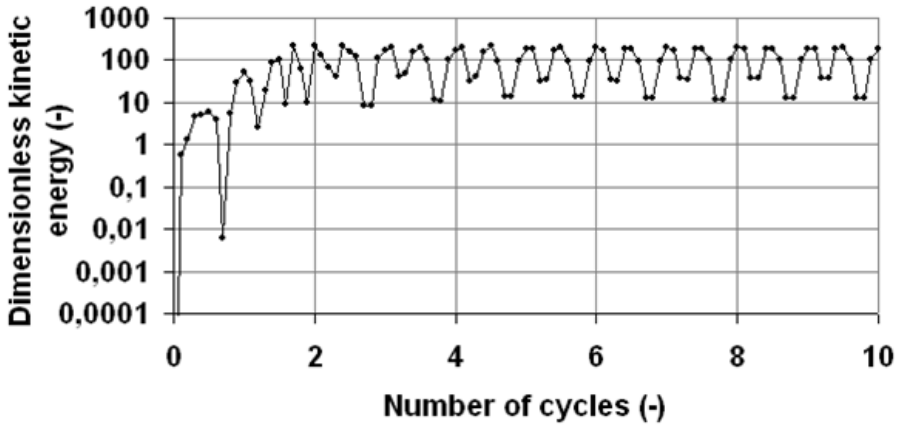

Figure 4-20: Evolution of the dimensionless kinetic energy in the sample during the vibration (A = 1.5 mm and Γ = 0.5).

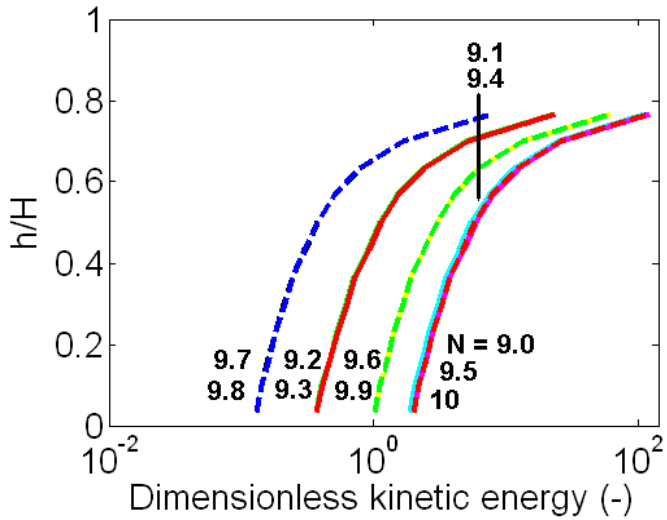

Figure 4-21: Dimensionless kinetic energy in the sample during the 10th cycle of vibration (A = 1.5 mm and Γ = 0.5).

Figures 4-17, 4-18 and 4-21 highlight the elastic character of the assembly, when subjected to low vibration (Γ = 0.5), in the steady vibratory regime, at the macroscopic scale.

At the microscopic scale of the grain

In the steady vibratory regime, the evolution of the contact density properties can be related to the sinusoidal motion of the container, as illustrated in Fig. 4-22. The contact number increases during the compacting phase and decreases during the dilating phase.

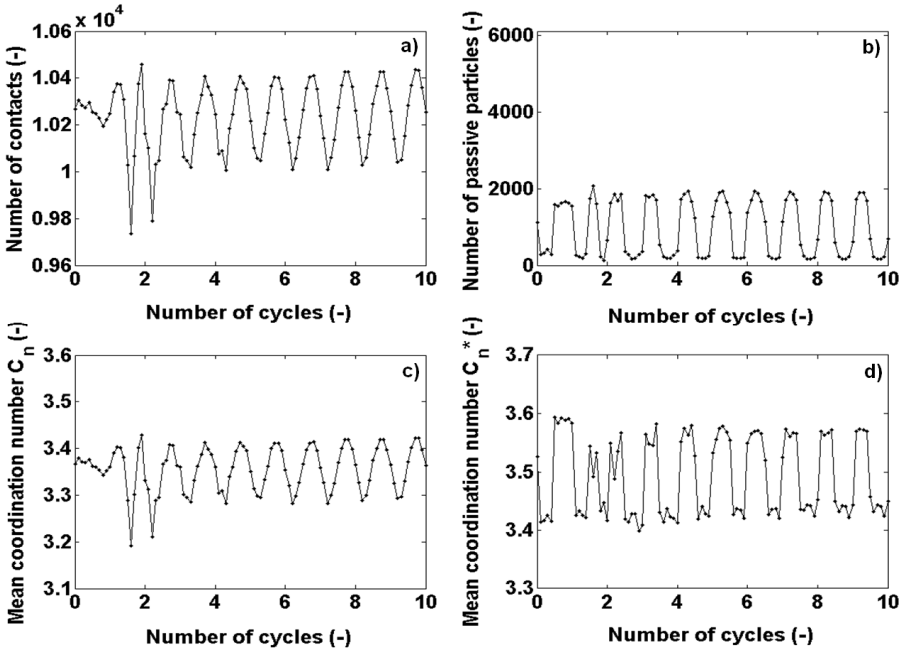

Figure 4-22: Relationships between the number of cycles and the total contact number (a), the total number of passive particles (b), the mean coordination numbers C_n (c), and C_n* (d) for the whole sample (A = 1.5 mm and Γ = 0.5).

The mean coordination number similarly varies and fluctuates around a value greater than 3 which is a good indicator of the "stable" character of the assemblage.

The number of passive particles varies in opposition to C_n. During the sample dilatation, it reaches one third of the total number of particles displaying the inelastic character of the assembly at the micro- scale of the grains. Indeed, the active state of that grains is not preserved during the whole cycle.

Figure 4-23 illustrates the variation of the number of passive particles in the sample for the 10th cycle of vibration. This number decreases with the depth due to the increase of the vertical stresses. The dilatation results in an increase of the number of passive particles, especially in the zone located near the free surface where the vertical stresses are limited. Actually, a lot of contacts, characterized by weak normal force, vanish during the dilatation, the grain settles on two contacts and displays a passive state. That can explain the difference between the elastic solution and the measured values for the ratio σ_{11}/σ_{22}.

The mean coordination number, C_n*, fluctuates with respect to the number of passive particles, as illustrated in Fig. 4-22d.

As illustrated in Fig. 4-24, there is no global destruction of the contact network during the 10th cycle of vibration.

Figure 4-25 illustrates the evolution of the force chains during the 10th cycle of vibration. The magnitude of the contact forces sinusoidally varies. They are maximal for N = 9.7 and 9.8 and minimal for N = 9.2 and 9.3. Secondary force chains vanish during the dilating phase of the cycle resulting in the increase of the number of passive particles. This matter of fact will be discussed in Section 4.2.1c.

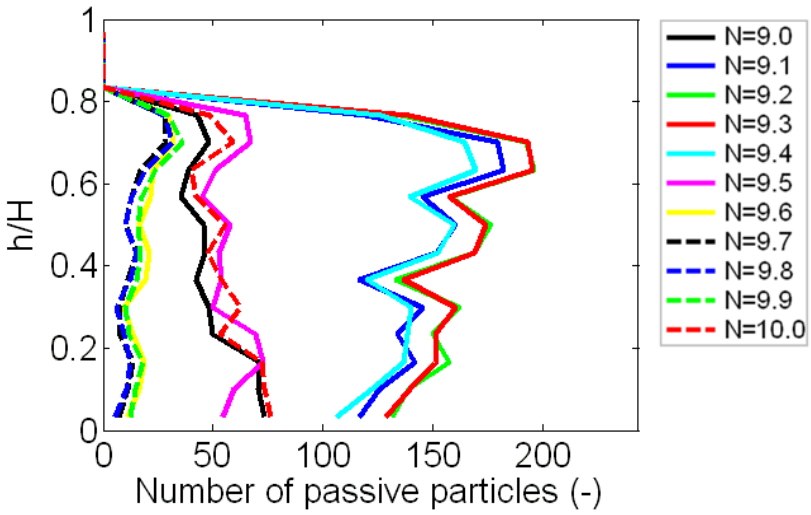

Figure 4-23. Passive particles in the sample for the 10th cycle of vibration (A = 1.5 mm and Γ = 0.5).

b. Coupled influence of the displacement and the frequency

Figures 7-30 to 7-36, presented in Appendix 7-7, illustrate the comparison between three simualtions performed at similar acceleration amplitude, $\Gamma = 0.5$ (-) for different displacement amplitudes (0.8, 1.5 and 2 mm).

No fundamental difference was observed between the simulation results leading to the significant conclusion that dimensionless acceleration amplitude, η_2, is the governing motion parameter of the vibrated granular material behavior at least for $\Gamma = 0.5$. There is no individual influence of the frequency or the displacement amplitude for T/T_0 included in the range [18 - 28].

c. Discussion of the results

Dilating and compacting phases

In the steady vibratory regime, there is a cyclic variation of the material properties. The porosity sinusoidally varies and there are successive compacting and dilating phases of the assembly during each cycle corresponding to upward ($\eta_2 > 0$) and downward acceleration of the container ($\eta_2 < 0$). In spite of the limited volume change (on the order of 1 ‰), a significant variation of the contact force magnitude is observed throughout the force chains.

Macroscopic elastic behavior of the vibrated granular assembly

In the steady vibratory regime, the granular sample expands and compacts but its state seems to be recovered, at the macroscopic scale, between each cycle of vibration. In Fig. 4-18 and 4-21, the curves of stresses and dimensionless kinetic energy superimpose for points which correpsonds to similar acceleration amplitude regardless of the downward or upward container displacement.

A difference is still noticed considering the evolution of the ratio σ_{11}/σ_{22} in Fig. 4-19. It is related to the changes occuring in the contact network during vibration.

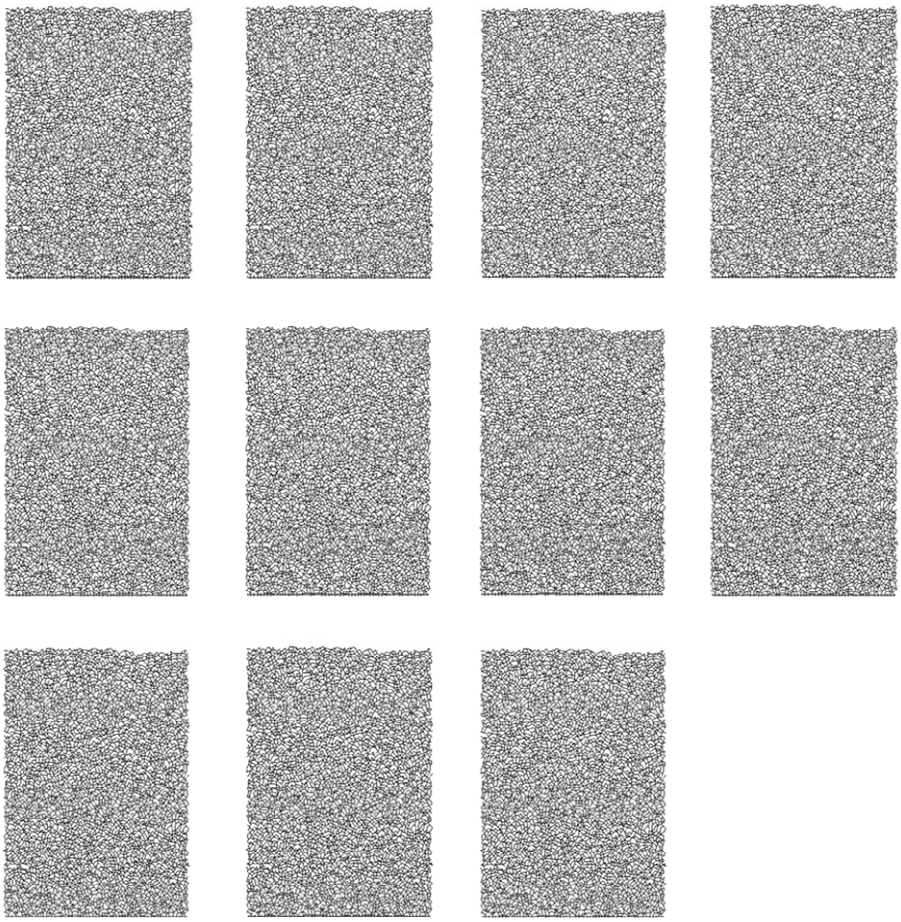

Figure 4-24: Conservation of the contact network during the 10th cycle of vibration (A = 1.5 mm and Γ = 0.5).

During the compacting part of the cycle, most of the particles contribute to the collective work taking part in the force chains. On the contrary, during the dilating phase, many particles become freer in the sense of the force chains and the number of passive particles swiftly increases.

In the steady vibratory regime, preferential or principal force chains are preserved during all the cycles. In addition, the onset of secondary force chains, which take place during the compacting phase and vanish during dilatation, is observed.

Preferential force chains are essential to the stress transmission throughout the granular sample.

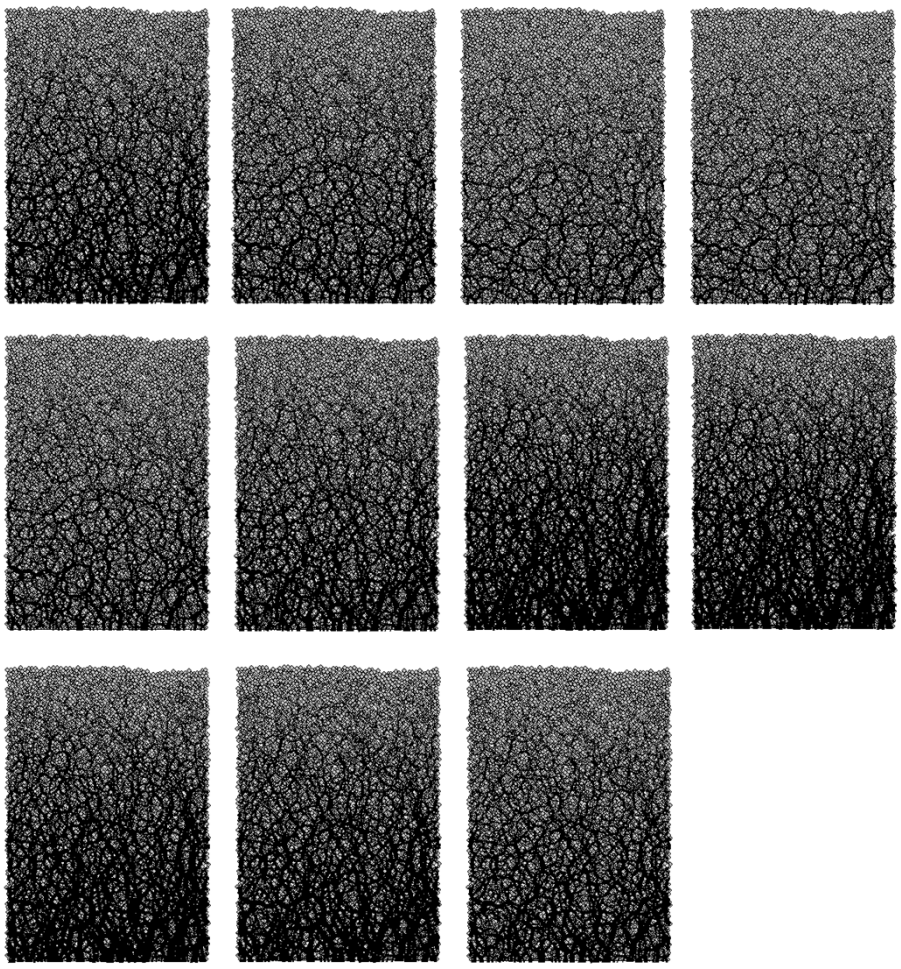

Figure 4-25: Evolution of the force chains during the 10th cycle of vibration (A = 1.5 mm and Γ = 0.5).

They are conserved during all the cycles of vibration and only varies in magnitude during the dilating or compacting phases of each cycle. They are represented by black lines in Fig. 4-25.

Conversely, secondary force chains can concern single contacts which are created between some particles when the assembly is compressed but their role is also to bring an additional support to the preferential force chains during the compacting phase of the cycle. Figure 4-26 illustrates the emergence of a secondary force chains resulting from the transformation of the grey-colored (dark-shaded) grain from a passive to an active state during the transition from the dilating to the compacting phase of the 10th cycle. The magnitude of the contact force created

during the compacting phase is very limited in comparison with the magnitude of the contact forces pertained to the principal force chains.

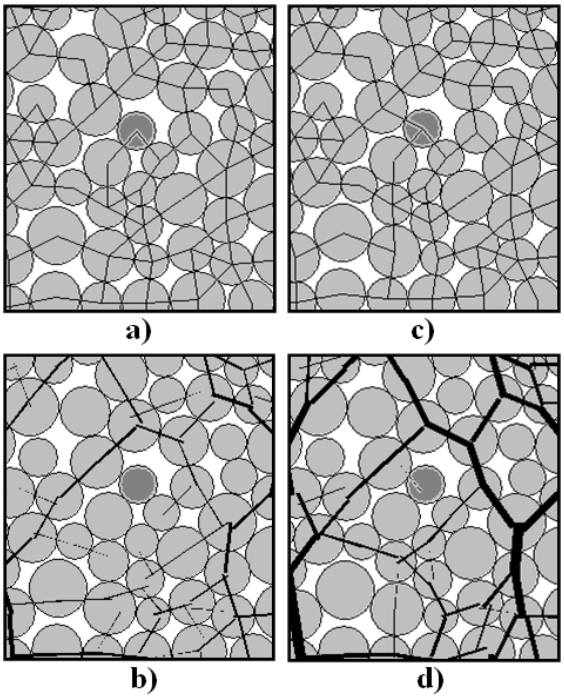

Figure 4-26: Emergence of a secondary force chain illustrated by the transformation of the grey colored (dark-shaded) grain from a passive to an active state. Contact network a) and force chains b) during the dilatation. Contact network c) and force chains d) during the compaction. Vibration performed at A = 1.5 mm and $\Gamma = 0.5$.

If a lot of contacts develop during the compacting phase of the cycle, the details of the contact network highlight the fact that some particles, which are active during the dilatation, become passive during the compaction. It is due to the emergence of "arches" in the granular structure which are caused by the increase of the contact normal forces between particles. But the occurrence of this phenomenon still remains limited in comparison with the outbreak of secondary force chains. Figure 4-27 illustrates this phenomenon with the transformation of the grey-colored (dark-shaded) grain from an active to a passive state during the transition from the dilatation to the compaction of the sample. The arch is distinctly visible in Fig. 4-27d where the force chains prevent the grain from contributing to the transmission of the external forces. As observed in Fig. 4-27b, the intensity of the initial contact force applying to the grey-colored grain is weak and is not included in a principal force chain.

Moreover, the physics of the contact is modelled with the help of elastic stiffness, viscous damping and friction coefficient. Any sliding motion occuring between contacting particles will lead to energy loss and to inelasticity at the contact scale. As a perspective, it will be interesting to compute the sliding fraction of contacts in the sample during vibration.

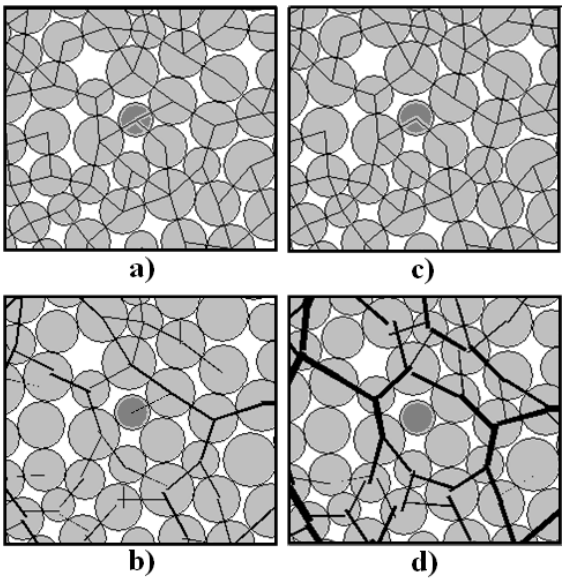

Figure 4-27: Emergence of an arch illustrated by the transformation of the grey colored (dark-shaded) grain from an active to a passive state. Contact network a) and force chains b) during the dilatation. Contact network c) and force chains d) during the compaction. Vibration performed at A = 1.5 mm and $\Gamma = 0.5$.

The transition between active and passive states for several particles and the sliding contact fraction are therefore the principal causes of the inelasticity of the system which still remains restrained at the microscopic scale of the grains.

Hence, in a first approximation, it can be considered that in the steady vibratory regime, the granular assembly behaves like an elastic solid, at the macroscopic scale.

From micro- to macroscopic scale

The distribution of contact orientation and the angular distribution of normal and tangential contact forces are well approximated by the analytical expressions (4-27), (4-28) and (4-29) proposed by Rothenburg and Bathurst (1989). Figure 4-28 illustrates this comparison with the measured values represented by black lines and the analytical expressions by red lines in the steady vibratory regime.

Figure 4-29 illustrates the evolution of the directions of contact, average normal contact force and average tangential contact force anisotropy during vibration. Except for a short part of each cycle for the direction of tangential contact force, θ_a, θ_f and θ_t remain close to 0°.

Figure 4-30 presents the variation of the anisotropy coefficients a, a_n and a_t during the vibration and the deduced mobilized friction angle, ϕ_{mob}, computed on the basis of the equation (4-31). a, a_n, a_t and ϕ_{mob} increase when the vertical stress σ_{22} increases, i.e. during the compacting phase.

The connection from micro- to macro- has been performed. Microstructural parameters (a, a_n, a_t) are related to the measure of deviatoric load by considering the evolution of the mobilized friction angle.

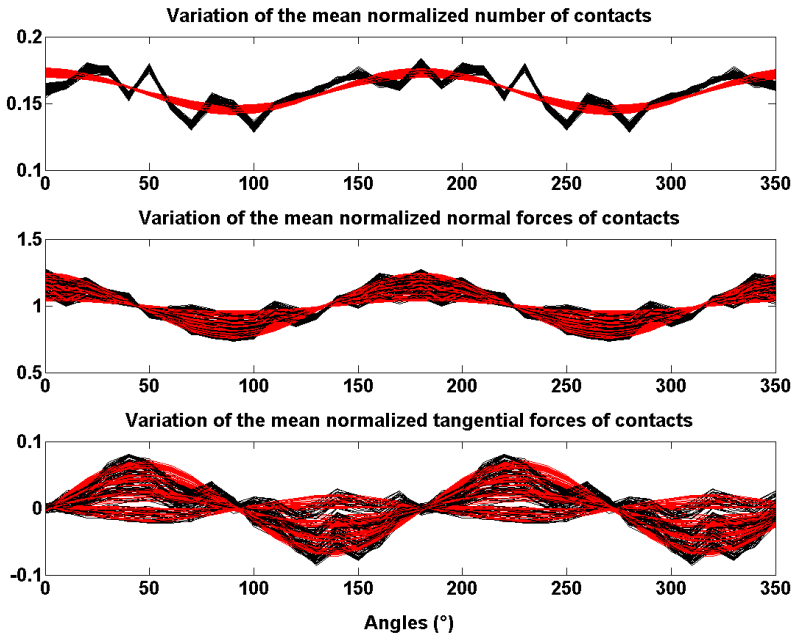

Figure 4-28: Characteristics of fabric of the numerical assembly in steady vibratory regime (A = 1.5 mm and Γ = 0.5).

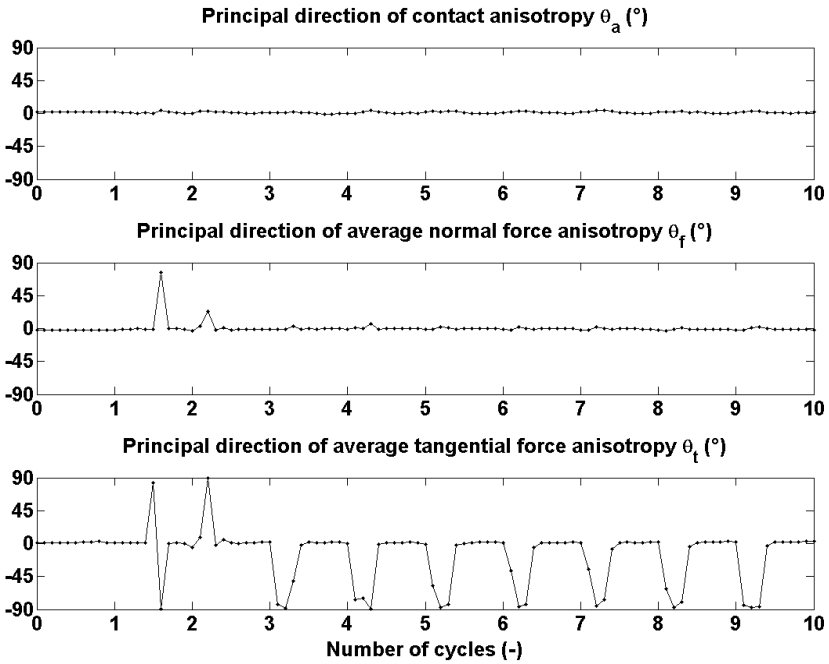

Figure 4-29: Principal directions of contact, average normal contact force and average tangential contact force anisotropy during the vibration (A = 1.5 mm and Γ = 0.5).

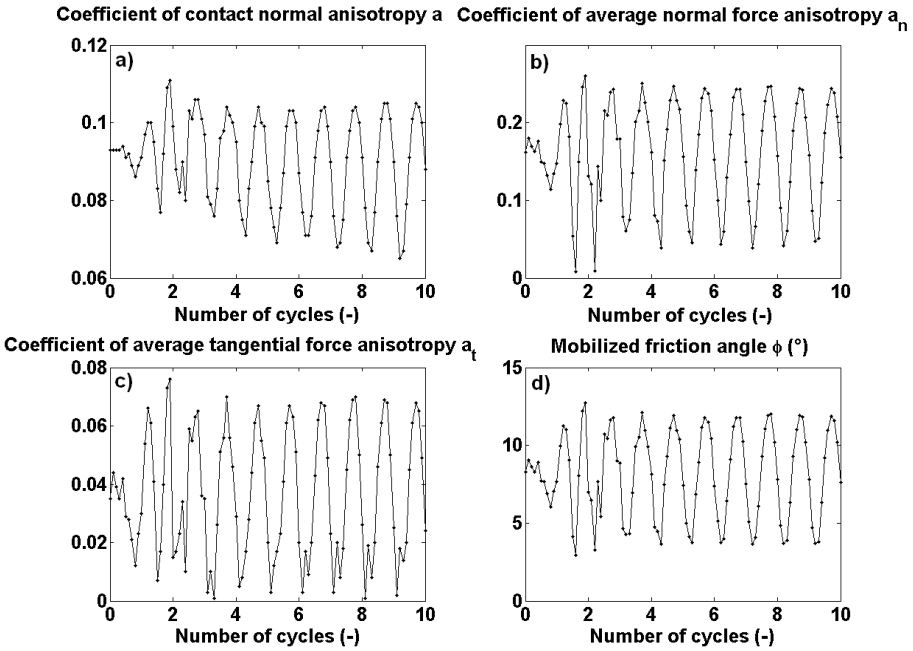

Figure 4-30: Relationships between the number of cycle and the coefficient of contact normal anisotropy, a (a), the coefficient of average normal force anisotropy, a_n (b), the coefficient of average tangential force anisotropy, a_t (c) and the mobilized friction angle, ϕ_{mob} (d).

The analysis of the contact orientation is made possible by the conservation of the contact network. Nevertheless, this technique is very sensitive to the contact stability. Even if the contact network is preserved during the vibration, slips can momentarily occur at contacts leading to an instability in the measurement of the contact orientation and of the contact force angular distributions. Moreover, some contacts are not preserved during the whole cycle. Hence, quasi-static conditions of contact are not ensured. The analysis of the fabric characteristics must be therefore considered with caution.

Mobilized angle of friction

Figure 4-31 illustrates the comparison between the mobilized friction angle, ϕ_{mob}, deduced from the stress-force-fabric relationship (black line), the friction angle computed on the basis of the measurement of the contact stresses in each measurement layer (continuous grey lines) and the friction angle calculated with the help of the Jaky formula (dashed grey line).

The stress-force-fabric relationship (4-31) connects microstructural characteristics of the assembly anisotropy with the level of deviatoric load. The mobilized friction angle is calculated with the help of the anisotropy coefficients.

It is possible to compute a mobilized friction angle in each measurement layer of the granular sample with the help of the following relationship:

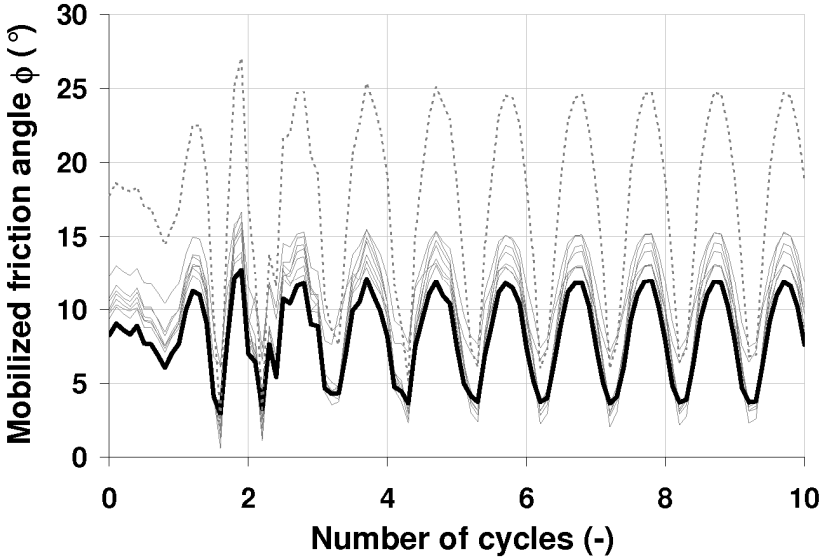

Figure 4-31: Variation of the mobilized friction angle, ϕ_{mob}, during the vibration. The black line, the continuous grey lines and the dashed grey line are respectively computed on the basis of the stress-force-fabric relationship, the measurement of the stress field in the layers and the Jaky formula.

$$\sin\phi_{mob} = \frac{2\sqrt{\left(\frac{\sigma_{22}-\sigma_{11}}{2}\right)^2 + \sigma_{12}^2}}{\sigma_{22}+\sigma_{11}} \qquad \text{(Eq. 4-46)}$$

considering that θ_a is the prefered direction for average forces and verifying it is close to the vertical direction (see Fig. 4-29). The contact stresses, σ_{ij}, are computed as explained in Appendix 7.6.

The empirical formula of Jaky considers the earth pressure coefficient, K_0:

$$K_0 = 1 - \sin\phi_{mob} \qquad \text{(Eq. 4-47)}$$

The mobilized friction angle is calculated considering the variation of the ratio σ_{11}/σ_{22} instead of the earth pressure coefficient, as illustrated in Fig. 4-19.

As a first result, the curve of mobilized friction angle computed on the basis of the stress-force-fabric relationship seems to approach with accuracy the different values of ϕ_{mob} calculated in each layer of the sample using equation (4-46). The differences between the continuous grey curves are mainly due to the action of the gravitational field. In the approach of Rothenburg and Bathurst (1989), the influence of this latter is removed from the analysis (Section 4.1.4c).

There is a significant difference between these results and the mobilized friction angle deduced from the Jaky formula. Nevertheless, according to Hendron (1963), it could be due to the fact that the Jaky formula has an empirical origin based on observations performed on real three-dimensional granular material, as sand grain assembly, where particles are characterized by an aspherical morphology.

The bidimensional character of the simulations and the circular shape of the particles cannot be neglected. Both play a major role in the way the results must be interpreted. The comparison with the Jaky formula becomes therefore irrelevant.

4.2.2 Vibro-fluidization of vibrated granular matter

a. Evolution of the internal state during vibration

At the macroscopic scale of the assembly

Once, the numerical sample is subjected to high dimensionless acceleration amplitude, $\Gamma = 1.02$ or $\Gamma = 2$, vibro-fluidization is noticed in both cases.

Figure 4-32 illustrates the porosity variation in the sample during the vibration at $\Gamma = 1.02$. The caption corresponds to the altitudes of the different measurement layers.

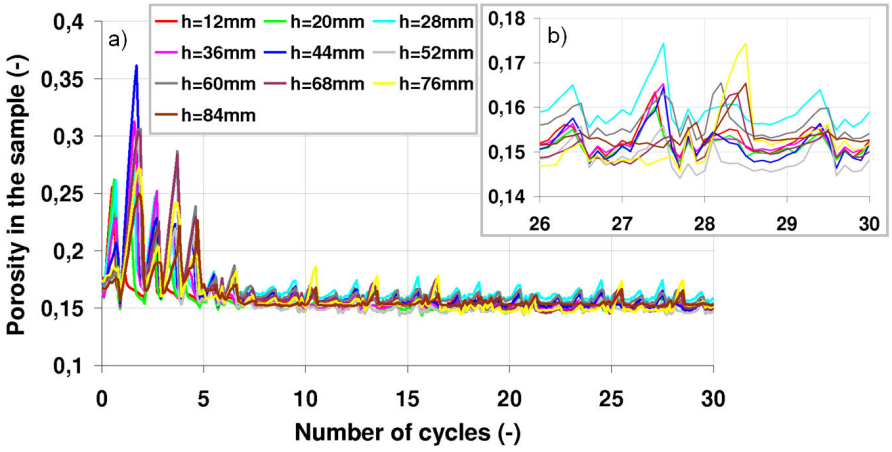

Figure 4-32: a) Porosity variation in the measurement layers of the granular sample during the vibration (A = 1.5 mm and $\Gamma = 1.02$), b) enlargement of the curves in the steady vibratory regime.

Once the numerical sample is vibrated at $\Gamma = 1.02$, there is a transient phase with a strong porosity variation in the assembly characterized by the propagation of a dilatation wave from the bottom to the free surface of the sample. It is clearly visible during the 2nd cycle of vibration, as illustrated in Fig. 4-33a. After ten cycles, the sample seems to reach a steady vibratory regime but the volume change still presents a more chaotic character as compared with the elastic range, for $\Gamma = 0.5$.

In the steady vibratory regime, the porosity variations are contained in a confined range (on the order of 2 %), as illustrated in Fig. 4-33b. The principal dilating phase corresponds to the downward acceleration phase ($\eta_2 < 0$).

When the sample is vibrated at $\Gamma = 2$, strong porosity variations are observed in the assembly. No steady vibratory regime is reached after 30 cycles. As illustrated in Fig. 4-34, the porosity spreads on a range of 30 %. The granular sample displays high dilating behavior. The length of the dilating phases varies. It can extend on one or two cycles, as observed in the inset of Fig. 4-34, where the

sequence of the cycles 26 to 29 is considered representative of the granular material behavior.

The way the porosity varies during vibration results in different particle velocity field in the sample.

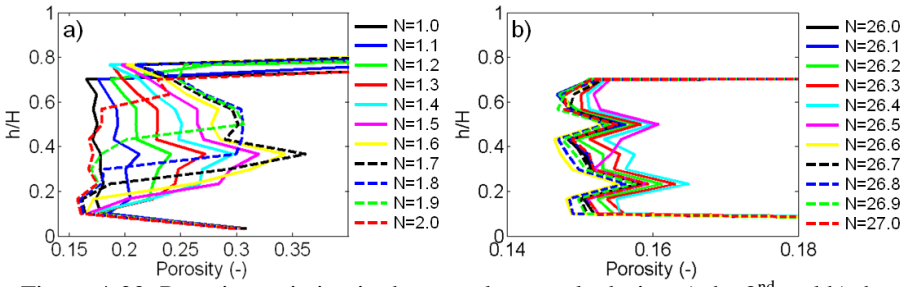

Figure 4-33: Porosity variation in the granular sample during a) the 2nd and b) the 27th cycles of vibration (A = 1.5 mm and Γ = 1.02).

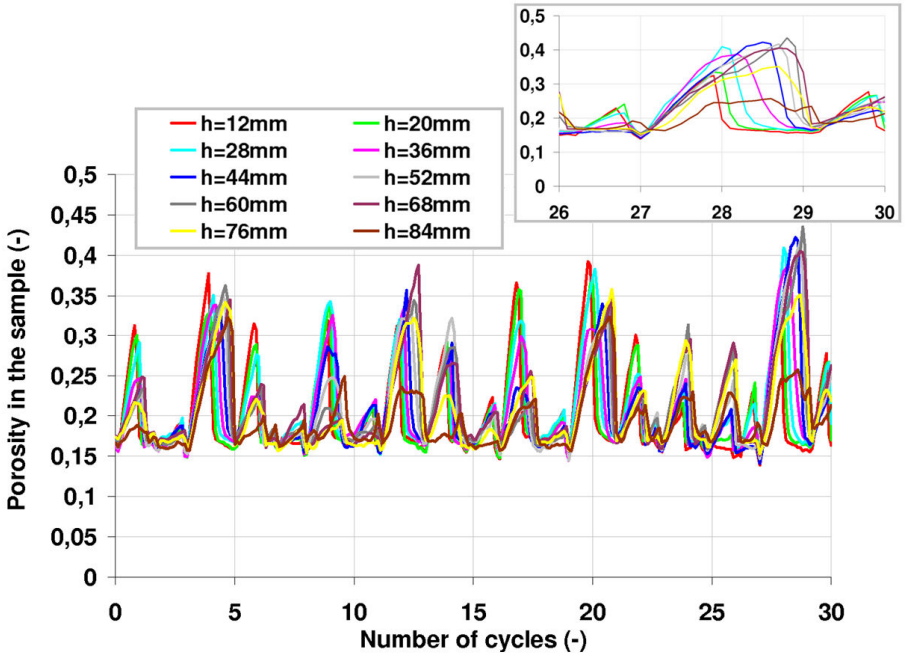

Figure 4-34: Porosity variation in the measurement layers of the granular sample (A = 1.5 mm and Γ = 2). Inset: enlargement of the curves.

Figure 4-35 displays the continuous character of the particle velocity field in the granular sample during the 27th cycle of vibration for A = 1.5 mm and Γ = 1.02. The grey arrows highlight the different trends. Figure 4-36 illustrates the vertical displacement of the grains during this cycle. A positive displacement corresponds to an upward motion of the grain. u_2^b defines the vertical particle location at the beginning of the cycle. The dashed grey lines represent the displacement imposed to the container bottom.

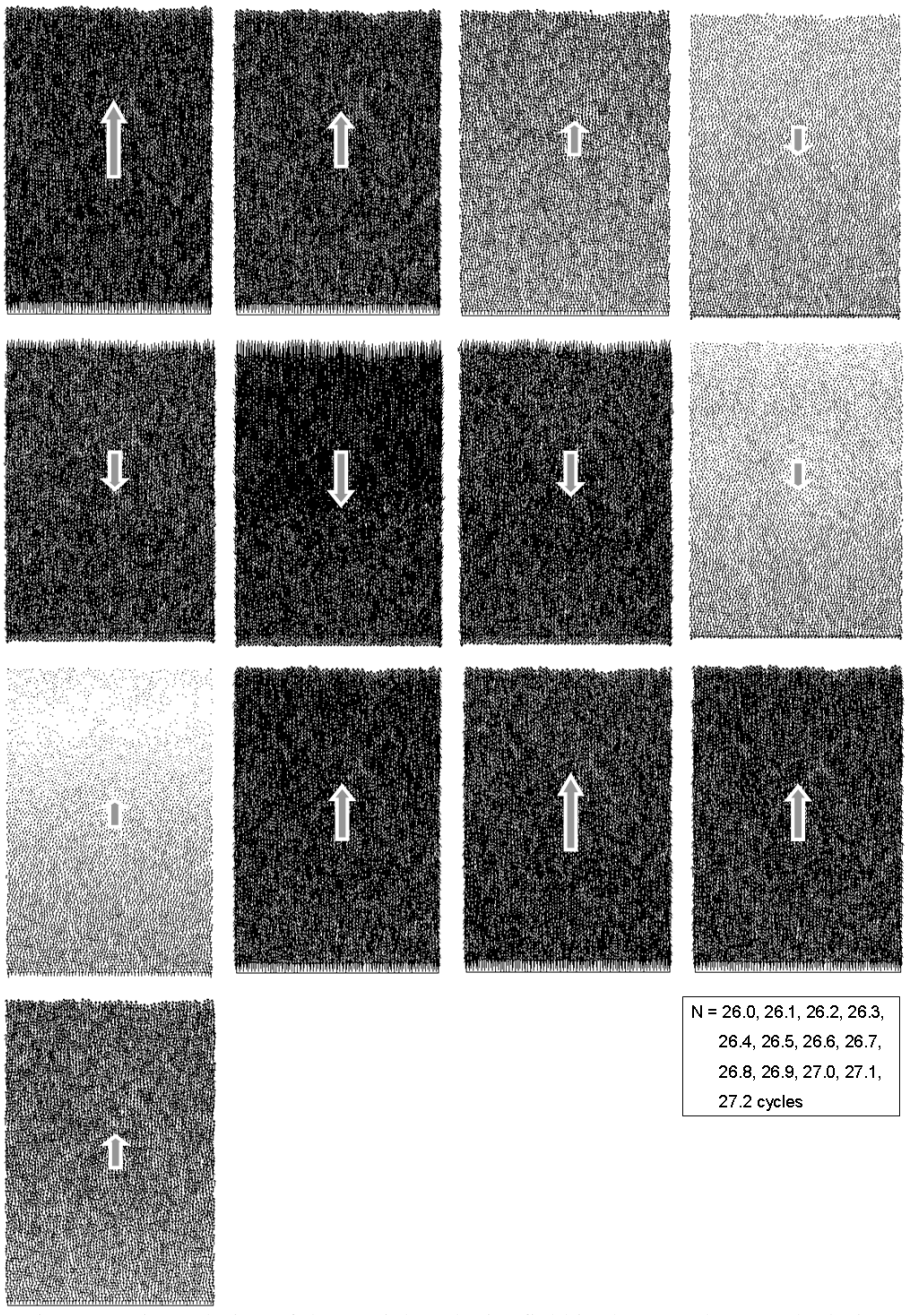

Figure 4-35: Evolution of the particle velocity field in the granular sample during the 27th cycle of vibration (A = 1.5 mm and Γ = 1.02).

During the downward acceleration phase ($\eta_2 < 0$), the particles are first pushed up by the rigid bottom of the container which is uprising ($A_2 > 0$).

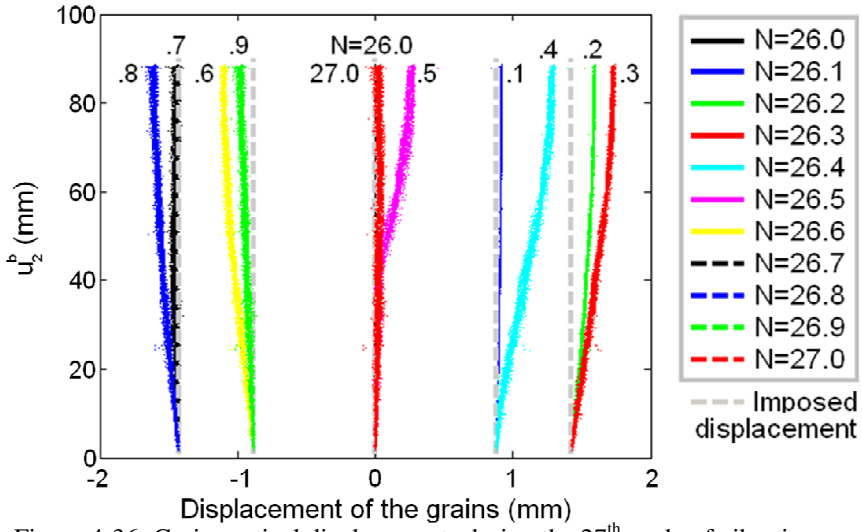

Figure 4-36: Grain vertical displacements during the 27th cycle of vibration (A = 1.5 mm and Γ = 1.02).

Figure 4-36 illustrates the progressive dilatation of the granular sample at N = 26.1 and N = 26.2. The energy is brought in the system at the container bottom and it continuously propagates upward in the sample. The particles transmit momentum to the surrounding upper particles. The grain displacements increase near the free surface where particles are freer to move because of the vertical stress decrease. They display vertical displacements higher than the vertical imposed displacement, A_2, and higher than the vertical displacement of a single particle subjected to similar vibration, as illustrated in the conclusion of this Chapter. Thus, there is an amplification effect. The introduced energy is sufficient to dilate the sample in spite of the energy loss due to the viscous damping model of contact. The particles are subjected to such vibration that they dilate the whole sample in such a way this latter can be characterized by a short-lived suspension of its constituents.

Between N = 26.2 and N = 26.3, the grains become in suspension under the gravitational field. They become passive with respects to the force chains. Then, the particles cannot fully follow the downward motion of the container and go into free-fall.

The falling grains begin to reach the container bottom at N = 26.4. Afterwards, the granular sample compacts during the upward acceleration phase of the cycle ($\eta_2 > 0$). A global settlement is observed in Fig. 4-36. In the upper part of the sample, the particles display higher downward motion mainly due to the accumulated downward displacements of the subjacent particles. At the end of the cycle, the sample goes back to a situation closer to its initial state.

Figures 4-37, 4-38 and 4-39 illustrate the particle velocity field for the 27th, 28th and 29th cycles of vibration for A = 1.5 mm and Γ = 2. The grey arrows highlight the different trends. Figure 4-40 illustrates the porosity variation in the sample during the 27th, 28th and 29th cycles. High-dilating behavior is observed during the 28th cycle.

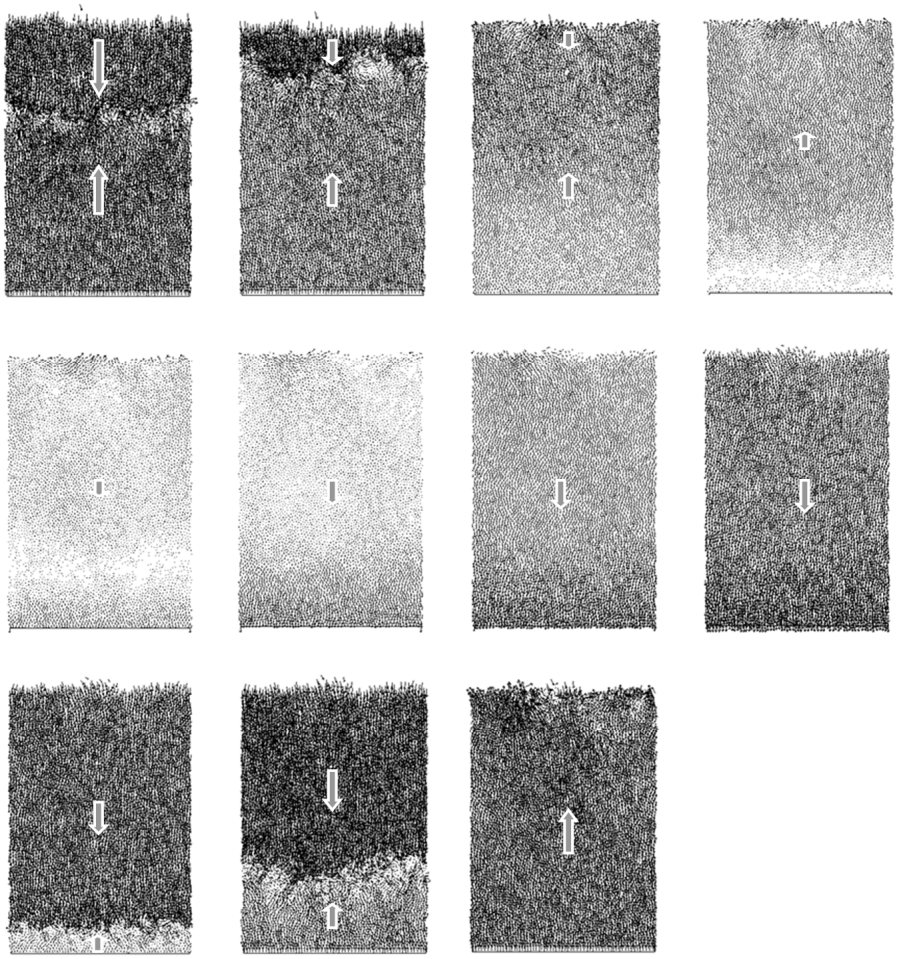

Figure 4-37: Evolution of the particle velocity field during the 27th cycle of vibration (A = 1.5 mm and Γ = 2).

In the course of the vibration, the granular assembly is so dilated that discontinuities begin to develop in the velocity field contrary to the continuous field displayed at 1.02g. These discontinuities are due to the successive impacts of the particles with the container bottom combined with the effect of the gravitational field.

The particles are subjected to such vibration that they dilate the whole sample in such a way it can be characterized by a long-range suspension of its constituents. The granular motion does not display a cyclic pattern contrary to the pattern, observed at 1.02g. Additionally, grain saltation is observed at the free surface.

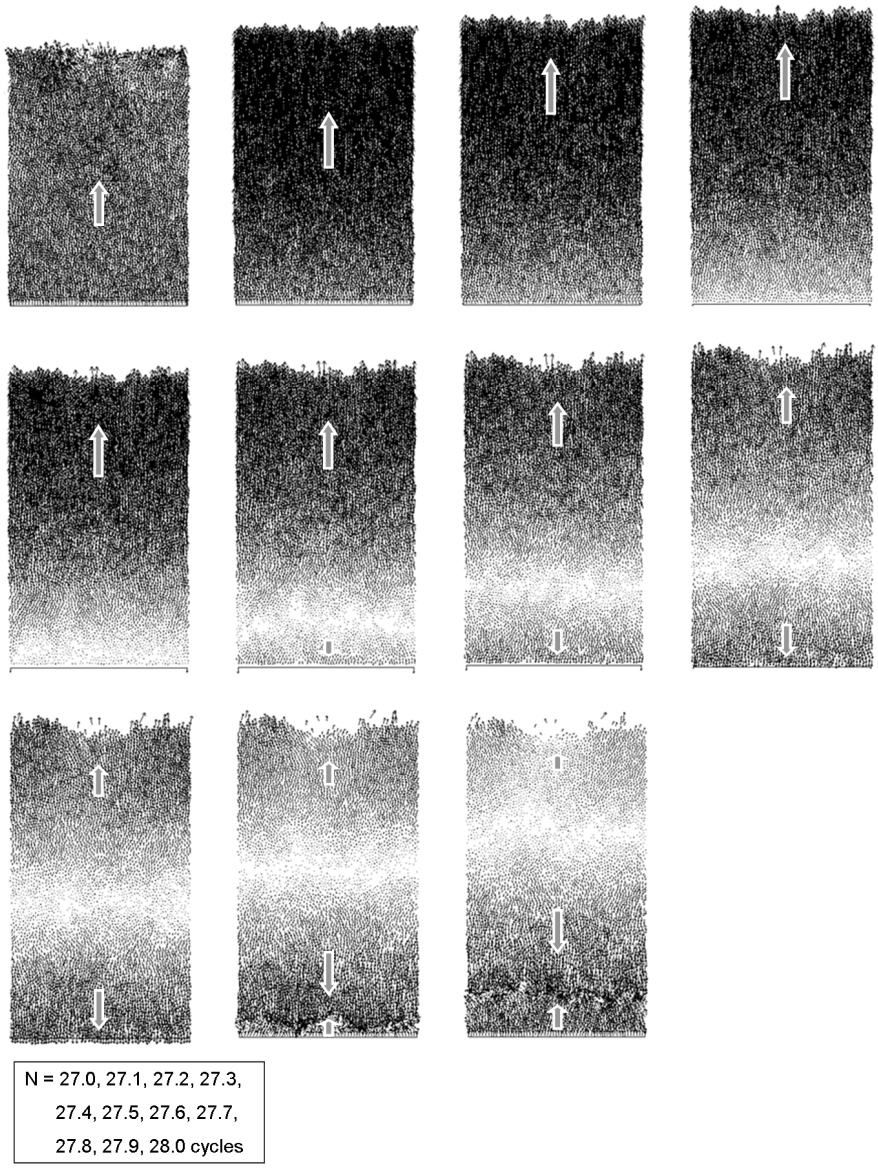

Figure 4-38: Evolution of the particle velocity field during the 28th cycle of vibration (A = 1.5 mm and $\Gamma = 2$).

Figure 4-41 focuses on the vertical stress, σ_{22}, in the granular sample during vibration respectively at $\Gamma = 1.02$ and $\Gamma = 2$.

At $\Gamma = 1.02$, the vertical stresses display a cyclic response to the vibration. During the downward acceleration phase ($\eta_2 < 0$), they vanish, at least once per cycle, in the whole sample. Similar observations can be made for the horizontal stress, σ_{11}. It testifies to the extensive vibro-fluidization of the granular material.

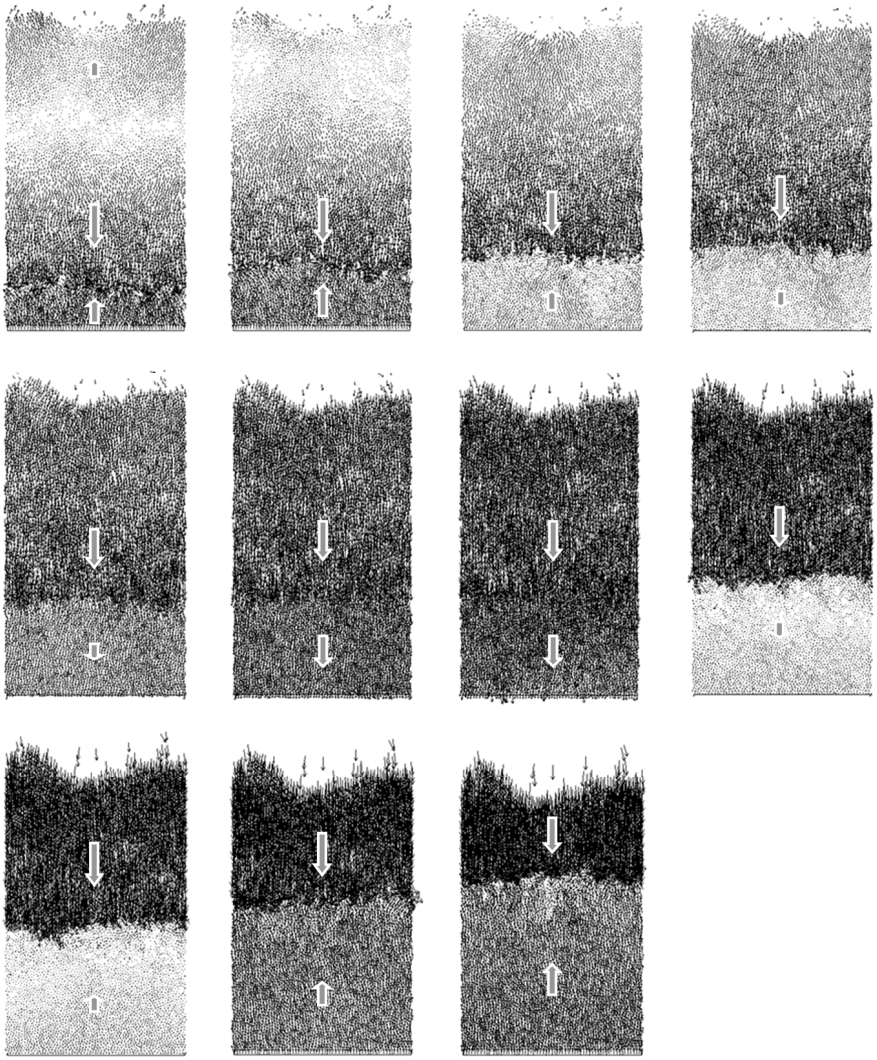

Figure 4-39: Evolution of the particle velocity field during the 29th cycle of vibration (A = 1.5 mm and $\Gamma = 2$).

Due to the absence of lateral rigid boundaries, σ_{12} and σ_{21} still remain close to zero during the vibration. During the upward acceleration phase ($\eta_2 > 0$), the vertical stress oscillates, as illustrated in the inset.

At $\Gamma = 2$, the vertical stresses periodically degrade but they do not present a cyclic degradation. They can vanish during several cycles. Horizontal stresses similarly behave. σ_{12} and σ_{21} remain close to zero during the vibration.

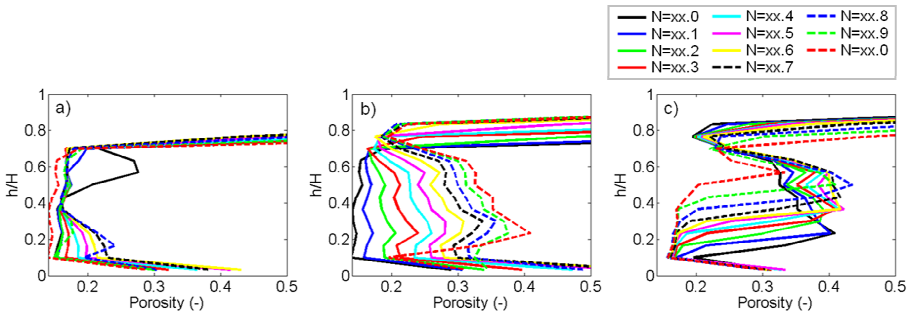

Figure 4-40: Evolution of the porosity in the measurement layers of the granular sample during a) the 27th, b) the 28th and c) the 29th cycle of vibration (A = 1.5 mm and Γ = 2).

Figure 4-42 displays the evolution of the vertical stresses in the granular material during the studied cycles of vibration.

At Γ = 1.02, the destruction of the stress field is observed during the downward acceleration phase of the cycle (N = 26.1 to 26.4). The vertical and horizontal stresses are close to zero. Then, there is a rapid increase of the stresses (N = 26.5 and N = 26.6).

Afterwards, σ_{11} and σ_{22} oscillate (N = 26.7 to N = 27.0) before once again vanishing during the first part of the 28th cycle. The way the degradation occurs varies from one cycle to another but the result is always the same: the full destruction of the stress field in the granular sample.

At Γ = 2, the assembly displays a more complex behavior and the stress field can vanish during the whole cycle, as illustrated in Fig. 4-42c.

Figure 4-43 illustrates the evolution of the total dimensionless kinetic energy during the vibration. Figure 4-44 investigates the studied cycles of vibration.

The curves, corresponding to the phase during which the granular material is vibro-fluidized, display high values of dimensionless kinetic energy. These values are much higher than in the solid range where the force chains predominate on the dynamic character of the particles. When the dimensionless kinetic energy is close to the unity, the action of the kinetic energy is balanced by the development of the vertical stresses in the sample.

As a first observation, dimensionless kinetic energy seems to be a good indicator of the vibro-fluidization. Nevertheless, the way the kinetic energy varies in the sample is hidden by the fact that vertical stresses are close to zero during vibro-fluidization. As a perspective, kinetic energy could be adimensionalized by mgd_{50}, where m would be an averaged value for the grains of the measurement layer.

At the microscopic scale of the grain

Figure 4-45 describes the evolution of the contact density properties during the vibration at Γ = 1.02. Figure 4-46 represents this evolution in the steady vibratory regime. During the downward acceleration phase ($\eta_2 < 0$), cyclic degradation of the contact number is observed. At that time, nearly all particles become passive. It is possible that it occurs during each cycle of vibration but the measurement discretization prevent us to extend this observation to all the cycles. The coordination number tends to zero once per cycle. That result highlights the cyclic degradation of the contact network.

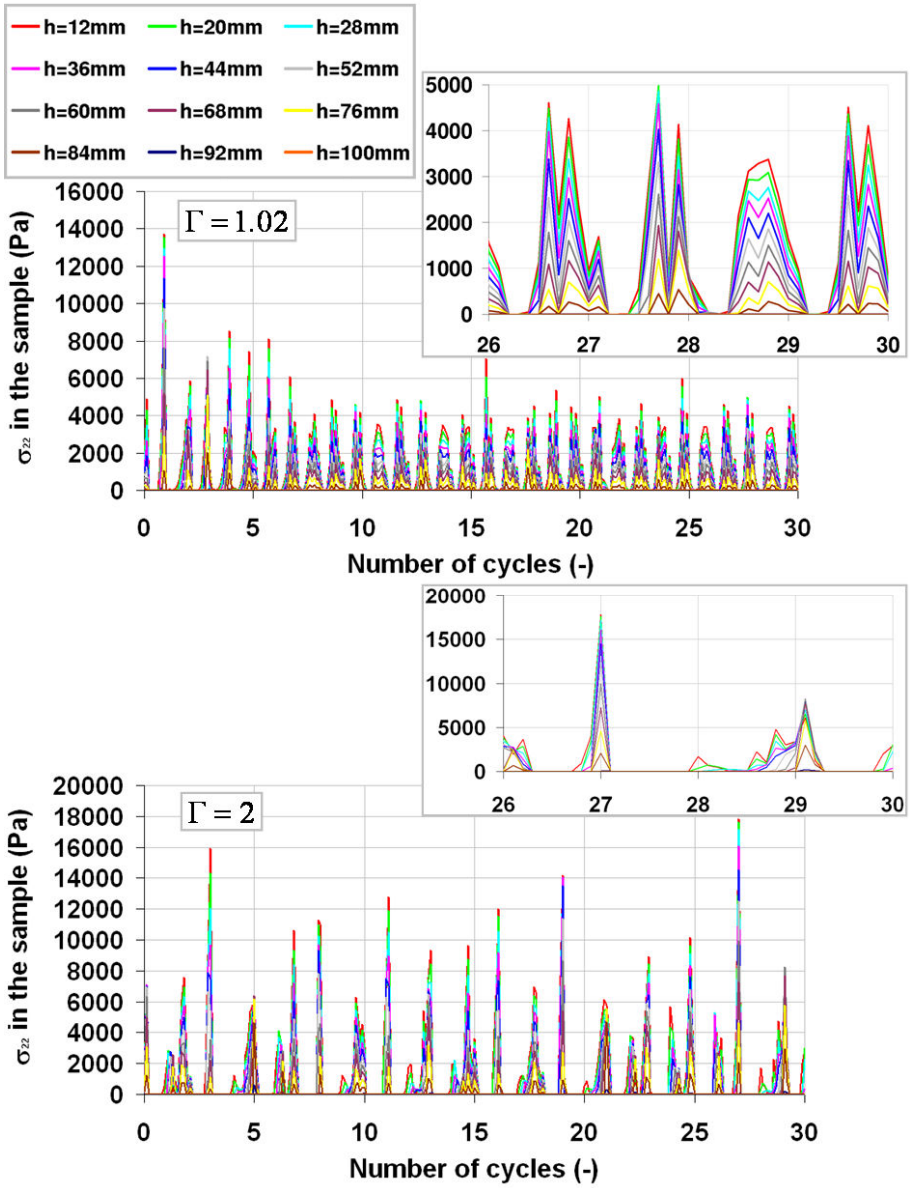

Figure 4-41: Evolution of the vertical stresses, σ_{22}, in the measurement layers of the granular sample at $\Gamma = 1.02$ and $\Gamma = 2$. Inset: enlargement of the curves.

As the passive particles include the particles settled on two contacts and the particles in suspension, it is proposed to only conserve the coordination number C_n for the description of the contact network.

Figures 4-47 and 4-48 respectively illustrate the evolution of the contact network and the force chains, in the steady vibratory regime, during the 27th cycle of vibration at $\Gamma = 1.02$. The first points of the 28th cycle are also represented to underline the cyclic behavior of the sample.

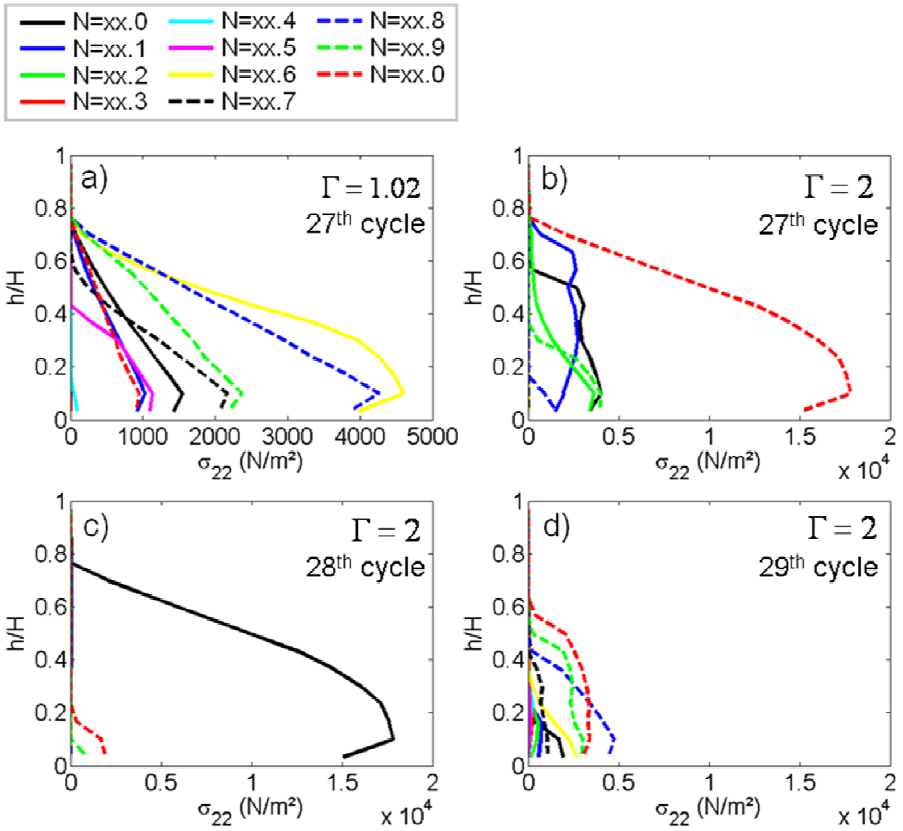

Figure 4-42: Evolution of the vertical stress in the numerical sample during the 27th cycle of vibration for A = 1.5 mm and Γ = 1.02 (a), and during the 27th (b), the 28th (c) and the 29th (d) cycle of vibration for A = 1.5 mm and Γ = 2.

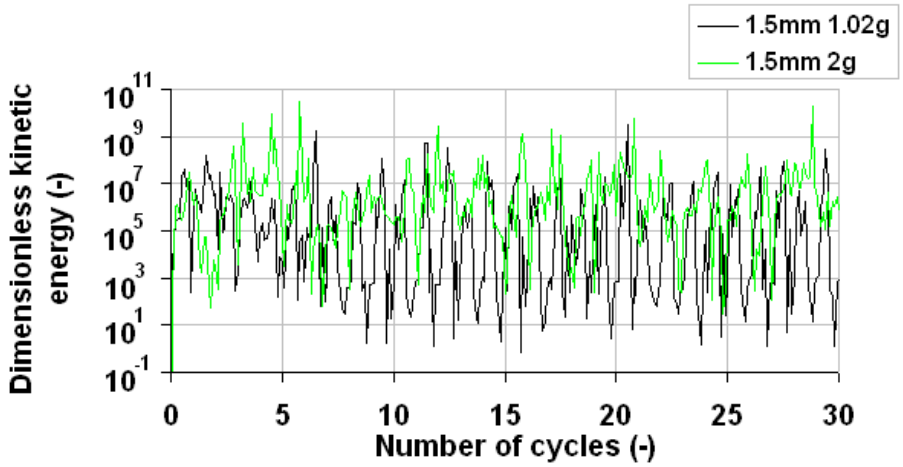

Figure 4-43: Total dimensionless kinetic energy in the sample during the vibration at Γ = 1.02 and Γ = 2.

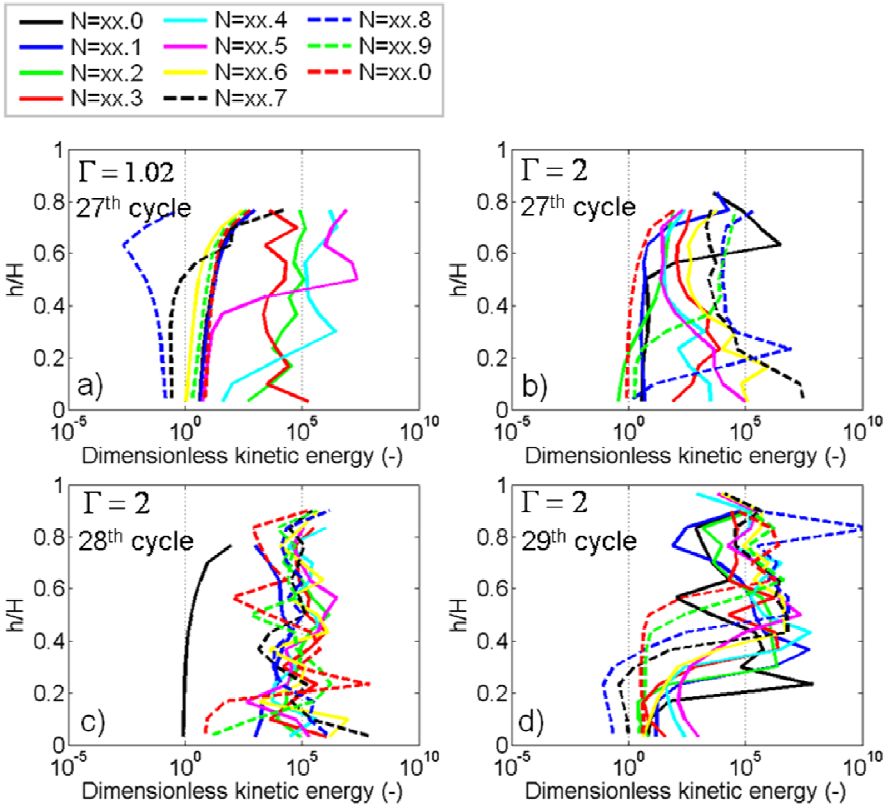

Figure 4-44: Evolution of the dimensionless kinetic energy in the numerical sample during the 27th cycle of vibration for A = 1.5 mm and Γ = 1.02 (a), and during the 27th (b), the 28th (c) and the 29th (d) cycle of vibration for A = 1.5 mm and Γ = 2.

The contact network is strongly degraded during the sample dilatation ($\eta_2 < 0$). That leads to a collapse of the contact number simultaneously accompanied with the emergence of a lot of passive particles, as illustrated in Fig. 4-49a and 4-49b. The coordination number is close to zero everywhere in the sample, as observed in Fig. 4-49c. Hence, no contact stress can develop in the sample wherein the force chains are fully destroyed, that corresponds to the fully vibro-fluidized state.

When the grains reach the container bottom (at N = 26.4), the contact network is progressively restored from the bottom of the granular sample. It is accompanied with the increase of the coordination number, C_n, in the sample and the simultaneous decrease of the number of passive particles, as illustrated in Fig. 4-49.

Actually, when the particles impact the bottom of the container, a stress wave emerges. It can propagate only in the part of the sample wherein the contact network is once again established. Because the ratio T/T_0 equals 17.09, the propagation velocity of the stress wave in the medium is higher than the restoration velocity of the contact network. Hence, the stress wave swiftly propagates in the "solid" part of the granular material and reflects on the climbing free surface resulting in an oscillating behavior of the assembly marked by the stress variations during the compacting phase ($\eta_2 > 0$).

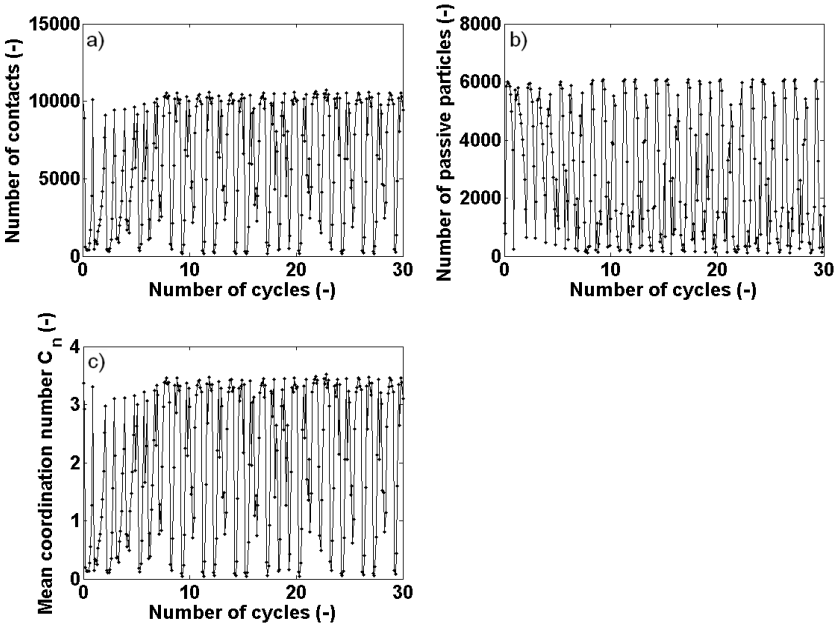

Figure 4-45: Relationships between the number of cycles (0 - 30) and the total contact number (a), the total number of passive particles (b) and the mean coordination number C_n (c) for the whole sample (A = 1.5 mm and Γ = 1.02).

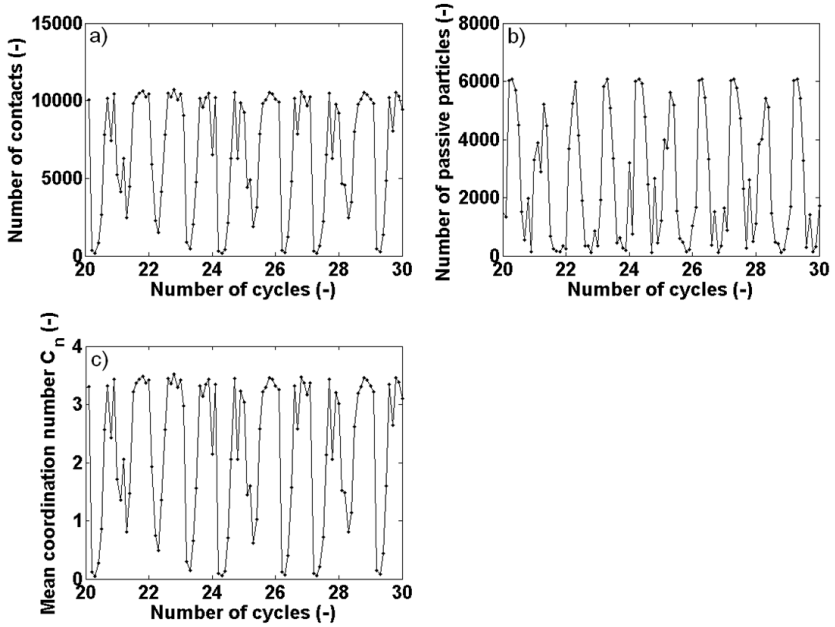

Figure 4-46: Relationships between the number of cycles (20 - 30) and the total contact number (a), the total number of passive particles (b) and the mean coordination number C_n (c) for the whole sample in the steady vibratory regime (A = 1.5 mm and Γ = 1.02).

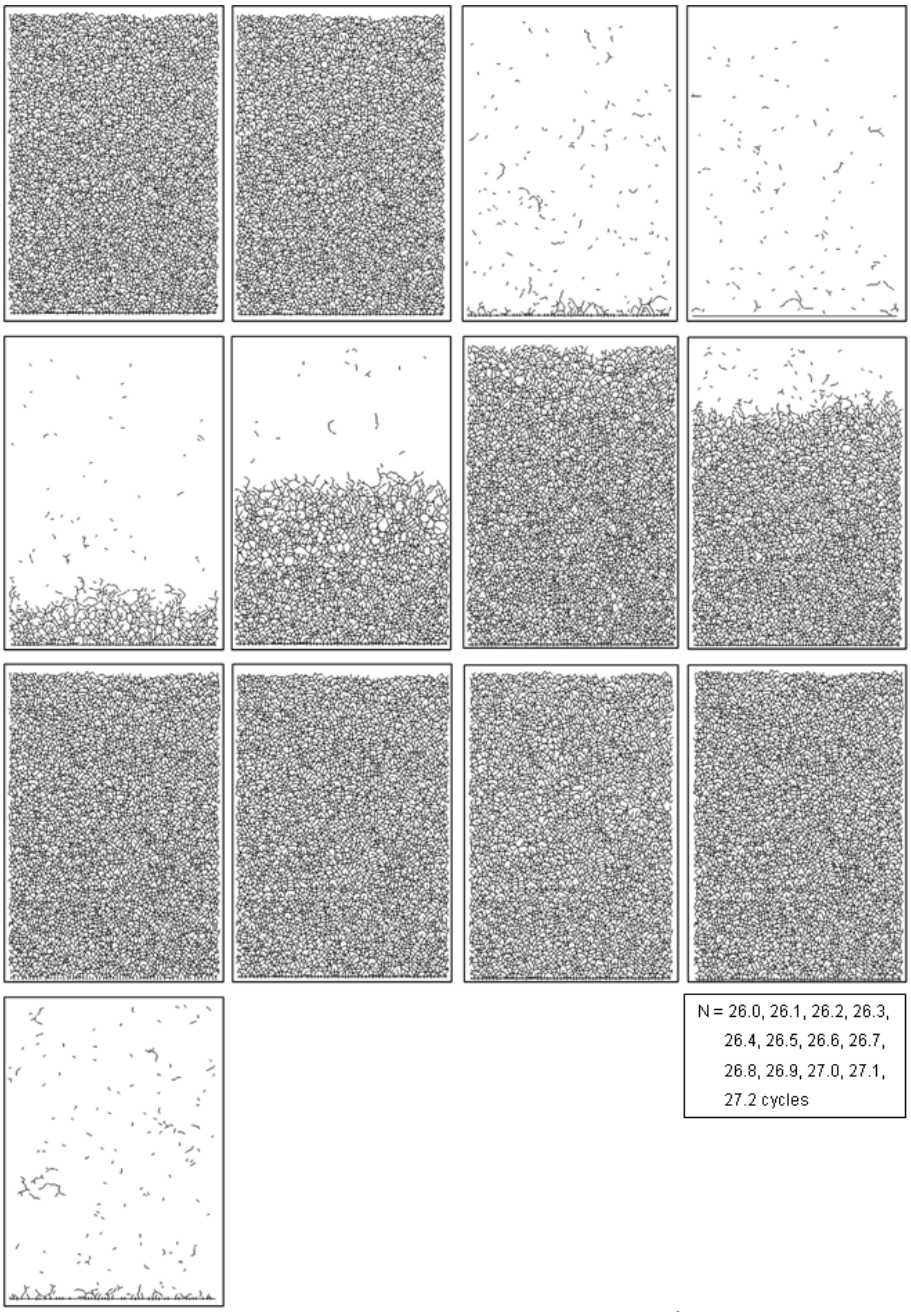

Figure 4-47: Evolution of the contact network during the 27th cycle of vibration (A = 1.5 mm and Γ = 1.02).

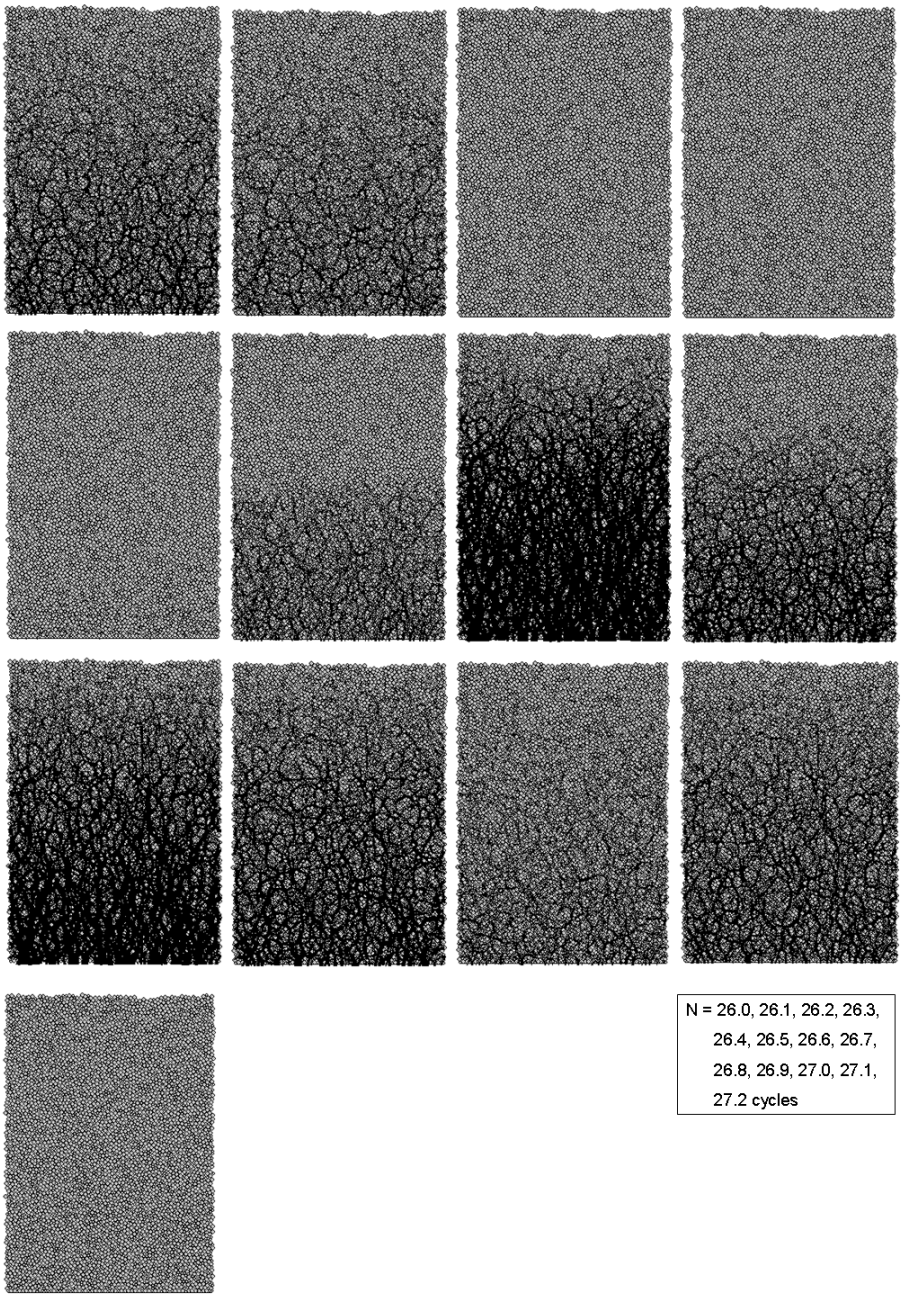

Figure 4-48: Evolution of the force chains during the 27th cycle of vibration ($A = 1.5$ mm and $\Gamma = 1.02$).

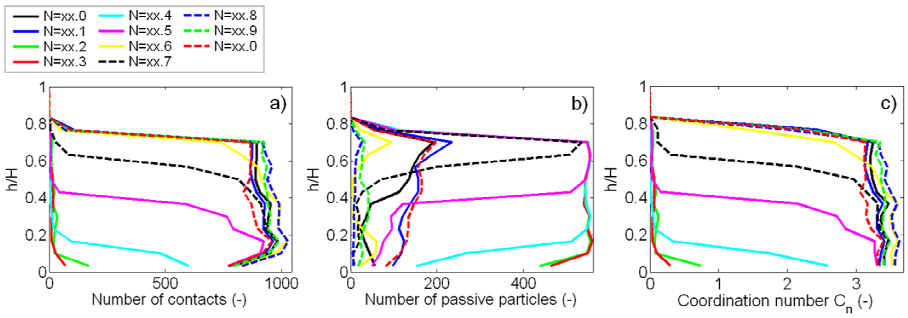

Figure 4-49: Evolution of a) the contact number, b) the number of passive particles and c) the coordination number, C_n, in the numerical sample during the 27th cycle of vibration (A = 1.5 mm and Γ = 1.02).

Considering the first points of the 28th cycle, there is a new degradation of the granular skeleton. This cyclic behavior was observed for all cycles of vibration in the steady vibratory regime, at Γ = 1.02.

Figure 4-50 describes the evolution of the contact density properties during the vibration at Γ = 2. Figure 4-51 represents this evolution during the cycles 26 to 30. The periodic degradation of the coordination number, C_n, corresponds to the dilating phases identified in Fig. 4-34. The phases, during which the contact network is not degraded, are very limited.

The curves of Fig. 4-51 present reversed appearance in comparison with the curves of Fig. 4-46. At Γ = 2, the coordination number remains close to zero during a major part of the cycle.

Figures 4-52, 4-53 and 4-54 illustrate the evolution of the contact network during the 27th, 28th and 29th cycles of vibration for A = 1.5 mm and Γ = 2. Figures 4-55, 4-56 and 4-57 represent the evolution of the force chains and figure 4-58 the evolution of the number of passive particles during the same cycles.

During the 27th cycle, force chains get unbound. Several contacts are still observed, in Fig. 4-52, in the upper part of the sample but they correspond to impacts and do not result in the development of force chains throughout the sample. At the end of the cycle, the contact network is momentarily restored.

During the 28th cycle, the granular sample displays high dilating behavior resulting in the degradation of the contact network and the force chains during the whole cycle. Most particles become passive, as observed in Fig. 4-58.

During the 29th cycle, there is a compaction from the bottom to the top of the granular sample. The contact network is progressively restored and force chains develop throughout the sample.

Considering the complexity of this behavior, it is necessary to define a criterium to quantitatively determine the state of the granular material. At the microscopic scale, the coordination number could play this role. Figure 4-59 presents the evolution of C_n during the 27th, the 28th and the 29th cycles of vibration (A = 1.5 mm and Γ = 2). Figure 4-60 compares the evolution of C_n for vibration at Γ = 1.02 and Γ = 2. In both cases, force chains seem to develop only when $C_n > 2.5$. Nevertheless, the coordination number is a microstructural parameter and it should be interesting to define a criterium describing the micro- and macro- characteristics of the behavior. This point will be discussed in the conclusion of this Chapter.

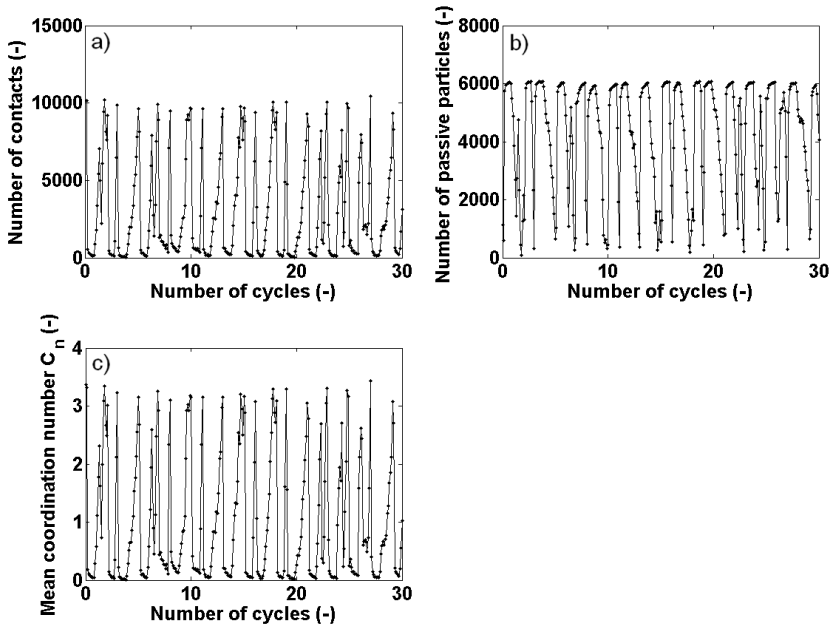

Figure 4-50: Relationships between the number of cycles (0 – 30) and the total contact number (a), the total number of passive particles (b) and the mean coordination number, C_n, (c) for the whole sample (A = 1.5 mm and Γ = 2).

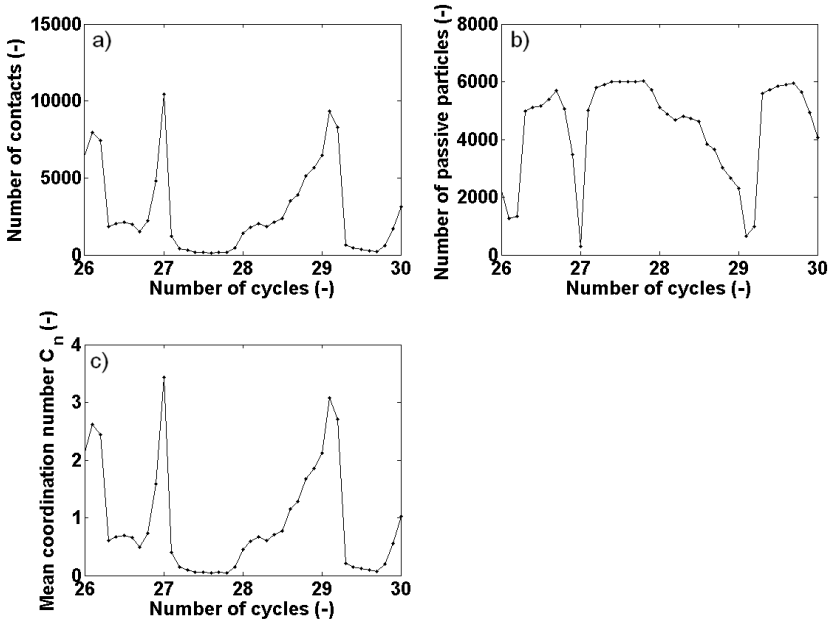

Figure 4-51: Relationships between the number of cycles (26 - 30) and the total contact number (a), the total number of passive particles (b) and the mean coordination number, C_n, (c) for the whole sample for the cycles 26 to 30 (A = 1.5 mm and Γ = 2).

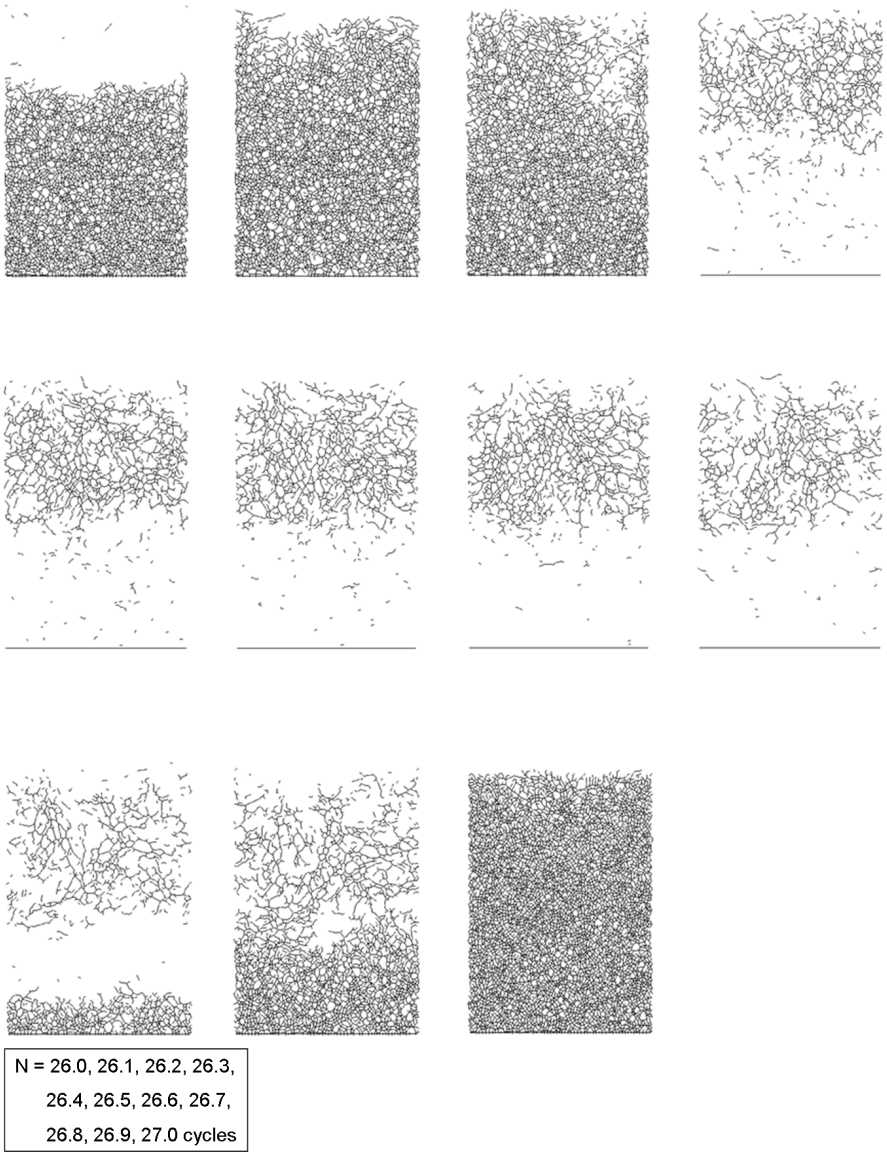

Figure 4-52: Evolution of the contact network during the 27th cycle of vibration (A = 1.5 mm and Γ = 2).

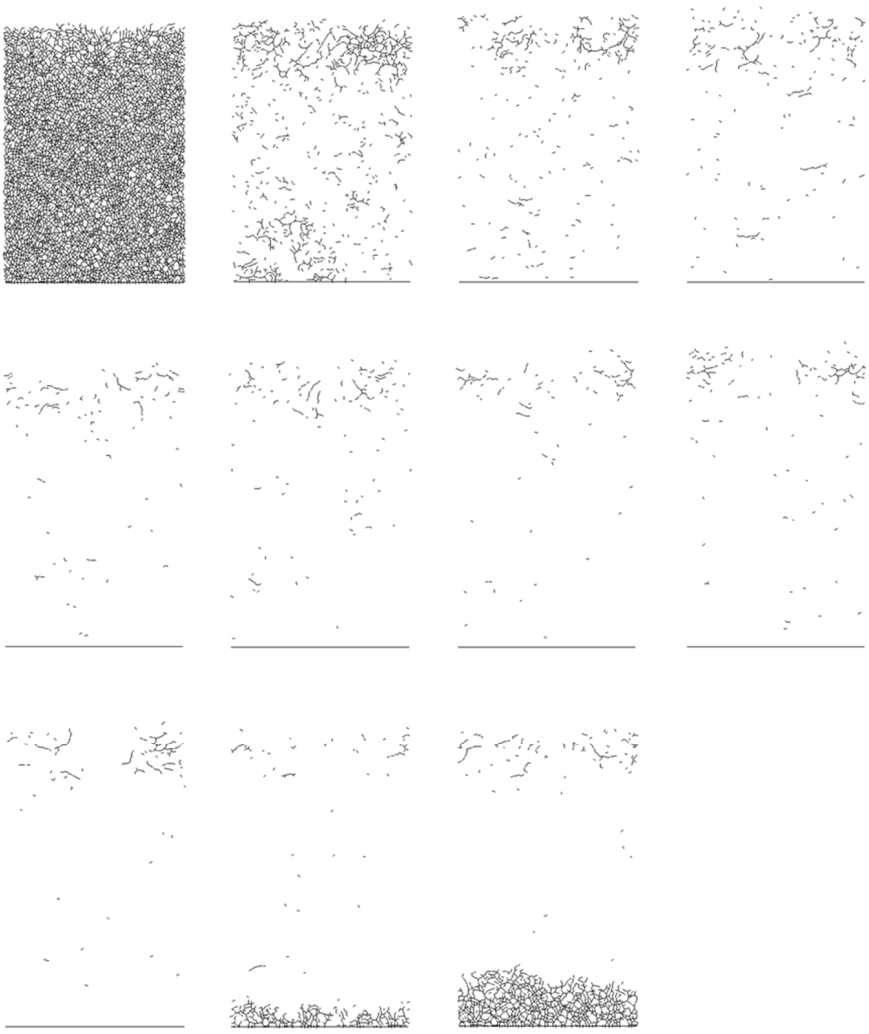

Figure 4-53: Evolution of the contact network during the 28th cycle of vibration (A = 1.5 mm and Γ = 2).

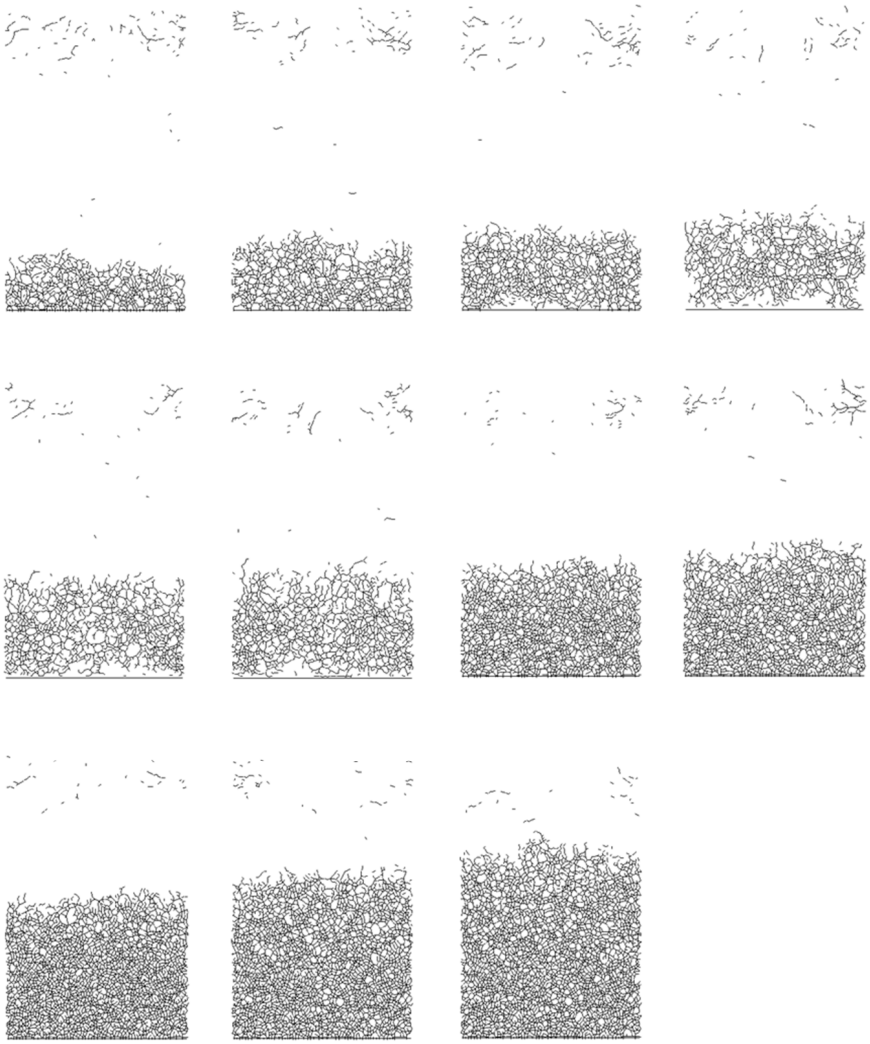

Figure 4-54: Evolution of the contact network during the 29th cycle of vibration (A = 1.5 mm and Γ = 2).

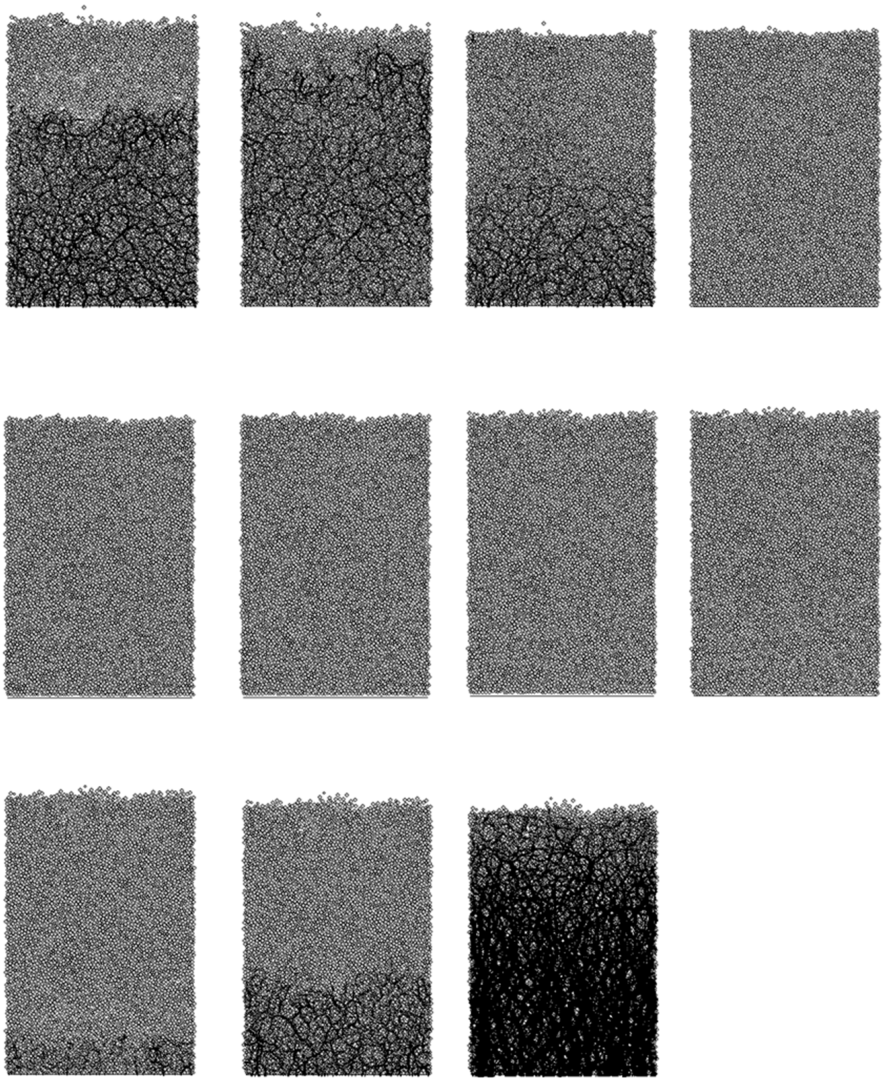

Figure 4-55: Evolution of the force chains during the 27th cycle of vibration (A = 1.5 mm and $\Gamma = 2$).

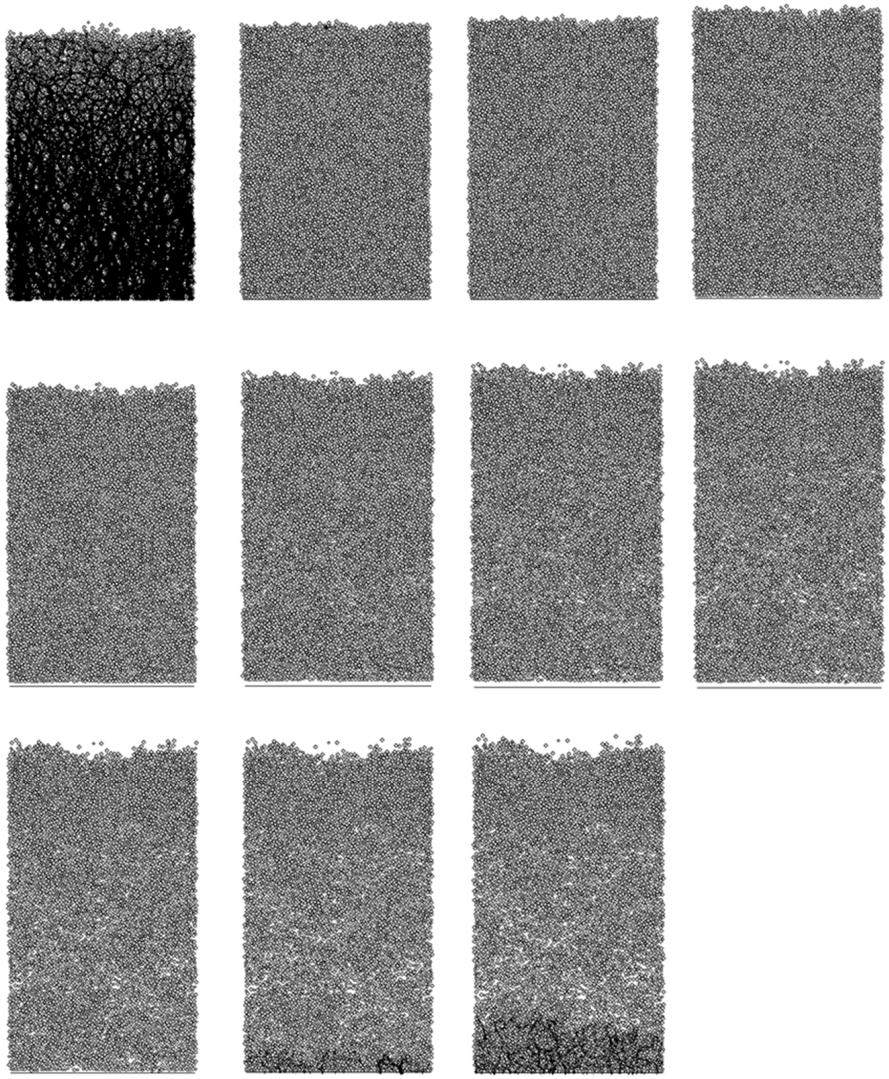

Figure 4-56: Evolution of the force chains during the 28th cycle of vibration (A = 1.5 mm and $\Gamma = 2$).

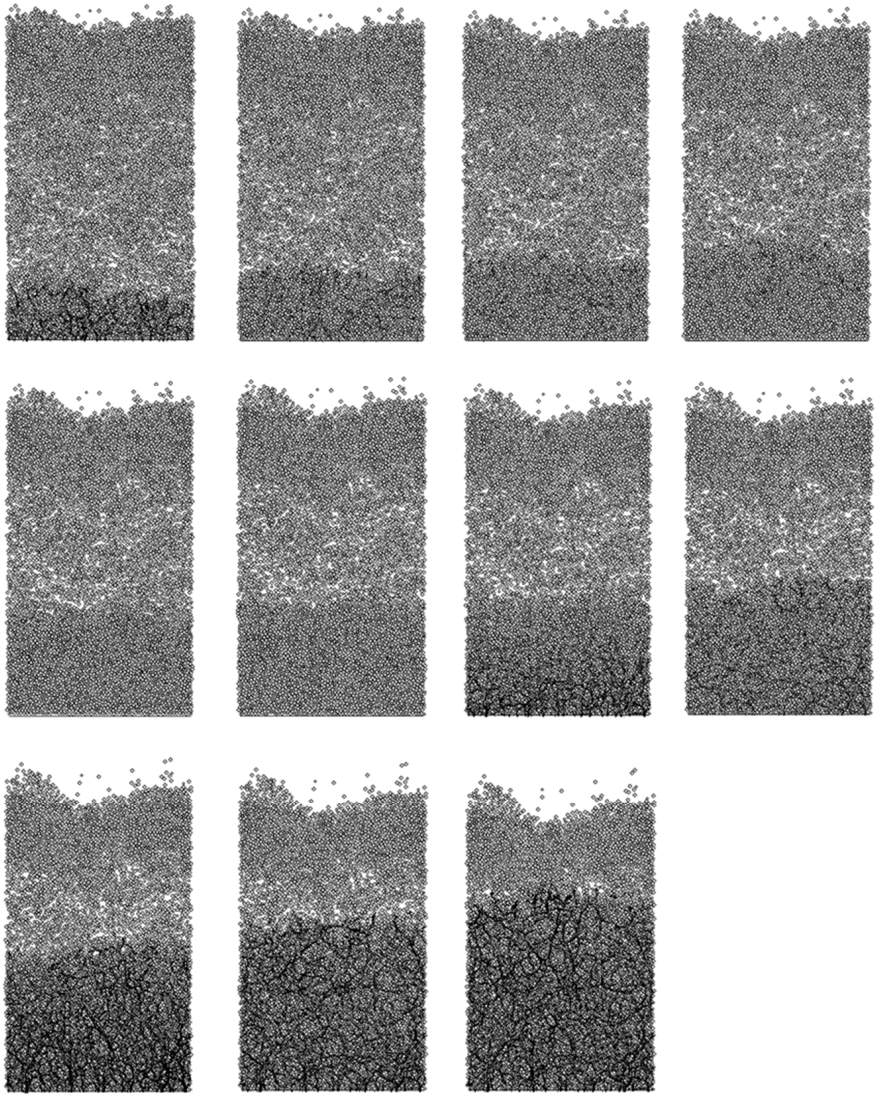

Figure 4-57: Evolution of the force chains during the 29th cycle of vibration (A = 1.5 mm and $\Gamma = 2$).

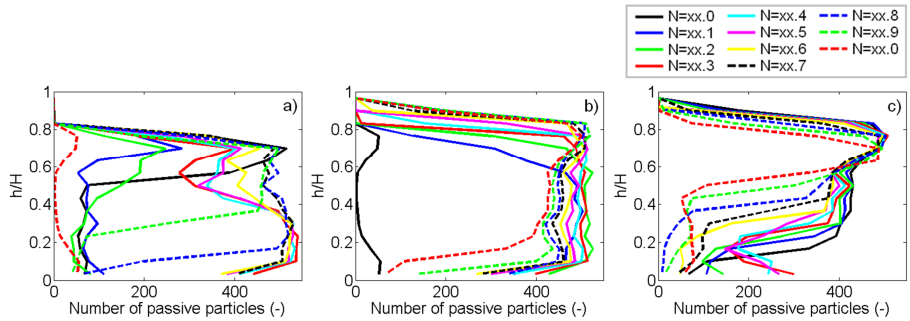

Figure 4-58: Evolution of the number of passive particles in the measurement layers of the granular sample during a) the 27th, b) the 28th and c) the 29th cycle of vibration (A = 1.5 mm and Γ = 2).

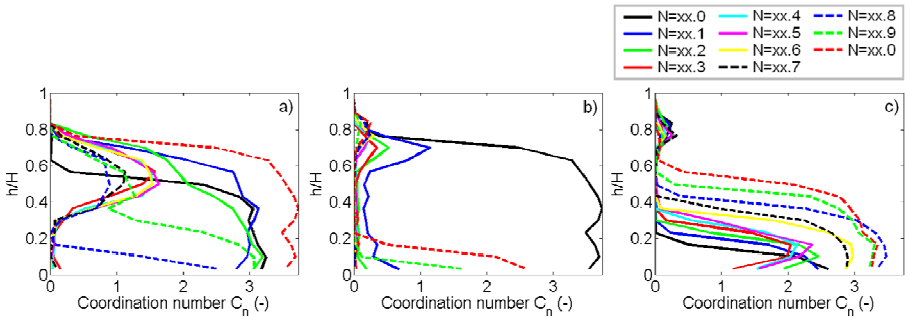

Figure 4-59: Evolution of the coordination number, C_n, in the measurement layers of the granular sample during a) the 27th, b) the 28th and c) the 29th cycle of vibration (A = 1.5 mm and Γ = 2).

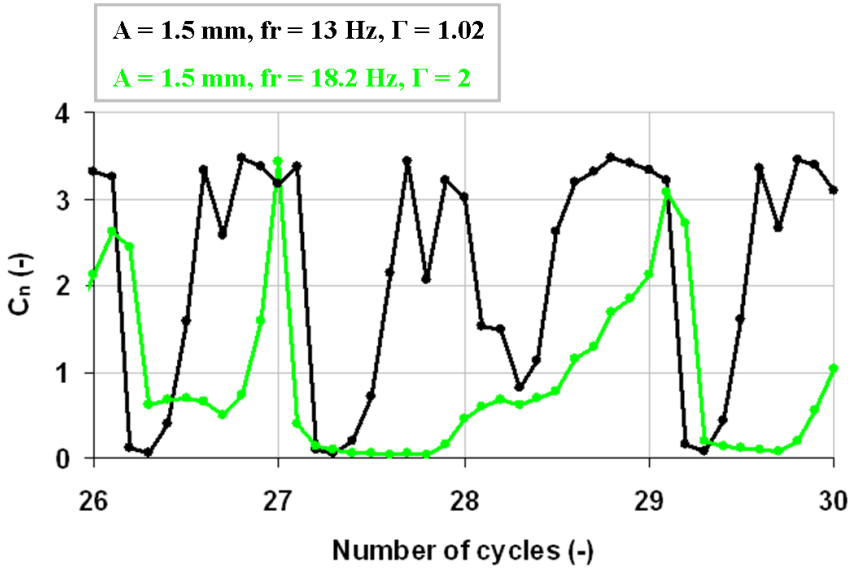

Figure 4-60: Comparison of the evolution of C_n for vibration at Γ = 1.02 and Γ = 2.

b. Coupled influence of the displacement and the frequency

Figures 7-37 to 7-40, presented in Appendix 7-8, illustrate the comparison between two simualtions performed at similar acceleration amplitude, $\Gamma = 1.02$ (-) for two displacement amplitudes (0.8 and 1.5 mm).

The assembly behavior is similar in the two simulations. The contact number and the coordination number cyclically collapse corresponding to an increase of the number of passive particles in both cases. Vibro-fluidization is obviously identified for the two frequencies with a cyclic degradation of the vertical stresses.

Considering the porosity variation (Fig. 7-37), there are peak values for the simulation performed at 0.8 mm and 17.8 Hz. These peaks occur in the measurement layers located near the free surface where the grain assemblage is very sensitive to the movement. Nevertheless, the general trend is similar to the volume change observed for 1.5 mm and 13 Hz.

Hence, no fundamental difference was highlighted between the two simulations leading to the significant conclusion that dimensionless acceleration amplitude, η_2, is the governing motion parameter of the vibrated granular material behavior in vibro-fluidized regime, at least for $\Gamma = 1.02$.

c. Discussion of the results

Factors affecting vibro-fluidization

When the sample is subjected to high acceleration vibration, $\Gamma = 1.02$, a steady vibratory regime is swiftly reached within cyclic vibro-fluidization occurs. In the steady vibratory regime, the porosity cyclically varies and successive dilating and compacting phases are observed. In spite of the weak porosity variations (on the order of 2%), contact network degradation is still observed. The coordination number collapses and the major part of the particles become passive. The force chains get unbound resulting in stress degradation in the sample. Full vibro-fluidization occurs during the downward acceleration phase of the cycle ($\eta_2 < 0$) supporting the dilatation of the granular sample. The continuous particle velocity field results in short-range suspension of particles and explains the cyclic character of the degradation.

At $\Gamma = 2$, discontinuities develop in the particle velocity field and lead to long-range suspension of particles. The strong sustained degradation of the stress field is a consequence of this chaotic motion pattern. Noncyclic vibro-fluidization is thus observed.

Actually, the state of the assembly is related to the volume change. The evolution of the interstices during the vibration is the major factor controlling the vibro-fluidization emergence. This latter occurs if the acceleration amplitude is high enough to result in the development of intergranular relative displacements. Finally, it is to note that the presence of the free surface, which does not restrain vertical granular displacements, supports the onset of the phenomenon.

From micro- to macroscopic scale

Figure 4-61 presents the distribution of contact orientation and the angular distributions of normal and tangential contact forces corresponding to the steady vibratory regime of vibration for A = 1.5 mm and $\Gamma = 1.02$. The measured values, represented by black lines, do not present a periodic behavior in comparison with

Fig. 4-28, for low acceleration vibration ($\Gamma = 0.5$). They can be no more approximated by the periodical expressions (4-27), (4-28) and (4-29), represented by red lines. During vibration at high acceleration amplitude ($\Gamma = 1.02$), the assembly is characterized by an instability of its contact network. As previously discussed, the study of induced anisotropy of contact becomes meaningless when dynamic conditions are encountered. Hence, the anisotropy coefficients, a, a_n, a_t and the mobilized friction angle, ϕ_{mob}, can be no more computed on the basis of this approach.

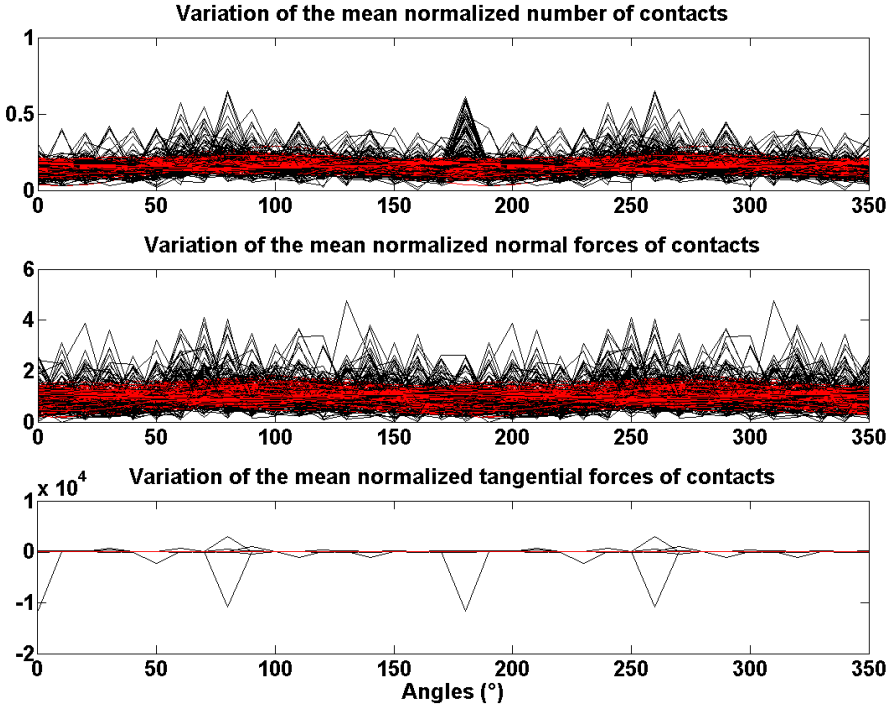

Figure 4-61: Characteristics of fabric of the numerical assembly in the steady vibratory regime (A = 1.5 mm and $\Gamma = 1.02$).

"Fluid" stresses

The dimensionless kinetic energy highlights the transition between the solid state – dominated by the development of contact stresses due to the force chains – and the vibro-fluid state. It displays a strong increase during vibro-fluidization before going back to a range of values similar to the range observed for low acceleration vibration ($\Gamma = 0.5$), wherein the granular sample approximately behaves like an elastic solid.

For the purpose of illustrating the fluid nature of the granular material at high dimensionless kinetic energy, the dynamic character of the sample is investigated with regards to the development of "fluctuation" stresses.

In granular materials, the stress tensor is the sum of three contributions (Moreau, 1997):

$$\sigma_{ij,t} = \sigma_{ij,c} + \sigma_{ij,fl} + \sigma_{ij,r} \qquad \text{(Eq. 4-48)}$$

where t indicates the total stress tensor, c the contact stresses, fl the "fluctuation" stresses and r the stresses due to the particle rotation.

The contact stresses, considered until now without index ($\sigma_{ij} = \sigma_{ij,c}$), result from the force chains developed throughout the sample (Christoffersen et al., 1981 and Kruyt and Rothenburg, 1996). They can be considered as intergranular stresses in the sense of the definition given by Terzaghi (Holtz and Kovacs, 1991). They highlight the static character of the assembly. The calculation of the contact stresses is available in Appendix 7.6.

The "fluctuation" stresses result from the velocity fluctuations of the grains:

$$\sigma_{ij,fl}^{m} = \frac{1}{V_m} \sum_{k=1}^{N_{p,m}} m_k \partial v_{k,i} \partial v_{k,j} \qquad \text{(Eq. 4-49)}$$

where m identifies the measurement layer m, V_m the volume of the measurement layer, k the particle k, $N_{p,m}$ the number of particles in the measurement layer m, m_k the particle mass and $\partial v_{k,i}$ the particle velocity fluctuation in the direction i. "Fluctuation" stresses can be correlated with "Reynolds" stresses, comparing the flux of particles to a fluid flow moving at the same averaged velocity.

The third term, related to the particle rotation, is generally very small (Moreau, 1997). It will be not considered in the present work.

Hereunder, the term "fluid" will be used instead of "fluctuation".

Figure 4-62 illustrates the evolution of the vertical "fluid" stresses, $\sigma_{22,fl}$, during the vibration at $\Gamma = 1.02$. Figure 4-62b presents the cyclic character of the fluid stresses in the steady vibratory regime. The magnitude of the fluid stresses is very small. They vanish two times per cycle. First time during vibro-fluidization when the particles become in suspension. Secondly, during the restoration of the contact network when the velocity imposed to the container bottom goes through zero. That is why the term "fluctuation" is more appropriate than "fluid" stress.

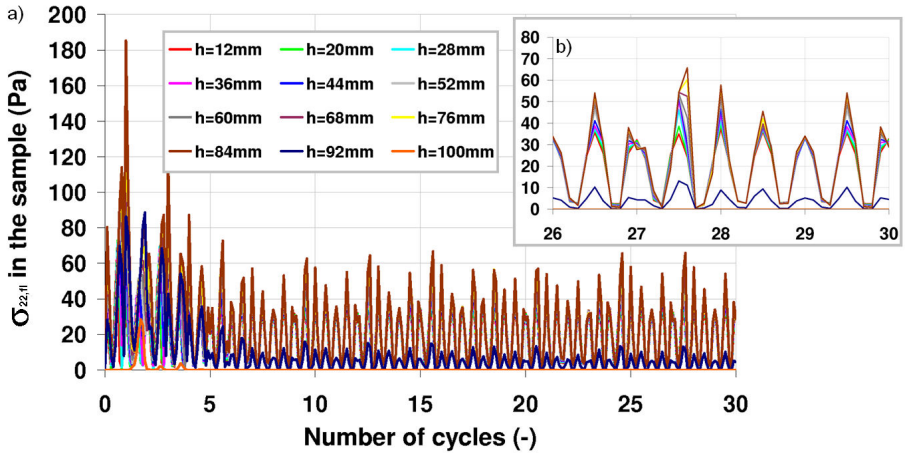

Figure 4-62: a) Vertical fluid stresses in the measurement layers of the sample during the vibration (A = 1.5 mm and $\Gamma = 1.02$), b) enlargement of the curves in the steady vibratory regime.

Figure 4-63 illustrates the evolution of the ratio of fluid stresses to contact stresses during the 27th cycle of vibration at Γ = 1.02. The comparison is similar to the consideration of the dimensionless kinetic energy. High ratio underlines vibro-fluidization and low ratio (close to unity) indicates contact network conservation and temporary stability.

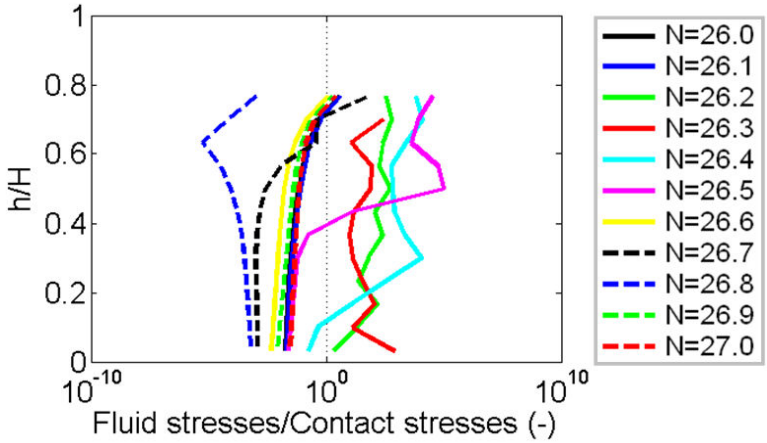

Figure 4-63: Evolution of the ratio of the fluid stresses to contact stresses during the 27th cycle of vibration (A = 1.5 mm and Γ = 1.02).

Hence, during vibro-fluidization, the fluid stresses must be considered in regard of the stress tensor (4-48). That observation witnesses to the short-lived fluid nature of the vibrated dry granular assembly and it justifies the designation "vibro-fluid" of the phenomenon.

Granular shear flows

There are similitudes between the elastic quasi-static regime observed in shear flows (Campbell, 2002) and the elastic solid range observed at low acceleration vibration (Γ = 0.5), in the present study. In both cases, the granular assembly behavior is dominated by the elastic properties of the particles and the formation of force chains. The total stress tensor (4-48) is then dominated by the contact term.

Similarly, the inertial regime of shear flows can be compared with the vibro-fluid behavior. In both cases, the force chains get unbound due to volume change. The inertial properties of the particles control the assembly behavior. Fluid stresses must be considered in the calculation of the total stress tensor (4-48) and the transition between elastic quasi-static and inertial regimes as well as; the transition between elastic and vibro-fluid behaviors occur for weak porosity variation (on the order of 2% in both cases), accompanied by three orders of magnitude of stress reduction.

4.3 Conclusion

Volume change and coordination number

In the present chapter, the behavior of a dry granular material subjected to vertical vibration was numerically studied. The influence of the acceleration

amplitude on the granular structure degradation was analyzed at macroscopic scale – with porosity, stress and kinetic energy measurements – and at microscopic scale – with the help of contact density and orientations, contact network and force chain analysis. Three acceleration amplitudes were tested, $\Gamma = 0.5$, $\Gamma = 1.02$ and $\Gamma = 2$.

For vibrations at $\Gamma = 0.5$, the granular material was shown to reach a steady vibratory regime where dilating and compacting phases were observed.

As a significant result, the dimensionless acceleration amplitude, Γ, was identified as the governing parameter of the granular material behavior, as illustrated in Fig. 7-30 to 7-36 in Appendix 7.7.

Volume change, which can be related to the container acceleration, displays very limited values (on the order of 1 ‰) and results in cyclic stress variation in the material. Nevertheless, preferential force chains are preserved. The material approximately behaves like an elastic solid at the macroscopic scale of the stresses. The inelasticities are restrained at the micro- scale of the grains. They are related to the tranformation of active to passive particles during the sample dilatation and to the interparticulate slips.

At $\Gamma = 1.02$, weak porosity variations (on the order of 2 %) were shown sufficient to result in cyclic vibro-fluidization characterized by a continuous particle velocity field.

Similar behavior was observed for two simulations performed at $\Gamma = 1.02$ for different displacement amplitudes, as illustrated in Fig. 7-37 to 7-40 in Appendix 7-8. As for the elastic regime, Γ is the governing motion parameter.

At $\Gamma = 2$, high dilating and noncyclic vibro-fluid behavior of the assembly was observed resulting in strong sustained degradation of the stress field.

Figure 4-64 illustrates the relationship between the coordination number and the porosity for the three types of behavior explored in this study, at $\Gamma = 0.5$, $\Gamma = 1.02$ and $\Gamma = 2$, considering all the measurement layers. For $\Gamma = 0.5$ and $\Gamma = 1.02$, only the cycles corresponding to the steady vibratory regime are regarded. Red data are the representative measurements of the elastic regime (at $\Gamma = 0.5$). They are located in a zone wherein C_n is close to 3.5 (-) and very limited porosity variation is displayed. Black points are the measurements performed for $\Gamma = 1.02$, where cyclic vibro-fluidization was observed for weak porosity variation. The green points are representative of the high-dilating regime where non cyclic vibro-fluidization was noticed accompanied with large porosity variation.

Granular motion

At high acceleration amplitude, the motion pattern and the discontinuities displayed by the particles govern the behavior and control the occurrence of vibro-fluidization.

It seems that the discontinuities are caused by the uncoupling between the grains and the container bottom. They depend on the time during which the particles remain into free fall, only subjected to the gravitational field, before impacting the rigid bottom.

In order to investigate the influence of this “group” free fall time, the trajectory of a reference particle (similar to the model particles with d = 1 mm), subjected to sinusoidal vibration, is considered. Figure 4-65 illustrates this trajectory for different imposed acceleration amplitude of vibration.

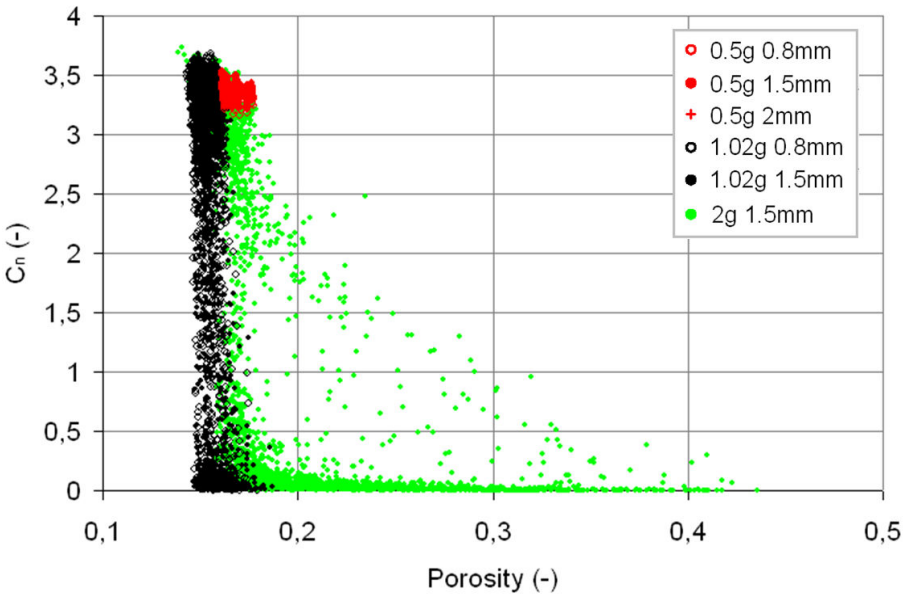

Figure 4-64: C_n vs. porosity: elastic, vibro-fluid and high-dilating behaviors at $\Gamma = 0.5$, $\Gamma = 1.02$ and $\Gamma = 2$ for all the measurement layers and all the cycles of vibration.

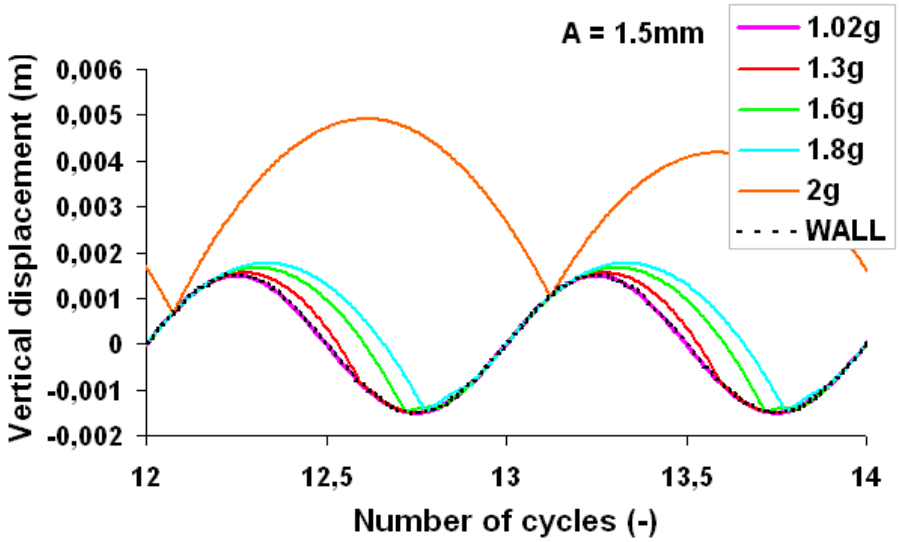

Figure 4-65: Trajectory of a reference particle subjected to vertical vibration.

At 1.02g, the particle accompanies the container motion during an important part of the cycle; while at 2g, the particle trajectory is described in terms of impact dynamics. It remains into free fall on a longer time interval, t*. After impact, the resultant particle velocity is a function of the relative velocity between the particle and the wall at the contact time. The resultant behavior is therefore related to the free fall time, t*.

It could be possible to extend this explanation to the analysis of the vibrated assembly behavior. Nevertheless, the particles will be also subjected to intergranular interactions. The granular motion pattern will be related to the kinetic energy transmission in the assembly throughout the contact areas considering the dissipations caused by the viscous contact model.

The emergence of discontinuities in the velocity field could be depending on an equivalent "group" free-fall time, t_{gr}*, developed by the assembly.

State diagram

Nevertheless, the purpose of the present research is to characterize the state of the vibrated granular matter and to identify the occurrence of vibro-fluidization regardless of the motion pattern developed by the particles.

Figure 4-66 illustrates the relationship between the mean contact stress and the coordination number at $\Gamma = 0.5$, $\Gamma = 1.02$ and $\Gamma = 2$. For $\Gamma = 0.5$ and $\Gamma = 1.02$, only the cycles corresponding to the steady vibratory regime are regarded. The mean contact stress ($\sigma_{11}+ \sigma_{22}$) is normalized by its value at the static equilibrium. Figure 4-66 plays the role of a state diagram in the sense it provides a micro – macro relationship describing the state of matter according to the coordination number and the internal stress field. It quantifies the vibro-fluid limit as a function of the coordination number. Below $C_n = 2.5$, the bi-dimensional granular assembly is vibro-fluidized with mean contact stress close to zero. The data displaying non zero stress value are representative of the measurement layers located near the free surface wherein the static mean contact stress is weak.

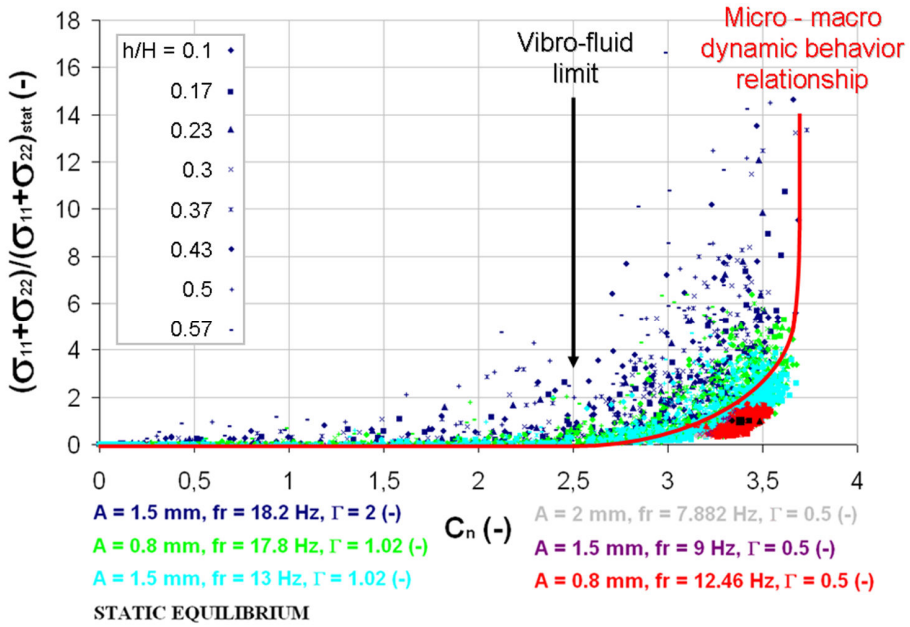

Figure 4-66: State diagram – Mean contact stress vs. coordination number for all the cycles of vibration.

5 Vibro-fluidization of vibrated dry sand within the framework of vibrodriving

The present chapter positions the results of the present research respectively to the vibratory driving process and highlights the common points between vibro-fluidization and liquefaction, both phenomena resulting in the shear strength degradation of granular soil.

5.1 Vibro-driving resistance of dry sand

According to Barkan (1963), when a pile or sheet-pile is inserted into the soil with the help of vibrations, the soil vibro-driving resistance consists in a coupled Coulomb frictional and viscous side resistance augmented by an elasto-plastic end resistance.

Side resistance

The Coulomb resistance is the external dry frictional resistance exerted by the soil on the pile shaft while the viscous resistance takes into account the penetration velocity of the pile. Barkan (1963) assumed that when a granular soil is subjected to vibrations, the dry frictional resistance progressively vanishes and then the soil behaves like a viscous liquid leading to the development of a viscous resistance taking into account the sand vibro-fluidization.

For the purpose of verifying the existence of the vibro-fluidization phenomenon, experiments were performed at UCL on dry Fontainebleau sand deposited in a cylindrical container. Vertical vibrations were applied to the granular material without static overload. During the experimental campaign, three different types of dynamic behavior, depending on the acceleration amplitude, were distinguished: the densification behavior ($\Gamma < 1$), the instability surface behavior ($\Gamma \approx 1$), and the vibro-fluid behavior ($\Gamma > 1$). Vibro-fluidization occurs in the range ($1 < \Gamma < 2$) and it was shown to be caused by grain-boundary interactions which spark off granular convection.

It is to note that Barkan (1963) introduced the viscous model of resistance based on the results of sphere penetration experiments (SPE's) from which he deduced a range of values for the vibro-viscosity coefficient. But the sinking logs of the SPE's conducted at UCL do not follow Stokes law. It seems that the "vibro-fluid" behavior of vibrated dry sand may not be assimilated to a purely fluid viscous model, as proposed by Barkan (1963). That could be related to the way the vibro-fluidization is supported in the UCL-SPE's, i.e. with the help of granular convection. According to Knight et al. (1996), in granular convection, the granular medium displays a dual behavior which can be related to a viscous Newtonian fluid – characterizing the particle flow – coupled with an effective pressure contribution, depending on granular interactions.

In order to free oneself from the granular convection phenomenon, DEM simulations were conducted to model the vibration of a granular sample under lateral periodic boundary conditions. In numerical modeling, vibro-fluidization is identified by the degradation of the contact network and the force chains. It is caused by volume change and intergranular relative displacements and results in the development of fluid stresses throughout the sample.

According to these observations, it is proposed to rename the resistance resulting from the vibro-fluidization: “vibro-fluid resistance”.

The vibro-fluid resistance would be computed considering the shear strength reduction induced by the increase of the acceleration amplitude, Γ, of the vibrations.

End resistance

The elasto-plastic resistance represents the tip resistance where the elasto-plastic characteristics assume lower values due to the vibration. According to Rodger (1976), vibro-fluidization can also occur beneath the pile due to the transmission of the vibration from the soil adjacent to the pile sides. He proposed to introduce two types of vibrodriving motion to take into account both concepts: “fast” and “slow” vibratory driving motions.

5.2 “Fast” and “slow” vibro-driving motions

“Fast” vibrodriving motion occurs in loose dry granular soils where the penetration corresponds to the progressive compactive collapse of the voids in the soil. The main restraint being the inertial forces accompanying the collapse. Hence, soil resistance is assumed to be almost wholly due to soil vibro-fluidization (Rodger, 1976).

If vibro-fluidization can spread beneath the pile tip in loose dry sands, it cannot alone explain experimentally observed phenomena such as the occurrence of an impact domain where the relative density of the material increases.

In dense granular soils, when the pile encounters sufficient resistance, the surcharge force becomes insufficient to prevent pile-soil uncoupling and the end resistance acts only during a portion of each cycle. Penetration is assumed to occur as in a classical elasto-plastic impact situation, the main restraint being bulk compressibility and shear strength from the surrounding soil. Restraint at the pile sides is assumed due to Coulomb frictional and vibro-viscous resistance. Conversely, in loose cohesionless soils, no reversal motion will occur (Rodger, 1976).

The analysis of the dynamic force waveforms, measured during vibro-penetration experiments performed by Rodger (1976), confirms these concepts: during vibrodriving in loose granular soil and during vibro-extraction, a sinusoïdal force response was obtained. In dense granular soils, an impact type of waveform was observed.

According to Rodger (1976), the two types of motion can be tentatively defined with reference to the void ratio, as illustrated in Fig. 5-1. He selected the position of the void ratio with regard to the critical void ratio as the deciding factor of vibrodriving motion. Penetration is only assumed to occur when the amplitude of acceleration, Γ, exceeds a threshold value for soil vibro-fluidization. As for the UCL experiments, this threshold value is included in the range ($1 < \Gamma < 2$). Below this value, impaction or compaction will occur depending on the initial density of soil. At high acceleration amplitude, slow and fast vibrodriving will be encoutered respectively in dense and loose granular soils.

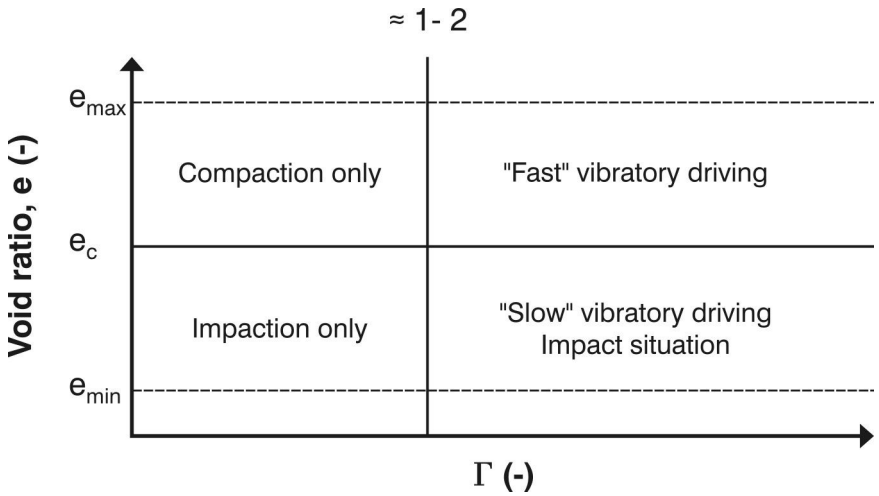

Figure 5-1: Types of vibrodriving motion as a function of the void ratio and the acceleration amplitude of the vibrations, after Rodger (1976).

Conversely, in the UCL experiments, vibro-fluidization was always reached in the range ($1 < \Gamma < 2$) regardless of the initial sand density because of the free surface configuration wherein the granular sample dilates without restraints. In such a way to model the behavior of dry sand along a vibrated profile, it will be necessary to explore the occurrence of vibro-fluidization under a confinement configuration with a control of the evolution of the (p', q, e) state during the vibration.

5.3 Micromechanical modeling of vibro-driving motion

Figure 5-2 proposes a conceptual micro-mechanical model of low vibratory driving motion occuring in dense sands. Restraint at the pile sides is assumed due to external dry frictional and "vibro-fluid" resistances.

The external dry frictional resistance results from the resistance of force chains represented by black lines. It is called dry Coulomb resistance because it depends on the stick-slip motions occuring at the interface between neighboring grains (see Section 7.1.3b). External dry frictional resistance is therefore related to the interparticular friction coefficient, μ.

The "vibro-fluid" resistance is due to the development of fluid stresses resulting from the momentum of the grains along the pile sides. It presents stress values several orders of magnitude lower than dry frictional stresses. In Fig. 5-2a, the red zone symbolizes the zone wherein the particles develop kinetic energy and free themselves from the contact network. In dense sands, partial vibro-fluidization occurs at the pile sides.

As illustrated in Fig. 5-2b, an impact situation is observed at the end of the pile. The end resitance can be characterized by an elasto-plastic resistance resulting from the bulk compressibility and the shear strength of the assemblage. If the relative movements between the pile and the soil lead to temporary suspension of some grains, the contact network is preserved during the reversal motion of the pile.

The dry Coulomb side resistance and the elasto-plastic end resistance spark off the low penetration velocities observed in dense sands.

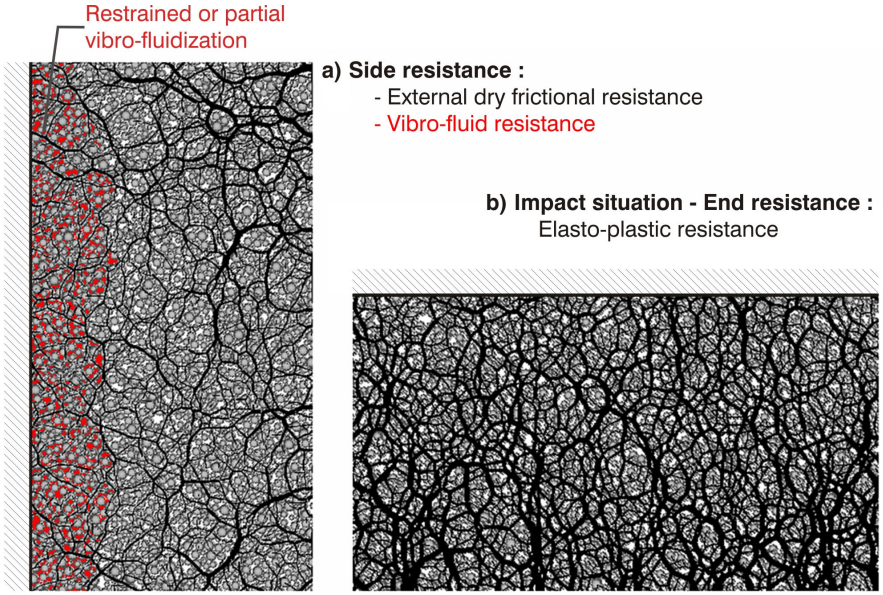

Figure 5-2: Conceptual micromechanical modeling of low virvatory driving: a) side resistance and b) end resistance.

Figure 5-3 illustrates a conceptual micro-mechanical modeling of fast vibratory driving motion occuring in loose sands. Full vibro-fluidization occurs along the pile sides. The red zone symbolizes the zone wherein vibro-fluidization occurs. A weak porosity variation (on the order of 2%) is sufficient to lead to the degradation of the contact network and the force chains. The coordination number tends to zero and the side resistance is fully vibro-fluid. The side resistance depends on the inertial characteristics of the particle flow moving along the pile sides. As observed in Fig. 5-3, vibro-fluidization occurs beneath the pile tip. The total soil resistance to the penetration is only related to vibro-fluid resistance characterized by low stress magnitude. Hence, high penetration velocities are observed in loose sands.

5.4 Liquefaction vs. vibro-fluidization

The vibration of a granular medium can result in the “fluidization” of its structure. Flow liquefaction and cyclic mobility phenomena are highlighted in saturated conditions and vibro-fluidization is put forward in dry conditions to explain sand shear strength degradation.

In the present work, vibro-fluidization was investigated at microscopic scale with the help of the Discrete Element Method.

Similarly, Zeghal and El Shamy (2004) have analyzed the liquefaction of a saturated granular sample of quartz sand particles with the help of a coupled continuum-discrete hydromechanical model. The fluid motion was modelled using averaged Navier-Stokes equations and the particle motions using Discrete Element Modeling.

The authors conducted numerical simulations to analyze saturated sand behavior subjected to horizontal vibration. The particles were pluviating within a parallelepiped domain with lateral periodic boundaries.

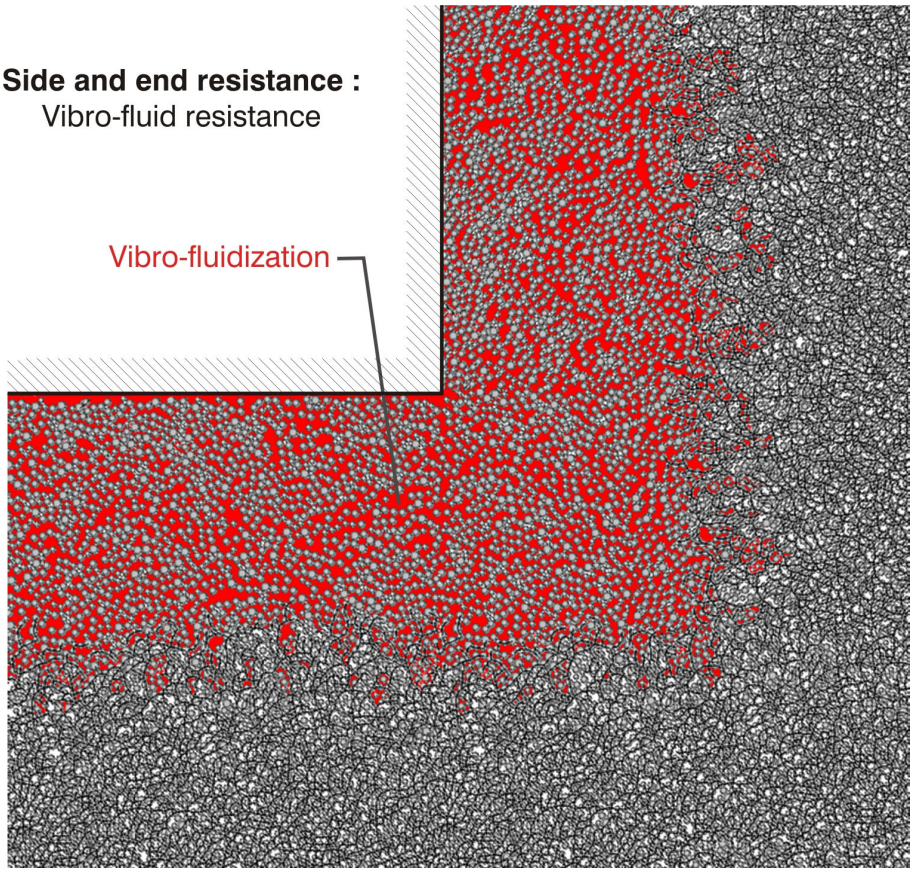

Figure 5-3: Conceptual micromechanical modeling of fast virvatory driving.

The normal contact indentation was idealized using the Hertz law (equation 7-3) and the tangential contact displacement with the help of equation (7-37) due to Mindlin (1949). A viscous damping model was introduced to take into account the energy dissipation at the contacts. Table 5-1 provides the characteristics of the simulations. In the present case, μ_{fl} is the fluid viscosity. The simulations were performed with a 30 g-level mimicing the conditions of a centrifuge testing of small-scale geotechnical models (Taylor, 1995). Thereof, the numerical model corresponds to a semi-infinite periodic prototype 5.70 m high with lateral dimensions of 4.2 m and 1.8 m.

The granular assemblage presents characteristics similar to the simulation parameters of this study (see Table 4-1). Volumetric mass, friction coefficient and contact stiffness can be compared as well as the ratio d_{max}/d_{min}.

The granular sample was subjected to a sinusoidal horizontal base vibration with acceleration amplitude, $\Gamma = 0.075$ and frequency, fr = 3 Hz (in prototype units). Average values of contact stresses and pore pressure were measured with the help of spherical control volumes along the vertical central axis of the deposit (Itasca, 2003). The radius of the measurement spherical volumes is not provided by the authors.

NUMERICAL MODEL (3D)	
Granulometry	
d_{max} = 7.2 mm d_{min} = 4.8 mm d_{50} = 6 mm	$d_{max}/d_{min} \approx 1.5$ C_u: no indication
Sample dimensions	
H_{eff} = 0.190 m L = 0.140 m L = 0.060 m 10058 particles	$H_{eff}/d_{50} \approx 31.6$ $L/d_{50} \approx 23$ $l/d_{50} \approx 10$
Particles properties	
ρ_s = 2.650 gr/cm³ G = 2.9 10^{10} N/m²	n = 0.41 μ_p = 0.5 ν = 0.15 ε and β: no indication
Fluid properties	
ρ_{fl} = 1.000 gr/cm³ μ_{fl} = 4.98 Pa.s	

Table 5-1: Numerical model description, after Zeghal and El Shamy (2004).

Figure 5-4a illustrates the time histories of averaged pore pressure ratios at selected locations along the vertical central axis of the deposit. The pore pressure ratio is defined as the ratio of fluid pore pressure to initial vertical effective stress. A value close to 1 indicates liquefaction of the selected layer. Liquefaction is observed to start near the free surface and propagate downward. At the macroscopic scale, liquefaction is therefore characterized by the dimensionless pore pressure ratio.

At the microscopic scale, liquefaction occurs when the resultant of the forces acting on each of the adjacent particles vanishes (Zeghal and El Shamy, 2004). The phenomenon can be therefore localized to specific zones of the granular sample. The micromechanical indicator of liquefaction is the coordination number, C_n. As illustrated in Fig. 5-4b, when the pore pressure ratio is close to 1 at specific heights (h/H = 0.37 and h/H = 0.63), the coordination number tends to zero. In the strata wherein the pore pressure ratio is not stabilized around unity, the coordination number displays higher values.

Because of the undrained condition imposed to the sample, no volume change is allowed during the vibration and liquefaction occurs when the pressure exerted by the pore fluid on the sand grains approaches or counterbalances the intergranular forces. That corresponds to the destruction of the force chains.

Although vibro-fluidization occurs in dry conditions with volume change, it is possible to make a first analogy with the liquefaction phenomenon.

According to the numerical results of the present work, vibro-fluidization occurs when the granular assemblage is subjected to high acceleration amplitude. Particles develop kinetic energy leading to force chain degradation. At a macroscopic scale, vibro-fluidization is then described with the help of the dimensionless kinetic energy or considering the dimensionless ratio of fluid stresses to contact stresses while at microscopic scale, it is indicated by values of the coordination number, C_n, close to zero, similarly to liquefaction.

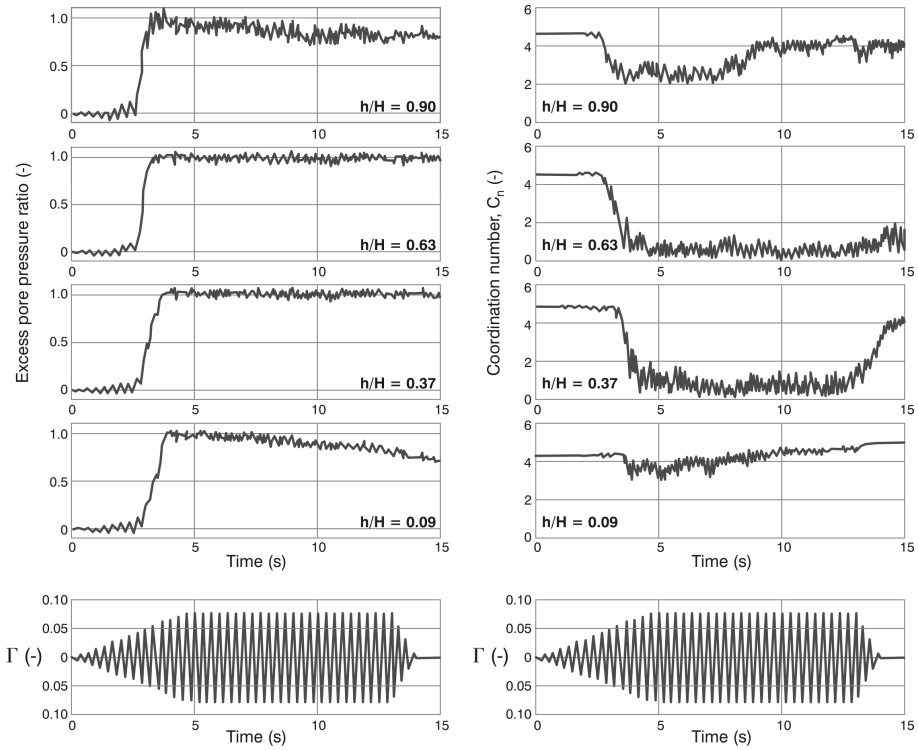

Figure 5-4: a) Averaged pore pressure ratios and b) coordination number at selected height locations as a function of time, after Zeghal and El Shamy (2004).

From a macromechanical point of view, dimensionless pore pressure ratio and dimensionless ratio of fluid to contact stresses, both highlight the degree of fluidization of the granular assemblage.

From a micromechanical point of view, both phenomena are characterized by the strong decrease of the coordination number, C_n.

The fluidization of the granular assemblage, in dry or saturated conditions, would be therefore related to the development of intergranular relative displacements. The vibrations would lead to successive reorganizations of the granular skeleton during which the grains would move freely without being in contact resulting in the degradation of the force chains and the shear strength of the material.

6 Conclusion and perspectives

6.1 Outline of the research

This PhD thesis focuses on the dynamic behavior of dry sand once subjected to vibrations. It concentrates on the shear strength degradation of vibrated dry sand. A multi-scale approach of the vibro-fluidization phenomenon is followed, at the microscopic scale of the grains, as well as, at the macroscopic scale of the assemblage.

The study is organized as follows: the review of the literature (Chapter 2), the laboratory investigation (Chapter 3), and the discrete element modeling (Chapter 4) of vibrated dry sand form the body of the text. The experimental and numerical approaches are integrated within the framework of vibrodriving in Chapter 5. In Appendix 7.1, contact mechanics of spherical bodies are treated. The description of contact mechanics theory supports the development of numerical simulations.

6.1.1 Review of the literature (Chapter 2)

a. Optimum vibrocompaction

The effect of vibrations on dry sand volume change is regarded considering the influence of the following parameters:

- the direction of the vibrations,
- the harmonic vibration parameters (A, fr and Γ),
- the duration of the vibrations,
- the size and the shape of the container,
- the grain size of the sand,
- and the surface overload, σ.

For soil vibrocompaction, the application of horizontal vibrations is recommended instead of vertical vibrations for two reasons. First, no decompaction is observed for horizontal vibrations regardless of the acceleration amplitude while with vertical vibrations, decompaction and heaping are observed for $\Gamma > 1$. Secondly, all other parameters remaining unchanged, the rate of compaction – characterized by the empirical coefficient β_t – is higher for horizontal vibration.

The acceleration amplitude, Γ, is the governing motion parameter of the process.

When subjected to vibrations, the sand undergoes a volume change and reaches the equilibrium void ratio (EVR), e_Γ, corresponding to the imposed acceleration amplitude, Γ. For horizontal vibrations, Barkan (1962) proposed empirical relationships to describe the volume reduction with time and to estimate the EVR for a given acceleration amplitude, Γ. These relationships are expected to remain valid for vertical vibrations while $\Gamma < 1$.

Sand granulometry also influences the efficiency of the process. The "vibrocompactibility" increases with the Uniformity coefficient, C_u.

The maximum sand density is reached without surface overload ($\sigma = 0$) and for a minimum of sand overburden.

b. Decrease of the shear strength

The internal friction coefficient ($f = \tan \phi_{mob} = \tau_{ds}/\sigma$) is shown to decrease with horizontal and vertical vibrations. Youd (1967) demonstrated that the equilibrium void ratio (EVR), e_Γ, is the critical void ratio (CVR), e_c, of the sand sample if sheared while subjected to similar vibrations. e_Γ, e_c and f exponentially decrease with the acceleration amplitude of the vibration, Γ.

c. Vibro-fluidization

The vibro-fluidization phenomenon characterizes the shear strength degradation of a dry granular material subjected to vibrations.

In addition, Barkan (1962) postulated that when dry sand is subjected to intense vibrations, its friction resistance vanishes and it behaves like a viscous fluid. He studied the vibro-viscous character of vibrated dry sand and performed sphere penetration experiments (SPE's) in order to determine vibro-viscosity coefficients.

The experiments and the numerical simulations of the present PhD thesis focus on the dynamic behavior of dry sand under vertical vibrations without surface overload. They are integrated to the domain of investigation defined by previous researchers within the framework of vibrodriving, as illustrated in Fig. 6-1.

6.1.2 Laboratory investigation (Chapter 3)

A new SPE apparatus has been designed and constructed at UCL. It consists in a cylindrical transparent polycarbonate container which is vertically actuated by a servo-controlled MTS hydraulic jack. Experiments were conducted on Fontainebleau sand (d_{50} = 0.19 mm, C_u = 1.6, e_{min} = 0.55 and e_{max} = 0.88) which was chosen for its subrounded or subangular character.

a. Volume change

The vibratory compaction curve of Fontainebleau sand was established. According to previous research, acceleration amplitude, Γ, is the parameter governing volume change. Empirical relationships are proposed to describe the evolution of the void ratio with time and with the number of cycles of vibration depending on Γ and on constant empirical coefficients (Eq. 3-1 to 3-3).

b. Dry sand vibratory behavior

Three distinct sand dynamic behaviors have been distinguished, depending on the acceleration amplitude, Γ:

- the densification behavior ($\Gamma<1$),
- the instability surface behavior ($\Gamma\approx1$), and
- the vibro-fluid behavior ($\Gamma>1$).

If the acceleration of the vibration is less than 1g, there is a densification of the sample. When the acceleration is increased beyond 1g, there is an instability in the sand mass which results in the emergence of an inclined free surface. If the acceleration amplitude is further increased, the free surface progressively flattens. A bulge develops and tends to expand the whole sample resulting in the vibro-fluidization of the granular material.

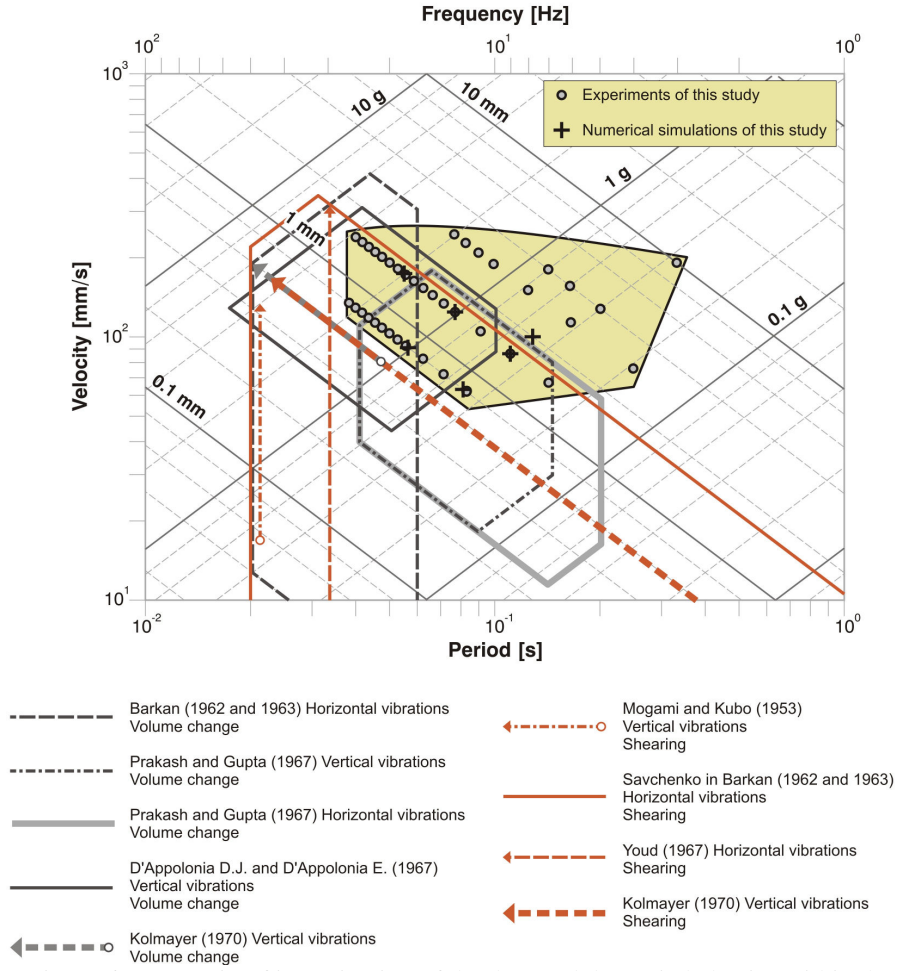

Figure 6-1: Domain of investigation of the dry sand dynamic behavior within the framework of vibrodriving.

Experimentally, vibro-fluidization is related to the development of granular convection resulting from particle-wall interactions. Considering the model of granular convection developed by Knight et al. (1996), vibrated dry sand behaves like a complex fluid simultaneously described by viscous terms – corresponding to Newtonian fluid properties – and by an effective pressure term – depending on granular interactions –. Granular convection results in a particular state of matter wherein solid and complex fluid characteristics of the granular flow play a role in the way dry sand reacts to the vibrations.

The instability surface behavior can be viewed as a succession of active and passive phases. The active phases allow relative interparticle motion and slope formation due to the convection and the assemblage asymmetry while the passive phases limit the angle of the inclined free surface.

c. Dry density after vibration

Dry densities after vibration, $D_{r,\Gamma}$, were succesfully compared with previous results of Prakash and Gupta (1967).

In the densification regime, there is a progressive increase of $D_{r,\Gamma,}$ until the acceleration amplitude reaches 1g. Beyond this value, dry density after vibrations progressively decreases to reach a value oscillating around $D_{r,\Gamma} = 60\%$ when the sand is vibrated in the vibrofluid range.

d. Sphere penetration experiments (SPE's)

In the densification regime, an exponentially decreasing penetration profile is observed although no refusal depth was reached.

In the instability surface regime, vibratory sinking logs are strongly disrupted by the convective rolls.

In the vibro-fluid regime, the sphere quickly sinks into the vibrated medium and stabilizes at a certain equilibrium penetration. The sphere penetrometer weight seems to be balanced by an equivalent "buoyant" force augmented by the flow of surrounding sand grains. The equilibrium penetration is determined by the displacement amplitude.

The sinking logs of the SPE's conducted at UCL do not follow Stokes law as observed in the 1962 Barkan experiments. Obtained curves do not show a penetration phase wherein the sphere sinking velocity is constant. Hence, the concept of vibro-viscosity coefficient, proposed by Barkan (1962), is to be reappraised in our opinion.

Moreover, the analysis of the transient sinking phase highlights the fact that the equilibrium penetration and the sphere sinking velocity are independent of the acceleration amplitude, Γ, in the vibro-fluid regime. Then, the governing parameters of the sphere position and the sphere sinking velocity become its apparent mass and its diameter.

6.1.3 Discrete Element Modeling (Chapter 4)

Discrete Element Modeling (DEM) of vibrated granular material was performed, under lateral periodic boundary conditions, considering only granular interactions, with the help of the PFC2D Particle-Flow model. Representative points of the simulated vibratory conditions are shown in Fig. 6-1. A stratified analysis was used to emphasize the transformation of the internal state of the sand during vibration.

The numerical simulations characterize the state of the sample considering its evolution at macroscopic scale – with measurements of porosity, stress field and kinetic energy – and at the microscopic scale – with the consideration of the fabric characteristics, the contact network and the force chains developed by the particles – during vertical vibrations.

a. Elastic behavior

When the sample is vibrated at low acceleration ($\Gamma = 0.5$), it swiftly reaches a steady vibratory regime within there is a cyclic variation of the material properties. There are successive compacting and dilating phases corresponding respectively to upward and downward acceleration of the numerical container. Principal force

chains of the contact network are still preserved during the whole cycle and the granular material behaves like an elastic solid at the macro- scale of the assembly.

As a significant result, acceleration amplitude, Γ, is shown to be the parameter governing the dynamic behavior of the vibrated granular assembly (see Appendix 7.7).

b. Vibro-fluid behavior

Once the acceleration amplitude is set to 1.02g, a steady vibratory regime is also observed. In spite of the weak porosity variations observed in this regime, cyclic vibro-fluidization is still noticed. The coordination number, C_n, collapses and the major part of the particles become "passive". The contact network is cyclically disintegrated and the force chains get unbound resulting in shear strength degradation. Vibro-fluidization occurs during the downward acceleration phase of the cycle supporting sample dilatation. The phenomenon is related to the development of intergranular relative displacements.

The vibro-fluid behavior is characterized by the emergence of "fluid" stresses in the sample. They represent a significant part of the total stress tensor in this range.

No fundamental difference was highlighted between the two simulations performed at similar acceleration amplitude ($\Gamma = 1.02$) for different displacement amplitudes (see Appendix 7.8).

Strongly dilating and noncyclic vibro-fluid behavior was observed at $\Gamma = 2$ resulting in marked sustained degradation of the stress field in the granular material. The motion pattern, displayed by the vertically vibrated particles, is complex and underlines the chaotic character of the assemblage behavior.

6.1.4 "Vibro-fluid" resistance (Chapter 5)

Chapter 5 focuses on the vibro-driving resistance of dry sand. "Fast" and "slow" vibratory driving motions are discussed with regards to the side and the end resistances encountered by profiles or piles in dense and loose sand. A conceptual micromechanical model of both types of motion is proposed wherein "vibro-fluid" resistance is assumed instead of "vibro-viscous" resistance, considering the experimental and numerical results of the present study.

In addition, vibro-fluidization is compared with liquefaction at microscopic and macroscopic scales.

6.2 Summary of the scientific contributions

Experiments, performed to study the volume change of the Fontainebleau sand, rely on previous results of Barkan (1962) and Prakash and Gupta (1967).

For vertical vibrations and without surface overload, three distinct sand dynamic behaviors are highlighted, depending on the acceleration amplitude, Γ, which is shown to be the governing motion parameter of the vibrated dry sand behavior. The motion patterns, displayed by sand grains, are described considering the recirculation phenomena observed within the densification regime ($\Gamma < 1$), the instability surface regime ($\Gamma \approx 1$) and the vibro-fluid regime ($\Gamma > 1$).

Experimentally, the vibro-fluidization has been characterized with the help of sphere penetration experiments and is shown to be related to granular convection.

The vibratory sinking logs do not follow the Stokes law, they are related to the dynamic regimes of vibration.

From the numerical simulations, elastic, vibro-fluid and strongly dilating behaviors are identified at macro- and microscopic scales respectively for acceleration amplitudes, Γ, equal to 0.5, 1.02 and 2. Acceleration amplitude is confirmed in the role of the parameter governing the dynamic behavior of vibrated dry granular material.

Vibro-fluidization of the sample is shown to be related to volume change in the sample and is illustrated by the development of fluid stresses – at the macroscopic scale – and by the collapse of the coordination number – at the microscopic scale –. The consideration of the state diagram, illustrated in Fig. 4-66, allows one to characterize the state of matter, anywhere in the granular material, during vibration.

6.3 Perspectives and future developments

6.3.1 Laboratory investigations

All the studies, represented in Fig. 6-1, identify the acceleration amplitude, Γ, as the governing parameter of the dry sand dynamic behavior. The control of the acceleration signal imposed to the container is therefore essential. For additional volume change and sphere penetration experiments, the use of a vibrating table generating vibrations with the help of counter-rotating eccentric masses is recommended in such a way to ensure the sinusoidal character of the acceleration, as illustrated in Fig. 2-4.

The domain of investigation should be extended in the range [20-50Hz]. The container shape and size influences could be also explored. Indeed, the tank geometry could modify the granular convection and thus, the way the vibro-fluidization occurs. Experiments have to be performed with various granular soils, characterized by different values for d_{50}, C_u, e_{min} and e_{max}.

6.3.2 Discrete Element Modeling

Additional simulations should be performed to explore the domain of investigation in-depth. The influence of the normal and tangential restitution coefficients, ε and β, on the assembly dynamic behavior has to be highlighted. Various granular materials with different Uniformity coefficients, C_u, could be considered taking into account the increase of the calculation time induced by the different particle sizes.

The pluviating process could be improved in order to obtain a numerical grain deposit presenting a well-defined character at rest.

The implementation of a discrete element model equipped with lateral rigid frictional boundaries should allow the study of recirculation phenomena. The effects of the walls would be investigated considering the dimensionless ratios: μ_w, H_{eff}/d_{50} and L/d_{50}. It still requires the design of an adapted mesh with rectangular measurement cells.

The bi-dimensional character of the simulations can lead to the observation of unrealistic behaviors. The design of a three-dimensional discrete element model would be most useful. The existence of the three dynamic behaviors, identified in the experiments of the present PhD thesis, would be verified with the help of rigid

boundaries. It must be noted that such a study requires significant computational possibilities.

6.3.3 Void ratio as the key of the degradation process

In the light of the present study, the key to mastering the cyclic degradation of dry granular materials lies in the control of the void ratio – at the macroscopic scale – and the coordination number – at the microscopic scale –. Both parameters testify the degree of vibro-fluidization of the assemblage.

When a pile or a sheet-pile is vibratory driven into granular soils, "fast" or "slow" vibrodriving motions can occur depending on the sand density along and beneath the profile (Rodger, 1976). That author selected the ratio between the void ratio and the critical void ratio, e/e_c, as the deciding factor of the type of vibrodriving motion. A similar conclusion was drawn by Vanden Berghe (2001). The prediction of the penetration speed of a profile is related to the consideration of a consitutive relationship: (τ-γ), where γ is the shear strain, based on the evolution of the void ratio, e, throughout the vibratory driving. But according to Youd (1967), a ratio $e/e_c(\Gamma)$ should be considered as the deciding factor according to the influence of the acceleration amplitude, Γ, on the critical void ratio (CVR).

In the experiments and the numerical simulations of the present study, vibro-fluidization was observed for vertical vibration regardless of the initial sand density because of the free surface configuration allowing granular sample to dilate without restraints.

In the future, the occurrence of vibro-fluidization has to be explored under confinement with a control of the evolution of the (p', q) state during the vibration in absence of volume change (in order to draw a parallel with liquefaction and cyclic mobility phenomena).

The design of a conceptual model test – allowing the vibration of an instrumented cell based on the triaxial apparatus – could answer this question with the perspective of developing new critical state lines and new dynamic complete state boundary surfaces in the (q: p': e) space for each acceleration amplitude of vibration, Γ.

The evolution of the internal state of the sample under deviatoric conditions could be investigated, with the DEM, in terms of the porosity, the fabric characteristics (contact density and orientations), the stress field, the contact network, the force chains and the kinetic energy developed by the particles during vibrations. Vibro-fluidization would then be described from micro- to macroscopic scale under confinement conditions in such a way to give a more realistic perspective of the dry sand behavior along the sides of the vibrated pile of sheet-pile and in order to confirm the micromechanical models of fast and slow vibrodriving motion proposed in Section 5.3.

7 Appendix

7.1 Contact mechanics of spherical bodies

7.1.1 Introduction

The present section focuses on contact mechanics of dissipative oblique contacts or impacts of spherical particles. The details of the contact between spherical bodies are highlighted for the purposes of providing contact and damping laws to the discrete element method (DEM).

The nature of these interactions is first investigated under static condition. Hertz's law for normal elastic contact is developed and the normal displacements and stresses around the contact area are presented. The normal indentation between particles is proposed in absence of friction.

Then, relative motions occurring at the contact are introduced with the definitions of sliding, spin and torsion. The tangential loading is reported in static and kinematic friction conditions considering the dual nature of sliding contact. Successively, "gross-slip" and "stick-slip" tangential behaviors are discussed at the microscopic scale of the particles with the help of the well-known slip Coulomb condition. The application of a cyclic tangential force at contact is treated, it leads to energy dissipation quantified by a hysteresis loop in the loading path.

In dynamic condition, elastic normal impact is firstly presented assuming the validity of Hertz's law in quasi-static contact condition. This hypothesis is discussed considering impact duration. The normal inelastic indentation of sphere is characterized in an elasto-plastic half-space. According to the previous work of Johnson (1985), a force-displacement relationship in the fully plastic regime is argued. The normal restitution coefficient is then defined considering elasto-plastic material spheres.

Elastic oblique impact is treated and different approaches are developed such as the 1953 Mindlin-Deresiewicz method and the 1976 Maw, Barber and Fawcett procedure.

Finally, inelastic oblique impact and tangential restitution coefficient are discussed in light of the 1986 Walton and Braun model describing the physics of impacts with the help of three coefficients of friction, normal and tangential restitution.

7.1.2 Normal elastic contact of solids

a. Normal elastic indentation of spheres

In 1882, Hertz was studying optical properties of glass lenses. He was disturbed by the influence of the contact deformation on the interference fringes in the gap between the lenses. His study results finally on the Hertz theory of elastic contact (Hertz, 1882), valid in static and quasi-static contact conditions. The underlying hypothesis can be expressed in these words : each body can be considered as an elastic half-space loaded over a small elliptical region of its plane surface. In the case of spherical bodies in contact, this contact region is circular. The significant dimensions of the contact area must be small in comparison with the

dimensions of each body in such a way that there is no influence of the boundaries of any bodies on the stress field developed in the contact area. Moreover, the significant dimensions of the contact area must be small in comparison with the curvature radius of each surface in such a way that contact deformations remain elastic and to conserve a plane surface outside the contact area. No friction is considered at the interface between the bodies, only a normal pressure is transmitted. The distribution of pressure proposed by Hertz (1882) is:

$$p = p_0 \left(1 - \left(\frac{r}{a} \right)^2 \right)^{1/2} \qquad \text{(Eq. 7-1)}$$

where p_0 is the maximum contact pressure, r the radial direction and a the radius of the contact area. It is possible to demonstrate that this normal pressure distribution is the sole solution of the problem of normal contact between two elastic bodies (Timoshenko and Goodier, 1970). Figure 7-1 illustrates normal contact between two spheres.

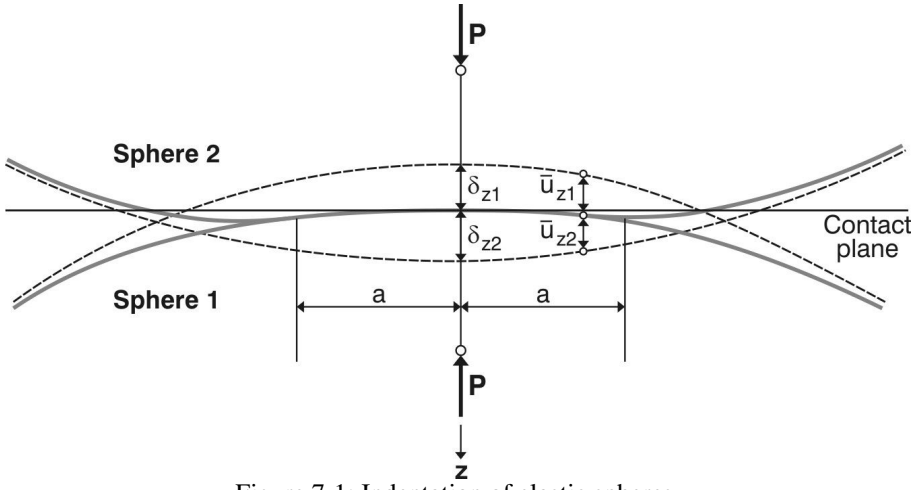

Figure 7-1: Indentation of elastic spheres.

u_z is the normal displacement at the surface of the contact area. The over bar denotes values at the surface of the contact area. P is the normal force transmitted at the interface between the bodies and δ_z is the normal contact indentation. δ_z is the sum of the two sphere indentation components, δ_{z1} and δ_{z2}. Hertz (1882) proposed the following relationships to describe the normal elastic contact of spheres:

$$a = \left(\frac{3PR^*}{4E^*} \right)^{1/3} \qquad \text{(Eq. 7-2)}$$

$$\delta_z = \frac{a^2}{R} = \left(\frac{9P^2}{16R^* E^{*2}} \right)^{1/3} \qquad \text{(Eq. 7-3)}$$

$$p_0 = \frac{3P}{2\pi a^2} = \left(\frac{6PE^{*2}}{\pi^3 R^{*2}} \right)^{1/3} \quad \text{(Eq. 7-4)}$$

where 1/R* is the relative curvature of the contact area:

$$\frac{1}{R^*} = \frac{1}{R_1} + \frac{1}{R_2} \quad \text{(Eq. 7-5)}$$

where R_1 and R_2 are the radius of the sphere 1 and 2. E^* depends on the elastic characteristics of the two spheres in contact:

$$\frac{1}{E^*} = \frac{1-\nu_1^2}{E_1} + \frac{1-\nu_2^2}{E_2} \quad \text{(Eq. 7-6)}$$

where E_1, E_2, ν_1 and ν_2 are the elastic constants of the bodies : the elastic modulus and the Poisson ratios. The relationship between the normal indentation, δ_z, and the normal force, P, is non linear as illustrated in Fig. 7-2.

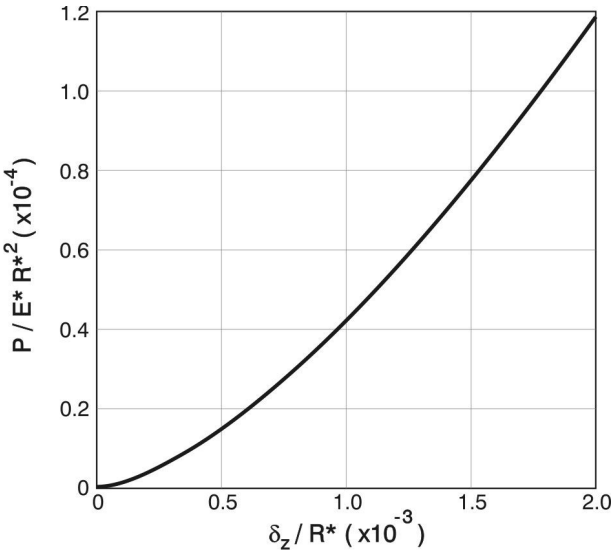

Figure 7-2: Relationship between normal indentation, δ_z, and normal force, P, for $R_1 = R_2$.

The normal force is given by:

$$P = \int_0^a p(r) 2\pi r \, dr = \frac{2}{3} p_0 \pi a^2 \quad \text{(Eq. 7-7)}$$

The secant contact normal stiffness is defined as $K_z = P/\delta_z$:

$$K_z = \frac{4}{3} \sqrt{\delta_z} \sqrt{R^*} E^* \quad \text{(Eq. 7-8)}$$

The tangent normal stiffness of the contact is defined as $k_z = dP/d\delta_z$:

$$k_z = \frac{1}{\xi_z} = 2a\left(\frac{1-\nu_1}{2G_1} + \frac{1-\nu_2}{2G_2}\right)^{-1} \qquad \text{(Eq. 7-9)}$$

k_z is the inverse of ξ_z, the normal contact compliance.

Integrating the normal Hertz pressure distribution over the whole contact area, the surface displacements are calculated considering the point loading of an elastic half-space (Timoshenko and Goodier, 1970). The normal surface displacement, for one of the two contacting spheres, is given in cylindrical polar coordinates by:

$$\overline{u}_{z1}(r) = \frac{1-\nu_1^2}{E_1}\frac{\pi\, p_0}{4a}\left(2a^2 - r^2\right), \; r \le a \qquad \text{(Eq. 7-10)}$$

This expression is valid in the loaded region, $r \le a$. Because of the symmetry of the problem, the tangential displacement, u_θ, is zero at the contact surface. The radial surface displacement is given in cylindrical polar coordinates by:

$$\overline{u}_{r1}(r) = -\frac{(1-2\nu_1)(1+\nu_1)}{3E_1}\frac{a^2}{r}\, p_0\left\{1-\left(1-\frac{r^2}{a^2}\right)^{3/2}\right\}, \; r \le a \qquad \text{(Eq. 7-11)}$$

From equations (7-10) and (7-11), expressions for surface strains are computed with the help of elastic equations and the surface stresses estimated according to the Hooke law (Timoshenko and Goodier, 1970 or Johnson, 1985). The following equations describe the surface stresses in the loaded area in cylindrical polar coordinates:

$$\frac{\overline{\sigma}_{r1}}{p_0} = \frac{1-2\nu_1}{3}\left(\frac{a^2}{r^2}\right)\left\{1-\left(1-\frac{r^2}{a^2}\right)^{3/2}\right\} - \left(1-\frac{r^2}{a^2}\right)^{1/2}, \; r \le a \qquad \text{(Eq. 7-12)}$$

$$\frac{\overline{\sigma}_{\theta 1}}{p_0} = -\frac{1-2\nu_1}{3}\left(\frac{a^2}{r^2}\right)\left\{1-\left(1-\frac{r^2}{a^2}\right)^{3/2}\right\} + 2\nu_1\left(1-\frac{r^2}{a^2}\right)^{1/2}, \; r \le a \qquad \text{(Eq. 7-13)}$$

$$\frac{\overline{\sigma}_{z1}}{p_0} = -\left(1-\frac{r^2}{a^2}\right)^{1/2}, \; r \le a \qquad \text{(Eq. 7-14)}$$

σ_{r1} is the radial stress, $\sigma_{\theta 1}$ the tangential stress and σ_{z1} the normal stress in the loaded area. Contact stresses are defined positive in tension. For expressions of surface displacements outside the loaded area, where $r > a$, Johnson (1985) proceeded in the same way and he obtained:

$$\overline{u}_{z1}(r) = \frac{1-\nu_1^2}{E_1}\frac{p_0}{2a} \times \left\{\left(2a^2 - r^2\right)\arcsin\left(\frac{a}{r}\right) + r^2\left(\frac{a}{r}\right)\left(1-\frac{a^2}{r^2}\right)^{1/2}\right\}, \; r > a \qquad \text{(Eq. 7-15)}$$

$$\overline{u}_{r1}(r) = -\frac{(1-2\nu_1)(1+\nu_1)}{3E_1}\frac{a^2}{r}\, p_0, \; r > a \qquad \text{(Eq. 7-16)}$$

The surface stresses outside the loaded contact area are derived from the displacements:

$$\frac{\overline{\sigma}_{r1}}{p_0} = \frac{-\overline{\sigma}_{\theta}}{p_0} = \frac{(1-2\nu_1)a^2}{3r^2}, \; r > a \qquad \text{(Eq. 7-17)}$$

$$\frac{\overline{\sigma}_{z1}}{p_0} = 0, \; r > a \qquad \text{(Eq. 7-18)}$$

By definition, the normal stress is nonexistent outside the contact area. The surface displacements around the contact area are presented in Fig. 7-3 for $p_0 = 1$ MPa, $E_1 = 10^6$ MPa and $\nu = 0.3$.

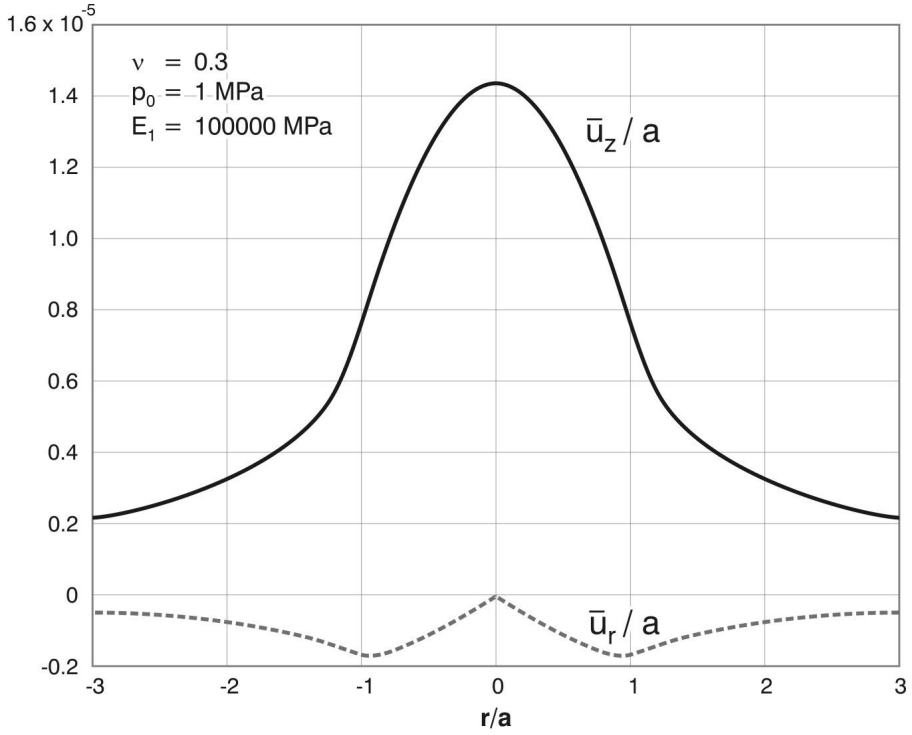

Figure 7-3: Displacements at the surface of the contact area.

The surface stress distributions around the contact area are presented in Fig. 7-4, for $\nu = 0.3$. p_m is the mean contact pressure, $p_m = P/\pi a^2$. The maximum pressure, p_0, is 3/2 times p_m. As observed in Fig. 7-4, the radial stress becomes in tension at the edge of the contact area leading to micro cracks when brittle spheres are pressed in contact. Outside the contact area, surface radial and tangential stresses have similar intensity but they develop respectively in tension and compression.

The stresses along the z-axis are expressed considering an annulus of concentrated force at a radius r (Timoshenko and Goodier, 1970). They are given by equations (7-19), (7-20) and (7-21) and illustrated in Fig. 7-5, for $\nu = 0.3$:

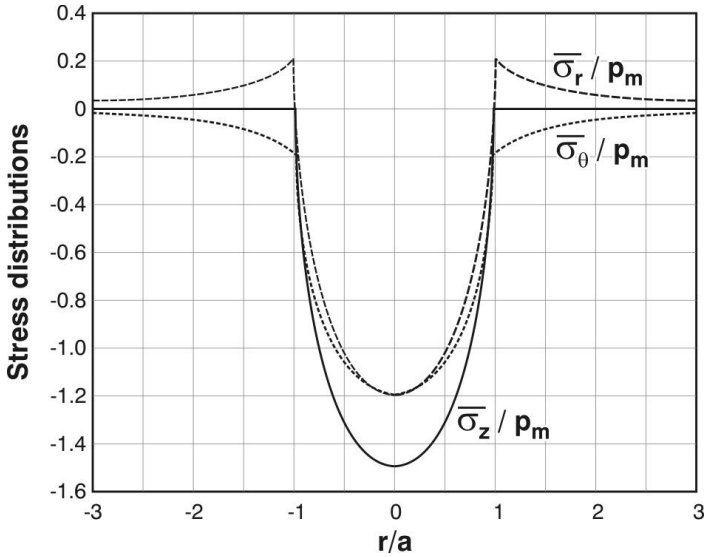

Figure 7-4: Distributions of surface stresses around the contact area, for ν = 0.3.

$$\frac{\sigma_{z1}(z)}{p_0} = -\left(1+\frac{z^2}{a^2}\right)^{-1} \qquad \text{(Eq. 7-19)}$$

$$\frac{\sigma_{r1}(z)}{p_0} = -(1+\nu_1)\left\{1-\left(\frac{z}{a}\right)\arctan\left(\frac{a}{z}\right)\right\}+\frac{1}{2}\left(1+\frac{z^2}{a^2}\right)^{-1} \qquad \text{(Eq. 7-20)}$$

$$\frac{\sigma_{\theta 1}(z)}{p_0} = \frac{\sigma_{r1}(z)}{p_0} \qquad \text{(Eq. 7-21)}$$

They are principal stresses. Along the normal to the contact surface, the tangential stresses begin with five-sixths of the normal stress magnitude. They swiftly decrease and become positive (in tension) at a depth of 1.67a. The shear stress, τ_1, is given by the half of the stress difference, $\tau_1 = (\sigma_{z1}-\sigma_{\theta 1})/2$. As observed in Fig. 7-5, $\tau_1 = 0.31p_o$ at z = 0.48a, beneath the surface of the contact area. It is the maximum shear stress found on the z axis (where r = 0) and on the field of the contact area exceeding the shear stress at the origin ($\tau_1 = 0.10p_o$) and the surface shear stress at the edge of the contact area ($\tau_1 = 0.13p_o$). Hence, the emergence of cracks and plastic deformations during frictionless contact will be located underneath the surface of the contact area leading finally to a failure cone in the indented sphere. The stresses at internal points of the bodies are estimated with the help of the expressions proposed by Huber (1904) and Morton and Close (1922) which notably allow computing stresses along any direction in the body.

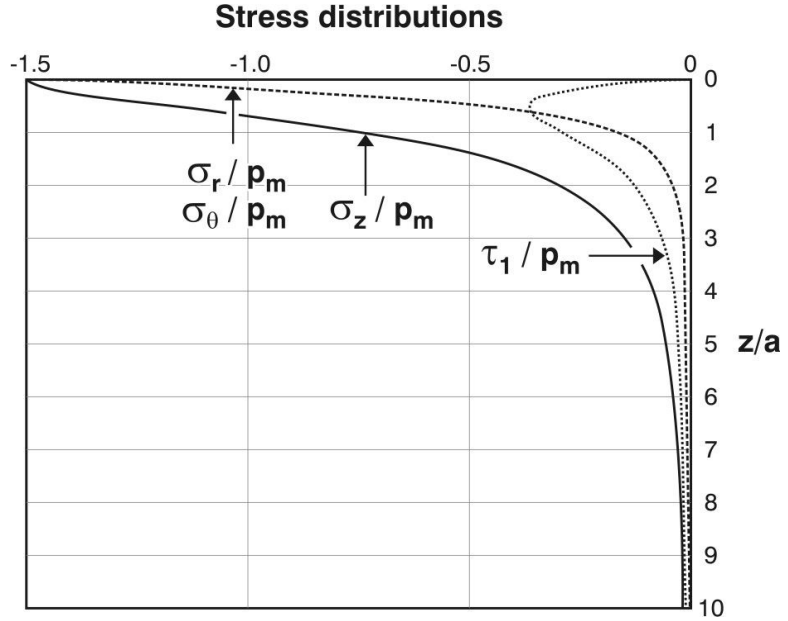

Figure 7-5: Distribution of stresses along the axis of symmetry, for ν = 0.3.

b. Relative motions of surface in contact

The previous section concentrates on normal contact condition without friction and tangential load. When granular matters are loaded, different relative motions can occur at the contact area of the particles : sliding, rolling and spin motion. Before presenting tangential loading and friction considerations, it is necessary to choose a convention to distinguish them. Johnson (1985) proposed to define sliding as the development of a relative translational velocity along an axis included in the contact plane. Sliding leads to tangential loading of the contact area. Rolling is caused by a relative angular velocity around an axis included in the contact plane. Rolling results either in 'tractive rolling' with tangential force transmission to the contact surfaces or in 'free rolling' without tangential stresses transfer. Finally, spin motion is defined by the emergence of a relative angular velocity around the axis perpendicular to the contact plane resulting in a torsional loading of the contact area.

7.1.3 Tangential loading and sliding contact

a. "Gross-slip" motion

Tangential loading occurs in kinetic or static conditions. In kinetic condition, there is the development of a relative translational velocity at the interface between the two contacting spheres, as illustarted in Fig. 7-6. There is no adhering point between both contacting surfaces. The sliding motion is defined as "gross-slip", the slip is complete. The apparition of a translational velocity results in a tangential force opposed to the movement. According to the Newton law of reciprocal actions, there is a second tangential force opposed to the first force in the second sphere.

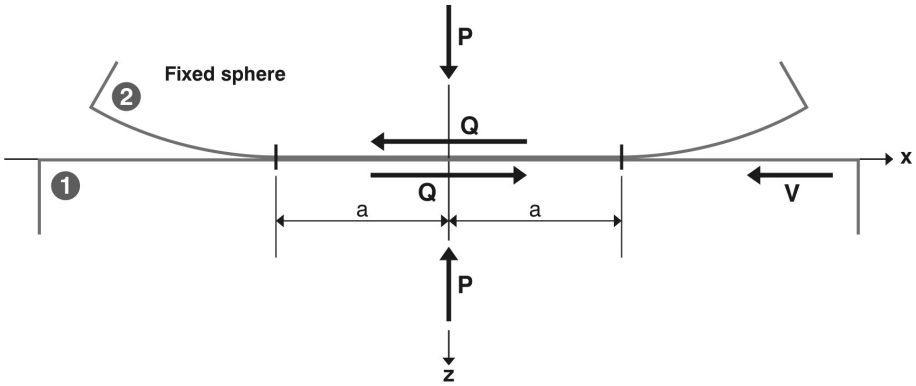

Figure 7-6: “Gross-slip” motion.

Historically, Amontons (1699) proposed the following relationship between tangential stresses and normal pressure, $|q| = \mu|p|$. This relationship is equivalent to the well-known slip Coulomb condition where μ is the kinetic friction coefficient (Coulomb, 1821). Its value depends on the nature of the bodies in contact and on the interface conditions. In “gross-slip” motion, hence in kinetic friction, Amontons law leads to the following tangential stress distribution:

$$q(r) = \mu p_0 \left(1 - \left(\frac{r}{a}\right)^2\right)^{1/2} \qquad \text{(Eq. 7-22)}$$

Integrating this distribution of tangential stress over the contact area and considering the problem of a concentrated tangential force on an elastic half-space, the displacements are determined throughout the sphere 1 in Cartesian coordinates (Johnson, 1985):

$$u_{x1} = \frac{Q}{4\pi G}\left[\frac{1}{\Theta} + \frac{x^2}{\Theta^3} + (1-2\nu)\left\{\frac{1}{\Theta+z} - \frac{x^2}{\Theta(\Theta+z)^2}\right\}\right] \qquad \text{(Eq. 7-23)}$$

$$u_{y1} = \frac{Q}{4\pi G}\left[\frac{xy}{\Theta^3} - (1-2\nu)\frac{xy}{\Theta(\Theta+z)^2}\right] \qquad \text{(Eq. 7-24)}$$

$$u_{z1} = \frac{Q}{4\pi G}\left[\frac{xz}{\Theta^3} + (1-2\nu)\frac{x}{\Theta(\Theta+z)}\right] \qquad \text{(Eq. 7-25)}$$

where Q is the tangential load in the x-direction, G the shear modulus of the half-space and $\Theta^2 = x^2+y^2+z^2$. The displacements are aligned in the tangential load direction and they are opposed to the sliding velocity. If the stress components can be only numerically derivated from these displacements considering elastic governing equations and Hooke’s law, Hamilton proposed stress equations based on the Green method (1949) for calculating stresses everywhere in the sphere (Hamilton and Goodman, 1966 and Hamilton, 1983). Explicit equations for stresses are also given by Sackfield and Hills (1983).

In section 7.1.4, concerning elastic normal impacts, the validity of the Hertz theory in kinetic conditions will be discussed. The normal displacements induced by the application of a tangential force on the contact area are given by equation (7-25). Considering Newton's law of reciprocal actions, the tangential stresses in the first sphere, $q_1(x,y)$, is equal and opposite to the tangential stresses in the second sphere, $q_2(x,y)$. Hence, equation (7-25) becomes:

$$\frac{G_1}{1-2\nu_1}\overline{u_{z,1}(x,y)} = -\frac{G_2}{1-2\nu_2}\overline{u_{z,2}(x,y)} \qquad \text{(Eq. 7-26)}$$

If the spheres have the same elastic constants, equation (7-26) is simplified:

$$\overline{u_{z,1}(x,y)} = -\overline{u_{z,2}(x,y)} \qquad \text{(Eq. 7-27)}$$

As a result, there is no modification of the normal pressure distribution considered in static conditions. The nature of the contact area is always referred to the Hertz definitions (7-2), (7-3) and (7-4) assuming quasi-static contact conditions.

Bufler (1959) investigated contact mechanisms occurring at interface between bodies characterized by different elastic properties. These differences lead, in rare cases, to small displacement of the centre of the contact area. The normal pressure distribution is also slightly stretched. But for usual contact condition, there is no influence of the difference in elastic constants. Subsequently, the tangential loading will be estimated independently from the normal pressure distribution.

b. "Stick-slip" motion

In static condition, there is no relative translational velocity between contacting spheres but they are subjected to tangential load leading to progressive sliding defined as "stick-slip" or partial slip motion. In static friction, the tangential loading is also considered having no influence on the normal pressure distribution. When static friction occurs, under constant normal force, there is the development of two concentric zones within the contact area. The first region is a circle centered on the symmetry axis of the contact area. In this region, there is no slip, the surfaces in contact adhere, this is the "stick area" or "stick circle" and $|Q| < \mu|P|$ where μ represents the static friction coefficient.

Around this zone, there is the development of the "slip ring" where $|Q| = \mu|P|$. This annulus is marked by the emergence of "micro-slips". Figure 7-7 illustrates the presence of the 'stick-slip' zones within the contact area where c is the stick circle radius.

In the stick region, the tangential force Q leads to the emergence of a rigid tangential displacement, δ_{x1}, balanced by elastic tangential surface displacement, $\overline{u}_{x1}$. The energy of the tangential loading is stocked in an elastic recoverable way. There is no slip component resulting in energy dissipation. Hence, in the stick circle, $|Q| < \mu|P|$ and $\delta_{x1} = \overline{u}_{x1}$. The tangential rigid contact displacement is then defined as:

$$\delta_x \equiv \left(\delta_{x1} - \delta_{x2}\right) = \left(\overline{u}_{x1} - \overline{u}_{x2}\right) \qquad \text{(Eq. 7-28)}$$

If the spheres have the same elastic properties, all the points of the contact area are subjected to the same tangential displacement and $\delta_{x1} = \delta_{x2}$.

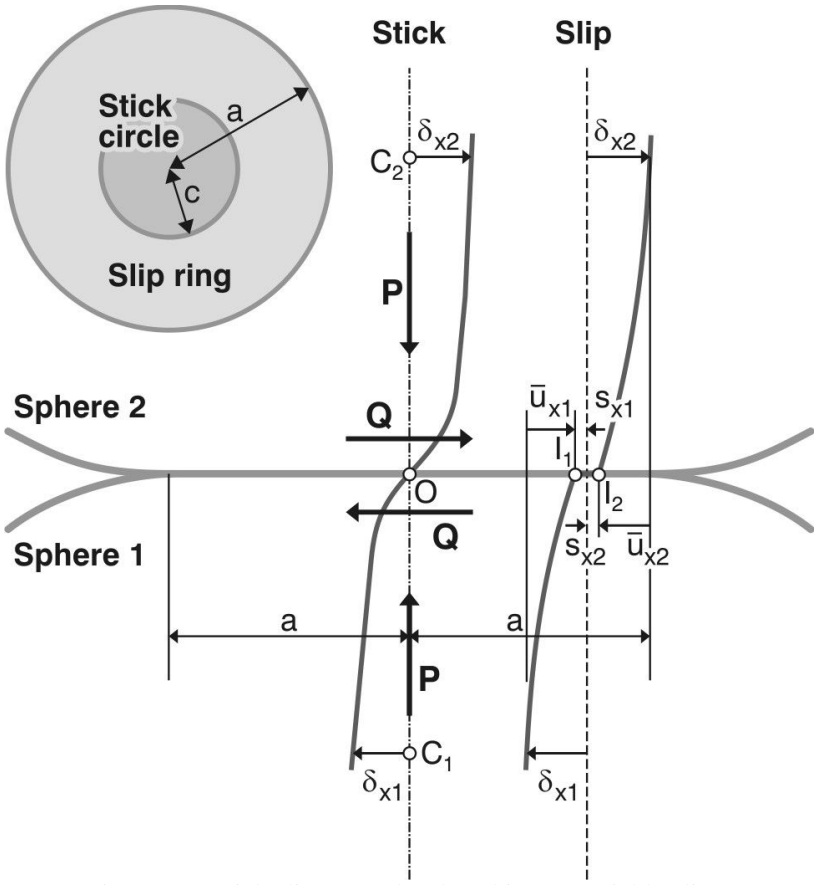

Figure 7-7: Stick-slip zones developed in tangential loading.

In the slip region, under the action of the tangential force, the point C_1 moves through tangential rigid displacement, δ_{x1}, relative to the point 0. This rigid displacement leads to a surface elastic tangential displacement of the point I_1 relative to the point C_1, $\bar{u}_{x1}$. The absolute displacement of the point I_1 relative to the point 0 is the slip component, $s_{x1} = \bar{u}_{x1} - \delta_{x1}$. The contact slip component between I_1 and I_2 is defined as:

$$s_x \equiv s_{x1} - s_{x2} = \left(\bar{u}_{x1} - \delta_{x1}\right) - \left(\bar{u}_{x2} - \delta_{x2}\right) \qquad \text{(Eq. 7-29)}$$

The successive micro-slips lead to energy dissipation. Hence, the motion is not reversible in the sense of energy conservation. In the slip annulus, the slip Coulomb condition is encountered, $|Q| = \mu|P|$, and $s_{x1} = \bar{u}_{x1} - \delta_{x1}$. Moreover, the sliding motion is opposed to the tangential force in each body.

Before determining the expression of δ_x, it is necessary to investigate the tangential stress distribution on the different regions of the contact area.

First, the entire contact area is assumed in stick condition and presents uniform tangential displacement, the condition $|Q| < \mu|P|$ is valid everywhere in the

contact area and there is no slip motion. To ensure this condition, there is only one valid tangential stress distribution:

$$q(r) \div \left(1 - \frac{r^2}{a^2}\right)^{1/2} \qquad \text{(Eq. 7-30)}$$

This distribution theoretically results in infinite values at the edges of the contact area where the normal pressure vanishes. Hence, to conserve contact at the edges of the contact area, it should be necessary to require physically impossible infinite friction coefficient to ensure the no slip condition (7-28). The tangential stress distribution (7-30) results then in micro-slips at the edge of the contact area leading to the emergence of the slip ring presented in Fig. 7-7. In the centre of the contact area, the normal pressure is maximal and the tangential stresses are reduced resulting in the stick circular region (as shown in Fig. 7-7).

Mindlin (1949) proposed to consider a method of superposition to take into account the partial slip nature of the contact. He superposed two tangential stress distributions to model the simultaneous stick-slip contact condition.

When the contact is on the point to begin "gross-slip" motion, the tangential stress at the surface of the contact area can be expressed as:

$$q'(r) = \mu p_0 \left(1 - \frac{r^2}{a^2}\right)^{\frac{1}{2}} \qquad \text{(Eq. 7-31)}$$

valid in the entire contact area, $r \leq a$. To compute the tangential displacements resulting from this distribution, the problem of uni-directional tangential force applied on circular region is considered. Tangential displacements within the loaded area are given in Maw et al. (1976) in the direction of the traction, u_{x1}, and in the direction perpendicular to the traction, u_{y1}, in cylindrical polar coordinates:

$$\overline{u}_{x1}^{'} = \frac{\pi \mu p_0}{32 G_1 a}\left\{2(2-\nu_1)(2a^2 - r^2) + \nu_1 r^2 \cos 2\theta\right\} \qquad \text{(Eq. 7-32a)}$$

$$\overline{u}_{y1}^{'} = \frac{\pi \mu p_0}{32 G_1 a}\nu_1 r^2 \sin 2\theta \qquad \text{(Eq. 7-32b)}$$

Then, Mindlin (1949) considers a second tangential stress distribution only valid on the stick region, $r \leq c \leq a$:

$$q''(r) = -\frac{c}{a}\mu p_0 \left(1 - \frac{r^2}{c^2}\right)^{\frac{1}{2}} \qquad \text{(Eq. 7-33)}$$

The tangential displacements, computed as for the previous distribution, are given for the stick region:

$$\overline{u}_{x1}^{''} = -\frac{c}{a}\frac{\pi \mu p_0}{32 G_1 c}\left\{2(2-\nu_1)(2c^2 - r^2) + \nu_1 r^2 \cos 2\theta\right\} \qquad \text{(Eq. 7-34a)}$$

$$\bar{u}''_{y1} = -\frac{c}{a}\frac{\pi \mu p_0}{32 G_1 c}\nu_1 r^2 \sin 2\theta \qquad \text{(Eq. 7-34b)}$$

For the micro-slips region, the stress distribution (7-33) leads to the following tangential displacements:

$$\bar{u}''_{x1} = \frac{\mu\, p_0}{16 G_1 a}\left[2(2-\nu_1)\left\{(2a^2 - r^2)\arcsin\left(\frac{a}{r}\right) + a\left(r^2 - a^2\right)^{1/2}\right\}\right.$$

$$\left. + \nu_1\left\{r^2 \arcsin\left(\frac{a}{r}\right) + \frac{a\left(3a^2 - r^2\right)\left(r^2 - a^2\right)^{1/2}}{r^2}\right\}\cos 2\theta\right] \qquad \text{(Eq. 7-35a)}$$

$$\bar{u}''_{y1} = \frac{\mu\, p_0 \nu_1}{16 G_1 a}\left\{r^2 a \sin\left(\frac{a}{r}\right) + \frac{a\left(3a^2 - r^2\right)\left(r^2 - a^2\right)^{1/2}}{r^2}\right\}\sin 2\theta \qquad \text{(Eq. 7-35b)}$$

The resultant elastic tangential displacements are given in the stick region adding equation (7-32) and (7-34) while in the slip region adding equations (7-32) and (7-35). The radius of the stick zone can be estimated integrating the tangential stress distributions, q' over the whole contact area and q'' over the stick circle. The integration leads to $c = a(1-Q/\mu P)^{1/3}$. This relationship is illustrated in Fig. 7-8.

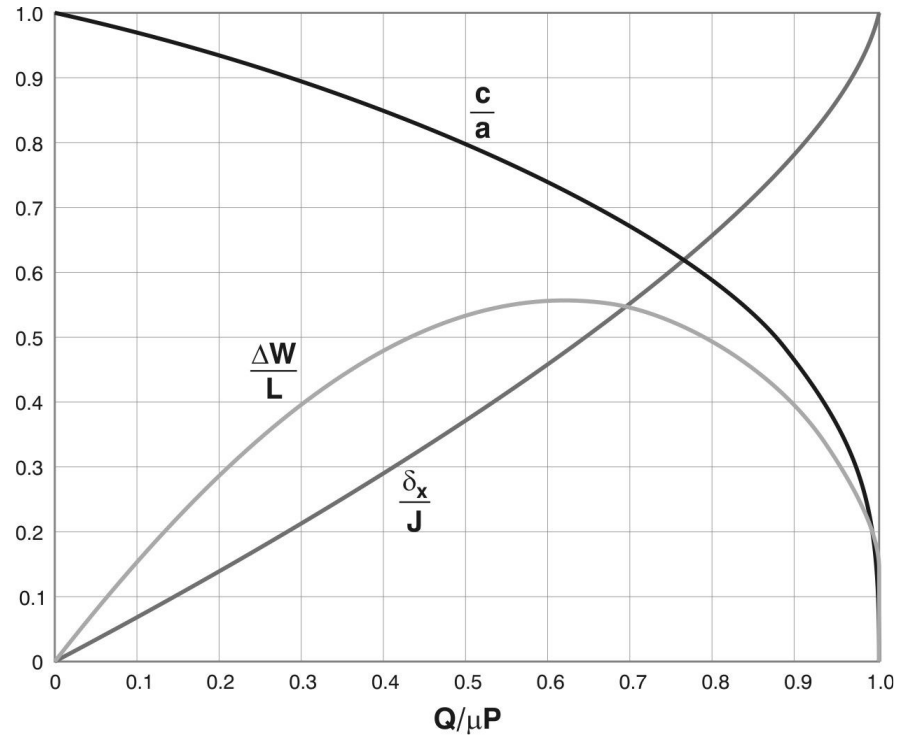

Figure 7-8: Relationship between the stick circle radius, c, the tangential rigid displacement, δ_x, the energy loss, ΔW, and the tangential force, Q.

Once the elastic tangential displacements are known, the tangential rigid displacement can be expressed.

In the "stick circle", $\delta_{x1} = \bar{u}_{x1}$ where $\bar{u}_{x1}$ is given by equations (7-32a) and (7-34a). There is no slip components s_x and s_y. The tangential rigid displacement is then given by:

$$\delta_x = \frac{3\mu P}{16a}\left(\frac{2-\nu_1}{G_1}+\frac{2-\nu_2}{G_2}\right)\frac{a^2-c^2}{a^3} \qquad \text{(Eq. 7-36)}$$

Considering $c = a(1-Q/\mu P)^{1/3}$:

$$\delta_x = \frac{3\mu P}{16a}\left(\frac{2-\nu_1}{G_1}+\frac{2-\nu_2}{G_2}\right)\left\{1-\left(1-\frac{Q}{\mu P}\right)^{2/3}\right\} \qquad \text{(Eq. 7-37)}$$

The relationship between the tangential rigid displacement, δ_x, and the tangential load, Q, is non linear, as illustrated in Fig. 7-8, where:

$$J = \frac{3\mu P}{16a}\left(\frac{2-\nu_1}{G_1}+\frac{2-\nu_2}{G_2}\right) \qquad \text{(Eq. 7-38)}$$

In the "slip ring", the slip component s_x is computed with the help of equation (7-29) where δ_x is given by equation (7-37) and u_x adding equations (7-32a) and (7-35a) for the two spheres. When slip occurs at contact edge, there is the development of a sliding velocity resulting in the decrease of the tangential stress transmission in the "slip ring". The micro-slips relax the tangential stresses in the slip annulus and cancel it at the contact edge. Hence, according to the method of superposition of Mindlin (1949), the tangential stresses and the singularities at the edges of the contact area vanish.

The slip component s_y, perpendicular to the tangential force direction, is computed as $s_y = u_y$ where u_y is obtained adding equations (7-32b) and (7-35b) for the two spheres. The slip component, s_y, and the elastic displacement, u_y, are different from zero. But they can be neglected under several conditions. Indeed, the non-axisymmetric terms in sin θ and cos θ add at the most around 9% to the terms in r^2 and in certain circumstances, they can even cancel out. The readers can refer to Maw et al. (1976) for more considerations about the treatment of these particular terms. In a general way, the tangential stress distribution, proposed by Mindlin (1949), which is everywhere parallel to the contact force direction, is assumed to be a good solution to describe the "stick-slip" nature of elastic sphere contact.

c. Torsional loading

Torsional loading can result from spin motion applied around the normal axis of contact. For a circular contact area, assuming firstly the entire contact area in stick condition, the tangential stresses are expressed by the following equation:

$$q(r) = q_0 r\left(a^2 - r^2\right)^{-1/2} \qquad \text{(Eq. 7-39)}$$

where q_0 is the maximum tangential stress. This distribution leads to a rigid rotation in the sphere, $\beta_1 = \pi q_0/4G_1$ and a twisting moment, $M_z = 4\pi a^3 q_0/3$. Introducing this latter in equation (7-39), the tangential stress distribution producing spin motion and no slip anywhere in the contact area becomes:

$$q(r) = \frac{3M_Z r}{4\pi a^3}\left(a^2 - r^2\right)^{-1/2} \qquad \text{(Eq. 7-40)}$$

This distribution presents infinite values at the contact area boundaries in such a way that a slip ring appears. Hence, as for tangential loading, two concentric zones are defined within the contact area, a stick circle and a micro-slips ring. If M_z increases, the stick region is progressively reduced until it contracts to a single point. The contacting spheres are free to spin and there is a constant maximum residual twisting moment depending on the friction coefficient, as demonstrated by Lubkin (1951):

$$M_Z = \frac{3\pi\mu Pa}{16} \qquad \text{(Eq. 7-41)}$$

Figure 7-9 illustrates the change of the twisting moment, M_z, as a function of the total rigid rotation at the contact : $\beta = \beta_1 + \beta_2$.

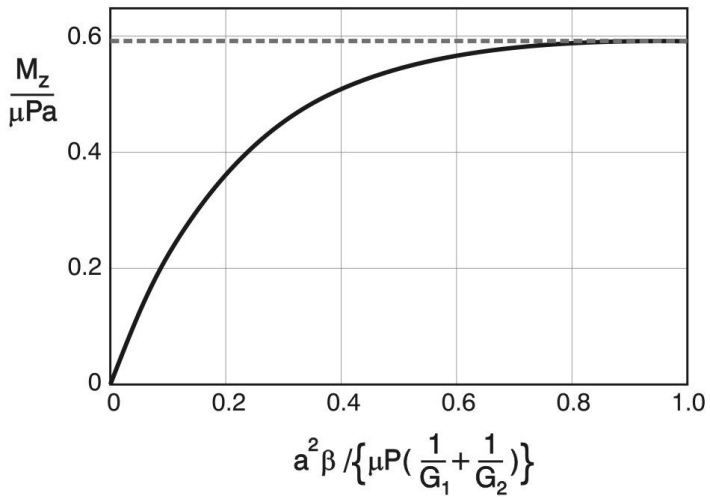

Figure 7-9: Relationship between the twisting moment and the rigid rotation at the contact, after Johnson (1985).

As for tangential loading, the normal pressure distribution and the radius of the contact area can be defined by Hertz's law.

d. Rolling contact

Rolling contact is caused by a relative angular velocity around an axis included in the contact plane. Sliding motion can occur at the interface between the spheres leading to the emergence of a tangential force in the body. Even if there is no sliding at the contact, it does not mean that there is no tangential load transfer between the spheres. As for tangential and torsional loading, the normal pressure

distribution and the contact area dimensions can be described by Hertz's law. 'Stick-slip' regions develop within the contact area during rolling motion. This latter can be considered with the help of tangential loading approach, presented in section 7.1.3a and 7.1.3b, due to the similitude between both problems although in rolling, the influence of the elastic surface deformations on the velocities of the surface points should be taken into account. Indeed, these deformations result in additional slip motions called "creep" which influence the interaction between the elastic contacting spheres.

e. Energy loss during tangential cyclic loading

Considering oscillating tangential loading of a circular contact area, Mindlin et al. (1952) demonstrated the existence of a symmetrical hysteresis loop in the δ_x-Q loading diagram, as illustrated in Fig. 7-10.

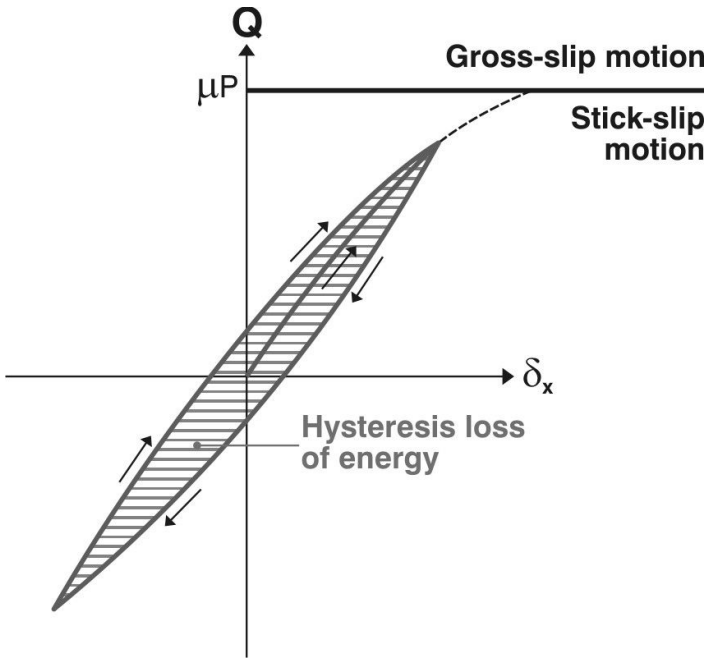

Figure 7-10: Hysteresis loop for an oscillating tangential loading.

The work done by the tangential force Q is dissipated by the reversal of the micro-slip in the slip ring : $c \leq r \leq a$. Mindlin et al. (1952) proposed the following relationship to express the energy loss per cycle at the contact area:

$$\Delta W = \frac{9\mu^2 P^2}{10a}\left(\frac{2-\nu_1}{G_1}+\frac{2-\nu_2}{G_2}\right)\left[1-\left(1-\frac{Q}{\mu P}\right)^{5/3}-\frac{5Q}{6\mu P}\left\{1-\left(1-\frac{Q}{\mu P}\right)^{2/3}\right\}\right]$$

$$\times\left[1-\left(1-\frac{Q}{\mu P}\right)^{5/3}-\frac{5Q}{6\mu P}\left\{1-\left(1-\frac{Q}{\mu P}\right)^{2/3}\right\}\right] \qquad \text{(Eq. 7-42)}$$

During cyclic loading, the tangential load Q could lead to the fatigue of the slip ring surface in the form of attrition or micro-cracks. An experimental study of Goodman & Brown (1962) supports equation (7-42).

The relationship between the energy loss, ΔW, and the tangential load, Q, is illustrated in Fig. 7-8, where:

$$L = \frac{9\mu^2 P^2}{10a}\left(\frac{2-\nu_1}{G_1}+\frac{2-\nu_2}{G_2}\right) \qquad \text{(Eq. 7-43)}$$

7.1.4 Elastic normal impact

Elastic normal impact between spherical bodies can be considered with the help of Hertz's law assuming quasi-static conditions of contact. Herewith, the deformations are restrained to the contact area and given by the static theory. The validity of this hypothesis will be critiqued afterwards. Figure 7-11 illustrates the impact between two spheres.

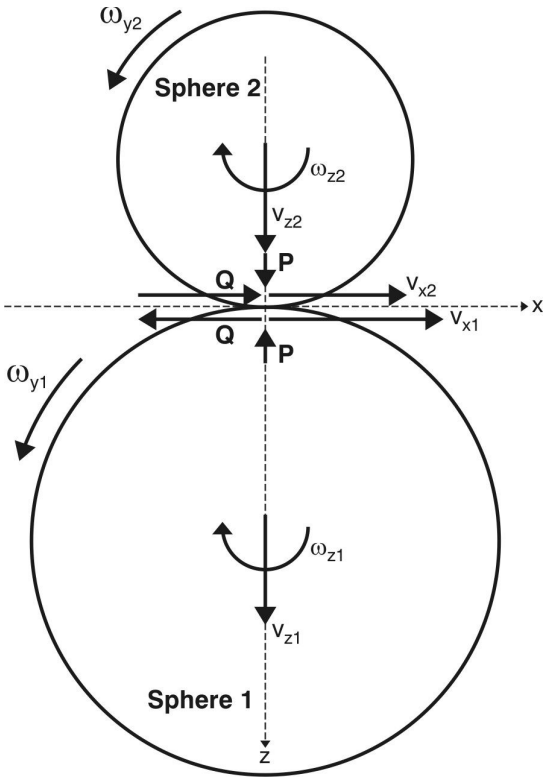

Figure 7-11: Impact of spheres.

Assuming normal impact, $\omega_{z1} = \omega_{z2} = \omega_{y1} = \omega_{y2} = v_{x2} = v_{x1} = Q = 0$. The normal impact velocity, V_z, is defined by:

$$V_z = v_{z2} - v_{z1} = \frac{d\delta_z}{dt} \qquad \text{(Eq. 7-44)}$$

where t is the time. The conservation of the momentum at the contact leads to:

$$P = m_1 \frac{dv_{z1}}{dt} = m_2 \frac{dv_{z2}}{dt} \qquad \text{(Eq. 7-45)}$$

Inserting equation (7-44) into equation (7-45):

$$-\frac{m_1 + m_2}{m_1 m_2} P = \frac{d}{dt} V_z = \frac{d^2 \delta_z}{dt^2} \qquad \text{(Eq. 7-46)}$$

The maximum normal indentation during the impact, δ_z^{max}, is calculated integrating equation (7-46):

$$\delta_z^{max} = \left(\frac{15 m V_z^2}{16 \sqrt{R^*} E^*} \right)^{\frac{2}{5}} \qquad \text{(Eq. 7-47)}$$

where m is the equivalent mass : $1/m = 1/m_1 + 1/m_2$. Deresiewicz (1968) obtained, by double integration of equation (7-46), the evolution of the normal indentation as a function of the impact time:

$$t = \frac{1}{V_z} \int_0^{\delta_z^{max}} \frac{d\delta_z}{\sqrt{1 - \left(\delta_z / \delta_z^{max} \right)^{5/2}}} \qquad \text{(Eq. 7-48)}$$

The impact duration is deduced from this latter:

$$T_c = \frac{2}{V_z} \int_0^{\delta_z^{max}} \frac{d\delta_z}{\sqrt{1 - \left(\delta_z / \delta_z^{max} \right)^{5/2}}} = 2.94 \frac{\delta_z^{max}}{V_z} \qquad \text{(Eq. 7-49)}$$

The accuracy of equation (7-49) was verified by Greszczuk (1980) with the help of impact experiments between aluminium and composite plates impacted by steel spheres. Figure 7-12 presents the evolution of the normal indentation as a function of the impact time.

Considering equation (7-47), the impact duration becomes:

$$T_c = 2.87 \left(\frac{m^2}{R^* E^{*2} V_z} \right)^{1/5} \qquad \text{(Eq. 7-50)}$$

The preceding relationships are valid assuming quasi-static contact conditions. The deformation is quasi-static if the impact duration allows the stress waves to travel several times the impacted particle diameter assuming stress free particles prior to impact.

Love (1952) suggested that this condition is encountered if the minimum impact duration is $4R/c_0$, where R is the impacted particle radius and c_0 the one-dimensional elastic propagation velocity of the stress wave in the material.

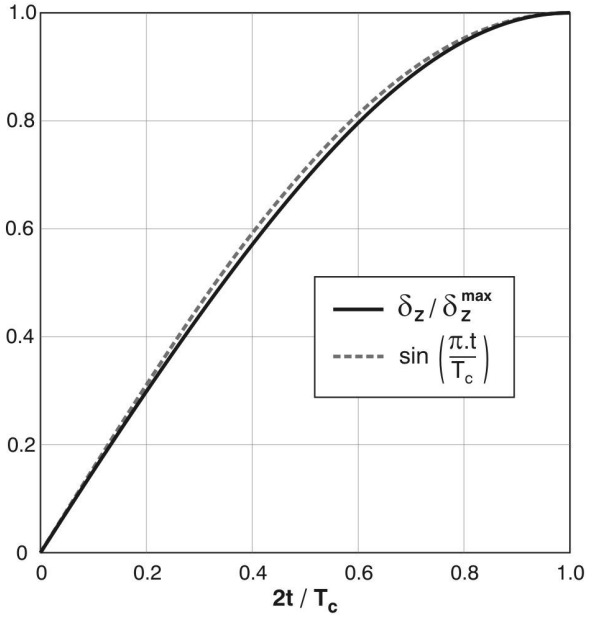

Figure 7-12: Relationship between the normal indentation and the time during impact.

c_0 depends on the material elastic properties and on its density: $c_0 = (E/\rho)^{1/2}$. Hence, the impact is quasi-static if the contact duration is greater than the propagation time of the stress wave in the material or $(c_0/V_z)^{1/5} >> 1$. It is possible to understand the limitation of such condition considering the impact of spheres very different in terms of their diameter.

Hunter (1957) considered the impact response of an half-space. He proposed to model it with a spring-dashpot model, the spring representing the elastic response and the dashpot taking into account the energy dissipation. If the time constant of the model is smaller than the impact duration, the normal force variation during impact will be largely controlled by the elastic spring, in a quasi-static way, and the energy absorbed by the dashpot will be a weak amount of the total impact energy. As for the Love criterion, it is necessary that $V_z << c_0$ to reduce the time constant of the spring-dashpot model.

According to the Love criterion and the model of Hunter, the importance of the impact velocity on the impact behavior is remarked. Moreover, the concept of energy dissipation during impact has been introduced.

7.1.5 Inelastic normal impact

a. Normal inelastic indentation of spheres

As for elastic impact, the hypothesis of quasi-static contact is assumed while the impact velocity remains weak in comparison with the propagation velocity of the stress waves through the material. An elasto-plastic material is postulated for the two contacting spheres.

During normal impact, a contact pressure, p, develops at the contact interface between the two spheres. The maximal value of this pressure is p_0 and p_0 is 3/2 times the mean normal contact pressure. The shear stress at the contact, τ_1, is given by the half of the stress difference, $\tau_1 = (\sigma_{z1}-\sigma_{\theta 1})/2$. According to the Tresca criterion, the yield strength of the material is reached when max $|\sigma_{z1}-\sigma_{\theta 1}| = Y$, where Y is the yield stress. As observed in Fig. 7-5, the maximum value of τ_1 is $0.31p_o$ at $z = 0.48a$. Following the Tresca criterion, $\max|\sigma_{z1}-\sigma_{\theta 1}| = 0.62p_0 = Y$. Hence, once p_0 reaches Y/0.62, plastic deformations initiate beneath the surface of the contact area and the material reaches its elasto-plastic limit : $p_0 = 1.6Y$ and $p_m = 1.1Y$.

The normal load P, necessary to initiate the yielding maximum pressure, p_0, is derived from equation (7-4):

$$P_Y = \frac{\pi^3 R^2}{6E^{*2}}(p_0)_Y^3 \qquad \text{(Eq. 7-51)}$$

where indices Y represent value at the yield stress. The normal indentation at the yield stress is referred to equation (7-3) using the normal load P_Y supplied by equation (7-51).

In 1974, Richmond et al. have provided the solution for the theoretical indentation of a rigid-perfectly plastic solid by a rigid sphere and compared this solution with the experimental indentation of a near perfectly plastic material. The fully plastic regime was shown to be reached once $p_m = 3Y$.

Between $p_m = 1.1Y$ and $p_m = 3Y$, the impact behavior is considered as elasto-plastic. The transition between the elastic regime and the perfectly plastic regime is difficult to describe. Once the yield stress is reached, the plastic deformations are first restrained by the material, which continues to behave as in the elastic regime, and their magnitudes are similar to the corresponding elastic deformations. In this particular regime, it is difficult to build a rigorous theoretical relationship between the normal indentation and the normal force.

Successively, Hill (1950) and Ford and Alexander (1963) proposed stress-strain relationships for an elasto-perfectly plastic material.

In 1971, Hardy et al. performed a finite element study of the contact behavior in the elasto-plastic regime. They concentrated their analysis on the deformations and stresses occurred, in an elasto-perfectly plastic half-space, by the indentation of a sphere. This study provides a finite element description of the stress distribution around the contact area in the elasto-plastic regime.

Developed by Marsh (1964) and Johnson (1970), the cavity model allows describing normal indentation in elasto-plastic regime with the help of a hydrostatic core included in elastic-perfectly plastic material.

In 1980, Matthews proposed a non-linear model, based on the 1928 Norbury and Samuel experiments. This model, valid until the plastic regime, is in agreement with the study of Richmond et al. (1974) which performed a rigorous theoretical study of the indentation of a rigid-perfectly plastic solid by a rigid sphere and compared their results with experimental indentation of a near perfectly plastic material.

Follansbee and Sinclair (1984) studied, with finite element code, the quasi-static normal indentation of an elastic-plastic half-space by a rigid sphere and analyzed in detail the contact response in the plastic regime.

According to Johnson (1985), it is possible to define some relationship between the normal force and the normal indentation in the plastic regime. This relationship was build with the help of equations (7-51) and (7-3) resulting from Hertz's law and assuming the underlying hypotheses: $p_0 = 1.6Y$ at the yield stress and $p_m = 3Y$ at the onset of the perfectly plastic regime. In the fully plastic domain:

$$\frac{P}{P_Y} = 5.6\frac{\delta_z}{\delta_{zY}} \qquad \text{(Eq. 7-52)}$$

In elastic contact conditions, normal indentation and deflexion (the recovery of the initial contact curvature) occur similarly without energy loss and without permanent deformation. When plastic deformations occur, the contact between the spheres occurs with energy dissipation. A permanent crater is formed. Hence, it is necessary to define the normal indentation, δ_z, during loading and the elastic deflexion, δ_{ze}, during unloading in such a way to estimate the depth of the residual permanent indentation, δ_{zR}, assuming $\delta_z = \delta_{ze}+\delta_{zR}$.

During loading, δ_z is estimated with the help of equation (7-52). During unloading, elastic deflexion is considered because after impact, the recovered material is the elastic part of the crater deformation. Elastic deflexion is computed considering equations (7-2) and (7-3) resulting from Hertz's law and equation (7-52):

$$\frac{P}{P_Y} = 0.355\left(\frac{\delta_{ze}}{\delta_Y}\right)^2 \qquad \text{(Eq. 7-53)}$$

Equation (7-53) is the expression for elastic normal deflection during impact.

Figure 7-13 illustrates the relationship between normalized normal force and normalized normal indentation in the fully plastic regime. The elastic range is described by Hertz's law. The elasto-plastic range can be approximated by Hertz's law resulting in a weak error. In the perfectly plastic range, the plastic indentation curve is computed with the help of equation (7-52). The crater depth curve is computed assuming $\delta_{zR}=\delta_z-\delta_{ze}$ and considering equation (7-53) for the elastic deflexion which is presented in Fig. 7-13 as the gap between the crater depth curve and the plastic indentation curve.

Similar developments are presented more recently in Stronge (2000) who provides a complete synopsis of the different relationships between normal force and indentation, in the elastic, elasto-plastic and fully plastic ranges.

b. Normal coefficient of restitution

Another way to take into account the energy dissipation during normal impact is to define a coefficient of normal restitution in terms of the resultant velocity of the impacting spheres. This coefficient quantifies the kinetic energy restituted to the body after impact. Starting from kinetic equations before and after the normal impact, the normal restitution coefficient, ε, may be defined as:

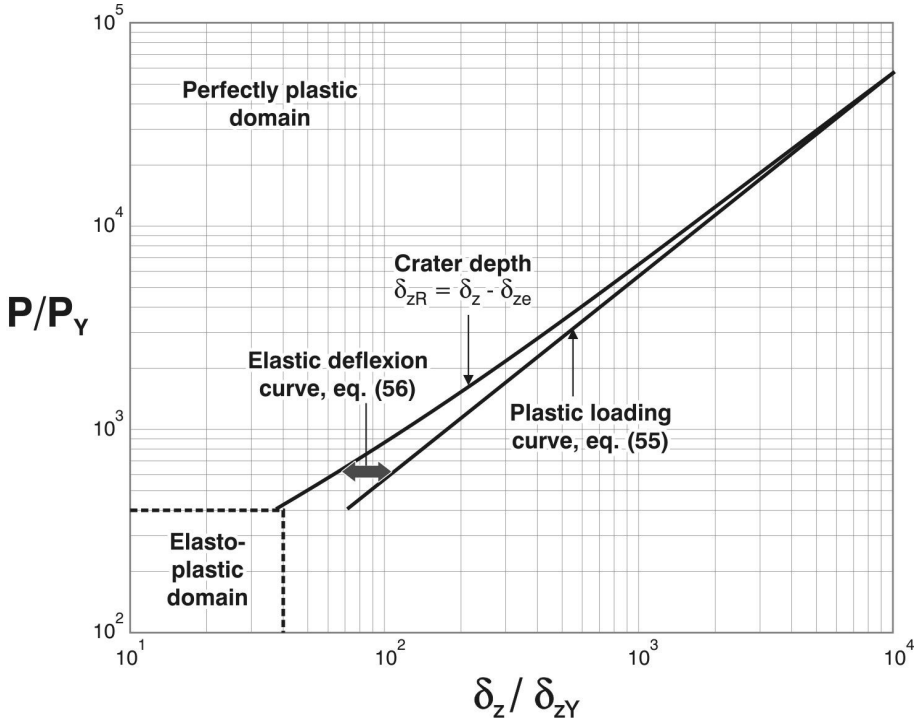

Figure 7-13: Elasto-plastic indentation of a sphere into an elasto-plastic half-space.

$$\varepsilon^2 = \frac{W'}{W} = \frac{\frac{1}{2}m\left(v'_{z2} - v'_{z1}\right)^2}{\frac{1}{2}m\left(v_{z2} - v_{z1}\right)^2} = \left(\frac{V'_z}{V_z}\right)^2 \qquad \text{(Eq. 7-54)}$$

where W is the kinetic energy before normal impact, W' the restored kinetic energy after normal impact, m the equivalent mass and the indices ' indicate that the variables are considered after impact. Hence,

$$\varepsilon = \frac{V'_z}{V_z} \qquad \text{(Eq. 7-55)}$$

The inelastic normal impact behavior is then described in a kinematic way. The normal restitution coefficient can be determined with the help of impact experiments with spheres of different materials for different normal impact velocities.

The normal restitution coefficient can be also expressed in an analytical way, introducing expressions for P in plastic regime and P' in elastic deflexion. The kinetic energy before normal impact is equivalent to the work carried out by the normal force during loading:

$$W = \frac{1}{2}mV_z^2 = \int_0^{\delta_z^{max}} P d\delta_z \qquad \text{(Eq. 7-56)}$$

After the maximal normal indentation is reached, the kinetic energy of the rebound equals the work recovered from the elastic deflexion:

$$W' = \frac{1}{2} m V_z'^2 = \int_0^{\delta_z^{max}} P' d\delta_{ze} \qquad \text{(Eq. 7-57)}$$

Considering expressions for P in plastic regime and P' in elastic deflexion, the restitution coefficient is given by:

$$\varepsilon^2 \equiv \frac{W'}{W} = \frac{3\pi^{5/4} 4^{3/4}}{10} \left(\frac{p_d}{E^*} \right) \left(\frac{\frac{1}{2} m V_z^2}{p_d R^{*3}} \right)^{-1/4} \qquad \text{(Eq. 7-58)}$$

where p_d is the dynamic mean pressure estimated for different materials in Tabor (1948) and Crook (1952). Assuming $p_d = 3Y_d$ in the fully plastic regime, the normal restitution coefficient becomes:

$$\varepsilon \approx 3.8 \left(\frac{Y_d}{E^*} \right)^{1/2} \left(\frac{\frac{1}{2} m V_z^2}{Y_d R^{*3}} \right)^{-1/8} \qquad \text{(Eq. 7-59)}$$

where Y_d is the dynamic yield stress. Experiments of Tabor (1948) confirm the accuracy of this development, as illustrated in Fig. 7-14.

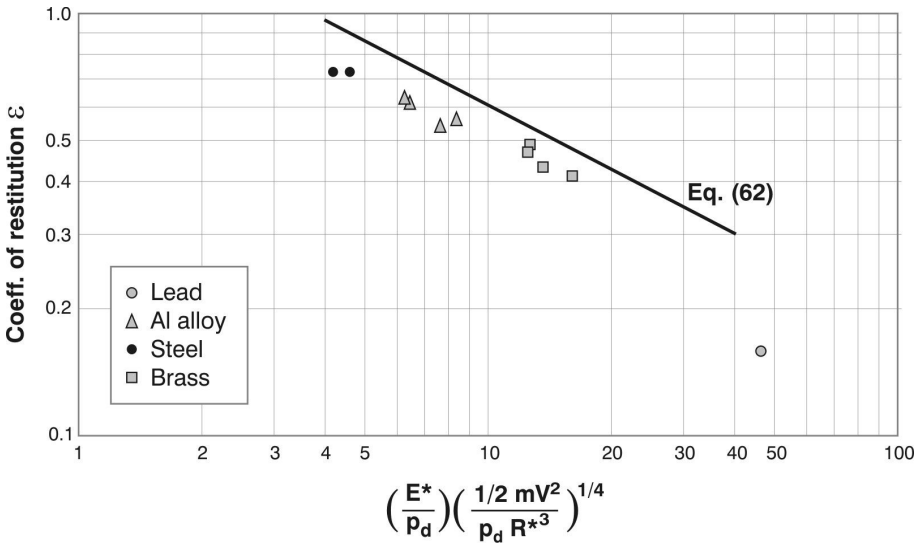

Figure 7-14: Variation of the normal restitution coefficient for different materials and impact velocities, after Tabor (1948).

The normal restitution coefficient depends on the elastic properties, on the dimensions and masses of the contacting particles, on the dynamic yield stress of the particle materials and on the impact velocity, as illustrated in Fig. 7-15.

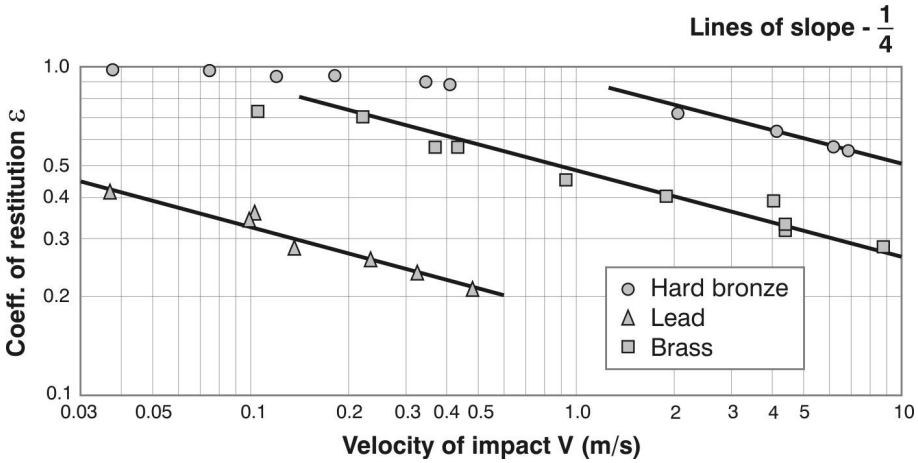

Figure 7-15: Influence of the impact velocity on the normal restitution coefficient of a steel ball impacting different material blocks, after Goldsmith (1960) and Johnson (1985).

In 1997, Thornton proposed an analytical solution for the normal restitution coefficient for the contact between elastic-perfectly plastic spheres (neglecting the elasto-plastic transition). Thornton expressed the restitution coefficient considering the ratio of impact velocity to yield velocity rather than in terms of material properties such as yield stress which remains difficult to estimate.

The normal restitution coefficient is also described for impacts of viscoelastic spherical bodies in Johnson (1985) and Stronge (2000) or more recently in Pöschel et al. (2008) which characterize the restitution coefficient notably for viscoelastic and adhesive viscoelastic spheres. It is to note that the Maxwell viscoelastic model results in a normal restitution coefficient which is not dependant of the normal impact velocity.

The impact duration is also modified by the energy dissipation. The curve presented in Fig. 7-12 is no longer valid for inelastic impact. The impact duration is the sum of the plastic indentation time and the elastic rebound time: $T_c = t_p + t_e$ (Johnson, 1985).

7.1.6 Elastic oblique impact

As for the normal impact, the contact will be considered as quasi-static. The conservation of the momentum for oblique impact is expressed as:

$$\frac{\left(1+\frac{m_i R_i^2}{I_i}\right)}{m_i} Q = \frac{d^2\delta_x}{dt^2} \qquad \text{(Eq. 7-60)}$$

where i refers to the particle i. $I = 2mR^2/5$ for spherical bodies and $I = mR^2/2$ for two dimensional cylinders where R is the particle radius. The oblique impact is illustrated in Fig. 7-11 where ω_{y1}, ω_{y2}, v_{x2}, v_{x1} and Q are non zero values.

In section 7.1.3a, the effect of the tangential stresses on the normal pressure distribution has been discussed. There is no influence of the tangential stress distribution so long as the sphere materials are elastically similar. The coefficient, ζ, introduced by Dundurs and Lee (1972), characterizes the influence of elastic constants:

$$\varsigma = \frac{1}{2}\left[\frac{\left\{\frac{(1-2\nu_1)}{G_1}\right\} - \left\{\frac{(1-2\nu_2)}{G_2}\right\}}{\left\{\frac{(1-\nu_1)}{G_1}\right\} + \left\{\frac{(1-\nu_2)}{G_2}\right\}}\right] \qquad \text{(Eq. 7-61)}$$

$\zeta = 0$ when the elastic constants of the spheres are similar. Even if their elastic constants differ, the effect of this difference is often weak (Maw et al. 1976 and 1981). Nevertheless, during oblique impact, simultaneous variations in normal and tangential forces are observed and they result in micro-slips and changes in tangential force intensity. It seems that the frictional and stick-slip nature of the contact does not only depend on the normal and tangential forces but also on their history.

a. The Mindlin and Deresiewicz (MD) approach (1953)

In 1953, Mindlin and Deresiewicz proposed a theory describing elastic sphere contact under varying oblique forces. Their analysis of oblique contact condition is based on the development of different approaches summarized hereafter in three different cases of contact conditions. Under the quasi-static hypothesis, these considerations are directly applicable to elastic oblique impact.

Normal force varying, tangential force zero

The first Mindlin and Deresiewicz approach is the simple case of varying normal force assuming the absence of tangential force. This approach corresponds to the Hertz theory.

Normal force constant, tangential force varying

In this second approach, the contact is considered at a particular moment wherein the normal force is constant and the tangential force is varying. The normal indentation is described by Hertz's law. An incremental approach – where the micro-slips, at the edges of the contact area, are considered – is defined to compute the tangential rigid displacement. This approach is firstly described in Mindlin (1949) and is explained in section 7.1.3b.

There is always a part of the contact area wherein the slip Coulomb condition is encountered. If the entire contact area is sliding, there is "gross-slip" motion and $|q| = \mu|p|$ everywhere.

In this approach, the evolution of the tangential force during loading or unloading is considered with a constant normal force. Hence, only the history of the tangential loading or unloading is analyzed. The reasoning is also valid with

displacement considerations. Figure 7-16 illustrates the tangential loading and unloading path for a constant normal force.

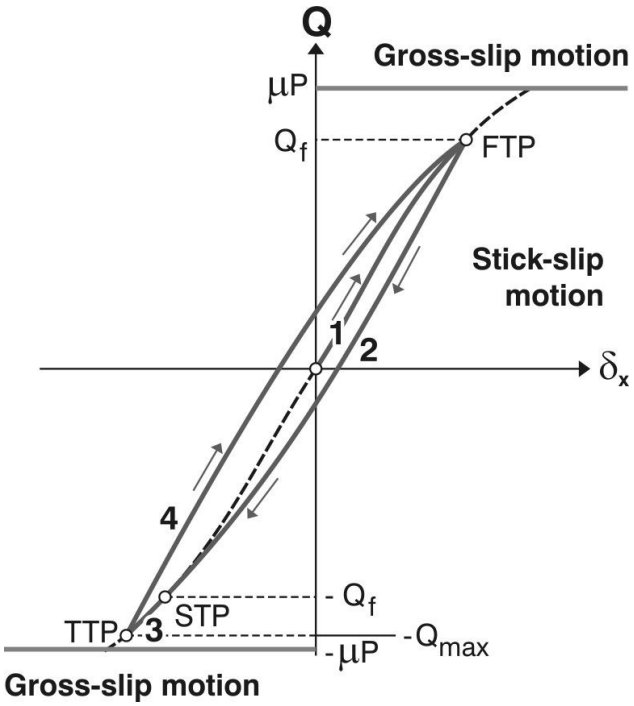

Figure 7-16: Tangential loading and unloading path for the case of constant normal force.

During tangential loading, the relationship between tangential rigid displacement and tangential force may be described by the curve 1 (in Fig. 7-16) corresponding to equation (7-37). The tangential compliance for the case of constant normal force and monotonically increasing tangential force is then given by $\xi_x = d\delta_x/dQ$:

$$\xi_x = \frac{d\delta_x}{dQ} = \frac{1}{8a}\left(\frac{2-\nu_1}{G_1} + \frac{2-\nu_2}{G_2}\right)\left(1-\frac{Q}{\mu P}\right)^{-1/3} \qquad \text{(Eq. 7-62)}$$

The tangential compliance is the inverse of the tangential contact stiffness, k_x:

$$k_x = \frac{dQ}{d\delta_x} = 8a\left(\frac{2-\nu_1}{G_1} + \frac{2-\nu_2}{G_2}\right)^{-1}\left(1-\frac{Q}{\mu P}\right)^{1/3} \qquad \text{(Eq. 7-63)}$$

If the contact is tangentially relaxed before the onset of "gross-slip" motion, there is a first turning point (FTP) on the δ_x - Q path, for $Q=Q_f$. The tangential unloading path may be described by curve 2 corresponding to the following equation:

$$\delta_x = \frac{3\mu P}{16a}\left(\frac{2-\nu_1}{G_1}+\frac{2-\nu_2}{G_2}\right)\left\{2\left(1-\frac{Q_{FTP}-Q}{2\mu P}\right)^{\frac{2}{3}}-\left(1-\frac{Q_{FTP}}{\mu P}\right)^{\frac{2}{3}}-1\right\} \qquad \text{(Eq. 7-64)}$$

The tangential stiffness for the case of constant normal force and unloading tangential force is given by:

$$k_x = \frac{dQ}{d\delta_x} = 8a\left(\frac{2-\nu_1}{G_1}+\frac{2-\nu_2}{G_2}\right)^{-1}\left(1-\frac{Q_f-Q}{2\mu P}\right)^{1/3} \qquad \text{(Eq. 7-65)}$$

Afterwards, the tangential force reaches a second turning point (STP), at $Q = -Q_f$. The tangential unloading path becomes:

$$\delta_x = \frac{3\mu P}{16a}\left(\frac{2-\nu_1}{G_1}+\frac{2-\nu_2}{G_2}\right)\left\{1-\left(1+\frac{Q}{\mu P}\right)^{\frac{2}{3}}\right\} \qquad \text{(Eq. 7-66)}$$

This equation is described by the curve 3 and it is valid until the tangential load reaches its maximal value, $Q=-Q_{max}$, just before "gross-slip" motion. The tangential stiffness for this unloading tangential curve 3 is given by:

$$k_x = 8a\left(\frac{2-\nu_1}{G_1}+\frac{2-\nu_2}{G_2}\right)^{-1}\left(1+\frac{Q}{\mu P}\right)^{1/3} \qquad \text{(Eq. 7-67)}$$

The third turning point (TTP) is encountered and there is tangential reloading path described by curve 4 and corresponding to:

$$\delta_x = -\frac{3\mu P}{16a}\left(\frac{2-\nu_1}{G_1}+\frac{2-\nu_2}{G_2}\right)\left\{2\left(1-\frac{Q_{TTP}+Q}{2\mu P}\right)^{\frac{2}{3}}-\left(1-\frac{Q_{TTP}}{\mu P}\right)^{\frac{2}{3}}-1\right\} \qquad \text{(Eq. 7-68)}$$

The tangential stiffness for the reloading tangential curve 4 is given by:

$$k_x = 8a\left(\frac{2-\nu_1}{G_1}+\frac{2-\nu_2}{G_2}\right)^{-1}\left(1-\frac{Q-Q_{TTP}}{2\mu P}\right)^{1/3} \qquad \text{(Eq. 7-69)}$$

With the previous relationships due to Mindlin and Deresiewicz (1953), the tangential loading and unloading path for the case of constant normal force has been described.

Normal force varying, tangential force varying

As explained previously, the description of the elastic oblique impact behavior should take into account the coupled evolution of normal and tangential forces which simultaneously vary. The underlying concept of the complete Mindlin-Deresiewicz (MD) method (1953) is constructing tangential loading and unloading path for a constant normal displacement, considering the previous and the current normal displacements and travelling from one curve to another by the way of a series of elementary steps.

The following hypotheses are assumed. Firstly, the surface of the contact area and the normal pressure distribution are computed with the help of Hertz's theory. Secondly, the variations of the normal and tangential displacements are unconnected. The problem can be considered by means of the superposition of both normal and lateral effects. Thirdly, rolling and torsional effects are neglected. Finally, each incremental step begins from a simple loading history condition. This later may be defined as the condition in which the state of the system (δ_z, δ_x, P, Q) may be also reached with the help of a first single tangential loading, unloading and reloading path for a constant normal displacement, regardless of the actual loading path.

Figure 7-17 illustrates simultaneous increasing of normal and tangential forces.

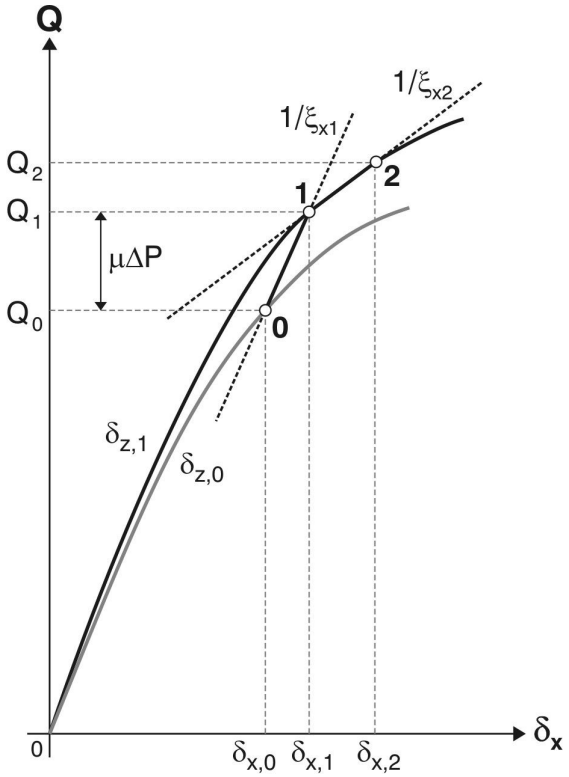

Figure 7-17: Tangential loading paths for increasing normal and tangential forces, after Di Renzo and Di Maio (2004).

Considering the current state of the system is located at point 0 and assuming the simple loading history condition, point 0 is considered as positioned on a constant normal displacement curve, δ_{z0}, starting from the graph origin. During tangential loading, if the following slippage condition is encountered, $Q_1-Q_0 \geq \mu|\Delta P|$, there is a transition from the normal displacement loading curve δ_{z0} to δ_{z1}. It is therefore interesting to consider both occurrences which occur during loading from the point 0 to the points 1 and 2 respectively.

If the increment of tangential force ΔQ is smaller than $\mu \Delta P$, there is no change in constant normal curve. The tangential force, is smaller than Q_1 and given by:

$$Q = Q_0 + \frac{(\delta_x - \delta_{x,0})}{\xi_{x1}} \qquad \text{(Eq. 7-70)}$$

where ξ_x is the tangential compliance of the contact, $\xi_x = d\delta_x/dQ$. Mindlin and Deresiewicz (1953) proposed to compute ξ_{x1} considering $\xi_{x1} = d\delta_x/dQ|_{Q=0}$ where δ_{x1} is given by equation (7-37) and considered at point 1 where the radius of the contact area is a_1. Hence, the tangential load Q becomes:

$$Q = Q_0 + (\delta_x - \delta_{x,0}) 8 a_1 \left(\frac{2-\nu_1}{G_1} + \frac{2-\nu_2}{G_2} \right)^{-1} \qquad \text{(Eq. 7-71)}$$

According to Mindlin and Deresiewicz (1953), the relationship between δ_x and Q is momentarily linear before the slip Coulomb condition is encountered everywhere in the contact area.

If the increment of tangential force ΔQ is greater than $\mu \Delta P$, there is a change in constant normal curve. The calculation is performed in two steps. Q_1 is given by equation (7-71) where $Q = Q_1$ and Q_2 is computed considering $Q_1+\Delta Q$ where ΔQ is estimated along the constant normal displacement curve δ_{z1}, considering equation (7-37) for tangential loading.

Mindlin and Deresiewicz (1953) describe, in the same way, the different cases which may occur during contact: P decreasing and Q increasing, P increasing and Q decreasing and finally P decreasing and Q decreasing. All the particular contact conditions around the turning points are also developed. The complete MD method is also explained more recently by Vu-Quoc and Zhang (1999) or Di Renzo and Di Maio (2004).

b. Maw, Barber and Fawcett (MBF) approach (1976, 1981)

In their papers of 1976 and 1981, Maw et al. proposed a new approach to consider elastic oblique impact of spheres on an elastic half space. The main principle of their method is to consider the contact area divided in a finite number of concentric rings for which the normal and tangential stress distributions are estimated for each calculation time step. Summarizing, the tangential stresses are derivated from the tangential displacements provided in section 7.1.3b and considering the "stick-slip" nature of the contact.

The main hypotheses behind the MBF approach are similar to the first and second hypotheses of Mindlin and Deresiewicz (1953) procedure : the surface of the contact area and the normal pressure distribution are computed with the help of the Hertz theory and the variations of the normal and tangential displacements are unconnected. The MBF method is less restrictive than the complete MD method because rolling and torsional loading are considered and the simple loading history condition vanishes.

The particularity of the MBF approach is describing the incident conditions with dimensionless parameter ψ_1:

$$\psi_1 = \frac{\kappa\left(v_{x2} - v_{x1}\right)}{\mu\left(v_{z2} - v_{z1}\right)} \qquad \text{(Eq. 7-72)}$$

where ψ_1 is a dimensionless angle of incidence and $\kappa = k_x/k_z$. κ is the stiffness contact ratio. This latter is a constant close to unity, depending on the material properties. Considering equation (7-9) for the normal stiffness and equation (7-63) with Q = 0 for the tangential contact stiffness:

$$\frac{1}{\kappa} = \frac{\frac{\left(1-\frac{\nu_1}{2}\right)}{G_1} + \frac{\left(1-\frac{\nu_2}{2}\right)}{G_2}}{\frac{(1-\nu_1)}{G_1} + \frac{(1-\nu_2)}{G_2}} \qquad \text{(Eq. 7-73)}$$

The contacting spheres behavior depends on the dimensionless parameter χ:

$$\chi = \frac{\kappa\left(1+\frac{m_i R_i^2}{I_i}\right)}{2} \qquad \text{(Eq. 7-74)}$$

where i refers to the particle i. Figure 7-18 illustrates the tangential force variation as a function of the impact time for a steel disk impacting a half-space of similar material.

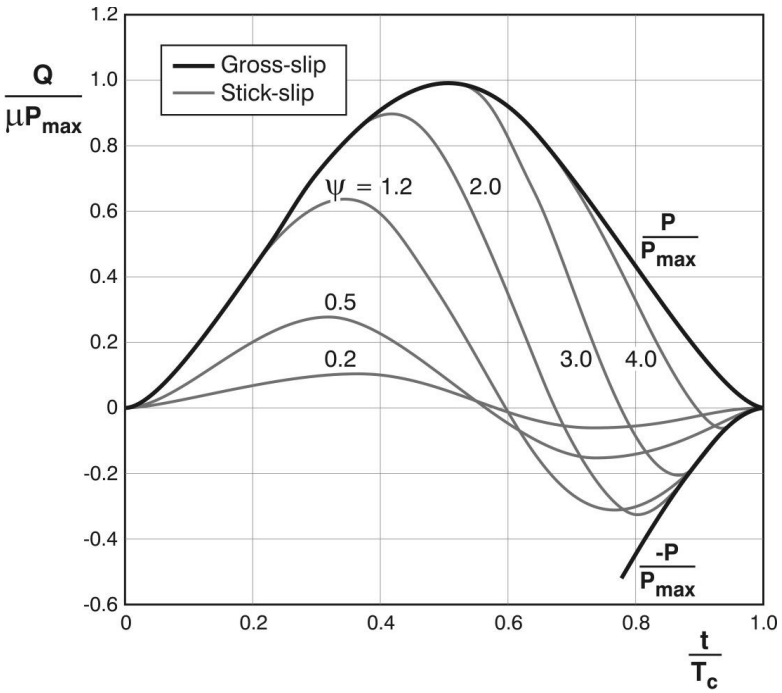

Figure 7-18: Normalized tangential force, for different angles of incidence, as a function of the normalized impact time, for a steel disk ($\nu = 0.28$, $\chi = 1.256$).

When $\psi_1 \leq 1$, the incident impact angle is small, there is no "gross-slip" motion at the beginning of the impact, the sphere sticks to the half space. This condition is represented by curves $\psi_1 = 0.2$ and $\psi_1 = 0.5$ in Fig. 7-18. While these curves do not coincide with the dimensionless normal curve of impact P/P_{max}, the contact behaves in "stick" or "stick-slip" regime. When the sphere vertically penetrates the half space due to the normal contact pressure, the contact area grows. Once the maximum compression point is reached, the surface of the contact area decreases and the interface cannot sustain the traction at the edges of the contact area, micro-slips then occur. A slip ring spreads inward the contact area and if the whole contact area slides, there is "gross-slip" motion.

When $1 < \psi_1 < 4\chi\text{-}1$, the incident angle increases and the impact begins and finishes with "gross-slip". The curves $\psi_1 = 1.2$, $\psi_1 = 2.0$, $\psi_1 = 3.0$ and $\psi_1 = 4.0$ in Fig. 7-18 illustrate this behavior. Due to friction, the uniform sliding velocity decreases, during contact, until zero and the two contacting surfaces are then completely stuck. Energy dissipations are also expected with "micro-slip" events after the maximum compression point.

Finally, if $\psi_1 \geq 4\chi\text{-}1$, "gross-slip" motion occurs during all the impact time. In the tangential direction, the surface can be considered as a tangential spring. Considering the case where $\psi_1 = 1.2$, "gross-slip" motion occurs at the beginning of the impact. There is the development of a sliding velocity and the friction forces load the spring with elastic energy. Around $t/T_c = 0.25$, the contact area behaves in "stick-slip" mode but the tangential spring continues to extend. The normalized tangential force oscillation cycles normally until the end of the impact time, where there is "gross-slip". Indeed, the ratio of tangential to normal natural frequencies of contact is larger than unity and given by:

$$\frac{\omega_x}{\omega_z} = \left(\kappa \left(1 + \frac{m_i R_i^2}{I_i} \right) \right)^{1/2} = \sqrt{2\chi} \qquad \text{(Eq. 7-75)}$$

If the radius of giration, $(I/m)^{1/2}$, is decreased, χ is increased and the number of reversals in the tangential force during the cycle is increased, as illustrated in Maw et al. (1976).

Introducing a dimensionless parameter, ψ_2, it is possible to describe the reflection conditions of the oblique impact:

$$\psi_2 = \frac{\kappa\left(v'_{x2} - v'_{x1}\right)}{\mu\left(v_{z2} - v_{z1}\right)} \qquad \text{(Eq. 7-76)}$$

where ψ_2 is a dimensionless angle of reflexion in the same sense that ψ_1. With these two parameters, it is possible to determine the tangential velocity direction at the exit of the impact. A positive reflective angle is one for which the tangential velocity before and after impact are oriented in the same sense.

Maw et al. (1981) have checked their theoretical model of oblique collisions using disks of different materials sliding on an air table and colliding a clamped block of similar material. The disk floats on an air film maintained by a series of jets in a level table. Frictionless conditions are thus provided. Figures 7-19 and 7-20 present dimensionless angles of reflexion, ψ_2, for sphere impact with different materials.

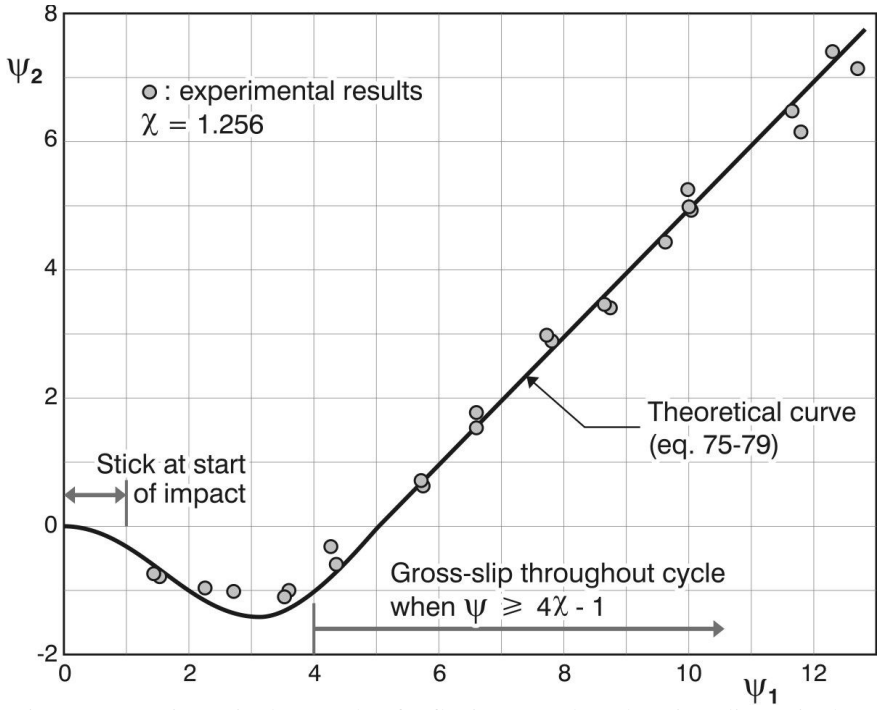

Figure 7-19: Dimensionless angle of reflexion, ψ_2, plotted against dimensionless angle of incidence, ψ_1, for a steel disk ($\nu = 0.28$, $\chi = 1.256$), from Maw et al. (1981).

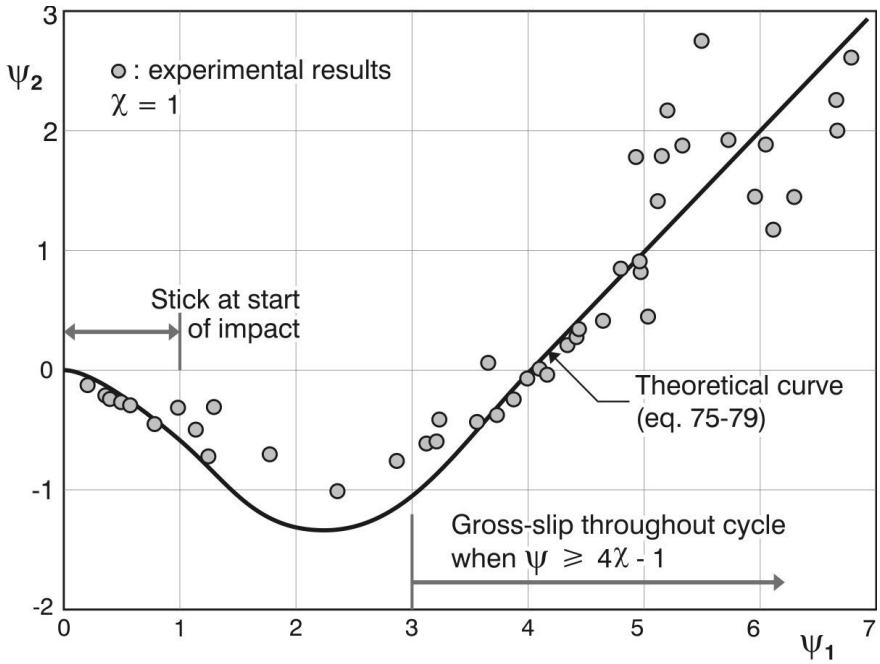

Figure 7-20: Dimensionless angle of incidence, ψ_2, plotted against dimensionless angle of incidence, ψ_1, for a "rubber" disk ($\nu = 0.5$, $\chi = 1.0$), from Maw et al. (1981).

The black lines illustrate the relationship between ψ_1 and ψ_2 described by the MBF procedure (equations 7-72 to 7-76). The experimental results of Maw et al. (1981) seem to be generally in agreement with the previous theory.

In Fig. 7-19, steel spheres impacts ($\nu = 0.28$ and $\chi = 1.256$) were recorded. When $\psi_1 < 4\chi$, negative angles of reflexion were obtained demonstrating the effects of the tangential elasticity of the contact area within the "stick-slip" regime. These negative angles of rebound are generally supported by high friction coefficient. It can be noted that, in this "stick-slip" regime, the values of ψ_2 were lower than the values asserted by the theory (black line). It is explained by the dissipation of energy occuring during tangential loading of the contact area. Actually, it is necessary to recall that, as in the complete MD method, there is no consideration of the contact inelasticity in the MBF approach.

In Fig. 7-20 presenting "rubber" disk impacts, the inelastic character of the contact is again accentuated with lower experimental values than the predicted values.

The MBF solution seems to be currently the most precise approach to describe elastic oblique impact, as critiqued recently in Di Renzo and Di Maio (2004).

More recently, Sondergaard et al. (1990) have also studied oblique impact of rigid sphere on flat plate.

7.1.7 Inelastic oblique impact

The calculation of the contact pressure necessary to initiate the onset of yield in sliding contact has been made notably by Jonhson and Jefferis (1963) studying plastic flow and residual stresses in rolling and sliding contact. Considering the well-known Tresca and von Mises criteria, they described the influence of the friction coefficient on the elastic limit and on the shakedown limit.

According to the Tresca criterium, the onset of the normal yield is located underneath the surface of the contact area while $\mu < 0.25$. Then, when $0.25 < \mu < 0.44$, there is lateral yielding of the contact area. Beyond $\mu = 0.44$, yielding occurs at the contact surface.

According to the von Mises criterium, when $\mu < 0.3$ the onset of the yield is located underneath the surface of the contact area. If the friction coefficient increases beyond these limits, yielding occurs at the surface. Following this approach, the physical actors of the yielding, for "gross-slip" motion and partial slip regime, are the friciton coefficient, μ, the poisson ratio, ν, and the elastic limit in simple shear. Nevertheless, the friction coefficient seems to be the governing parameter.

As explained in section 7.1.6b, Maw et al. (1976 and 1981) have established three regimes of oblique impact. When $\psi_1 < 4\chi$, negative angles of reflexion, ψ_2, were obtained demonstrating the effects of the tangential elasticity within the stick regime. The energy is stocked in tangential elastic deformations and restored during impact leading to reversible tangential velocities at the contact area. The emergence of these negative angles of rebound depends on the stiffness contact ratio, κ (itself depending on ν and G) and mainly on μ.

Walton (1982) and Walton and Braun (1986) introduced a simple model, inspired by the work of Cundall and Strack (1979), and including three coefficients to describe completely the impact behavior: ε, μ and β.

In the Walton's model, ε is the normal restitution coefficient, characterizing the incomplete restitution of the normal component of the impact velocity.

μ is the friction coefficient. Friction intervenes in the model when "gross-slip" is occurring. The normal and tangential velocity components are then linked with μ.

β is the rotational or tangential restitution coefficient. Actually, it seems that, as in normal loading, there is an energy dissipation during tangential rigid displacement and hence it could be possible to define, in a similar way, a tangential restitution coefficient:

$$\beta = \frac{V_x^{'}}{V_x} \qquad \text{(Eq. 7-77)}$$

This latter is used for collisions which restore, to the tangential velocity, a part of the energy stored in the tangential deformations of the contact surface. For real particles, β ranges within -1 for smooth, frictionless particles to 1 for perfectly rough, perfectly elastic particles. As explained in Drake (1988), when β = 1, the relative tangential velocity is not influenced by the collision. There is no loss or transfer of spin energy into translational energy. When β=-1, all the stored elastic energy is recovered, the relative tangential velocity is reversed. There is no energy loss but it can be transformation of spin energy into translational energy. It could correspond to the black line represented by Maw et al. (1981) in Fig. 7-19 and Fig. 7-20, for which the rebound angle would be located on the black line, in the range $\psi_1 < 4\chi$. According to the MBF approach, the tangential restitution coefficient should depend on μ and on the elastic constants of the particle material (ν and G).

During a frictional contact, the tangential impulse transferable from the first sphere to the second is limited by the friction coefficient and the normal impulse according to slip Coulomb condition. Requiring the conservation of angular momentum at the contact, Walton and Braun (1986) demonstrated that this conservation condition can be translated in terms of the tangential restitution coefficient:

$$\beta < -1 + \mu\left(1 + \frac{mR^2}{I}\right)\left|\frac{(v_{z2} - v_{z1})}{(v_{x2} - v_{x1})}\right|(1 + \varepsilon) \qquad \text{(Eq. 7-78)}$$

where mR^2/I is 2 for disks and 5/2 for spheres. With respect to this relationship, the tangential restitution coefficient seems to be dependant on the friction coefficient, on the inertial and geometrical particle properties, on the normal and tangential impulses and on the normal restitution coefficient.

In the Walton model, the friction and the tangential restitution are properties of the contact area. Hence it is not possible to determine their values a priori without knowing the nature of the rebound, this latter occurring with or without sliding motion.

Contrarily to the MD and to the MBF approaches, the Walton model imposes that there is no simultaneous sticking and sliding regions. The contact is in stick regime with or without elastic energy loss until the slip Coulomb condition is reached, and then there is "gross-slip" motion.

Foerster et al. (1994) compared some experimental results of binary collisions between spheres and collisions between sphere and frictional flat plate

with the MBF and the Walton models. To build the comparison, dimensionless incidence and reflexion angles, ψ_1 and ψ_2, were introduced for the Walton model:

$$\psi_2 = -\beta\psi_1 \qquad \text{(Eq. 7-79)}$$

in no slip condition and

$$\psi_2 = \psi_1 - \frac{7}{2}(1+\varepsilon)\mu\,\mathrm{sgn}(v_{x2} - v_{x1}) \qquad \text{(Eq. 7-80)}$$

in "gross-slip" condition. In both regimes, the relationship between the dimensionless angles is linear, contrarily to the relationship for the MBF model.

When binary collisions between glass spheres are considered with ζ closed to zero, both models fit the data very well (Foerster et al., 1994).

In Fig. 7-21, impact results between glass spheres and an aluminium plate with ζ close to zero are presented.

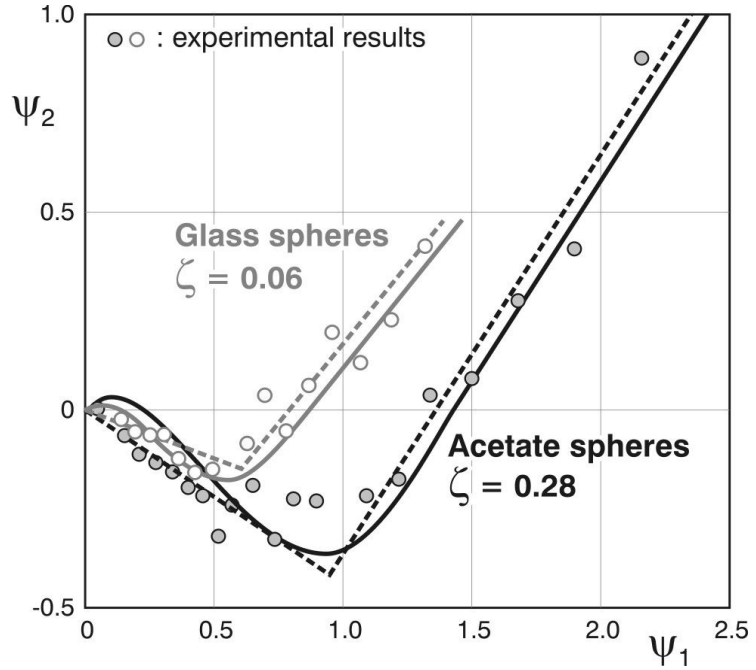

Figure 7-21: Collisions of 3 mm glass spheres and 6 mm acetate spheres on an aluminum plate, with respectively $\zeta = 0.06$ and $\zeta = 0.28$, after Foerster et al. (1994).

The MBF model presents a better concordance with the data, in the stick regime, probably due to the consideration of the stick-slip nature of the contact. In the "gross-slip" regime, the Walton model seems to fit the data with more accuracy, taking into account the energy loss during sliding motion (equation 7-80).

In Fig. 7-21, impact results between acetate spheres and an aluminium plate with $\zeta = 0.28$ are reported. The MBF model becomes less adapted to the contact description, even in the stick regime, because of the disregard of the inelasticity in this model.

The MBF model seems to be convenient for binary impacts or particle-frictional flat plate collisions between bodies elastically similar. The Walton model, based on three governing dimensionless coefficients, seems to be suitable for a large range of incidence angles and it is particularly adapted to binary collisions.

7.1.8 Conclusions

In DEM, the details of the contact between particles are based on the force-displacement relationships corresonding to the contact laws described in the present section.

Considering normal elastic contact of solids, the interactions between the particles occur over a vanishingly small area and the magnitude of these interpenetrations is limited relatively to the particle size respecting the hypotheses of Hertz theory in such a way that contact deformations remain elastic and that there is no influence of the boundaries of any bodies on the stress field developed in the contact area.

The elastic normal indentation, δ_z, is presented in Fig. 7-1 and it can be computed with the help of Hertz's law (7-3). Normal indentation is estimated with the secant or tangent normal contact stiffnesses, K_z or k_z, defined by equations (7-8) and (7-9) and the normal load applied to the contact area, P.

Different relative motions can occur at the contact between the particles: sliding, rolling and spin motion.

Sliding is defined as the development of a relative translational velocity along an axis included in the contact plane. Sliding leads to the emergence of a tangential load, Q, on the contact area. Tangential loading occurs in kinetic or static conditions.

In kinetic condition, there is the development of a relative translational velocity at the interface between the two contacting spheres, as illustarted in Fig. 7-6. There is no adhering point between both surfaces in contact. The sliding motion is then defined as "gross-slip", the slip is complete. $|Q|=\mu|P|$ is observed, this is the well-known slip Coulomb condition where μ is the kinetic friction coefficient. In kinetic condition, the tangential loading has no influence on the normal force-displacement relationship (7-3).

In static condition, there is no relative translational velocity between the spheres in contact but they are subjected to tangential load leading to progressive sliding defined as "stick-slip" or partial slip motion. When static friction occurs, under constant normal force, there is the development of two concentric zones within the contact area, as illustrated in Fig. 7-7. The first region is a circle centered on the symmetry axis of the contact area. In this region, there is no slip, the contacting surfaces adhere, this is the "stick area" or "stick circle" and $|Q| < \mu|P|$ where μ represents the static friction coefficient. Around this first zone, there is the development of the "slip ring" where $|Q| = \mu|P|$ and this annulus is marked by the emergence of "micro-slips". Figure 7-7 illustrates the presence of the 'stick-slip' zones within the contact area where c is the stick circle radius. The successive "micro-slips" lead to energy dissipation. Hence, the motion is not reversible in the sense of energy conservation. In static friction, the tangential loading has no influence on the normal force-displacement relationship.

Rolling is caused by a relative angular velocity around an axis included in the contact plane. 'Stick-slip' regions develop within the contact area during rolling motion. Hertz's law still remains valid.

Spin motion is defined by the emergence of a relative angular velocity around the axis perpendicular to the contact plane resulting in a torsional loading of the contact area. Hertz's law still remains valid.

The elastic tangential displacement at the contact can be estimated by means of several methods.

It can be computed with the help of equation (7-37) due to Mindlin (1949) in simple tangential loading condition with a constant normal force, as implemented by Cundall (1988).

Then, it can be described with the 1953 Mindlin and Deresiewicz procedure – called MD method – considering the following loading, unloading and reloading relationships (7-37), (7-64), (7-66) and (7-68) for the case of constant normal force or with the complete MD method for the case of simultaneous varying normal and tangential forces (Section 7.1.6a).

Elastic tangential displacement can be computed with more accuracy using the Maw, Barber and Fawcett (1976 and 1981) approach – called MBF approach (Section 7.1.6b).

Alternative models can still be implemented to compute normal and tangential stiffnesses between contacting particles such as viscoelastic model, ductile model with softening or hardening, Burger's model, hysteretic or viscous damping model and hypoplastic model (Cambou, 1998).

Elastic normal impact between spherical bodies can be considered with the help of Hertz's law assuming quasi-static contact conditions while the impact velocity remains weak in comparison with the propagation velocity of the stress waves through the material. Therefore, the elastic normal indentation during impact, δ_z, can be also computed with the help of equation (7-3).

Considering inelastic normal impact between spherical bodies, the hypothesis of quasi-static contact is still assumed. Several developments are presented in Section 7.1.5a or in Johnson (1985) and Stronge (2000) who provide a complete synopsis of the different relationships between normal force and indentation, in the elastic, elasto-plastic and fully plastic ranges.

Another way to consider the energy dissipation during normal impact is to define a normal restitution coefficient, ε, quantifying the energy loss in terms of the resultant velocity of the impacting spheres. It is defined with equation (7-55). The normal restitution coefficient can be determined with the help of impact experiments with spheres of different materials and for different impact velocities. Considering elasto-plastic hypothesis, ε depends on the elastic properties, the dimensions and masses of the contacting particles, on the dynamic material yield stress and on the impact velocity (Johnson, 1985 and Stronge, 2000), as illustrated in Fig. 7-15. The normal restitution coefficient is also described for impact of viscoelastic spherical bodies in Johnson (1985) and Stronge (2000) or more recently in Pöschel et al. (2008) which characterize the restitution coefficient notably for viscoelastic and adhesive viscoelastic spheres.

Elastic oblique impact between spherical bodies can be considered with the help of the MD method and the MBF approach.

Considering inelastic oblique impact, Walton (1982) and Walton and Braun (1986) introduced a simple model, including three coefficients: ε, the normal restitution coefficient, μ, the friction coefficient and β, the coefficient of rotational or tangential restitution defined with equation (7-77). This latter is used for collisions which restore, to the tangential velocity, a part of the energy stored in the tangential deformations of the contact surface.

Contrarily to both elastic MD and MBF approaches, the Walton model imposes that there is no simultaneous sticking and sliding regions. The contact is in stick regime, with or without loss of elastic energy, until the slip Coulomb condition is reached, and then there is "gross-slip" motion. The real difficulty to model inelastic oblique impact is related to the building of a physical rheological model able to take simultaneously into account the tangential restitution of energy and the partial slip phenomenon.

Several recent theories of rapid granular flow neglect the distinction between collisions in "gross-slip" and "stick-slip" regimes. They propose a model only based on both restitution coefficients, ε and β. Nevertheless, experimental research has demonstrated the importance of the friction coefficient on the contact behavior. Moreover, as explained previously, the restitution coefficients cannot be considered as constant. There are other models where the energy dissipation is not at all taken into account. Both kinds of approach must be considered with caution and the consequences of the modeling must be looked through a magnifying glass.

The tangential dissipation of energy is often neglected because of the complexity of the mechanisms in play. Admittedly, the boundary between friction phenomena and tangential dissipation of energy is still not clearly defined (Johnson, 2009).

Finally, it is noted that in the present chapter, only the spherical or circular bodies have been treated but various shape of the grain, as in natural soil, results in geometrical stresses and modification of the assemblage behavior (Williams et al. 1985).

7.2 Roughness analysis of the container and the sphere

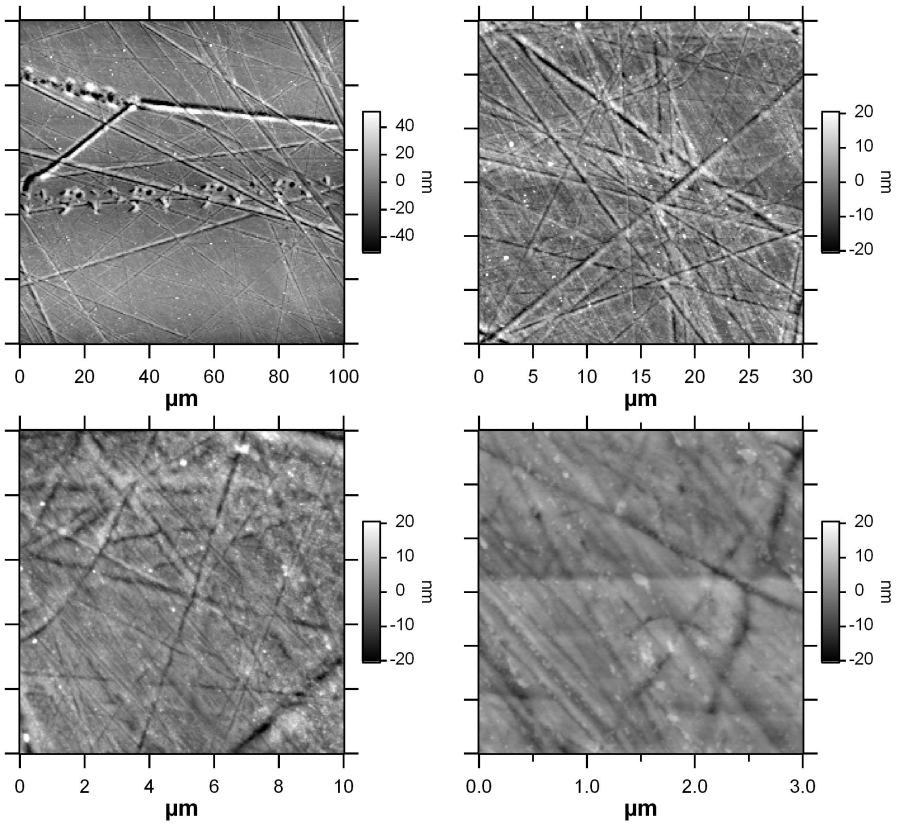

Figure 7-22: Surface roughness of the transparent polycarbonate container.

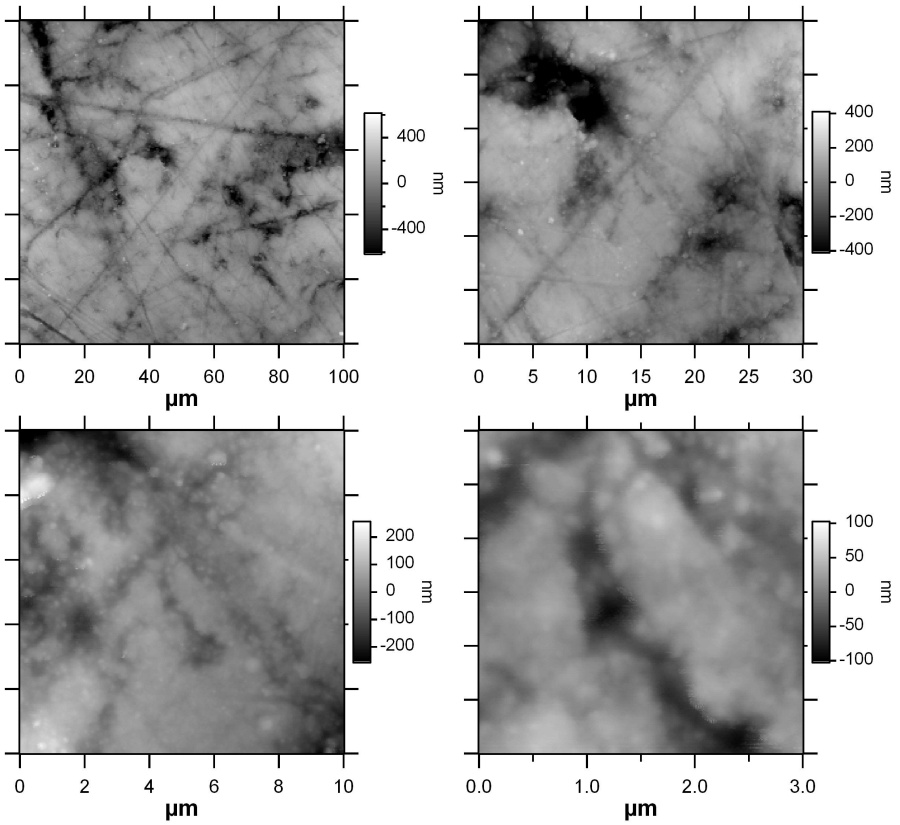

Figure 7-23: Surface roughness of the phenolic resin sphere.

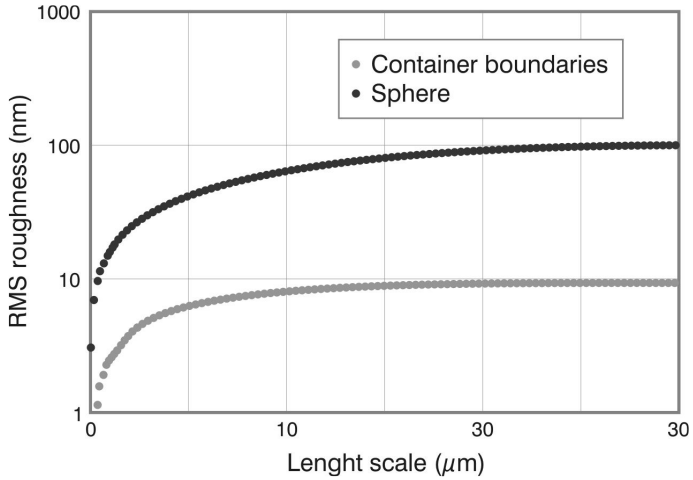

Figure 7-24: RMS roughnesses of the polycarbonate boundaries of the container and the phenolic resin sphere considering the length scale.

7.3 Sphere penetration logs in the densification range

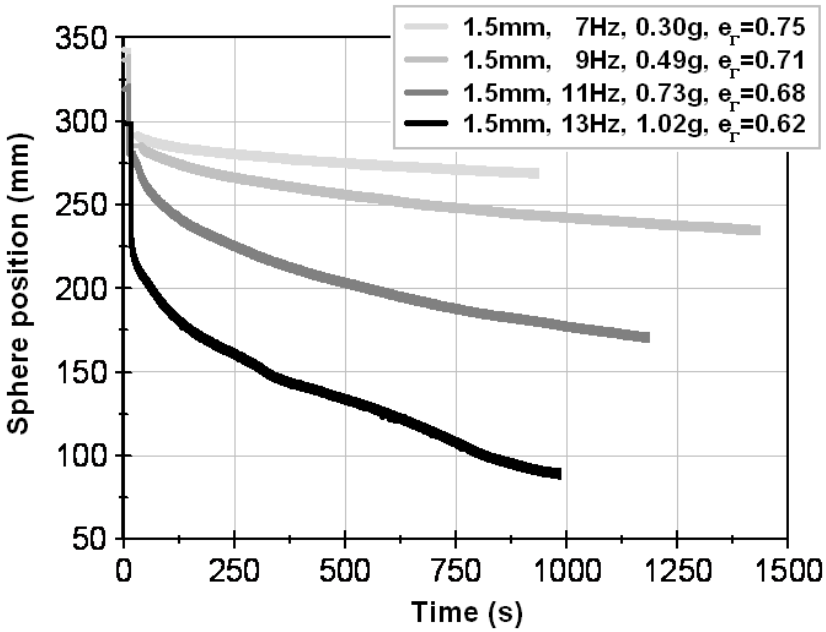

Figure 7-25: Sphere penetration logs for A = 1.5mm and various frequencies in the densification range.

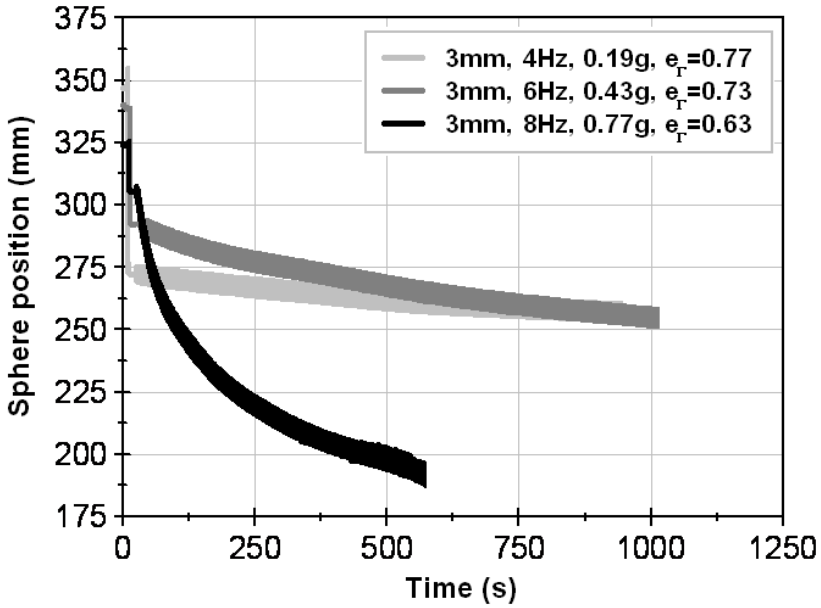

Figure 7-26: Sphere penetration logs for A = 3 mm and various frequencies in the densification range.

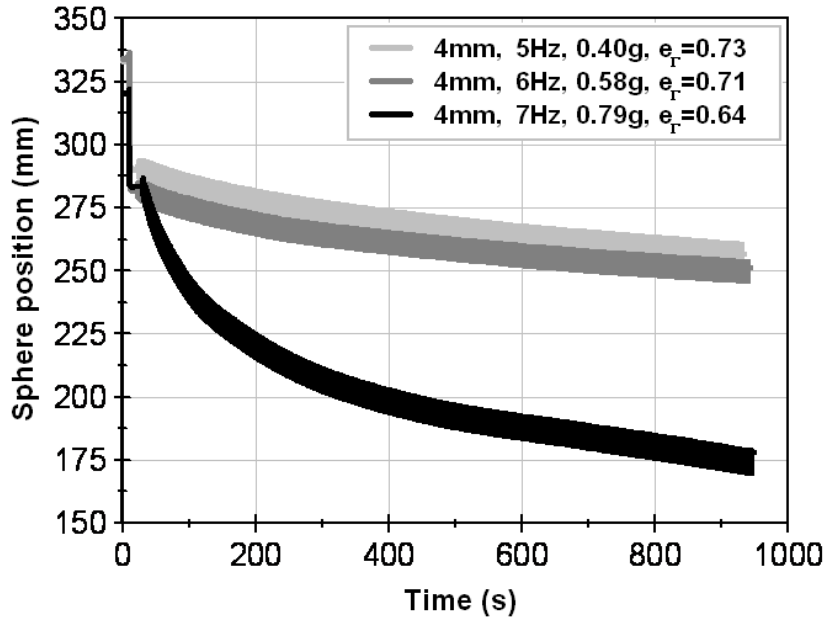

Figure 7-27: Sphere penetration logs for A = 4 mm and various frequencies in the densification range.

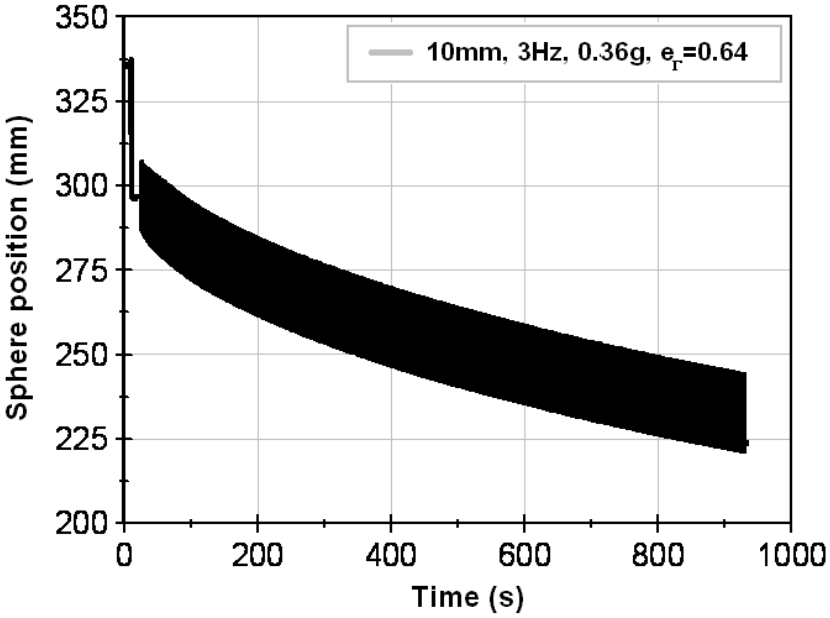

Figure 7-28: Sphere penetration logs for A = 10 mm and various frequencies in the densification range.

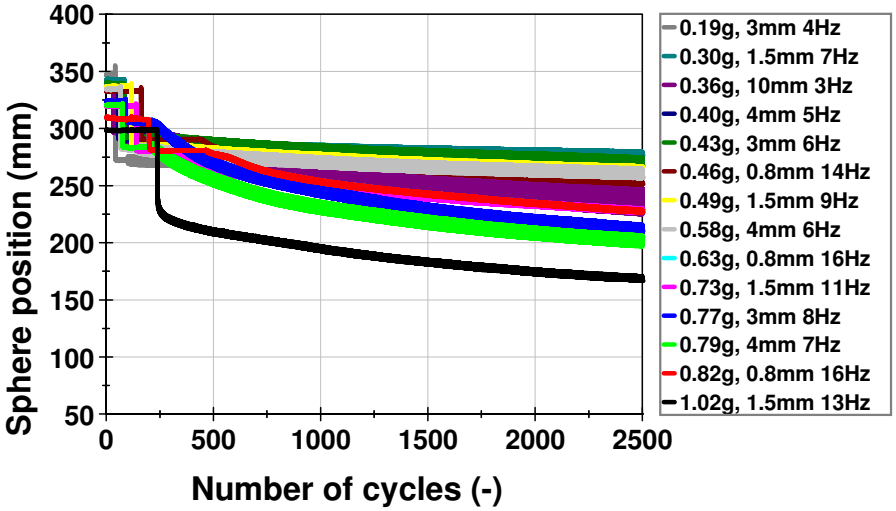

Figure 7-29: Sphere penetration logs in the densification range for different amplitudes of vibration as a function of the number of cycles.

7.4 Influence of the contact laws on the behavior of a granular assemblage in DEM

The influence of the choice of different displacement-force contact models on the accuracy of DEM simulation results was recently studied by Di Renzo and Di Maio (2004). The linear approach, the complete MD method and a no-slip MD method were compared at microscopic and macroscopic scales with experimental results (Kharaz et al., 2001) and with the MBF approach observing the solutions of the frictional-elastic oblique impact of a sphere and a flat wall. In this particular case, no significant improvements were attained using the advanced models. The no-slip MD method neglects the micro-slips phenomena. It is based on a linear tangential force-displacement relationship depending on the normal displacement (Tsuji et al., 1992).

The purposes of the modeling must be investigated before considering a model instead of another.

If the construction of a robust contact model allows to simulate precise conditions of impact, the discrete element modeling of a granular medium must be also considered at the macroscopic scale of the grain assemblage. In the hypothesis of a system containing an infinite number of particles, it can be demonstrated that the volume average stress tensor, which is a macroscopic characteristic of the assemblage, becomes independent of the details of the contact (Landau and Lifshitz, 1959). When the particle number increases in the sample, the geometrical character of the assemblage becomes increasingly important in comparison with the details of the contact. The contact law is then absorbed by the complexity of the granular structure rearrangement.

Deresiewicz (1958) has studied the regular packing modes of equal size sphere. Each different configuration leads to its own particular coordination number and porosity. Considering these equal size sphere packings, isotropic compression and hysteretic phenomena can be explained regarding the contact deformations (Schlosser, 1974).

However, in the present study, the granular matter – i.e. dry sand grains – will be modelled with an irregular packing of different size spheres and it will be subjected to vibrations. The influence of the contact deformations on the response of the grain skeleton will be probably very limited in comparison with the structural rearrangement. Hence, the linear contact model seems to be sufficient for the present simulations.

7.5 Calculation of the damping forces in the Discrete Element Model

Normal and tangential damping forces, D_z and D_x, are proportional to the relative velocities of approach between the particles, V_z and V_x:

$$D_z = c_z|V_z| \quad \text{(Eq. 7-81)}$$

and:

$$D_x = c_x|V_x| \quad \text{(Eq. 7-82)}$$

The viscous damping forces are computed in normal and tangential directions with the help of normal and shear damping constants, c_z and c_x, defined by:

$$c_z = \lambda_z c_z^{crit} \quad \text{(Eq. 7-83)}$$

and:

$$c_x = \lambda_x c_x^{crit} \quad \text{(Eq. 7-84)}$$

where c_z^{crit} and c_x^{crit} are the critical damping constants:

$$c_z^{crit} = 2\sqrt{mk_z} \quad \text{(Eq. 7-85)}$$

and:

$$c_x^{crit} = 2\sqrt{mk_x} \quad \text{(Eq. 7-86)}$$

where m is the mass of the particle.

λ_z and λ_x are the critical damping ratios defining the nature of the viscous damping at the contact (Ginsberg and Genin, 1984). When $\lambda<1$, the system is oscillating and underdamped. When $\lambda>1$, the system response is exponentially decaying and overdamped. Finally, when $\lambda=1$, the system is critically damped, the response decays rapidly to zero.

It is possible to link the critical damping ratio to the restitution coefficient. In 1993, Tsuji et al. derived these relationship considering the equation of motion for free vibration with viscous damping. The critical damping ratio is then given by:

$$\lambda_z = \frac{\ln(\varepsilon)}{\sqrt{\ln^2(\varepsilon)+\pi^2}} \quad \text{(Eq. 7-87)}$$

7.6 Calculation of the contact stresses in the Discrete Element Model

As explained in Section 4.1.4c, stress is a continuum quantity. Considering the discrete character of the granular model, it is necessary to establish an averaging procedure taking into account the contact forces acting on particles to obtain the macro-stress tensor in terms of a continuum model.

In the present model, the averaging procedure is based on the previous works of Rothenburg and Bathurst (1989) and Bagi (1999) and is implemented considering the PFC2D model of Itasca (2004).

The average stress tensor, $\overline{\sigma_{ij}}$, in a volume V of material, is defined by:

$$\overline{\sigma_{ij}} = \frac{1}{V}\int_V \sigma_{ij} dV \qquad \text{(Eq. 7-88)}$$

where σ_{ij} is the stress tensor acting throughout the volume. For a granular medium, the stresses only exist in the grains. The integral is then replaced by a sum, over the N_p particles of the volume V:

$$\overline{\sigma_{ij}} = \frac{1}{V}\sum_{N_p} \overline{\sigma_{ij}}^{(p)} V^{(p)} \qquad \text{(Eq. 7-89)}$$

where $\overline{\sigma_{ij}}^{(p)}$ is the average stress tensor acting in the volume $V^{(p)}$ of the particle (p). Considering equation (7-88), this latter can be expressed as:

$$\overline{\sigma_{ij}}^{(p)} = \frac{1}{V^{(p)}}\int_V \sigma_{ij}{}^{(p)} dV^{(p)} \qquad \text{(Eq. 7-90)}$$

Assuming the stresses to be continuous and in equilibrium, in each grain, and considering that the particles are loaded by contact forces acting at discrete locations, the integral can be replaced by a sum, over the N_c contacts:

$$\overline{\sigma_{ij}}^{(p)} = \frac{1}{V^{(p)}}\sum_{N_c} u_i^{(c)} F_j \qquad \text{(Eq. 7-91)}$$

where $u_i^{(c)}$ is the force location. Considering the unit-normal vector of contact $\vec{z}$, it is possible to rewrite the force location:

$$u_i^{(c)} = u_i^{(p)} + \left| u_i^{(c)} - u_i^{(p)} \right| z_i \qquad \text{(Eq. 7-92)}$$

where $u_i^{(p)}$ is the particle center location, for the direction i = ($\vec{1}$, $\vec{2}$). The global coordinate system is defined in Section 4.1.2.

For a particle in equilibrium:

$$\overline{\overline{\sigma_{ij}}}^{(p)} = \frac{1}{V^{(p)}} \sum_{N_c} \left| u_i^{(c)} - u_i^{(p)} \right| z_i F_j \qquad \text{(Eq. 7-93)}$$

The equation (7-93) could be inserted in the definition (7-89), considering all the particles of the volume, to compute the average stress tensor, $\overline{\overline{\sigma_{ij}}}$. But, as a stratified analysis is implemented, the particles can intersect the boundary between the measurement layers. In the present model, only the particles with centroids included in the measurement layer are considered in the calculation of the stress field. In such a way to take into account the additional area of the neglected particles, a correction factor is applied. It is based on the computation of the porosity in the measurement stratum. The correction factor is determined assuming an uniform stress field, σ_0, in the measurement layer. Then, the average stress tensor for the measurement layer volume, V_m, is expressed with the help of two expressions:

$$\overline{\overline{\sigma_{ij}}} = \frac{1}{V_m} \sum \overline{\sigma}^{(p)} V^{(p)} = \frac{1}{V_m} \overline{\sigma}^{(p)} \sum V^{(p)} = \sigma_0 \left(\frac{\sum V^{(p)}}{V_m} \right) = \sigma_0 \left(1 - n_m\right) \qquad \text{(Eq. 7-94)}$$

where the sum concerns all the particles or portions of particles included in the volume of the measurement layer, V_m, and n_m is the porosity of the measurement layer.
The alternative expression to estimate the average stress tensor is given by:

$$\tilde{\sigma} = \frac{1}{V_m} \sum_{N_p} \overline{\sigma}^{(p)} V^{(p)} = \sigma_0 \left(\frac{\sum_{N_p} V^{(p)}}{V_m} \right) \qquad \text{(Eq. 7-95)}$$

where the sum takes only into account the N_p particles with centroids included in the measurement layer. Thus, this expression is incorrect. Dividing equation (7-94) by equation (7-95):

$$\frac{\overline{\sigma}}{\tilde{\sigma}} = \left(\frac{1 - n_m}{\sum_{N_p} V^{(p)}} \right) V_m \qquad \text{(Eq. 7-96)}$$

Considering equation (7-95), V_m can be rewritten as:

$$V_m = \frac{1}{\tilde{\sigma}} \sum_{N_p} \overline{\sigma}^{(p)} V^{(p)} \qquad \text{(Eq. 7-97)}$$

Including this latter in equation (7-96):

$$\overline{\sigma} = \left(\frac{1 - n_m}{\sum_{N_p} V^{(p)}} \right) \sum_{N_p} \overline{\sigma}^{(p)} V^{(p)} \qquad \text{(Eq. 7-98)}$$

With respect to the definition (7-93) of the average stress tensor in a particle, the final expression for the calculation of the average stress tensor in the measurement layers is given by:

$$\overline{\sigma}_{ij} = \left(\frac{1 - n_m}{\sum_{N_p} V^{(p)}} \right) \sum_{N_p} \sum_{N_c} \left| u_i^{(c)} - u_i^{(p)} \right| z_i F_j \qquad \text{(Eq. 7-99)}$$

where the sum takes into account the particles with centroids included in the measurement layer and the contacts acting on them.

7.7 Influence of the displacement and the frequency in the elastic range (Γ = 0.5) for DEM simulations

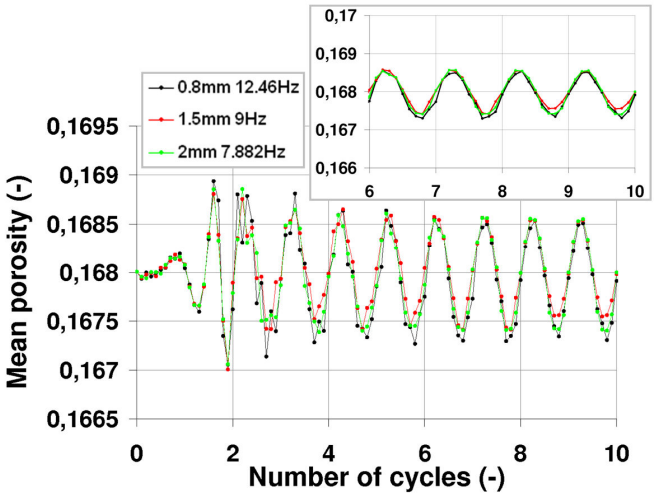

Figure 7-30: Comparison of the mean porosity variation of the granular sample during the vibration for different displacement amplitudes and similar acceleration of vibration, Γ = 0.5. Inset: enlargement of the curves in the steady vibratory regime.

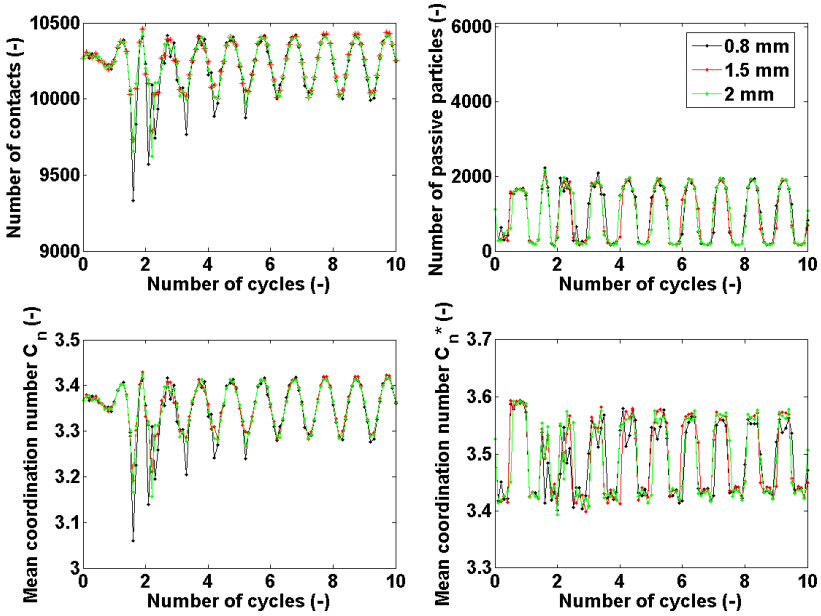

Figure 7-31: Comparison of the variation of the contact density properties (contact number, number of passive particles, mean coordination numbers C_n and C_n*) of the granular sample during the vibration for different displacement amplitudes and similar acceleration of vibration, Γ = 0.5.

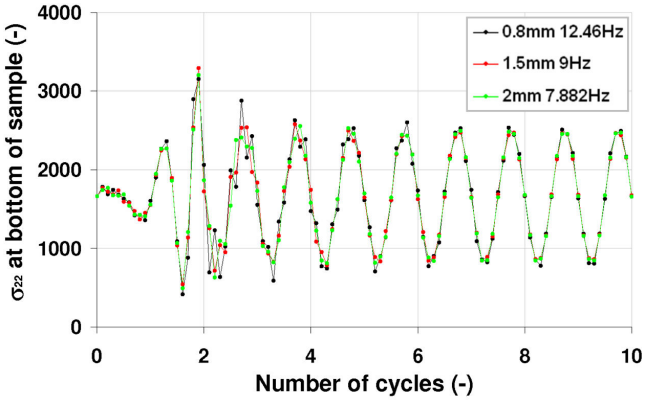

Figure 7-32: Comparison of the variation of the vertical stress, σ_{22}, at the bottom of the sample during the vibration for different displacement amplitudes and similar acceleration of vibration, $\Gamma = 0.5$.

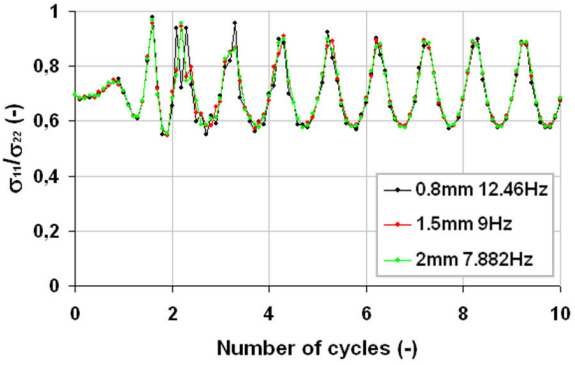

Figure 7-33: Comparison of the ratio of horizontal to vertical stresses, during the vibration for different displacement amplitudes and similar acceleration of vibration, $\Gamma = 0.5$.

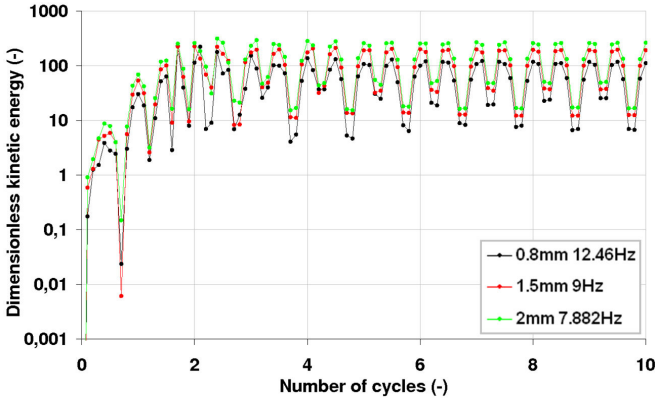

Figure 7-34: Comparison of the dimensionless kinetic energy in the sample during the vibration for different displacement amplitudes and similar acceleration of vibration, $\Gamma = 0.5$.

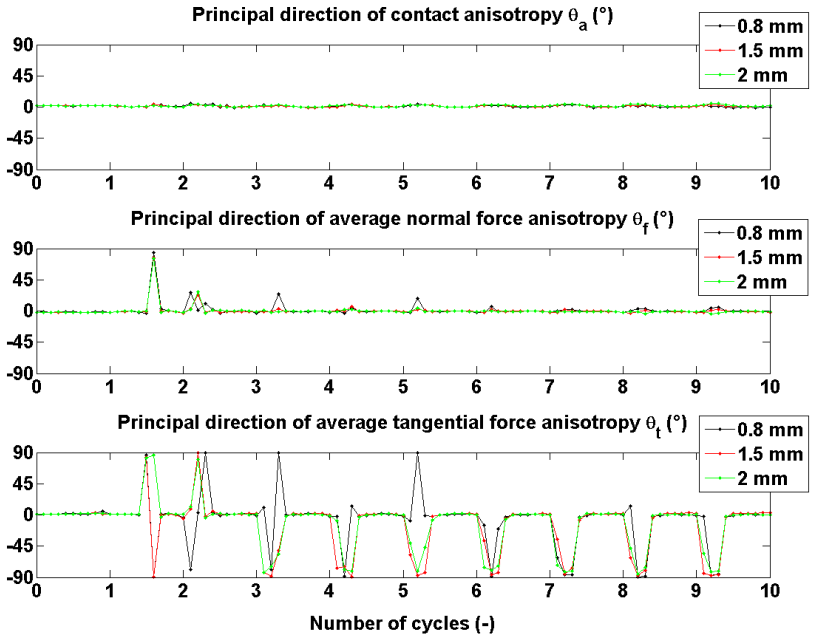

Figure 7-35: Principal directions of contact, average normal contact force and average tangential contact force anisotropy during the vibration for different displacement amplitudes and similar acceleration of vibration, $\Gamma = 0.5$.

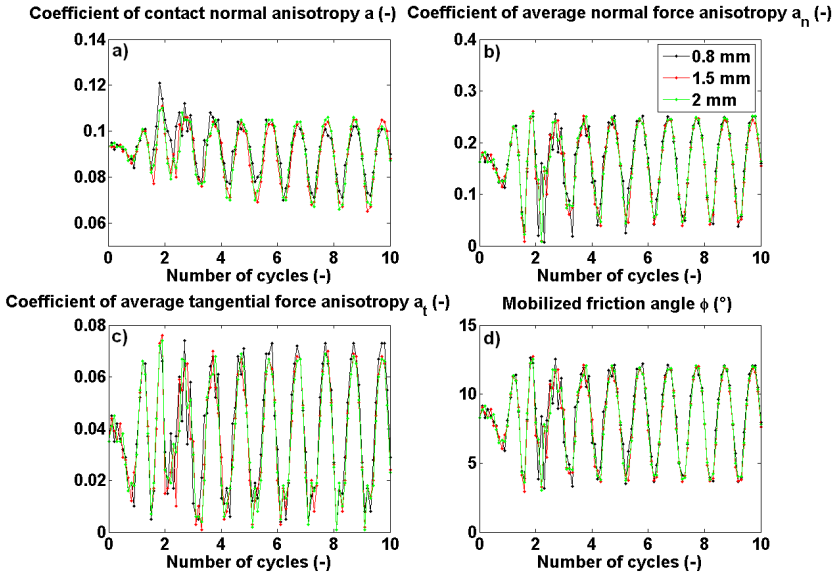

Figure 7-36: Relationships between the number of cycle of vibration and the coefficient of contact normal anisotropy, a (a), the coefficient of average normal force anisotropy, a_n (b), the coefficient of average tangential force anisotropy, a_t (c) and the mobilized angle of friction, ϕ_{mob} (d) during the vibration for different displacement amplitudes and similar acceleration of vibration, $\Gamma = 0.5$.

7.8 Influence of the displacement and the frequency in the vibro-fluid range (Γ = 1.02) for DEM simulations

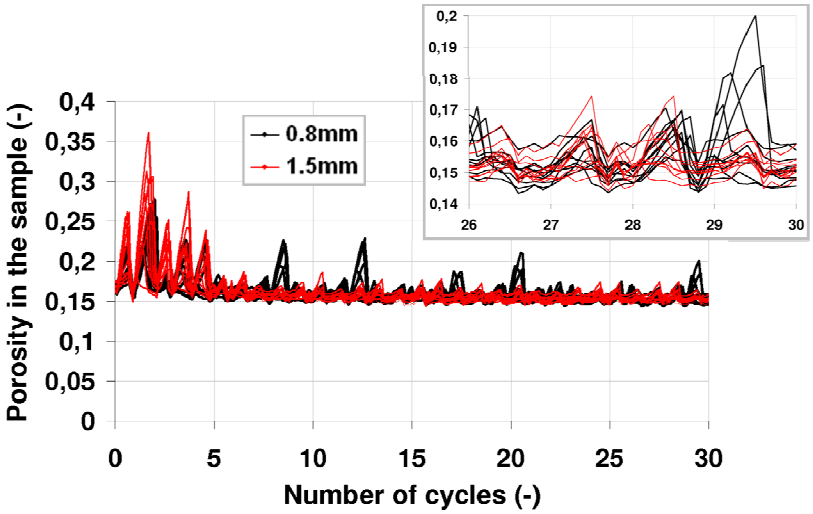

Figure 7-37: Comparison of the mean porosity variation in the measurement layers of the granular sample for different displacement amplitudes and similar acceleration of vibration, Γ = 1.02. Inset: enlargement of the curves in the steady vibratory regime.

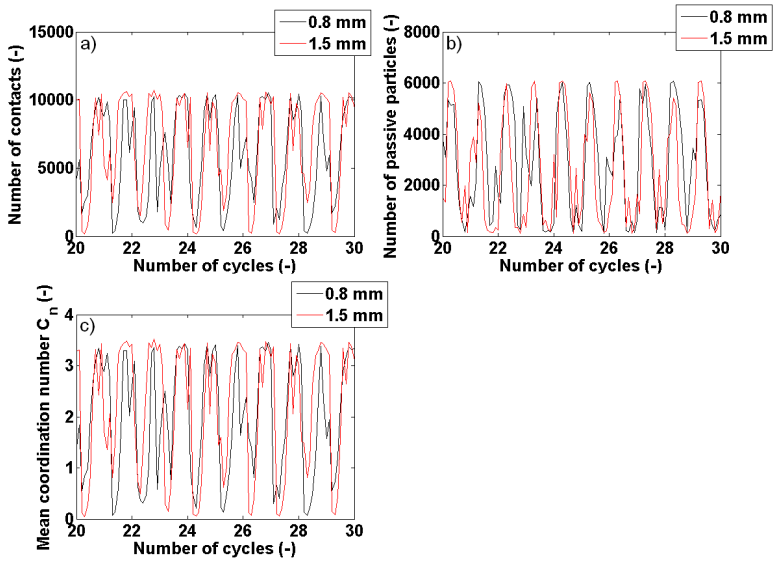

Figure 7-38: Comparison of the evolution of the contact density properties (contact number, number of passive particles and mean coordination number, C_n, of the granular sample in the steady vibratory regime for different displacement amplitudes and similar acceleration of vibration, Γ = 1.02.

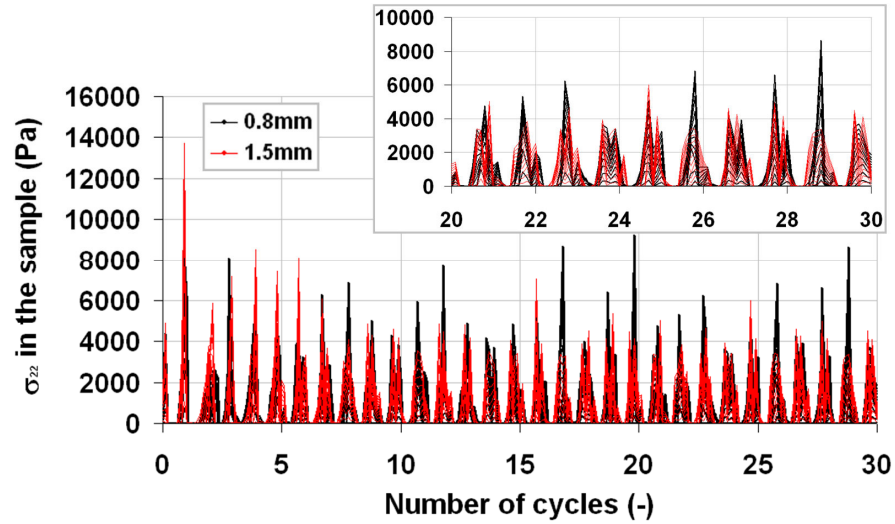

Figure 7-39: Comparison of the vertical contact stress variation in the measurement layers of the granular sample for different displacement amplitudes and similar acceleration of vibration, Γ = 1.02. Inset: enlargement of the curves in the steady vibratory regime.

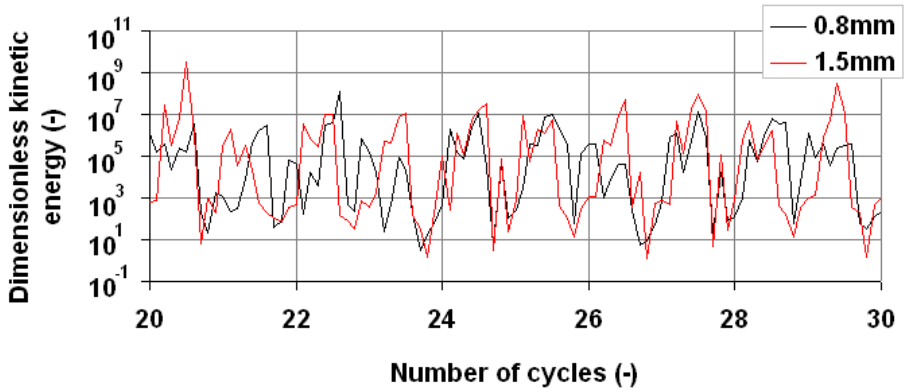

Figure 7-40: Comparaison of the dimensionless kinetic energy in the sample in the steady vibratory regime for different displacement amplitudes and similar acceleration of vibration, Γ = 1.02.

8 Bibliography

AGNOLIN, I. and ROUX, J.-N. (2007). "*Internal states of model isotropic granular packings. II. Compression and pressure cycles*". Physical Review E, Vol. 76, 061303, 11 p.

ALYANAK, I. (1961). "*Vibration of sands with special reference to the minimum porosity test for sands*". Proceedings of Midland Soil Mechanics and Foundation Engineering Society, Birmingham, England. pp. 37-72.

AMONTONS, G. (1699). "*De la résistance causée dans les machines*". Mémoire de l'Académie Royale des Sciences de Paris, A, pp. 257-282.

ATKINSON, J.H. and BRANSBY, P.L. (1978). "*The Mechanics of Soils: An Introduction to Critical State Soil Mechanics*". McGraw-Hill, London.

ATKINSON, J.H. (1993). "*An introduction to the mechanics of soils and foundations*". McGraw-Hill.

BAGI, K. (1999). "*Microstructural stress tensor of granular assemblies with volume forces*". Journal of Applied Mechanics, Trans. ASME, Vol. 66, N°4, pp. 934-936.

BARDET, J.P. (1998). "*Introduction to computational granular mechanics*". Behavior of granular materials. International Centre for Mechanical and Sciences, CISM courses and lectures, N°385. Springer Wien New York, Cambou, B. (ed.), pp. 99-169.

BARKAN, D.D. (1962). "*Dynamics of bases and foundations*". McGraw-Hill, New-York.

BARKAN, D.D. (1963). "*Méthodes de vibration dans la construction*". Dunod, Paris.

BATHURST, R.J. and ROTHENBURG, L. (1988). "*Micromechanical aspects of isotropic granular assemblies with linear contact interactions"*. Journal of Applied Mechanics, Trans. ASME, Vol. 55, pp. 17-23.

BBRI. (1994). "*High performance vibratory pile drivers base on novel electromagnetic actuation systems and improved understanding of soil dynamics*". Progress reports of the BRITE/EURAM research contract CT91-0561, 1994.

BELHEINE, N., PLASSIARD, J.-P., DONZE, F.-V., DARVE, F., SERIDI, A. (2009). "Numerical simulation of drained triaxial test using 3D discrete element modeling". Computers and Geotechnics, Vol. 36, pp. 320–331.

BERNHARD, R.K. (1967). "*Fluidization phenomena in soils during vibro-compaction and vibro-pile-driving and -pulling*". US Army Cold Regions Research and Engineering, Hanover, NH 1967, 58 p.

BIAREZ, J. and HICHER, P. (1994). "*Elementary mechanics of soil behavior*", A.A. Balkema, Rotterdam.

BILLET, P. and SIFFERT, J.G. (1989). "*Soil-sheet pile interaction in vibro-piling*". Journal of the Geotechnical Engineering Division, ASCE, Vol. 115, N°8, pp. 1085-1101.

BINDER, K. and HERMANN, D.W. (2002). "*Monte Carlo simulation in statistical physics: an introduction*". Springer, fourth edition.

BOLTON, M.D. (1986). "*The strength and dilatancy of sands*". Géotechnique, Vol. 36, N°1, pp. 65-78.

BOREL, S., BUSTAMENTE, M. and GIANESELLI, L. (2002). "*Two comparative field studies of the bearing capacity of vibratory and impact driven sheet piles*". Proceedings of the International Conference on Vibratory Pile Driving and Deep Soil Vibratory Compaction, TRANSVIB 2002, Louvain-la-Neuve, Belgium, A.A. Balkema, Holeyman, A., Venden Berghe, J.-F. and Charue, N. (eds.), pp. 167-174.

BROMWELL, L.G. (1966). "*The friction of Quartz in High Vacuum*". Sc.D. Thesis, M.I.T., Cambridge, Mass, USA.

BUFLER, H. (1959). "*Zur Theorie der rollenden Reibung*". Archive of Applied Mechanics, Vol. 27, N°3, pp. 137-152.

CAMBOU, B. (1998). "*Behavior of granular materials*". International Centre for Mechanical and Sciences, CISM courses and lectures, N°385. Springer Wien New York, Cambou, B. (ed.), 400p.

CAMPBELL, C. S. (1990). "*Rapid granular flow*". Annual Review of Fluid Mechanics, Vol. 22, pp. 57–90.

CAMPBELL, C.S. (2002). "*Granular shear flows at the elastic limit*". Journal of Fluid Mechanics, Vol. 465, pp. 261-291.

CASAGRANDE, A. (1938). "*The shearing resistance of soils and its relation to the stability of earthdams*". Proceedings of the Soils and Foundations Conference of the US Engineering Department, Boston, USA.

CASAGRANDE, A. (1971). "*On liquefaction phenomena*". Geotechnique, Vol. 21, N°3, pp. 197-202.

CASTRO, G. (1969). "*Liquefaction of sands*". PhD Thesis, Harvard University, U.S.A.

CASTRO, G. (1975). "*Liquefaction and cyclic mobility of saturated sands*". Journal of the Geotechnical Engineering Division, ASCE, Vol. 101, N°6, pp. 551-569.

CASTRO, G. and POULOS, S.J. (1977). "*Factors affecting liquefaction and cyclic mobility*". Journal of the Geotechnical Engineering Division, ASCE, Vol. 103, N°6, pp. 501-516.

CHRISTOFFERSEN, J. MEHRABADI, M.M. and NEMAT-NASSER, S. (1981). "*A micromechanical description of granular material behavior*". Journal of Applied Mechanics, Trans. ASME, Vol. 48, N°2, pp. 339-344.

CLEMENT, E., DURAN, J. and RAJCHENBACH, J. (1992). "*Experimental study of heaping in a two-dimensional "Sandpile"*". Physical Review Letters, Vol. 69, N°8, pp. 1189-1192.

COMBE, G. and ROUX, J.-N. (2010). Personal communication.

COULOMB, C.A. (1821). "*Théorie des machines simples*". Bachelier, Libraire, Paris.

CROOK, A.W. (1952). "*A study of some impacts between metal bodies by a piezoelectric method*". Proceedings of Royal Society A, Vol. 212, pp. 377-390.

CUNDALL, P.A. (1971). "*A computer model for simulating progressive large scale movements of blocky rock systems*". Proceedings of the Symposium of the International Society of Rock mechanics, Nancy, France, Vol. 1, pp. 129-132.

CUNDALL, P.A. and STRACK, O.D.L. (1979). "*A Discrete Numerical Model for Granular Assemblies*". Géotechnique, Vol. 29, pp. 47-65.

CUNDALL, P.A. (1988). "*Computer simulations of dense sphere assemblies*". Micromechanics of granular materials. Elsevier Science Publishers, Satake, M. and Jenkins, J.T. (eds.), pp. 113-123.

D'APPOLONIA, D.J. and D'APPOLONIA, E.D. (1967). "*Determination of the maximum density of cohesionless soils*". Proceedings of the Third Asian Conference on Soil Mechanics and Foundation Engineering, Haifa, Israel, Vol. 1, pp. 266-268.

DE JAEGER, J. (1991). "*Influence de la morphologie des sables sur leur comportement mécanique*". PhD Thesis, Université catholique de Louvain, Belgium.

DENIES, N. and HOLEYMAN, A. (2007). "*Discrete element modeling of sinking sphere in a vibrating granular medium*". 18th European Young Geotechnical Engineers Conference, Ancona, Italy, CD-ROM proceedings, 8 p.

DENIES, N. and HOLEYMAN, A. (2008). "*Vibratory driving and segregation in granular matter*". 8th International Conference on the Application of Stress-Wave Theory to Piles, Lisbon, Portugal, pp. 549-557.

DENIES, N., CANOU, J., ROUX, J.-N. and HOLEYMAN, A. (2009). "*Solid-liquid behavior of vertically vibrated sand*". 17th International Conference on Soil Mechanics and Geotechnical Engineering, Bibliotheca Alexandrina, Alexandria, Egypt, Vol. 3, pp. 2370-2373.

DENIES, N., CANOU, J., ROUX, J.-N. and HOLEYMAN, A. (2010). "*Sphere penetration experiments in vertically vibrated sand*". Fifth International Conference on Recent Advances in Geotechnical Earthquake Engineering and Soil Dynamics, San Diego, CA, USA, CD-ROM proceedings, 12 p.

DERESIEWICZ, H. (1958). "*Mechanics of granular matter*". Advances in applied mechanics Vol. 5, Elsevier Science & Technology Books, Von Karman, T. and Dryden H.L (eds.), pp. 233-306.

DERESIEWICZ, H. (1968). "*A note on Hertz impact*". Acta Mechanica, Vol. 6, pp. 110-112.

DICKEY, J.W. (1966). "*Frictional Characteristics of Quartz*". S.B. Thesis, M.I.T., Cambridge, Mass., USA.

DI RENZO, A. and DI MAIO, F.P. (2004). "*Comparison of contact-force models for the simulation of collisions in DEM-based granular flow codes*". Chemical Engineering Science, Vol. 59, pp. 525-541.

DOBRY, R. and VUCETIC,M. (1987). "*State-of-the-art report: Dynamic properties and response of soft clay deposits*". Proc. Intern. Symp. on Geo Engrg of Soft Soils, Mexico City, Vol. 2, pp. 51-87.

DRAKE, T.G. (1988). "*Experimental flows of granular material*". PhD Thesis, University of California, Los Angeles, USA.

DUNDURS, J. and LEE, M.-S. (1972). "*Stress concentration at a sharp edge in contact problems*". Journal of Elasticity, Vol. 2, pp. 109-112.

DUPLA, J.-C. and CANOU, J. (1994). "*Détermination de caractéristiques mécaniques du sable de Fontainebleau en compression et en extension triaxiales*". Rapport de recherche IREX, Projet National Clouterre, 40 p.

DUPLA, J.-C. and CANOU, J. (2005). "*Etude comparative du processus de pluviation à partir de différents dispositifs d'essai*". Document interne, ENPC-CERMES.

EL NAGGAR, M. and NOVAK, M. (1994). "*Nonlinear model for dynamic axial pile response*". Journal of Geotechnical Engineering, ASCE, Vol. 120, N° 2, pp. 308-329.

EMAM, S., ROUX, J.-N., CANOU, J., CORFDIR, A. and DUPLA, J.-C. (2005) "*Granular packings assembled by rain deposition: an experimental and numerical*

study". Powders and Grains 2005, Leiden, A.A. Balkema, Garcia Rojo, R., Herrmann, H.J. and McNamara, S. (eds.), pp. 49–52.

EMAM, S., CANOU, J., CORFDIR, A., DUPLA, J.-C. and ROUX, J.-N. (2006). "*Elaboration et comportement mécanique de matériaux granulaires solides modèles: expériences et simulations numériques*". Rhéologie des pâtes et des matériaux granulaires. Sciences pour le génie civil, n°12. Laboratoire central des ponts et chaussées, Cazacliu B. and Roux, J.-N. (eds.), pp. 105-145.

ERMOLAEV, N.N. and SENIN, N.V. (1968a). "*Vibrocompression of soils*". Soil Mechanics and Foundation Engineering, Vol. 5, N°4, pp. 246-250.

ERMOLAEV, N.N. and SENIN, N.V. (1968b). "*Shear strength of soil in the presence of vibrations*". Soil Mechanics and Foundation Engineering, Vol. 5, N°1, pp. 15-18.

EVESQUE, P. and RAJCHENBACH, J. (1989). "*Instability in a sand heap*". Physical Review Letters, Vol. 62, N°1, pp. 44-46.

FOERSTER, S.F., LOUGE, M.Y., CHANG, H. and ALLIA, K. (1994). "*Measurements of collision properties of small spheres*". Physics of Fluids, Vol. 6, pp. 1103-1115.

FOLLANSBEE, P.S. and SINCLAIR, G.B. (1984). "*Quasi-static normal indentation of an elastic-plastic half-space by a rigid sphere*". International Journal of Solids and Structures, Vol. 20, pp. 81-91.

FORD, H. and ALEXANDER, J.M. (1963). "*Advanced Mechanics of Materials*". Longmans, London.

GAZETAS, G. and DOBRY, R. (1984). "*Simple radiation damping model for piles and footings*". Journal of the Engineering Mechanics Division, Vol. 110, N°6, pp. 937-956.

GDRMiDi, Groupement De Recherche Milieux Divisés. (2004). "*On dense granular flows*". The European Physical Journal E, Vol. 14, pp. 341-365.

GEUZE, E.C.W.A. (1948). "*Critical density of some dutch sands*". Proceedings of the 2nd International Conference on Soil Mechanics and Foundation Engineering, Vol. 3, Rotterdam, The Netherlands, pp. 125-130.

GINSBERG, J.H. and GENIN, J. (1984). "*Dynamics*". John Wiley and Sons, New York, second edition.

GOLDSMITH, W. (1960). "*Impact*". Arnold, London.

GOODMAN, L.E. and BROWN, C.B. (1962). "*Energy dissipation in contact friction : constant normal and cyclic tangential loading*". Journal of applied Mechanics, Trans. ASME, Series E, Vol. 29, pp. 17-22.

GREEN, A.E. (1949). "*On Boussinesq's problem and penny-shaped cracks*". Proceedings Cambridge Philosophical Society, Vol. 45, pp. 251-257.

GREENFIELD B.J. and MISIASZEK, E.T. (1968). "*Vibration-settlement characteristics of four gradations of Ottawa sand*". Proceedings of the International Symposium on Wave Propagation and Dynamic Properties of Earth Materials, University of New Mexico, Alburquerque, NM, USA, pp. 787-795.

GRESZCZUK, L.B. (1980). McDonnell Douglas Astronautics Company Contract Report, DAC60869.

GROSSMAN, E.L. (1997). "*Effects of container geometry on granular convection*". Physical Review E, Vol. 56, N°3, pp. 3290-3300.

HAFF, P.K. (1983). "*Grain flow as a fluid mechanical phenomenon*". Journal of Fluid Mechanics, Vol. 134, p. 401-430.

HAMILTON, G.M. and GOODMAN, L.E. (1966). "*The stress field created by a circular sliding contact*". Journal of Applied Mechanics, Trans. ASME, Vol. 33, pp. 371-376.

HAMILTON, G.M. (1983). "*Explicit equations for stresses beneath a sliding spherical contact*". Proceedings of Institution of Mechanical Engineers Vol. 197C, pp. 53-59.

HARDY, C., BARONET, C.N. and TORDION, G.V. (1971). "*Elastoplastic indentation of a half-space by a rigid sphere*". Journal of Numerical Methods in Engineering, Vol. 3, pp. 451-462.

HART, R., CUNDALL, P.A. and LEMOS, J. (1988). "*Formulation of a three-dimensional distinct element model—Part II. Mechanical calculations for motion and interaction of a system composed of many polyhedral blocks*". International Journal of Rock Mechanics and Mining Sciences, Vol. 25, N°3, pp. 117-125.

HEMMEN, B.R. and BLES, T. (2005). "*GeoBrain Funderingstechniek: Ervaringsdatabase voorspelt uitvoeringsrisico*". Civiele Techniek, Vol. 60, N°2, pp. 24-25.

HENDRON, A.J. (1963). "*The behavior of sand in one-dimensional compression*". PhD Thesis, University of Illinois, USA.

HERTZ, H. (1882). "*Über die Berührung fester elastischer Körper (On the contact of elastic solids)*". Journal fur die Reine und Angewandte Mathematik, Vol. 92, pp. 156–171.

HILL, R. (1950). "*Theory of plasticity*". Oxford University Press.

HOLEYMAN, A., LEGRAND, C. and VAN ROMPAEY, D. (1996). "*A method to predict the driveability of vibratory driven piles*". Proceedings of the 3rd

International Conference on the Application of Stress-Wave Theory to Piles, Orlando, USA, pp. 1101-1112.

HOLEYMAN, A. (2000). "*Keynote lecture: Vibratory driving analysis*". Proceedings of the VIth International Conference on the Application of Stress-Wave Theory to Piles, São Paulo, Brazil, pp. 479-494.

HOLEYMAN, A. and WHENHAM, V. (2008). "*Sheet pile vibrodriving: Power pack-vibrator-sheet pile-soil interactions*". Proceedings of the VIIIth International Conference on the Application of Stress-Wave Theory to Piles, Lisbon, Portugal, pp. 569-575.

HOLTZ, R.D. and KOVACS W.D. (1981). "*An introduction to Geotechnical Engineering*". Prenctice-Hall Inc., Englewood Cliffs, New Jersey, USA.

HOULSBY, G.T. and WROTH, C.P. (1991). "*The variation of shear modulus of a clay with pressure and overconsolidation ratio*". Soils and Foundations, Vol. 31, N°3, pp. 138-143.

HUBER, M.T. (1904). "*Zur Theory der Berührung fester elastische Körper*". Ann. Der Phys, Vol. 14, pp. 153-163.

HUNTER, S.C. (1957). "*Energy absorbed by elastic waves during impact*". Journal of Mechanics and Physics of Solids, Vol. 5, N°3, pp. 162-171.

ITASCA. (2003). "*Particle Flow Code, PFC3D, release 3.0*". Itasca Consulting Group, Inc., Minneapolis, Minnesota.

ITASCA. (2004). "*Particle Flow Code, PFC2D, release 3.1*". Itasca Consulting Group, Inc., Minneapolis, Minnesota.

JEAN, M. (1999). "*The non-smooth contact dynamics method*". Computer Methods in Applied Mechanics and Engineering, Vol. 177, pp. 235-257.

JENKINS, J.T. and SAVAGE, S.B. (1983). "*A theory for the rapid flow of identical, smooth, nearly elastic particles*". Journal of Fluid Mechanics, Vol. 130, pp. 187-202.

JOHNSON, K.L. and JEFFERIS, J.A. (1963). "*Plastic flow and residual stresses in rolling and sliding contact*". Proc. Institution of Mechanical Engineers Symposium on Rolling Contact fatigue, London, p. 54-65.

JOHNSON, K.L. (1970). "*The correlation of indentation experiments*". Journal of Mechanics and Physics of solids, Vol. 18, pp. 115-126.

JOHNSON, K.L. (1985). "*Contact mechanics*". Cambridge University Press.

JOHNSON, K.L. (2009). Personal communication.

KHARAZ, A.H., GORHAM, D.A. and SALMAN, A.D. (2001). "*An experimental study of the elastic rebound of spheres*". Powder Technology, Vol. 120, pp. 281-291.

KNIGHT, J.B., JAEGER, H.M. and NAGEL, S.R. (1993). "*Vibration induced size separation in granular media: the convection connection*". Physical Review Letters, Vol. 70, N°24, pp. 3728-3731.

KNIGHT, J.B., EHRICHS, E.E., KUPERMAN, V.Y., FLINT, J.K., JAEGER, H.M. and NAGEL, S.R. (1996). "*Experimental study of granular convection*". Physical Review E, Vol. 54, N°5, pp. 5726-5738.

KOLBUSZEWSKI, J. (1948). "*An experimental study of the maximum and minimum porosities of sands*". Proceedings of the Second International Conference on Soil Mechanics and Foundation Engineering, Rotterdam, The Netherlands, Vol. 1, pp. 158-165.

KOLMAYER, R. (1970). "*Contribution à l'étude du compactage par vibration des matériaux pulvérulents*". PhD Thesis, Université de Grenoble, France, 183 p.

KOMODROMOS, P.I. and WILLIAMS, J.R. (2004). "*Dynamic Simulation of Multiple Deformable Bodies Using Combined Discrete and Finite Element Methods*". Special Issue of International Journal of Computer Aided Methods in Engineering - Engineering Computations Vol. 21, N°2/3/4, pp. 431-448.

KOPPEJAN, A.W., WAMELEN, B.M. and WEINBERG, L.J. (1948). "*Coastal flow slides in the Dutch province of Seeland*". Proceedings of the 2nd International Conference of Soil Mechanics and Foundation Engineering, Vol. 5, Rotterdam, The Netherlands, pp. 89-96.

KOZICKI, J. and DONZE, F.V. (2008). "*A new open-source software developed for numerical simulations using discrete modeling methods*". Computer Methods in Applied Mechanics and Engineering, Vol. 197, pp. 4429–4443.

KRAMER, S.L. (1996). "*Geotechnical earthquake engineering*". Prentice-Hall, inc. Upper Saddle River, New Jersey.

KRUYT, N. and ROTHENBURG, L. (1996). "*Micromechanical definition of the strain tensor for granular materials"*. Journal of Applied Mechanics. Trans. ASME, Vol. 63, N°3, pp. 706-711.

KUDROLLI, A. (2004). "*Size separation in vibrated granular matter*". Reports on Progress in Physics, Vol. 67, pp. 209-247.

LADE, P.V. and YAMAMURO, J.A. (1999). "*Physics and mechanics of soil liquefaction*". A.A. Balkema, Rotterdam.

LANDAU, L.D. and LIFSHITZ, E.M. (1959). "*Statistical physics*". Course of theoretical physics, Vol. 5. Pergamon Press, Oxford.

LEE, J. (1994). "*Heap formation in two-dimensional granular media*". Journal of Physics A, Vol. 27, N°9, p. 257.

LEE, K.L. and SEED, H.B. (1967). "*Cyclic stress conditions causing liquefaction of sand*". Journal of the Soil Mechanics and Foundations Division, Vol. 93, n°1, pp. 47-70.

LE THIET, T. (2005). "*Etude du processus de vibrofonçage d'inclusions cylindriques en chambre d'étalonnage: Application aux pieux*". PhD Thesis, Ecole Nationale des Ponts et Chaussées, France.

LE THIET, T., CANOU, J. and DUPLA, J.-C. (2006). "*Fréquence de sollicitation et vibrofonçabilité des pieux*". Proceedings of the International Symposium on Vibratory Pile Driving and Deep Soil Vibratory Compaction, TRANSVIB 2006, Paris: LCPC, pp.177-184.

LOHSE, D., RAUHE, R., BERGMANN, R. and VAN DER MEER, D. (2004). "*Creating a dry variety of quicksand*". Nature, Vol. 432, pp. 689-690.

LOVE, A.E.H. (1952). "*A treatise on the Mathematical Theory of Elasticity*". Cambridge University Press, fourth edition.

LUBKIN, J.L. (1951). "*Torsion of elastic spheres in contact*". Journal of Applied Mechanics, Trans. ASME, Series E, Vol. 18, pp. 183-187.

LUDING, S., HERRMANN, H.J. and BLUMEN, A. (1994). "*Simulations of two-dimensional arrays of beads under external vibrations: Scaling behavior*". Physical Review E, Vol. 50, N°4, pp. 3100-3108.

MARSH, D.M. (1964). "*Plastic flow in glass*". Proceedings of Royal Society A, Vol. 279, pp. 420-435.

MATTHEWS, J.R. (1980). "*Indentation hardness and hot pressing*". Acta Metallurgica, Vol. 28, pp. 311-318.

MAW, N., BARBER, J.R. and FAWCETT, J.N. (1976). "*The oblique impact of elastic spheres*". Wear, Vol. 38, pp. 101-114.

MAW, N., BARBER, J.R. and FAWCETT, J.N. (1981). "*The role of tangential compliance in oblique impact*". Journal of lubrication technology, Trans. ASME, series F, Vol. 103, pp. 74-80.

MELO, F., UMBANHOWAR, P.B. and SWINNEY, H.L. (1995). "*Hexagons, kinks, and disorder in oscillated granular layers*". Physical Review Letters, Vol. 75, N°21, pp. 3838-3841.

MICHAELIDES, O., GAZETAS, G., BOUCKOVALAS, G. and CHRYSIKOU, E. (1998). "*Approximate non-linear dynamic axial response of piles*". Géotechnique, Vol. 48, N°1, pp. 33-53.

MINDLIN, R.D. (1949). "*Compliance of elastic bodies in contact*". Journal of Applied Mechanics, Trans. ASME, Series E, Vol. 16, pp. 259-268.

MINDLIN, R.D., MASON, W.P., OSMER, J.F. and DERESIEWICZ, H. (1952). "*Effects of an oscillating tangential force on the contact surfaces of elastic spheres*". Proc. 1st US National Congress of Applied Mechanics, pp. 203-208.

MINDLIN, R.D. and DERESIEWICZ, H. (1953). "*Elastic spheres in contact under varying oblique forces*". Journal of Applied Mechanics, Trans. ASME, Series E, Vol. 20, pp. 327-344.

MOGAMI, T. and KUBO, K. (1953). "*The behavior of soil during vibration*". Proceedings of the Third International Conference on Soil Mechanics and Foundation Engineering. Switzerland, Vol. 1, pp. 152-155.

MOREAU, J.-J. (1997). "*Numerical investigation of shear zones in granular materials*".
Friction, Arching, Contact Dynamics, World Scientific Publishing Company, London, Wolf D.E. and Grassberger, P. (eds.), pp. 233–247.

MORTON, W.B. and CLOSE, L.J. (1922). "*Notes on Hertz' theory of contact problems*". Philosophical magazine, Vol. 43, pp. 320-329.

NEWTON, I. (1687). "*Philosophiae Naturalis Principia Mathematica*". S. Pepys Imprimatur. Londini.

NORBURY, A.L. and SAMUEL, T. (1928). "*The recovery and sinking-in or piling-up of material in the Brinell test*". Journal of the Iron and Steel Institute, Vol. 117, pp. 673-687.

O'NEILL M.W., VIPULANANDAN, C. and WONG, D. (1990). "*Laboratory modeling of vibro-driven piles*". Journal of the Geotechnical Engineering Division, ASCE, Vol. 116, N°8, pp. 1190-1209.

PAK, H.K. and BEHRINGER, R.P. (1993). "*Surface waves in vertically vibrated granular materials*". Physical Review Letters, Vol. 71, N°12, pp. 1832-1835.

PÖSCHEL, T., BRILLIANTOV, N., FORMELLA, A., HECKEL, M., KRÜLLE, C., MÜLLER, P., SALUEÑA, C. and SCHWAGER, T. (2008). "*Contact of granular particles and the simulation of rapid flows using event-driven molecular dynamics*". European Journal of Environmental and Civil Engineering, Vol. 12, N°7-8, pp. 827-870.

POULOS, S.J. (1981). "*The steady state of deformation*". Journal of the Geotechnical Engineering Division, ASCE, Vol. 107, N°5, pp. 553-562.

POULOS, H.G. (1988). "*Cyclic stability diagram for axially loaded piles*". Journal of the Geotechnical Engineering Division, ASCE, Vol. 113, N°8, pp. 877-895.

PRAKASH, S. and GUPTA, M.K. (1967). "*Compaction of sand under vertical and horizontal vibrations*". Proceedings of the Southeast Asian Regional Conference on Soil Engineering, Bangkok, Thailand, pp. 201-210.

RAO, P.M. (1993). "*Effect of pile geometry and soil saturation in the behavior of nondisplacement piles installed by vibration*". MSc thesis, University of Houston, Texas, USA.

RESEAU GENIE CIVIL ET URBAIN. (2006). "*Vibratory Pile-Driving: Technical guide*". Presses de l'Ecole Nationale des Ponts et Chaussées, Paris.

RICHMOND, O., MORRISON, H.L. and DEVENPECK, M.L. (1974). "*Sphere indentation with application to the Brinell hardness test*". International Journal of Mechanical Sciences, Vol. 16, pp. 75-82.

RODGER, A.A. (1976). "*An experimental and theoretical investigation of the parameters influencing the vibratory penetration of dry cohesionless soils*". PhD Thesis. University of Aberdeen.

RODGER, A.A. and LITTLEJOHN, G.S. (1980). "*A study of vibratory driving in granular soils*". Géotechnique, Vol. 30, N°3, pp. 269-293.

ROTHENBURG L. and BATHURST, R.J. (1989). "*Analytical study of induced anisotropy in idealized granular materials*". Géotechnique, Vol. 39, n°4, pp. 601-614.

ROUX, J.-N. (2010). Personal communication.

RUSSEL, R.D. and TAYLOR, R.E. (1937). "*Bibliography on roundness and shape of sedimentary particles*". Rept. Comm. Sed., 1936-1937, Nat. Research Council, pp. 65-80.

SACKFIELD, A. and HILLS, D.A. (1983). "*A note on Hertz contact problem : Correlation of standard formulae*". Journal of strains analysis, Vol. 18, pp. 195-197.

SCHLOSSER, F. (1974). "*Influence des déformations des grains dans les milieux granulaires*", Rheologica Acta, Vol. 13, pp. 650-657.

SCHMID, W.E. and HILL, H.T. (1966). "*The driving of piles by longitudinal vibrations*". Engineering Research Series, Princeton University.

SEED, H.B. and LEE, K.L. (1966). "*Liquefaction of saturated sands during cyclic loading*". Journal of the Soil Mechanics and Foundations Division, ASCE, Vol. 92, N°6, pp. 105-134.

SEED, H.B. and LEE, K.L. (1967). "*Undrained strength characteristics of cohesionless soils*". Journal of the Soil Mechanics and Foundations Division, ASCE, Vol. 93, N°6, pp. 333-360.

SELIG, E.T. (1963). "*Effect of vibration on density of sand*". Proceedings of the Second Pan American Conference on Soil Mechanics and Foundation Engineering, Brazil, Vol. 1, pp. 129-144.

SIEFFERT, J.-G. (2004). "*Essais de Merville. Interprétation et modélisation*". Research report IREX LC/03/VBR/29, 127 p.

SLADEN, J.A., D'HOLLANDER, R.D. and KRAHN, J. (1985). "*The liquefaction of sands, a collapse surface approach*". Canadian Geotechnical Journal, Vol. 22, N°4, pp. 564-578.

SONDERGAARD, R., CHANEY, K. and BRENNEN, C.E. (1990). "*Measurements of solid spheres bouncing off flat plates*". Journal of Applied Mechanics, Trans. ASME, Vol. 57, pp. 694-699.

STRONGE, W.J. (2000). "*Impact mechanics*". Cambridge University Press.

TABOR, D. (1948). "*A simple theory of static and dynamic hardness*". Proceedings of Royal Society A, Vol. 192, pp. 247-274.

TAYLOR, R. (ed.) (1995). "*Geotechnical Centrifuge technology*". Chapman and hall, London.

THORNTON, C. (1997). "*Coefficient of restitution for collinear collisions of elastic-perfectly plastic spheres*". Journal of Applied Mechanics, Trans. ASME, Vol. 64, pp. 383-386.

TIMOSHENKO, S.P. and GOODIER, J.N. (1970). "*Theory of Elasticity*". McGraw-Hill, third edition.

TSUJI, Y., TANAKA, T. and ISHIDA, T. (1992). "*Lagrangian numerical simulation of plug flow of cohesionless particles in a horizontal pipe*". Powder Technology, Vol. 71, pp. 239-250.

TSUJI, Y., KAWAGUSHI, T. and TANAKA, T. (1993). "*Discrete particle simulation of two-dimensional fluidized bed*". Powder Technology, Vol. 77, pp. 79-87.

VANDEN BERGHE, J.-F. (2001). "*Sand strength degradation within the framework of vibratory pile driving*". PhD Thesis, Université catholique de Louvain, Belgium.

VIKING, K. (1997). "*Vibratory driven pile and sheet-piles – a literature survey*". Division of Soil and Rock Mechanics, Royal Institute of Technology, Sweden, Report 3035, 75 p.

VIKING, K. (1998). "*Driveability studies of vibro-driven model piles in non-cohesive soils – laboratory simulations*". MSc thesis, Royal Institute of Technology, Sweden.

VIKING, K. (2002). "*Vibro-driveability – A field study of vibratory driven sheet piles in non-cohesive soils*". PhD Thesis, Royal Institute of Technology, Sweden.

VUCETIC, M. and DOBRY, R. (1991). "*Effect of soil plasticity on cyclic response*". Journal of Geotechnical Engineering, ASCE, Vol. 117, N°1, pp. 89-117.

VUCETIC, M. (1994). "*Cyclic threshold shear strains in soils*". Journal of Geotechnical Engineering, ASCE, Vol. 120, N°12, pp. 2208-2228.

VU-QUOC, L. and ZHANG, X. (1999). "*An accurate and efficient tangential force–displacement model for elastic frictional contact in particle-flow simulations*". Mechanics of Materials, Vol. 31, pp. 235–269.

WALTON, O.R. (1982). "*Explicit particle dynamics model for granular materials*". Numerical methods in geomechanics, Edmonton 1982, Vol 3, pp. 1261-1268.

WALTON, O.R. and BRAUN, R.L. (1986). "*Viscosity, granular-temperature, and stress calculations for shearing assemblies of inelastic, frictional disks*". Journal of rheology, Vol. 30, pp. 949-980.

WANG, H. (1994). "*Experimental study and finite element analysis of driveability and static behavior of various piles installed by vibratory driving*". PhD Thesis, University of Houston, Texas, USA.

WHENHAM, V. HUYBRECHTS, N., LEGRAND, C., BOURDOUXHE, M.-P. and SCHMITT, A. (2006). "*Energy consumption during sheet piles vibro-driving: experimental results*". Proceedings of the International Symposium on Vibratory Pile Driving and Deep Soil Vibratory Compaction, TRANSVIB 2006, Paris: LCPC, pp. 31-52.

WHENHAM, V., AREIAS, L., ROCHER-LACOSTE, F., VIE, D., BOURDOUXHE, M.-P. and HOLEYMAN, A. (2009). "*Full scale sheet pile vibro-driving*". Proceedings of the XVIIth International Conference on Soil Mechanics and Geotechnical Engineering, Alexandria, Egypt, pp. 1354-1357.

WHENHAM, V. and HOLEYMAN, A. (2010). "*Vibrodriving prediction models vs. experimental results*". Proceedings of the Vth International Conference on Recent Advances in Geotechnical Earthquake Engineering and Soil Dynamics, San Diego, USA, CD-Rom Proceedings, 12 p.

WILLIAMS, J.R, HOCKING, G, MUSTOE, G.G.W. (1985). "*The theoretical basis of the discrete element method*". NUMETA '85, Numerical Methods in Engineering, Theory and Application, Conference in Swansea, January 7–11. A.A. Balkema, Rotterdam, 1985, pp. 897–906.

YOUNG, H.D. and FREEDMAN, R.A. (2000). "*University physics with modern physics*". Addison Wesley Longman, Inc.

YOUD, T.L. (1967). "*Reduction of critical void ratio during steady state vibrations*". Proceedings of the International Symposium on Wave Propagation and Dynamic Properties of Earth Material, New-Mexico, pp. 737-744.

ZEGHAL, M. and EL SHAMY, U. (2004). "*Dynamic response and liquefaction of saturated granular soils: a micro-mechanical approach*". Proccedings of the International Conference on cyclic behaviour of soils and liquefaction phenomena, Bochum, Germany, A.A. Balkema, Triantafyllidis, Th. (ed.), pp. 589-602.

9 List of Symbols

9.1 Soil mechanics notations

9.1.1 Roman symbols

a : acceleration amplitude of vibration (m/s²)
A : single amplitude of the dynamic mass (mm) or displacement amplitude of vibration (mm)
b : empirical factor ($Pa^{-1}.sec^{-1}$)
C_u : Uniformity coefficient of Hazen (-)
d : grain diameter (mm)
d_{50} : sand median diameter (mm)
D_r : relative density of sand percent
$D_{r,\Gamma}$: dry relative density of sand percent at vibratory equilibrium void ratio
e : void ratio (-)
e_c : critical void ratio (-)
e_{init} or e_0 : initial void ratio (-)
e_{max} : maximum void ratio, void ratio in loosest condition (-)
e_{min} : minimum void ratio, void ratio in densest condition (-)
e_Γ : vibratory equilibrium void ratio (-)
f : internal friction coefficient (-)
f_{res} : asymptotical value of the friction coefficient (-)
f_{st} : static internal friction coefficient without vibration (-)
fr : frequency of the vibrator (Hz) or frequency of the vibration (Hz)
F : total load applied on the soil during vibratory pile driving (N)
F_0 : static or bias load (N)
F_{cyc} : cyclic load (N)
F_v : sinusoidal vertical force (N)
g : gravitational acceleration (m/s²)
G : shear modulus of the soil (Pa)
G_{ff} : shear modulus of the soil in the far field (Pa)
$j_d(z)$: downward flux along the lateral walls of the container (kg/s)
$j_i(z)$: inward transverse flux (kg/s)
$j_u(z)$: upward flux in the central region of the container (kg/s)
K_0 : earth pressure coefficient (-)
me : total eccentric moment of the vibrator (kg.m)
M_c : mass of the clamping device (kg)
M_{eb} : mass of the exciter block (kg)
M_{ib} : mass of the isolator block, sometimes called bias mass (kg)
M_p : mass of the pile (kg)
M_{vib} : mass of the vibrator (kg)
N : number of cycles of vibration (-)
p : total effective stress (kPa)
p' : effective mean stress (kPa)
q : deviator (kPa)
Q_c : static load capacity (kN)

r : radial distance (m)
R : pile radius (m)
R_M : minimum dynamic side resistance (kN)
R_S : dynamic side resistance (kN)
R_{St} : static side resistance (kN)
s : sphere penetrometer displacement (mm)
s_0 : single amplitude of the vibrator (mm)
S_{sp} : double amplitude of the movement for a free hanging vibrator (mm)
t : time (s)
T : period of harmonic vibration (s)
T_c : retaining force applied by the carrier (N)
u : pore pressure (kPa)
v : average velocity of sand particles (mm/s)
V : steady sinking velocity ($m.sec^{-1}$) or velocity amplitude of vibration (mm/s)
z : depth (m)

9.1.2 Greek symbols

α_1 : empirical coefficient (-)
α_t : index of vibratory compaction (-)
β_n : empirical coefficient characterizing the rate of compaction (-)
β_t : empirical coefficient characterizing the rate of compaction (min^{-1})
γ_1 : equivalent sphere unit weight ($N.m^{-3}$)
γ_2 : fluid unit weight ($N.m^{-3}$)
Γ : dimensionless acceleration amplitude (-)
Γ_0 : relative threshold dimensionless acceleration (-)
ε : empirical factor (-)
ε_a : axial strain (%)
θ : dynamic angle of the inclined free surface (°)
λ : vibro-shear exponent (-)
μ : soil vibro-viscosity (Pa.sec)
ρ_s : volumetric mass of sand grains (kg/m^3)
ρ : dry sand density (gr/cm^3)
ρ_{max} : maximum volumetric mass of dry sand (gr/cm^3)
ρ_{min} : minimum volumetric mass of dry sand (gr/cm^3)
σ : normal stress (kPa)
σ_1 : axial total normal stress (kPa)
σ_1' : effective axial normal stress (kPa)
σ_3 : radial total normal stress (kPa)
σ_3' : effective radial normal stress (kPa)
σ_S : shaking pressure (kPa)
τ : shear strength (kPa)
τ_{ds} : ultimate shear strength of dry sand (kPa)
τ_{res} : asymptotical value of the shear strength (kPa)
τ_{ss} : ultimate shear strength of saturated sand (kPa)
τ_{st} : static shear strength (kPa)
ϕ_{mob} : mobilized friction angle (°)
Φ_c : critical state friction angle (°)
ω : angular frequency of the vibrator (rad/s)

9.1.3 Abbreviations

BBRI : Belgian Building Research Institute
CERMES : Centre d'Enseignement et de Recherche en Mécanique des Sols
CSSM : Critical State Soil Mechanics
CVR : Critical Void Ratio
ENPC : Ecole Nationale des Ponts et Chaussées
EVR : vibratory Equilibrium Void Ratio
FRIA : Fonds pour la formation à la Recherche dans l'Industrie et dans l'Agriculture
RGCU : Réseau Génie Civil et Urbain
SPE's : Sphere Penetration Experiments
UCL : Université catholique de Louvain-la-Neuve

9.2 DEM and contact mechanics notations

9.2.1 Roman symbols

a : coefficient of contact normal anisotropy (-) or radius of the contact area (m)
a_n : coefficient of average normal force anisotropy (-)
a_t : coefficient of average tangential force anisotropy (-)
A : displacement amplitude of vibration (mm)
A_2 : vertical displacement amplitude of vibration (mm)
c : radius of the 'stick circle' (m)
c_0 : one-dimensional elastic propagation velocity of the stress wave in the particle material (m/s)
c_x : tangential damping constant (kg/s)
c_x^{crit} : critical tangential damping constant (kg/s)
c_z : normal damping constant (kg/s)
c_z^{crit} : critical normal damping constant (kg/s)
C_{22} : elastic modulus (MPa)
C_n : coordination number (-)
C_n* : coordination number taking into account the active particles of the assembly (-)
C_u : Uniformity coefficient of Hazen (-)
d_{50} : sand median diameter (mm)
d_{max} : maximum diameter (mm)
d_{min} : minimum diameter (mm)
D_c : contact density of the granular assembly (1/m³)
D_x : tangential viscous damping force acting on the contact area (N)
D_z : normal viscous damping force acting on the contact area (N)
E(θ) : analytical expression of the contact orientation distribution (-)
E : elastic modulus of the particle material (N/m²)
E_0 : compressibility coefficient (N/m²)
E* : equivalent elastic modulus of contact (N/m²)
F : resultant forces acting on particle (N)
$\overline{f_0}$: average normal contact force (N)
$f_n(\theta)$: normal contact force (N)

$\overline{f_n}(\theta)$: analytical expression of the angular distribution of the normal contact forces (-)
$f_t(\theta)$: tangential contact force (N)
$\overline{f_t}(\theta)$: analytical expression of the angular distribution of the tangential contact forces (-)
fr : frequency of the vibration (Hz)
g : gravitational acceleration (m/s²)
G : shear modulus of the particle material (N/m²)
H_{eff} : effective height of the particle assembly (m)
$\dot{H}$: angular moment of the particle (N.m)
I : principal moment of inertia of the particle (rad/s²)
k : wave number (1/m)
k_x : tangential contact stiffness (N/m)
k_z : tangent normal contact stiffness (N/m)
K_0 : earth pressure coefficient (-)
K_z : secant normal contact stiffness (N/m)
L : lateral size of the numerical container (m)
m : particle mass (kg)
M : resultant moment acting on the particle (N.m)
M_z : twisting moment at the surface of the sphere during torsional loading (N.m)
n : porosity of the assembly (-)
N_{ap} : number of active particles (-)
N_c : contact number (-)
N_p : particle number (-)
N_{pp} : number of passive particles (-)
p : normal pressure acting on the contact area (N/m²)
p_0 : maximum normal pressure acting on the contact area (N/m²)
$(p_0)_Y$: maximum normal pressure acting on the contact area at the yield stress (N/m²)
p_d : dynamic mean normal pressure acting on the contact area (N/m²)
p_m : mean normal pressure acting on the contact area (N/m²)
P : normal force acting on the contact area (N)
P^{max} : maximum normal force acting on the contact area (N)
P_Y : normal force acting on the contact area at the yield stress (N)
q : tangential stress acting on the contact area (N/m²)
Q : tangential force acting on the contact area (N)
r : radial direction (m)
R : radius of the particle (m)
R* : equivalent radius of contact (m)
s_x : slip component at the surface of the contact area acting in the parallel direction to tangential loading (m)
s_y : slip component at the surface of the contact area acting in the perpendicular direction to tangential loading (m)
t : time (s)
t_c or T_c : contact time (s)
t_e : elastic deflexion time (s)
t_{ev} : average time between collision events (s)

t_p : plastic indentation time (s)
t^* : free fall time of the particle (s)
t_{gr}^* : equivalent "group" free-fall time (s)
T: period of harmonic vibration (s)
T_0 : one-dimensional propagation time of the stress wave in the particle material (s)
$u_j^{(A)}$: location of the center of particle A
$u_j^{(C)}$: location of the contact point C
u_r : elastic radial displacement of the contact area (m)
u_x : elastic tangential displacement of the contact area occurring in the parallel direction to tangential loading (m)
u_y : elastic tangential displacement of the contact area occurring in the perpendicular direction to tangential loading (m)
u_z : elastic normal displacement of the contact area (m)
$\ddot{u}$: particle acceleration (m/s^2)
v_2 : vertical velocity amplitude of vibration (mm/s)
V : velocity amplitude of vibration (mm/s) or impact velocity (mm/s)
V_m : volume of the measurement layer (m^3)
V_x : tangential relative velocity of approach between impacting particles (m/s)
V_z : normal relative velocity of approach between impacting particles (m/s)
W : kinetic energy before impact (N.m)
W' : kinetic energy after impact (N.m)
W_{kin} : kinetic energy (N.m)
x : tangential direction of contact (-)
Y : yield stress of the particle material (N/m^2)
Y_d : dynamic yield stress of the particle material (N/m^2)
z : normal direction of contact (-)

9.2.2 Greek symbols

β : tangential restitution coefficient (-)
β_1 : rigid rotation at the surface of the sphere during torsional loading (rad)
Γ : dimensionless acceleration amplitude (-)
δ_x : tangential deformation of the contact area (m)
δ_z : normal indentation of the contact area (m)
δ_{ze} : elastic normal deflexion of the contact area (m)
δ_{zR} : residual normal permanent indentation of the contact area (m)
δ_{zY} : normal indentation of the contact area at the yield stress (m)
δ_z^{max} : maximum normal indentation of the contact area (m)
ΔW : hysteretic loss of energy in cyclic tangential loading (N.m)
ε : normal restitution coefficient (-)
ε_{22} : vertical deformation (-)
ζ : coefficient of Dundurs and Lee (1972) which controls the elastic similarity between the impacting particles (-)
η_2 : dimensionless vertical acceleration of vibration (-)
θ : orientation (°)
θ_a : direction of contact anisotropy (°)
θ_f : direction of average normal contact force anisotropy (°)
θ_t : direction of average tangential contact force anisotropy (°)
κ : stiffness contact ratio (-)

κ^* : dimensionless stiffness parameter (-)
λ_x : critical tangential damping ratio (-)
λ_z : critical normal damping ratio (-)
μ_{fl} : fluid viscosity (Pa.s)
μ_p : interparticular friction coefficient (-)
μ_w : wall friction coefficient (-)
ν : Poisson's ratio of the particle material (-)
ξ_x : tangential contact compliance (m/N)
ξ_z : normal contact compliance (m/N)
ρ_{fl} : fluid density (gr/cm³)
ρ_s : volumetric mass of the particle material (kg/m³)
σ_{11} : horizontal contact stresses in the assembly (Pa)
σ_{22} : vertical contact stresses in the assembly (Pa)
σ_c : contact stresses (Pa)
σ_{fl} : fluid stresses (Pa)
σ_r : stresses due to the rotation of the particles (Pa) or radial stress at the contact area (Pa)
σ_z : normal stress at the contact area (N/m²)
σ_t : total stress tensor (Pa)
σ_θ : tangential stress at the contact area (N/m²)
τ : shear strength (N/m²)
τ_1 : principal shear stress of the contact (N/m²)
ϕ_{mob} : mobilized friction angle (°)
Φ : solid concentration (-)
χ : dimensionless coefficient which determines the impact behavior (-)
ψ_1 : dimensionless incident angle of the impact (-)
ψ_2 : dimensionless reflective angle of the impact (-)
ω : particle angular velocity (rad/s) or angular frequency of the vibration (rad/s)
ω_x : tangential natural frequency of the impact (1/s)
ω_z : normal natural frequency of the impact (1/s)
$\dot{\omega}$: particle angular acceleration (rad/s²)

9.2.3 Abbreviations

CD : Contact Dynamics method
DEM : Discrete Element Method or Modeling
ED : Event-Driven approach
FTP : First Turning Point
LPBC : Lateral Periodic Boundary Conditions
MBF : Maw, Barber and Fawcett approach
MC : statistical Monte-Carlo approach
MD : Molecular Dynamics or Mindlin-Deresiewicz approach
PBC : Periodic Boundary Conditions
STP : Second Turning Point
TTP : Third Turning Point

10 List of figures

Figure 1-1: Steel pile driven with vibrator in Belleville (F) (http://www.leductp.com/)..... 1
Figure 2-1: Vibrodriving : engineering issues, after Holeyman (2000)..... 7
Figure 2-2: Vibrodriver PTC 50HD2 (http://www.ptc.fayat.com/)..... 8
Figure 2-3: Components of the hydraulic vibrator, Holeyman 2000..... 8
Figure 2-4: Working principle of the vibrator. 9
Figure 2-5: Reduction of the mechanical properties of the soil during vibratory driving. 13
Figure 2-6: Influence of acceleration amplitude of the oscillations imposed by the vibratory hammer on the friction forces of the sand on lateral surface of two types of sheet-piles (after Barkan, 1963)..... 14
Figure 2-7: Undrained tests on fully saturated sands, after Castro and Poulos (1977). 17
Figure 2-8: Cyclic mobility phenomenon occuring during a cyclic undrained triaxial test a) Stress path followed during a cyclic triaxial test. b) Comparison between the evolution of maximum shear stress τ and pore pressure u during a cyclic triaxial test, Vanden Berghe (2001)..... 19
Figure 2-9: Grain structure degradation during undrained cyclic loading: a) initial saturated state and b) liquefied state, after www.ce.washington.edu..... 21
Figure 2-10: a) Patterns in the sand at rest, b) and c) disturbance of patterns in the sand when it is vibrated, after Mogami and Kubo (1953). 23
Figure 2-11: Vibratory compressibility curve of sand fill, after Barkan (1962)..... 23
Figure 2-12: Void ratio versus time for horizontal and vertical vibrations, after Prakash and Gupta (1967). 25
Figure 2-13: Void ratio change vs acceleration amplitude for horizontal and vertical vibrations, after Prakash and Gupta (1967). 26
Figure 2-14: Dry density of dune sand vs. acceleration amplitude (D'Appolonia D. J. and D'Appolonia E., 1967)..... 27
Figure 2-15: Variation of dry density after vibration with peak acceleration for dune sands of various granulometry, after (D'Appolonia D. J. and D'Appolonia E., 1967). 28
Figure 2-16: Variation of dry density after vibration with peak acceleration and surcharge, after D'Appolonia D. J. and D'Appolonia E. (1967). 29
Figure 2-17: Variation of the coefficient β_t with the acceleration amplitude and the static surcharge, after Kolmayer (1970). 30
Figure 2-18: Experimental scheme of Mogami and Kubo shear box tests. 32
Figure 2-19: Relationship between the shearing strength of dry Soma sand and the acceleration of the vibration for constant frequency (48 Hz) and various static surcharges, after Mogami and Kubo (1953). 32
Figure 2-20: Experimental set-up used for investigation of the shearing resistance of soil, after Barkan (1962)..... 33
Figure 2-21: a) Relationship between the coefficient of internal friction of sand a) and the acceleration of vibrations for various displacement amplitudes and frequencies, b) Relationship between the effect of vibrations and the diameter of sand grains (A = 0.35 mm for both curves), after Barkan (1962)..... 33

Figure 2-22: Experimental scheme of Youd shear box tests. 34
Figure 2-23: tan ϕ versus initial void ratio (before shearing), after Youd (1967)..... 35
Figure 2-24: EVR and CVR values as a function of the acceleration of the vibration, after Youd (1967). 36
Figure 2-25: Experimental scheme of Kolmayer shear box tests. 38
Figure 2-26: Influence of acceleration amplitude on the intrinsic curve of sand, after Kolmayer (1970). 38
Figure 2-27: Influence of the acceleration amplitude on the internal friction coefficient and on the shaking pressure of dry sand, after Kolmayer (1970). 39
Figure 2-28: Sphere penetration experiments (after Barkan, 1962)..... 40
Figure 2-29: Domains of investigation of the studies characterizing the influence of vibrations on the volume change of dry sand. 44
Figure 2-30: Domains of investigation of the studies characterizing the influence of vibrations on the shear strength of dry sand. 46
Figure 2-31: Influence of the acceleration amplitude, Γ, on the internal friction coefficient, f, of dry sand. 47
Figure 2-32: Coupled influence of the acceleration amplitude, Γ, and the initial void ratio, e_0, on the internal friction coefficient, f, after Youd (1967). 47
Figure 2-33: The complete state boundary surface in q: p': e space, after Atkinson and Bransby (1978). 48
Figure 3-1: UCL Sphere Penetration Experiment (SPE) apparatus, after Denies et al. (2009). 52
Figure 3-2: Experimental scheme of the UCL-SPE apparatus. 53
Figure 3-3: MTS hydraulic jack. 54
Figure 3-4: Servovalve Moog. 54
Figure 3-5: Working scheme of the servo-hydraulic system. 55
Figure 3-6: Triaxial set-up of accelerometers PCB. 56
Figure 3-7: Data acquisition equipment for SPE measurements. 56
Figure 3-8: Inductive HBM standard displacement transducer. 56
Figure 3-9: Grain size curve of Fontainebleau sand. 57
Figure 3-10: Grain shape of Fontainebleau sand. 58
Figure 3-11: Grain shape and surface roughness of both Fontainebleau sand particles. 59
Figure 3-12: Data for drained triaxial compression tests on Fontainebleau sand (after Dupla and Canou, 1994). 59
Figure 3-13: Laboratory funnel used for sample preparation. 60
Figure 3-14: Bi-logaritmic diagram of the domain of vibrations. 61
Figure 3-15: Void ratio-time curves for UCL experiments for $\Gamma < 1$, with displacement amplitudes of vibration: A = 0.8, 1.5, 3, 4 and 10 mm. 63
Figure 3-16: Repeatability of the process of volume change of the sample during vibration for two acceleration amplitudes. 64
Figure 3-17: Void ratio versus time for two acceleration amplitudes $\Gamma \approx 0.45$ and $\Gamma \approx 0.8$ for different amplitudes of displacement and various frequencies. 65
Figure 3-18: Vibratory compressibility curve of Fontainebleau sand. 65
Figure 3-19: Relationship between β_t and the amplitude of acceleration, Γ, for Fontainebleau sand. 66
Figure 3-20: Relationship between α_t and the acceleration amplitude, Γ, for Fontainebleau sand. 66
Figure 3-21: Variation of void ratio for specimens of various heights. 67

Figure 3-22: Void ratio-number of cycles curves for UCL experiments for $\Gamma < 1$, with displacement amplitudes of vibration: A = 0.8, 1.5, 3, 4 and 10 mm. 68
Figure 3-23: Influence of the acceleration amplitude, Γ, on the empirical coefficient β_n. 68
Figure 3-24: Densification behavior. 69
Figure 3-25: Instability surface behavior: inclined free surface in the vibrated sample. 70
Figure 3-26: Convective behavior of the grains along the sides during vertical vibrations. a) during relative upward motion of the grains relative to the side, b) during relative downward motion of the grains relative to the side, c) Relationship between absolute cumulated displacement of the grains and time during convection. 71
Figure 3-27: Instability surface behavior. 72
Figure 3-28: Destruction of the inclined free surface. 73
Figure 3-29: Relationship between the dynamic angle of the inclined free surface, θ, and the acceleration amplitude, Γ. 74
Figure 3-30: Vibro-fluid behavior. 74
Figure 3-31: Relative density of dry sand after vibration vs. acceleration amplitude, Γ. In Denies et al. (2010), the displacement amplitude of vibration is set to 1.5 mm for all experiments. 75
Figure 3-32: Shutdown of the vibration for A = 1.5 mm and fr = 9, 20 and 24 Hz respectively. 77
Figure 3-33: Conventions related to the penetration of the sphere in the sand sample. 78
Figure 3-34: Dimensionless quasi-static penetration of the sphere as a function of the relative density, $D_{r,\Gamma}$. 78
Figure 3-35: Sphere penetration logs for A = 0.8 mm and various frequencies in the densification range. 79
Figure 3-36: Sphere penetration logs in the densification range for different amplitudes of vibration. 80
Figure 3-37: Sphere motion during vibratory sinking in the densification range, for several displacement amplitudes and various frequencies. 80
Figure 3-38: Normalized vibratory sphere sinking after 500s as a function of the acceleration for different displacement amplitudes. 81
Figure 3-39: Normalized vibratory sphere sinking after 2500 cycles as a function of the acceleration for different displacement amplitudes. 81
Figure 3-40: Repeatability of the SPE in the densification range. 82
Figure 3-41: SPE's for specimens of various depth: a) Sphere position with time, b) Sphere sinking with time. 83
Figure 3-42: Sphere penetration logs for A = 1.5 mm at two frequencies within the instability surface range. 83
Figure 3-43: Sphere penetration logs for A = 1.5 mm and various frequencies in the vibro-fluid range. 84
Figure 3-44: Repeatability of the SPE in the vibro-fluid range. 85
Figure 3-45: Sphere penetration logs for A = 0.8, 1.5 and 3 mm for various frequencies in the vibro-fluid range. 85
Figure 3-46: Transient sinking phase of the sphere penetrometer in the vibro-fluid range. 86
Figure 3-47: Sphere sinking velocities in the vibro-fluid range. 87

Figure 3-48: Influence of the sphere mass and diameter on its equilibrium height in the vibro-fluid regime. 87
Figure 3-49: Influence of the apparent sphere density on its equilibrium height in the vibro-fluid regime. 88
Figure 3-50: Influence of the sphere size on the maximum value of sphere sinking velocity in the vibro-fluid regime. 88
Figure 3-51: Influence of the the apparent sphere density on the maximum value of sphere sinking velocity in the vibro-fluid regime. 89
Figure 3-52: Synthesis of the SPE's performed in the three dynamic ranges. 89
Figure 3-53: Sphere displacement during vibratory sinking for vibrations with A = 1.5 mm and various frequencies. 90
Figure 3-54: Elasto-plastic and vibratory sinking regimes, Le Thiet (2005). 96
Figure 3-55: Cyclic stability diagram for Le Thiet experiments (2005). 97
Figure 4-1: Global and local coordinate systems. 101
Figure 4-2: The calulation cycle in PFC2D, after Itasca (2004). 103
Figure 4-3: Rheological model of contact. 103
Figure 4-4: Scheme of reference for relative motions arising at the contact area. 105
Figure 4-5: Numerical sample of sand grains. 108
Figure 4-6: Bottom of the granular assembly: development of the force chains. 109
Figure 4-7: Numerical particle size distribution curve. 109
Figure 4-8: Degree of uniformity of the numerical assembly. a) Porosity at rest (black line) and minimum porosity (grey line), b) number of particles (black line), number of active particles (grey line) and number of passive particles (light grey line), c) number of contacts, d) coordination number C_n (black line) and coordination number C_n* (grey line). The dashed black lines represent the effective height of the sample. 112
Figure 4-9: Illustration of a passive grain. 113
Figure 4-10: Characteristics of fabric of the numerical assembly: a) depth-averaged normalized orientations of contact (black line) and E(θ) (grey line), b) depth-averaged normalized normal contact force orientations (black line) and $\overline{f_n}(\theta)/\overline{f_0}$ (grey line), c) depth-averaged normalized tangential contact force orientations (black line) and $\overline{f_t}(\theta)/\overline{f_0}$ (grey line), d) ratio of the depth-averaged normalized tangential to normal contact force orientations. 115
Figure 4-11: Stress field in the numerical assembly. a) Development of the stress components: σ_{22} (continuous black line), σ_{11} (continuous grey line), σ_{12} (dashed black line), σ_{21} (dashed grey line). b) Development of the earth pressure coefficient K_0: slope of the straight line. 117
Figure 4-12: Computation of the elastic modulus C_{22}. 119
Figure 4-13: Propagation of an elastic longitudinal wave in the numerical sample: $t_1 = 0$ s, $t_2 = 1.40\ 10^{-3}$ s, $t_3 = 2.78\ 10^{-3}$ s and $t_4 = 4.17\ 10^{-3}$ s. 120
Figure 4-14: Domain of vibrations for numerical simulations and experiments. 121
Figure 4-15: Dynamic ramp. 121
Figure 4-16: Mean porosity variation of the granular sample during the vibration (A = 1.5 mm and Γ = 0.5). 122
Figure 4-17: Relationship between the vertical stress, σ_{22}, in the granular medium at the bottom of the sample and the number of cycles (A = 1.5 mm and Γ = 0.5) 123
Figure 4-18: Evolution of the stress field in the numerical sample during the 10^{th} cycle of vibration (A = 1.5 mm and Γ = 0.5). 124

Figure 4-19: Evolution of the ratio of the horizontal to vertical stresses during the vibration (A = 1.5 mm and Γ = 0.5)..... 125
Figure 4-20: Evolution of the dimensionless kinetic energy in the sample during the vibration (A = 1.5 mm and Γ = 0.5)..... 126
Figure 4-21: Dimensionless kinetic energy in the sample during the 10^{th} cycle of vibration (A = 1.5 mm and Γ = 0.5)..... 126
Figure 4-22: Relationships between the number of cycles and the total contact number (a), the total number of passive particles (b), the mean coordination numbers C_n (c), and C_n* (d) for the whole sample (A = 1.5 mm and Γ = 0.5)..... 127
Figure 4-23. Passive particles in the sample for the 10^{th} cycle of vibration (A = 1.5 mm and Γ = 0.5)..... 128
Figure 4-24: Conservation of the contact network during the 10^{th} cycle of vibration (A = 1.5 mm and Γ = 0.5)..... 129
Figure 4-25: Evolution of the force chains during the 10^{th} cycle of vibration (A = 1.5 mm and Γ = 0.5)..... 130
Figure 4-26: Emergence of a secondary force chain illustrated by the transformation of the grey colored (dark-shaded) grain from a passive to an active state. Contact network a) and force chains b) during the dilatation. Contact network c) and force chains d) during the compaction. Vibration performed at A = 1.5 mm and Γ = 0.5. 131
Figure 4-27: Emergence of an arch illustrated by the transformation of the grey colored (dark-shaded) grain from an active to a passive state. Contact network a) and force chains b) during the dilatation. Contact network c) and force chains d) during the compaction. Vibration performed at A = 1.5 mm and Γ = 0.5..... 132
Figure 4-28: Characteristics of fabric of the numerical assembly in steady vibratory regime (A = 1.5 mm and Γ = 0.5)..... 133
Figure 4-29: Principal directions of contact, average normal contact force and average tangential contact force anisotropy during the vibration (A = 1.5 mm and Γ = 0.5)..... 133
Figure 4-30: Relationships between the number of cycle and the coefficient of contact normal anisotropy, a (a), the coefficient of average normal force anisotropy, a_n (b), the coefficient of average tangential force anisotropy, a_t (c) and the mobilized friction angle, ϕ_{mob} (d)..... 134
Figure 4-31: Variation of the mobilized friction angle, ϕ_{mob}, during the vibration. The black line, the continuous grey lines and the dashed grey line are respectively computed on the basis of the stress-force-fabric relationship, the measurement of the stress field in the layers and the Jaky formula..... 135
Figure 4-32: a) Porosity variation in the measurement layers of the granular sample during the vibration (A = 1.5 mm and Γ = 1.02), b) enlargement of the curves in the steady vibratory regime..... 136
Figure 4-33: Porosity variation in the granular sample during a) the 2^{nd} and b) the 27^{th} cycles of vibration (A = 1.5 mm and Γ = 1.02)..... 137
Figure 4-34: Porosity variation in the measurement layers of the granular sample (A = 1.5 mm and Γ = 2). Inset: enlargement of the curves..... 137
Figure 4-35: Evolution of the particle velocity field in the granular sample during the 27^{th} cycle of vibration (A = 1.5 mm and Γ = 1.02)..... 138
Figure 4-36: Grain vertical displacements during the 27^{th} cycle of vibration (A = 1.5 mm and Γ = 1.02)..... 139

Figure 4-37: Evolution of the particle velocity field during the 27th cycle of vibration (A = 1.5 mm and Γ = 2). 140
Figure 4-38: Evolution of the particle velocity field during the 28th cycle of vibration (A = 1.5 mm and Γ = 2). 141
Figure 4-39: Evolution of the particle velocity field during the 29th cycle of vibration (A = 1.5 mm and Γ = 2). 142
Figure 4-40: Evolution of the porosity in the measurement layers of the granular sample during a) the 27th, b) the 28th and c) the 29th cycle of vibration (A = 1.5 mm and Γ = 2). 143
Figure 4-41: Evolution of the vertical stresses, σ_{22}, in the measurement layers of the granular sample at Γ = 1.02 and Γ = 2. Inset: enlargement of the curves. 144
Figure 4-42: Evolution of the vertical stress in the numerical sample during the 27th cycle of vibration for A = 1.5 mm and Γ = 1.02 (a), and during the 27th (b), the 28th (c) and the 29th (d) cycle of vibration for A = 1.5 mm and Γ = 2. 145
Figure 4-43: Total dimensionless kinetic energy in the sample during the vibration at Γ = 1.02 and Γ = 2. 145
Figure 4-44: Evolution of the dimensionless kinetic energy in the numerical sample during the 27th cycle of vibration for A = 1.5 mm and Γ = 1.02 (a), and during the 27th (b), the 28th (c) and the 29th (d) cycle of vibration for A = 1.5 mm and Γ = 2. 146
Figure 4-45: Relationships between the number of cycles (0 - 30) and the total contact number (a), the total number of passive particles (b) and the mean coordination number C_n (c) for the whole sample (A = 1.5 mm and Γ = 1.02). 147
Figure 4-46: Relationships between the number of cycles (20 - 30) and the total contact number (a), the total number of passive particles (b) and the mean coordination number C_n (c) for the whole sample in the steady vibratory regime (A = 1.5 mm and Γ = 1.02). 147
Figure 4-47: Evolution of the contact network during the 27th cycle of vibration (A = 1.5 mm and Γ = 1.02). 148
Figure 4-48: Evolution of the force chains during the 27th cycle of vibration (A = 1.5 mm and Γ = 1.02). 149
Figure 4-49: Evolution of a) the contact number, b) the number of passive particles and c) the coordination number, C_n, in the numerical sample during the 27th cycle of vibration (A = 1.5 mm and Γ = 1.02). 150
Figure 4-50: Relationships between the number of cycles (0 – 30) and the total contact number (a), the total number of passive particles (b) and the mean coordination number, C_n, (c) for the whole sample (A = 1.5 mm and Γ = 2). 151
Figure 4-51: Relationships between the number of cycles (26 - 30) and the total contact number (a), the total number of passive particles (b) and the mean coordination number, C_n, (c) for the whole sample for the cycles 26 to 30 (A = 1.5 mm and Γ = 2). 151
Figure 4-52: Evolution of the contact network during the 27th cycle of vibration (A = 1.5 mm and Γ = 2). 152
Figure 4-53: Evolution of the contact network during the 28th cycle of vibration (A = 1.5 mm and Γ = 2). 153
Figure 4-54: Evolution of the contact network during the 29th cycle of vibration (A = 1.5 mm and Γ = 2). 154
Figure 4-55: Evolution of the force chains during the 27th cycle of vibration (A = 1.5 mm and Γ = 2). 155

Figure 4-56: Evolution of the force chains during the 28th cycle of vibration (A = 1.5 mm and Γ = 2). 156
Figure 4-57: Evolution of the force chains during the 29th cycle of vibration (A = 1.5 mm and Γ = 2). 157
Figure 4-58: Evolution of the number of passive particles in the measurement layers of the granular sample during a) the 27th, b) the 28th and c) the 29th cycle of vibration (A = 1.5 mm and Γ = 2). 158
Figure 4-59: Evolution of the coordination number, C_n, in the measurement layers of the granular sample during a) the 27th, b) the 28th and c) the 29th cycle of vibration (A = 1.5 mm and Γ = 2). 158
Figure 4-60: Comparison of the evolution of C_n for vibration at Γ = 1.02 and Γ = 2. 158
Figure 4-61: Characteristics of fabric of the numerical assembly in the steady vibratory regime (A = 1.5 mm and Γ = 1.02). 160
Figure 4-62: a) Vertical fluid stresses in the measurement layers of the sample during the vibration (A = 1.5 mm and Γ = 1.02), b) enlargement of the curves in the steady vibratory regime. 161
Figure 4-63: Evolution of the ratio of the fluid stresses to contact stresses during the 27th cycle of vibration (A = 1.5 mm and Γ = 1.02). 162
Figure 4-64: C_n vs. porosity: elastic, vibro-fluid and high-dilating behaviors at Γ = 0.5, Γ = 1.02 and Γ = 2 for all the measurement layers and all the cycles of vibration. 164
Figure 4-65: Trajectory of a reference particle subjected to vertical vibration. 164
Figure 4-66: State diagram – Mean contact stress vs. coordination number for all the cycles of vibration. 165
Figure 5-1: Types of vibrodriving motion as a function of the void ratio and the acceleration amplitude of the vibrations, after Rodger (1976). 169
Figure 5-2: Conceptual micromechanical modeling of low virvatory driving: a) side resistance and b) end resistance. 170
Figure 5-3: Conceptual micromechanical modeling of fast virvatory driving. 171
Figure 5-4: a) Averaged pore pressure ratios and b) coordination number at selected height locations as a function of time, after Zeghal and El Shamy (2004). 173
Figure 6-1: Domain of investigation of the dry sand dynamic behavior within the framework of vibrodriving. 177
Figure 7-1: Indentation of elastic spheres. 184
Figure 7-2: Relationship between normal indentation, δ_z, and normal force, P, for $R_1 = R_2$. 185
Figure 7-3: Displacements at the surface of the contact area. 187
Figure 7-4: Distributions of surface stresses around the contact area, for ν = 0.3. 188
Figure 7-5: Distribution of stresses along the axis of symmetry, for ν = 0.3. 189
Figure 7-6: "Gross-slip" motion. 190
Figure 7-7: Stick-slip zones developed in tangential loading. 192
Figure 7-8: Relationship between the stick circle radius, c, the tangential rigid displacement, δ_x, the energy loss, ΔW, and the tangential force, Q. 194
Figure 7-9: Relationship between the twisting moment and the rigid rotation at the contact, after Johnson (1985). 196
Figure 7-10: Hysteresis loop for an oscillating tangential loading. 197
Figure 7-11: Impact of spheres. 198

Figure 7-12: Relationship between the normal indentation and the time during impact. 200
Figure 7-13: Elasto-plastic indentation of a sphere into an elasto-plastic half-space. 203
Figure 7-14: Variation of the normal restitution coefficient for different materials and impact velocities, after Tabor (1948). 204
Figure 7-15: Influence of the impact velocity on the normal restitution coefficient of a steel ball impacting different material blocks, after Goldsmith (1960) and Johnson (1985). 205
Figure 7-16: Tangential loading and unloading path for the case of constant normal force. 207
Figure 7-17: Tangential loading paths for increasing normal and tangential forces, after Di Renzo and Di Maio (2004). 209
Figure 7-18: Normalized tangential force, for different angles of incidence, as a function of the normalized impact time, for a steel disk ($\nu = 0.28$, $\chi = 1.256$). 211
Figure 7-19: Dimensionless angle of reflexion, ψ_2, plotted against dimensionless angle of incidence, ψ_1, for a steel disk ($\nu = 0.28$, $\chi = 1.256$), from Maw et al. (1981). 213
Figure 7-20: Dimensionless angle of incidence, ψ_2, plotted against dimensionless angle of incidence, ψ_1, for a "rubber" disk ($\nu = 0.5$, $\chi = 1.0$), from Maw et al. (1981). 213
Figure 7-21: Collisions of 3 mm glass spheres and 6 mm acetate spheres on an aluminum plate, with respectively $\zeta = 0.06$ and $\zeta = 0.28$, after Foerster et al. (1994). 216
Figure 7-22: Surface roughness of the transparent polycarbonate container. 220
Figure 7-23: Surface roughness of the phenolic resin sphere. 221
Figure 7-24: RMS roughnesses of the polycarbonate boundaries of the container and the phenolic resin sphere considering the length scale. 221
Figure 7-25: Sphere penetration logs for A = 1.5mm and various frequencies in the densification range. 222
Figure 7-26: Sphere penetration logs for A = 3 mm and various frequencies in the densification range. 222
Figure 7-27: Sphere penetration logs for A = 4 mm and various frequencies in the densification range. 223
Figure 7-28: Sphere penetration logs for A = 10 mm and various frequencies in the densification range. 223
Figure 7-29: Sphere penetration logs in the densification range for different amplitudes of vibration as a function of the number of cycles. 224
Figure 7-30: Comparison of the mean porosity variation of the granular sample during the vibration for different displacement amplitudes and similar acceleration of vibration, $\Gamma = 0.5$. Inset: enlargement of the curves in the steady vibratory regime. 230
Figure 7-31: Comparison of the variation of the contact density properties (contact number, number of passive particles, mean coordination numbers C_n and C_n^*) of the granular sample during the vibration for different displacement amplitudes and similar acceleration of vibration, $\Gamma = 0.5$. 230
Figure 7-32: Comparison of the variation of the vertical stress, σ_{22}, at the bottom of the sample during the vibration for different displacement amplitudes and similar acceleration of vibration, $\Gamma = 0.5$. 231

Figure 7-33: Comparison of the ratio of horizontal to vertical stresses, during the vibration for different displacement amplitudes and similar acceleration of vibration, $\Gamma = 0.5$. 231
Figure 7-34: Comparison of the dimensionless kinetic energy in the sample during the vibration for different displacement amplitudes and similar acceleration of vibration, $\Gamma = 0.5$. 231
Figure 7-35: Principal directions of contact, average normal contact force and average tangential contact force anisotropy during the vibration for different displacement amplitudes and similar acceleration of vibration, $\Gamma = 0.5$..... 232
Figure 7-36: Relationships between the number of cycle of vibration and the coefficient of contact normal anisotropy, a (a), the coefficient of average normal force anisotropy, a_n (b), the coefficient of average tangential force anisotropy, a_t (c) and the mobilized angle of friction, ϕ_{mob} (d) during the vibration for different displacement amplitudes and similar acceleration of vibration, $\Gamma = 0.5$..... 232
Figure 7-37: Comparison of the mean porosity variation in the measurement layers of the granular sample for different displacement amplitudes and similar acceleration of vibration, $\Gamma = 1.02$. Inset: enlargement of the curves in the steady vibratory regime. 233
Figure 7-38: Comparison of the evolution of the contact density properties (contact number, number of passive particles and mean coordination number, C_n, of the granular sample in the steady vibratory regime for different displacement amplitudes and similar acceleration of vibration, $\Gamma = 1.02$. 233
Figure 7-39: Comparison of the vertical contact stress variation in the measurement layers of the granular sample for different displacement amplitudes and similar acceleration of vibration, $\Gamma = 1.02$. Inset: enlargement of the curves in the steady vibratory regime. 234
Figure 7-40: Comparaison of the dimensionless kinetic energy in the sample in the steady vibratory regime for different displacement amplitudes and similar acceleration of vibration, $\Gamma = 1.02$..... 234